CRANFIELD UNIVERSITY

MOHAMMUD WASEEM KHODABUX

IMPROVEMENT OF STRUCTURAL HEALTH MONITORING PERFORMANCE FOR OFFSHORE WIND TURBINES SUBJECTED TO FATIGUE AND PITTING CORROSION

SCHOOL OF WATER ENERGY AND ENVIRONMENT
REMS CDT – Renewable Energy Marine Structures, Centre for Doctoral Training

EngD
Academic Year: 2015 – 2019

Supervisor: Dr Ali Mehmanparast
Associate Supervisor: Professor Feargal Brennan
July 2019

CRANFIELD UNIVERSITY

SCHOOL OF WATER ENERGY AND ENVIRONMENT
REMS CDT – Renewable Energy Marine Structures, Centre for Doctoral Training

EngD

Academic Year 2015 - 2019

MOHAMMUD WASEEM KHODABUX

IMPROVEMENT OF STRUCTURAL HEALTH MONITORING PERFORMANCE FOR OFFSHORE WIND TURBINES SUBJECTED TO FATIGUE AND PITTING CORROSION

Supervisor: Dr Ali Mehmanparast
Associate Supervisor: Professor Feargal Brennan
JULY 2019

This thesis is submitted in partial fulfilment of the requirements for the degree of EngD
(NB. This section can be removed if the award of the degree is based solely on examination of the thesis)

ABSTRACT

The offshore wind industry is growing fast in the UK. Structural health monitoring has been employed to assess the loads experienced by the structures but also to assess the damage for more intelligent inspection visits, thus reducing cost of maintenance and risk of injuries. Damage can exist in various forms but the two most detrimental ones are fatigue and corrosion.

This study delves into the technical aspect of SHM and applies interpolation (longitudinal and circumferential interpolation respectively) techniques to enable data fusion across the structure for fatigue damage assessment from bending strain gauge sensors (on offshore wind turbines). This gives a more refined interpretation of the most damaged locations, which can be used as a guide for targeted inspection rather than the traditional form. Also, it can be used in the design phases for improvement to consolidate the location the highest damage is more prone to. Further analysis has been done to improve the confidence in the readings and to reduce the sampling rate based on damage assessment.

Interpolation techniques have also been applied to quantify the damage with respect to pitting corrosion as a form of marine localised corrosion, which is vicious as it can be a prominent initiator for pit to crack transition. The algorithm developed marries for the first time in a data-driven approach pitting corrosion and a data-driven Structural Health Monitoring system. The main transitions from pit initiation to propagation with growth and an interface to capture the pit to crack transition and crack growth using linear elastic fracture mechanics have been developed. To improve the model, a field experiment has been done to express pit characteristics in a statistical fashion with respect to depth, which have been quantified using mass loss techniques, laser scanning and image processing.

Keywords:

Pit to crack transition, linear elastic fracture mechanics, data driven, data fusion

ACKNOWLEDGEMENTS

In the name of God the most Gracious the most Merciful.

I would first and foremost like to thank my supervisor Professor Feargal Brennan who has been a pillar and played a pivotal role in this doctorate journey. He has motivated, buoyed and supported me throughout and I can only say that it has been an absolute pleasure to work with a top brass of the structural and wind industry. I also thank Dr Ali Mehmanparast for his constant support throughout this REMS journey that we started together. I take the opportunity to also praise my sponsor ORE Catapult and industrial supervisor Hyunjoo Lee who have entrusted me with the sponsorship and also given me great opportunities to work on extremely interesting projects in the scope of my internship opening my mind-set to the current practice of the industry.

This project had a major part involving a field experiment and without the help of others, just to mention a few, Paul Causon, Anthony and Sally, who have stood steadfast and encouraged me to undertake such a colossal and risky task, this aspect of my doctorate would not have been fruitful. My close friend Carole Liao whom I have discussed at great lengths my project from which new ideas sprouted making this doctorate more interesting has the deepest thanks from the bottom of my heart. I'd also like to express my gratitude to one of my best friends Mr Roshan Bhurtha who has shared and rubbed his passion of laser scanning on me making possible one of the sub chapters.

Without the support of my sister and her constant encouragement from the very beginning to the last word typed, this task would have been more difficult. She has been my moral compass in trying times and may she be blessed forever for that. Thanking also my parents.

Last but not least, I would like to thank the REMS community that I have seen growing throughout the years. It has been an absolute joy to be part of this experience.

TABLE OF CONTENTS

LIST OF FIGURES

LIST OF TABLES

LIST OF ABBREVIATIONS

ABS	American Bureau of Shipping
ANN	Artificial Neural Network
ASTM	American Society for Testing and Materials
BSH	Bundesamt für Seeschifffahrt und Hydrographie
CAPEX	Capital Expenditure
DFF	Design Fatigue Factor
DNV-GL	Det Norske Veritas Germanischer Lloyd
EDS	Energy-dispersive X-ray spectroscopy
FBG	Fibre Bragg Grating
GL	Germanischer Lloyd
HISC	Hydrogen Induced Stress Cracking
IEC	International Electrotechnical Commission
LCOE	Levelised Cost of Energy
LEFM	Linear Elastic Fracture Mechanics
MIC	Microbial Induced Corrosion
OPEX	Operational Expenditure
OWF	Offshore Wind Farm
OWT	Offshore Wind Turbine
RBI	Risk Based Inspection
SCADA	Supervisory control and data acquisition
SCC	Stress Corrosion Cracking
SCF	Stress Concentration Factor
SEM	Scanning Electron Microscope
SHM	Structural Health Monitoring
SIF	Stress Intensity Factor
WT	Wind Turbine
XRD	X-Ray Diffraction

1 Introduction: Wind Energy

1.1 General Perspective

The high levels of carbon dioxide emitted as a result of the burning of fossil fuels for the production of electricity has reached alarming heights [1]. This trend has been manifesting and establishing itself in the past 70 years and a solution has to be found to curtail this effect to prevent an irreversible environmental impact (as shown in figure 1-1), carbon dioxide being a heavy weight of the greenhouse gases[2,3] . The fix lies in the harnessing of renewable energy for the production of electricity.

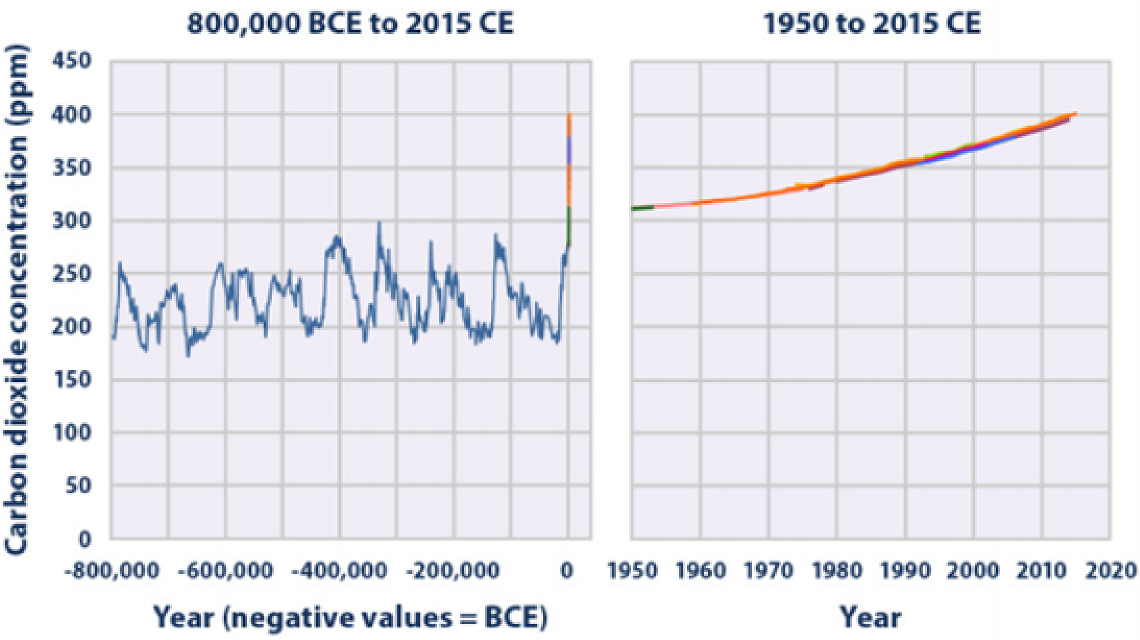

Figure 1-1: Carbon-dioxide variations over the years [1]

There are various forms of renewable energy sources from solar to wind to tidal and wave and geothermal amongst others[2]. The choice of the most appropriate resource is very often based on the availability of resources and, in Europe lately, there has been a major affinity towards wind energy indicated in figure1-2. The reason is that in the northern European countries, the high availability of wind resources has made it very attractive for wind energy to be exploited.

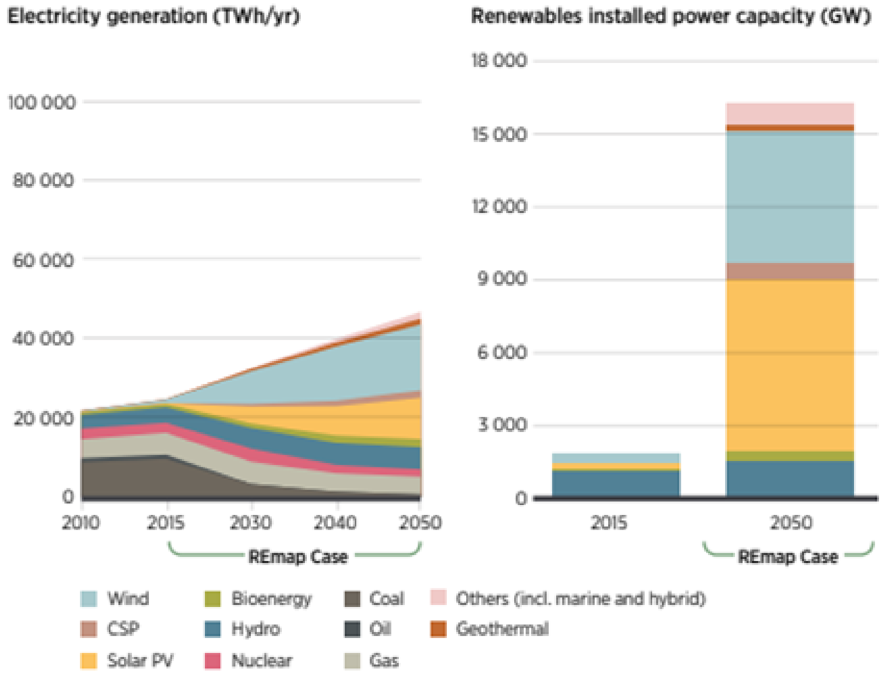

Figure 1-2: Share and growth of capacity in Europe [3]

The UK, being one of those countries, has jumped on board and has silently been undergoing an energy revolution.

The UK government is legally bound to reduce its carbon dioxide emissions by a solid 80%, from 1990 levels, by 2050 and generate 15% of the total energy by renewable energy by 2020[4].

The UK is recognised to have one of the best wind resources in Europe[5]. It, therefore, has to position itself as one of the pole players in its technological development. At the current stage, 7.7% of electrical generation is provided through wind energy. This figure (renewable energy production) is still on the low side when compared against the total energy demand (includes electricity, gas for heating purposes and transportation) of the UK where it represents only a mere 2%[6]. Despite this fact, this figure seems rather pessimistic, but the future trend does show a growth in the sector with further planned investments[7].

The whole concept of wind energy can be viewed as onshore wind and offshore wind, respectively. The technological maturity of the former is well established with more than 40 years of learning on its side[6]. Therefore, those improvements have made the onshore wind turbine more reliable and significantly helped in dropping the cost of energy. This said though, the social perspective vis-a-vis those turbines has not been so favourable. They are associated to the NIMBY (Not In My Back Yard) effect[8][9]. Many protests against such windfarms have been recorded leading to some cancellation of the projects and even some undergoing substantial unplanned modifications[10].

Offshore wind is also now a reality and despite having a near 20 year maturity lag behind its onshore counterpart, there have been heavy investments and major technological breakthroughs in the field[11]. The higher quality of the wind resource offshore made way for further exploration. The whole concept of NIMBY is totally obsolete in this case as most of those windfarms are far from shore and not in the field of sight. The complexity of the marine environment though makes the technology more expensive[6] but the offshore wind market is soldiering on and may represent an increase of the additional installed wind power capacity of up to 100 GW by 2030 and 400 GW by 2045 globally[12].

All the indicators show that both onshore and offshore wind is here to stay and flourish in the years to come. There are challenges ahead mostly in offshore wind where the Levelised Cost of Energy (LCOE) has to be significantly reduced to ensure the survival of this sector. Over the years, the LCOE has gone down from £205/MWh in 2001 to £157.50/MWh in 2015 as indicated in figure 1-3. 2017 was a particularly good year for the offshore wind sector where prices were seen to tumble to £57.50/MWh making it cheaper than gas and nuclear energy for the 2023 horizon[13]. This has opened a new potential investment opportunity of £17.5 billion for the next four years. Despite this fact, the contribution of the OPEX in the LCOE still requires attention to bring the cost further down shown in figure 1-4.

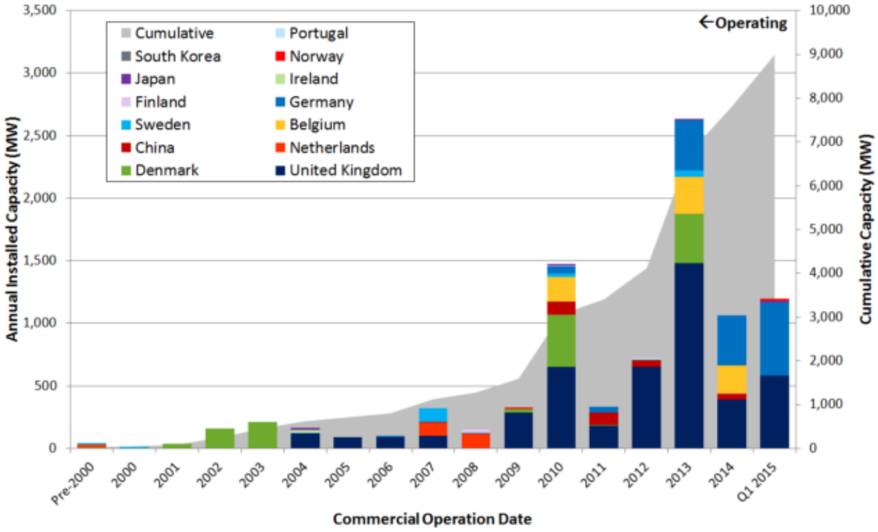

Figure 1-3: Growth in offshore wind at a worldwide level [14]

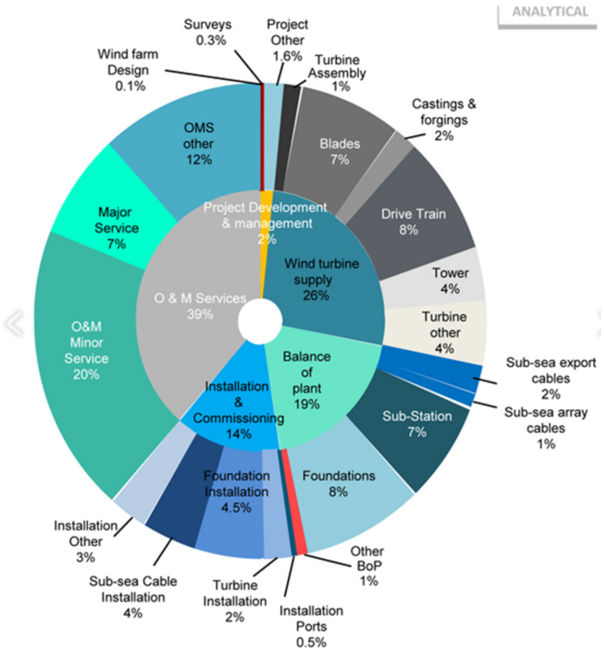

Figure 1-4: OPEX vs CAPEX[1]

1.2 History of Wind Energy

Ancient civilisations have used wind energy for work purposes albeit not producing electricity, which is a novel luxury in comparison to the history of

---

[1] https://eninconperspectives.com/opportunity-assessment-in-offshore-wind-for-value-chain-players/ (28/05/2019)

humans. It is interesting to observe that through various eras, the use of wind as a form of primary energy was used for different purposes. For instance, the ancient Egyptians used it to power sail boats, which is effectively still in use nowadays as a prime mover in modern catamarans and sailing boats. The more interesting part is the evolution of the mechanical and electrical components. Worthy to mention (despite the absence of any electrical parts) is the vertical axis windmill which dates back thousands of years ago that was discovered on the Persian-Afghan border[15]. Those Panemone windmills were used for grinding corn and flour and also pump water[16] and can still be found in working conditions to date.

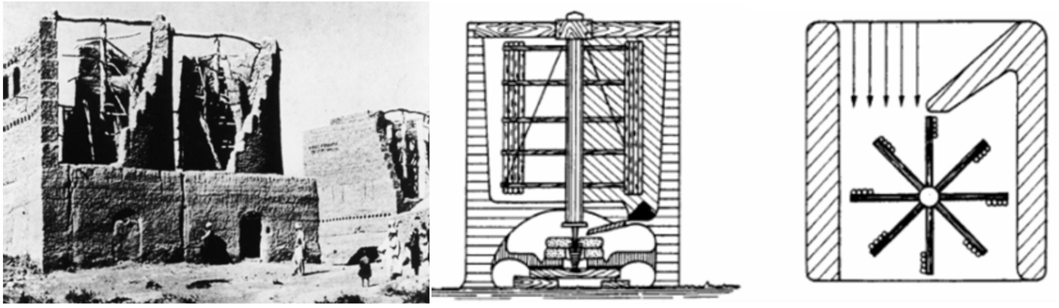

Figure 1-5: Persian windmill and schematic of mechanism [17]

From that time to 1887, the purposes of wind energy was to drive windmills for mostly pumping and grinding purposes where the Persian windmill is still an existing structure shown in figure 1-5. There was a major breakthrough in 1887, and a major departure from sole mechanical outputs, when Professor James Blyth designed and constructed a wind turbine that was 10m high and used cloth sails to drive the turbine. Accumulators were charged and the electricity used mainly for lighting purposes. His noble work was met with heavy opposition from the local residents who perceived his effort as ‘the work of the devil’[16].

Another important milestone was met by the Danish scientist Poul la Cour in 1908 whose contribution to the field of wind energy has been nothing short of legendary. He observed that fewer blades spin faster and are more effective than turbines with many blades, thus starting to ferment the idea of the 3 bladed turbine, which is now part of the print of modern wind turbines[18].

The Darrieus turbine (vertical axis wind turbine) was patented by Georges Jean Marie Darrieus in 1931; a turbine still used today for smaller powering applications. In the same year, a horizontal axis wind turbine was built with a 100kW capacity, 32m high and with a load factor of 32%[19].

In 1957, a student of Poul la Cour built a 3 bladed horizontal wind turbine with a rotor diameter of 24 metres. The wind turbine was rated at a power of 200kW. This turbine shares some similitude with its modern counterpart[16].

The world would not see the first multi-megawatt wind turbine until 1978 when some school teachers and students created a 2MW machine[16]. It was pioneering technology that enabled the greats in the industry to the likes of Siemens and Vestas to appropriate technology that would form the bedrock of the current wind turbine[20].

After that breakthrough, it did not since take long for wind farms to see the light of day and the first one came in 1980. More wind farms went up in Europe and the USA that then started a silent energy revolution.

The wind farms and wind turbines produced were all designed to be operated onshore. It took slightly more than a decade for the first offshore wind farm to appear in the southern part of Denmark. 11 wind turbines were deployed with a wind capacity of each turbine of 450 kW[21].

Meanwhile in the UK, the first onshore wind farm was developed in Cornwall that could power 2700 homes[16].

In 1995, Vestas produced the first offshore wind turbine and in 2003 the UK opened the first offshore wind farm in Wales consisting of 30 wind turbines capable of producing 2MW each.

Testing for various foundations from monopiles to jackets to tripod were undertaken but in 2009 a major milestone was reached as the first large capacity wind turbine started its operation off the coast of Norway[22].

The installation of offshore wind turbines increased exponentially in the UK and over 3 GW was installed since making it the highest in the world in 2012. The

London Array was completed making it the largest wind farm in the world having a total capacity of 630MW. To date the UK is still maintaining this trend as the country with the highest installed offshore wind turbines in the world[23].

1.3 Offshore Wind vs Onshore Wind

Offshore wind and onshore wind have great similarities but also have fundamental differences especially in terms of design considerations and maintenance.

Both have their pros and cons and are illustrated below[27-31]

1.3.1 Offshore Wind Advantages

- Transportation of larger wind turbines (bigger tower, rotors and nacelles) can be easily achieved and even larger structures in the oil and gas industry have been deployed.
- They are less intrusive as they are out at sea and, thus, remove the NIMBY effect completely.
- More wind resources are available, thus increasing the capacity factor of the wind turbines.
- Huge development in terms of creation of sea ports, offshore manufacturing plants and jobs.

1.3.2 Offshore Wind Disadvantages

- The cost of offshore wind farms is still more expensive when compared to fossil fuels or even onshore wind but the gap is closing fast.
- Inspection and maintenance tend to be more time consuming and costly.
- Low reliability of rotating components
- More prone to health and safety related accidents due to the nature of the offshore environment.

1.3.3 Onshore Wind Advantages

- Mature technology, which makes it relatively cheap.
- Easier and cheaper for inspection and maintenance.
- Faster installation.

1.3.4 Onshore Wind Disadvantages

- Deemed as an eye sore on the landscape.
- Blockages of the wind resource, such as buildings and hills.
- Can be noisy as it produces the same noise levels as a lawn mower.

1.4 Trends in Offshore Wind

The offshore wind industry is still a rather young one compared to its other renewable counterparts. That said, offshore wind has been growing very rapidly and over the next decade is expected to see an exponential boom especially in industrialised countries but also in the fast developing countries like China and India.

The trends to be observed are:

1. The reduction and the rate of reduction of the LCOE over the years and also the prediction through extrapolation.
2. The potential increase in offshore wind capacity over the years in the UK and finally,
3. The size of the turbines.

The reason for the choice of these three trends can be explained in the following terms. All engineering projects are governed by economics. In a competitive world where different sources of energy are being explored for production of electricity, it makes sense that the one which is economically more competitive takes the crown. Since the stage of development of most renewables is still not fully mature, time needs to be given for growth to maturity and the necessary financial and technological support is required to make those industries manage this challenging task.

1.4.1 Levelised Cost of Energy

Levelised cost of energy (or LCOE) is defined as the revenue required to earn a rate of return on investment equal to the discount rate over the life of the wind farm[25].

The LCOE can be calculated as follows:

$$\boldsymbol{LCOE = \frac{\sum_{t=1}^{n} \frac{I_t + M_t}{(1+r)^t}}{\sum_{t=1}^{n} \frac{E_t}{(1+r)^t}}}$$

Equation 1-1

Where:

- I_t investment expenditure in year t
- M_t operations and maintenance expenditure in year t
- E_t energy generation in year t
- r discount rate
- And n lifetime of the project in years

In general, the LCOE can be broken down as the following costs[26]:

- *Capital Expenditure (CAPEX):* costs for building and installing the wind turbine.
- *Operating Expenditure (OPEX):* costs for inspection and maintenance and proper operation of the wind turbine/wind farm.
- *Discount rate:* the return on investment required to attract project investors.
- *Net capacity factor:* the fraction of average power generated over the maximum possible electrical energy output

The LCOE is a clear indicator of the economic performance of the industry and its potential growth. Over the years, the trend in the offshore wind industry has shown a consistent decrease in the LCOE price and predictions for the future cost are showing further reduction. This represents a massive potential in the growth of the industry, which will contribute in the learning curve expertise and, thus, provide more knowledge in the field for improvement of the reliability of the components, for instance, or improvement in the design phase amongst others, thus further helping in reducing the costs for the next generation of offshore wind turbines.

The LCOE of offshore wind is still high compared to the other form of energy harnessed but the slope or rate of LCOE is far steeper, which implies that the cost decreases over time fall faster than the rest of the technology [18]. Within six years, it will be lower than solar, nuclear and gas in the UK. It has to be noted that those mentioned are mature technologies and this is the reason behind their considerably low rate. In the case of the non-renewable, the cost is increasing and this is due to the increase in the price of the primary/raw resource. This is one of the great advantages of renewables in general; the resource is free and upon proper choice of the location of deployment and installation, those resources can be optimised to increase the capacity factor [18].

After 2023, the selling cost of offshore wind continuing with that trend will be lower than the wholesale price of electricity in the UK. Also, following the trend, it might be possible that offshore wind will have a LCOE lower than onshore wind. At this stage, there are subsidies from the government that allow those new energy technologies to develop and become economically viable in the near future.

The concept of SCOE (Society Cost of Electricity) is brought to light[34] broadening the spectrum of the cost of electricity by introducing more parameters, such as partially hidden subsidies, grid access costs, variable costs, social costs, economic benefits and geopolitical impact. Using this parameter, in the not so far distant future, it can be observed that the cost of offshore wind will be as low as onshore wind in the UK and lower than coal represented in figure 1-6

Figure 1-6: SCOE vs. LCOE [27]

This shows a promising future for offshore wind with further investment on the horizon.

1.4.2 Wind Turbine Size

Onshore and offshore wind turbines have seen a dramatic increase in size over the years[28]. In a period of 30 years, the size of the turbines has more than quadrupled presented in figure 1-7. Some researchers have carried out various studies to try to provide scientific reasoning for this approach of commercial scaling up of wind turbines[28]. It was based on the energy output but also the energy required for building, transporting, maintaining and disposing of them. It also mentions that larger turbines produce a far larger amount of energy than their smaller counterparts but barely consumes additional energy to manufacture bigger turbines. It was also observed that with each doubling of the wind turbine manufacturing over time, the global potential per kilowatt-hour of electricity drops by 14 percent. [28]

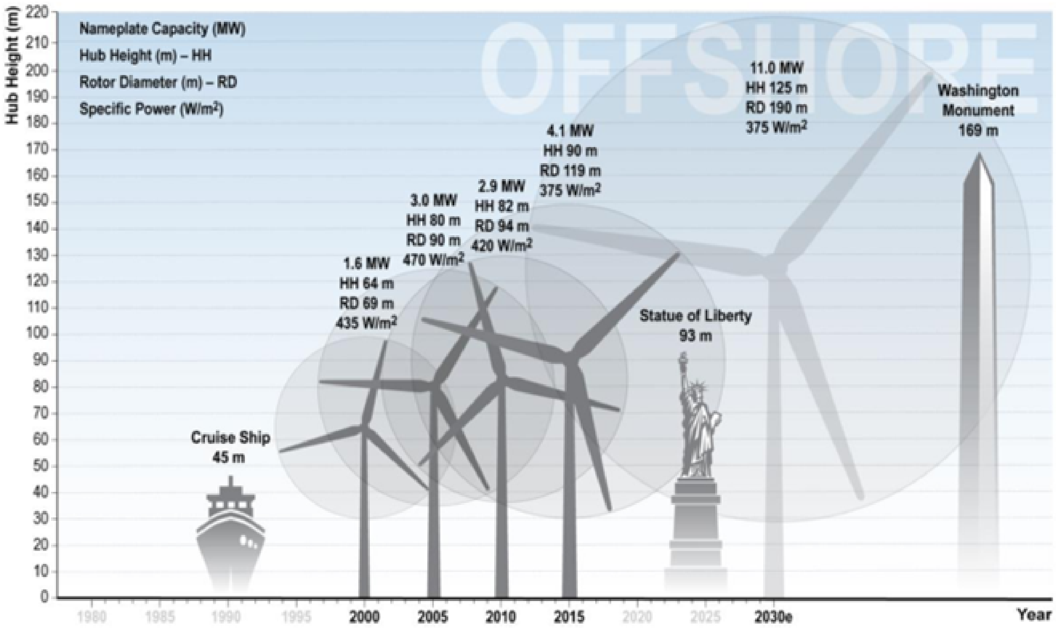

Figure 1-7: Increase of turbine size trend [29]

163 experts in the field of wind energy were asked to predict which major contributors will help to lower the cost of wind energy and, topping the list, the size of the rotor and turbine capacity will have to increase[30]. The outcomes are summarised in the table 1-1 below[29]:

Table 1-1: Main drivers for cost reduction of wind energy [29]

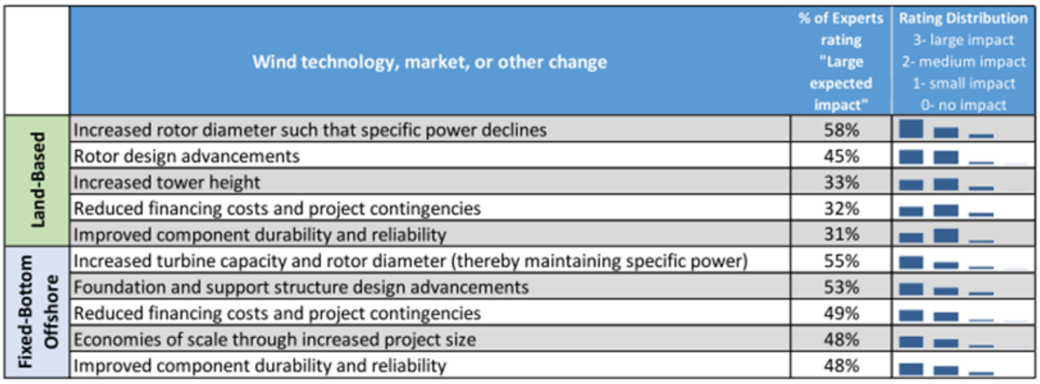

	Wind technology, market, or other change	% of Experts rating "Large expected impact"	Rating Distribution 3- large impact 2- medium impact 1- small impact 0- no impact
Land-Based	Increased rotor diameter such that specific power declines	58%	
	Rotor design advancements	45%	
	Increased tower height	33%	
	Reduced financing costs and project contingencies	32%	
	Improved component durability and reliability	31%	
Fixed-Bottom Offshore	Increased turbine capacity and rotor diameter (thereby maintaining specific power)	55%	
	Foundation and support structure design advancements	53%	
	Reduced financing costs and project contingencies	49%	
	Economies of scale through increased project size	48%	
	Improved component durability and reliability	48%	

1.4.3 Depth and Distance from Shore

Wind turbine deployment is dependent to a great degree on the resource availability. Figure 1-8 compares the various sites for OWT deployments in Europe and indicates that the deployments distance is different from countries to countries and the UK tends to have shallower waters than their European counterparts.

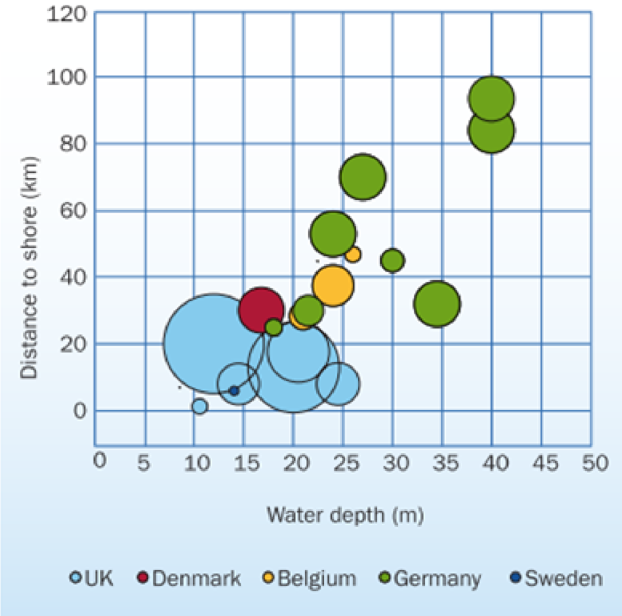

Figure 1-8: Deployments of wind turbine depth and distance to shore for different countries [31]

In general and when analysed on the time scale, the depth of deployment goes further and deeper as the shallower waters have already been exploited for other projects. In 2015, the average water depth of offshore wind farms was 27.2m, which is slightly more than the 22.4m in 2014 shown in figure 1-9. For the distance to shore, the difference was significantly more in 2015 where the average distance was 43.3km and in 2014 it was 32.9km[32].

The distance from shore is another important criteria. It is important for both CAPEX and OPEX.

The CAPEX is increased in the form of longer export cables and larger transportation distance from a port, amongst others.

The OPEX is increased in the form of transportation of the maintenance and inspection personnel[33][34] but the capacity factor might be increased, thus helping to balance the books.

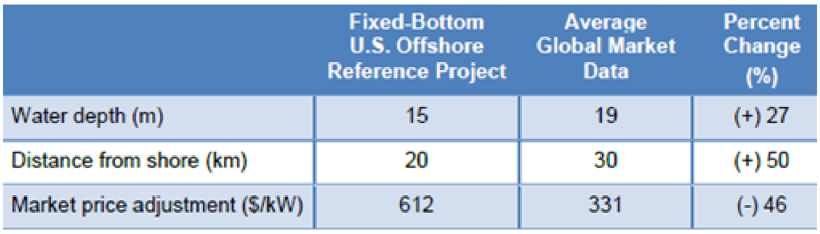

	Fixed-Bottom U.S. Offshore Reference Project	Average Global Market Data	Percent Change (%)
Water depth (m)	15	19	(+) 27
Distance from shore (km)	20	30	(+) 50
Market price adjustment ($/kW)	612	331	(-) 46

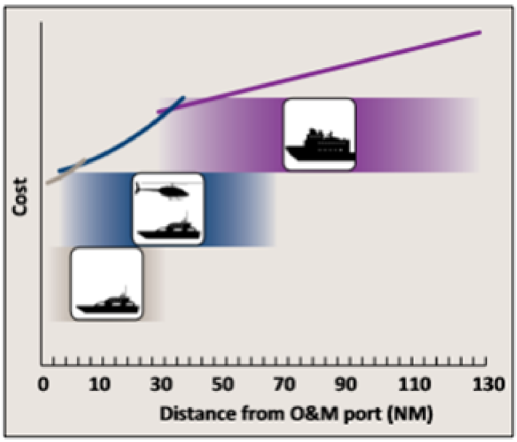

Figure 1-9: Cost vs distance from port [35]

1.5 Types of Foundations

In the offshore wind turbine (OWT) world, there are various kinds of foundations deployed often dependant on the depth of the water as indicated in figure 1-10.

Those foundations can be classified in two groups, namely:

- Bottom fixed structures
- Floating structures

The bottom fixed foundations consist mainly of[36][37]:

a) Monopile
b) Gravity base
c) Jacket
d) Tripile
e) Tripod

The floating foundation is a rather new concept and deployed mainly in regions of deep water where bottom fixed do not make any economic sense[38]. Currently, they represent a very small percentage of the market but are expected to grow with major projects to be seen in France, Japan and the USA.

The floating foundations consist mainly of:

f) Spar
g) Semi-submersible

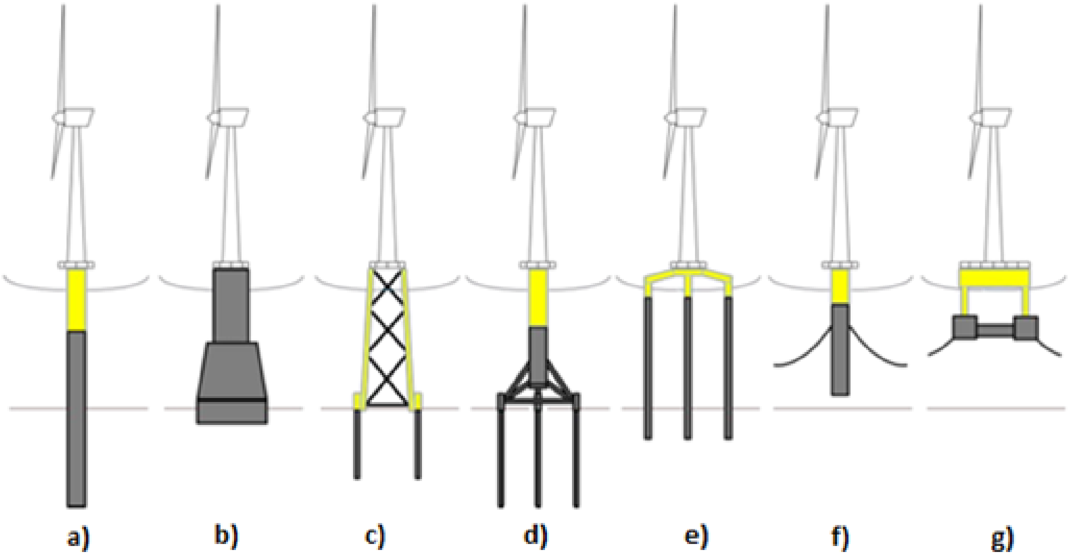

Figure 1-10: Foundation types [38]

1.5.1 Monopiles

Monopiles are deployed in shallow water of generally less than 30m even though the concept of XL-monopiles is now being considered. They are going to be giants of the ocean having dimensions over 10m in diameter with a 150mm thickness and expected to be operational in depths of up to 40m[38][39].

Monopiles currently take the largest part of the market representing 78% of the market in 2013 represented in figure 1-11. Of the installed capacity in 2015, 97% of those foundations were monopiles[39].

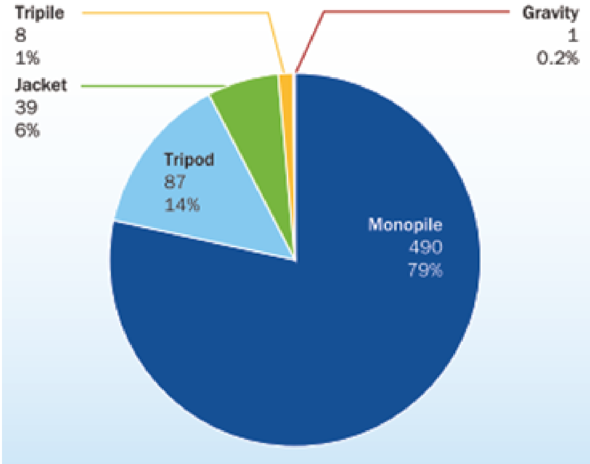

Figure 1-11: Portion of monopiles against other foundations in 2013 [31]

In general, the monopile is a long tube that is piled into the sea bed. The transition piece (TP) is slotted at the top of the pile where the tower is connected. The grouting mechanism is used to hold the two in place. The dimensions of the monopile consisting of diameter, thickness and length are determined by the loading, maximum water depth and sea bed conditions.

1.5.1.1 Advantages and Disadvantages of Monopiles

Advantages[36], [37]

- Simple and quick fabrication process proven concept.
- No seabed preparation required. Low price per ton of steel. High serial production

Disadvantages[36], [37]

- Limitations of fabrication and handling from certain sizes
- Limitations due to heavy installation equipment (hammers)
- Large scour protection required. Flexible at water depths
- Limited to large water depth. Difficult to remove after design life

1.5.2 Jacket Structure

Jackets are being used for water depths between 30 to 60m. The need to go into deeper waters was the main reason for this technology to be implemented for offshore energy. The roots of jacket structures, though, can be found in offshore oil and gas. The four legged jacket structure has braces welded to the four legs[43], [44], [47].

A transition piece is required to fit the tower and the turbine.

The jacket structure is becoming the most commonly used structure for water depths above 30m and future strategies are looking at deployments of up to 70m [48].

1.5.2.1 Advantages and Disadvantages of Jackets

Advantages[43-48]

- Lightweight and stiff structure
- Has a better load path compared to monopiles – the load is distributed across the braces and the legs
- For transitional and deep waters, it is economically effective
- No scour protection required
- Offers structural redundancy – if one brace is damaged, the structure will survive
- Good response to waves

Disadvantages[43-48]

- Complex manufacturing
- Complex inspection
- Complex connection to transition pieces

1.5.3 Gravity Base Foundations

The first support structure to be used in the first offshore wind park in 1991 was a gravity base and operates at water depth of up to 40 metres.[37], [41]. Gravity base foundations are generally a concrete based structure that can be ballasted using water, sand and rocks.

At the centre of the structure, there is a protruding steel shaft. The tower and the turbine can be connected to the shaft and, thus, does not require any transition piece.

1.5.3.1 Advantages and Disadvantages of Gravity Base Foundation

Advantages[37], [41].

- No requirement for the installation of a TP
- Structure can be floated
- Long lifetime
- No need for piling

Disadvantages[37], [41].

- High production cost
- Preparation of sea bed is critical
- Not suitable on soft seabed

1.5.4 Suction Caisson

The suction caisson is an interesting foundation in the sense that it does not require any piling or seabed preparation. It uses a water pump to reduce the water in the enclosed area, thus reducing the pressure inside. The outer pressure being higher then pushes the caisson further into the sea bed. The suction caisson is not heavily employed yet but there have been some demonstrators deployed[37], [41].

Their operating depth is between 30 to 60 metres.

1.5.4.1 Advantages and Disadvantages of Suction Caisson

Advantages[37], [41]

- Can prove a substantial cost reduction due to no or minimal seabed preparation
- Installation is environmentally friendly as there are no piling
- Transport and installation in one process

Disadvantages [37], [41]

- Still to be proven

1.5.5 Floating Foundations

With the structures going deeper and deeper to explore the richer wind resources, it is clear that the bottom fixed will not be economically viable. Some countries like France and Japan have deep waters and are compelled to explore such technology to join the wind race[39][42].

1.5.5.1 Advantages and Disadvantages of Floating Foundations

Advantages [39][42]

- Less sensitive to water depth and wave loads
- Can tap in better wind resources
- Visual effect reduction
- Ability to locate further offshore
- Installation of the full turbine can be done onshore

Disadvantages[39][42]

- Expensive mooring and platform costs
- Complex design
- Little experience

1.6 Challenges with Offshore Wind Structures

Irrespective of the type of foundation used, there is a common problem shared that has a substantial impact on the LCOE. This comes down to the OPEX.

The OPEX can be broken down as shown in figure 1-12:

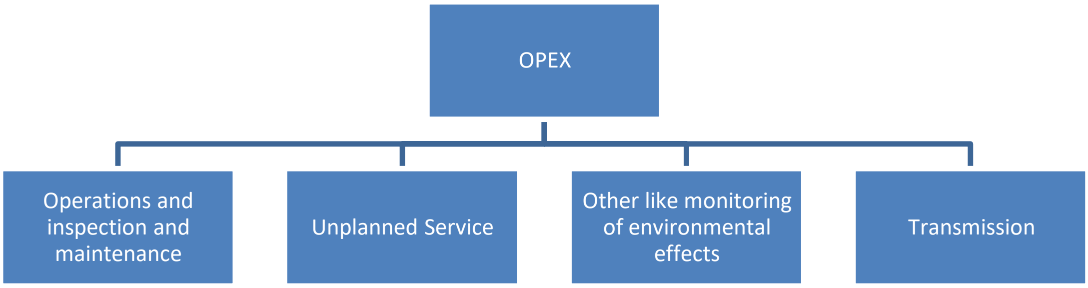

Figure 1-12: OPEX breakdown

The OPEX comprises 20 to 25 % of the LCOE according to different sources. Out of the 35% higher limit from the LCOE, 20% is represented by the transmission cost. The rest represents operations and maintenance.

Operations can be defined as activities contributing to high level management of the asset's remote monitoring, environmental monitoring, electricity sales, marketing, administration and other back office tasks. Operations represent a very small portion of O&M expenditure[35].

Inspection: consist of observations, measurements, tests, etc. to find the current condition of the wind turbine and to investigate a problem that has been flagged[43].

Maintenance: is the repair or replacement of worn or damaged parts. It can be broken down into corrective or preventative maintenance[43].

Corrective maintenance is the repair of an already damaged component. It tends to be useful for household components like a lawn mower. In offshore applications, it tends to be costly and will fall into the category of unplanned service, thus decreasing the availability of the turbine causing an increase in the LCOE.

Preventive maintenance is a smarter form of maintenance that includes proactive repair or replacement of worn components based on routine inspections or information from condition monitoring systems[35].

1.6.1 Inspections in the Offshore Wind Industry

There are various forms of inspections inscribed (some Standards also give a suggestion for the frequency of inspections).

- Periodic inspection: this involves the kind of inspection that happens on a regular basis.

The DNV Guideline[44] prescribes those types of inspection schedule for the foundation of the turbine based on the design fatigue factor(DFF). The more conservative the design is, the less inspection is required but the trade-off is the initial cost which will be higher. This balance is a challenging one. For instance, if the DFF is decreased, it implies that the design is less conservative requiring more inspections, which is also a rather costly feat. In addition to the cost, the safety of the inspection personnel is paramount. More inspections mean that there will be more frequent visits to the turbine and this substantially increases the risk of the personnel regarding injuries or fatalities.

Continuous inspection is required for a minimum of 20% of offshore wind foundations.

The **GL Guidelines** [45][46]indicate that periodic inspections must be carried out on the tower, substructure and foundation and that significant attention must be given for damage based on corrosion, corrosion protection, marine growth, deformation, damage cracks and abrasions. When necessary, underwater divers will have to be sent to further assess the structure for damage.

Continuous inspection is required for a minimum of 20% of offshore wind foundations.

The **IEC Guidelines** concentrate mostly on subsea inspection, which entails where the removal of marine growth has to be performed as well as maintenance of scour protection. Specifically mentioning corrosion, protection systems have to undergo an inspection regime.

ABS Guidelines firstly concentrate on the structure above water. When significant degradation is observed above, then an underwater inspection is undertaken. This requires a diver or a ROV to carry out the inspection. The submersed structural elements to be observed are underwater structure, scour protection, sea floor and the corrosion control system. It is also worth mentioning that the ABS practice demands that those inspections are undertaken by the owner and monitored by a surveyor.

Continuous inspection is required for a minimum of 20% of offshore wind foundations.

In terms of recommendations for inspection frequency, different countries have different policies.

Germany[47][48]**:** inspection is key in Germany if operators want to continue operating wind farms. An annual inspection is fundamental and regulated by the Bundesamt für Seeschifffahrt und Hydrographie – BSH.

The Standard “Design of Offshore Wind Turbines” and the “Guidance for use of the BSH Standard ‘Design of Offshore Wind Turbines’” are intended to provide legal and planning security for development, design, implementation, operation and decommissioning of offshore wind farms within the scope of the Marine Facilities Ordinance .

According to the above-mentioned BSH Standards, the entire system (turbine and support structure) shall be inspected in detail as part of the periodic inspections.

Periodic inspections shall be performed annually on 25% of the offshore wind turbines of an offshore wind farm, so that all offshore wind turbines will have been inspected after each block of four years. It is also requested by the BSH that 10% of the offshore wind turbines are monitored for condition monitoring.

Regarding the support structure, inspection must be carried out for corrosion, cracks, and scouring.

Denmark[48][47]**:**

Guidelines for Executive Order on a technical certification scheme for wind turbines no. 73 of January 25th 2013 takes into account of the whole process from construction to operation of wind turbines.

The Executive Order ensures that the installed wind turbines (WTs), both onshore and offshore, are used for production of electricity safeguarding that the environment and safety and the maintenance of the wind turbines are carried out as prescribed.

The annual inspection for the substructure comprises:

- The foundation is to be inspected for cracks.
- Seals are to be checked for functionality.
- Any bolted joints of the foundation are to be inspected for rust and corrosion.

Inspection every 3 years does not include any specifics for the turbine foundation but instead deals mostly with rotor blades.

- Risk based inspection - RBI

RBI is a method of inspection based on the risk, which takes into account the consequence of failure and the probability of failure of a component. The components of a large structure are analysed and the risk is computed for each of them. The components are then ranked based on the risk of failure and based on that, an inspection regime can be set up[49].

It helps in prioritising inspections and also introduces the idea of preventative maintenance, which in the case of offshore wind turbines will give adequate time for planning as they can be affected by adverse weather conditions especially during winter. Overall, RBI can be perceived as an inspection optimisation technique[50].

1.6.1.1 Dangers in the Offshore World

The offshore world can be an unforgiving one. It is a challenging environment to work in and has over the years encountered a significant number of incidents in which fatalities were registered. The addition of the wind industry to the offshore scenery has taken a fair share of the number of incidents.

In the UK a special body, the G+, has been implemented to deliver world class health and safety performance across all activities in the offshore wind industry. A few headlines in the newspaper brought a very negative reality to the general public with headlines such as ‘Offshore wind farms 'wild west' of renewable energy, union warns’ or ‘killer offshore wind parks’, amongst others[51]. This can cause a negative perception by the public and, thus, can slow progress.

Unfortunately, some registered fatalities and serious injuries have been documented in the offshore wind industry as shown in figure 1-13 [52].

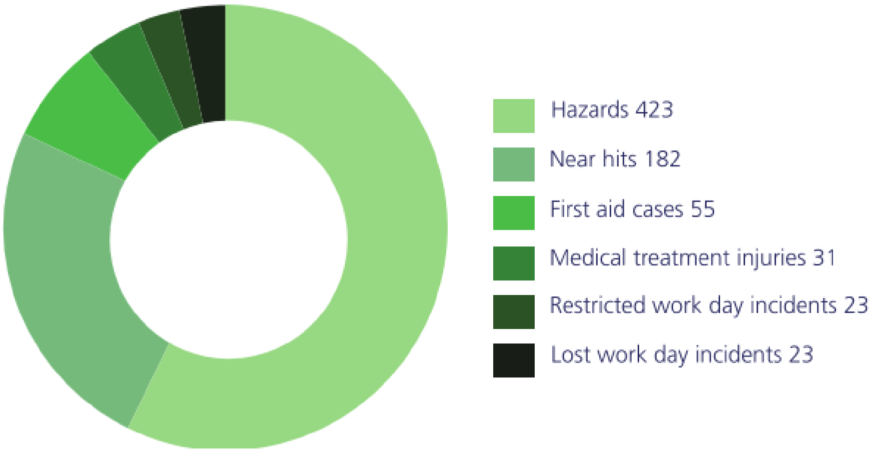

Figure 1-13 : Accidents related to offshore wind breakdowns [53]

In 2016, 737 incidents were reported at sea with no fatalities for offshore wind related activities broken down in figure 1-13.

1.6.2 What is the Solution?

To decrease the outings to wind farms and have a more effective and informed inspection schedule, contributing to lowering the health and safety hazard, a better system departing from the traditional one needs to be employed that limits human intervention and boat transfers. To do so, the concept of monitoring through the deployment of sensors and analysis of the data need to be examined. For a structure, this campaign is known as Structural Health Monitoring - SHM.

1.7 Structural Health Monitoring: What is SHM?

SHM can be defined as the process of acquiring and analysing data from on-board sensors to evaluate the health of a structure[54]. SHM has applications in large civil engineering projects but also in the automotive and aerospace fields, amongst others. Very often it is confused with condition monitoring (CM). The CM term is more often used when dealing with rotating bodies.

SHM is a highly interlinked field where structure, instrumentation, data analysis, and mechanical concepts are all combined for successful implementation. The idea of SHM is tied with the concept of damage. The whole process needs to give an output, which is often the damage of the structure. This damage gives an idea of the state of the structure. From there informed maintenance decisions can be taken, thus making it more effective for planning and helping in reducing the operational costs as a result.

The structure and implementation of SHM needs to be carefully planned for the process to be informative. To be able to do so, a guideline has been set up by the Los Alamos Lab in the USA[55]. This procedure consists of 4 blocks, as shown in the figure 1-14 below.

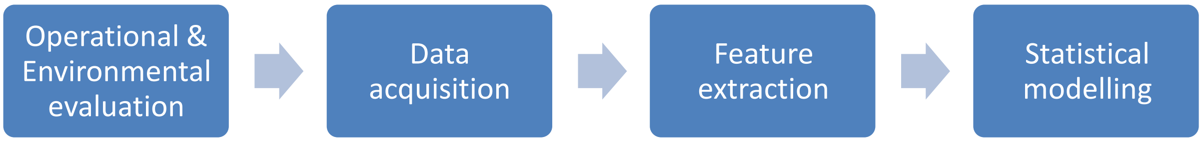

Figure 1-14: SHM blocks

To properly have such a system installed, various different aspects have to be considered.

The original framework [56]can be interpreted as follows. The authors looked at the problem as a series of questions that needs to be addressed to unveil the type of monitoring system to be implemented. Each of the above blocks in the figure are summarised below:

- *Operational and Environmental evaluation:* In this section, the type of damage to be considered for monitoring has to be defined. The right sensor will have to be chosen for this type of damage sensing. Once this is defined, the operational and environmental scenarios are assessed. This can be challenging as it can be loaded and non-loaded (corrosion happening) and have a significant impact on the structure. An example of a loaded structure will be the wind loads on a tall tower and non-loaded will be a corrosive environment.

One sensor will have to monitor one parameter. To measure more aspects and gauge any interaction, there will require different sensors monitoring independently the structure that will have their data linked together in the feature extraction stage. In OWT the environmental sensors, structural and operational sensors of different nature are combined together to understand the behaviour of the structure. For instance considering the loads for an offshore wind turbine subjected to a normal condition of wind speed of about 10m/s and a storm condition of wind speed of 30m/s, the loads on the OWT will be different which will affect the operations.

An important viewpoint is to also realise the limitations of the SHMs. This can be viewed in a technical and economical light. Technically, some limitations can exist in the inability of the sensors to detect the damage or the resolution of finding the damage. The economical perspective is an important aspect. All engineering projects have to be cost justified. If the damage to be assessed is not a costly or a risky one, then it is possible to neglect monitoring.

- *Data acquisition:* At this stage, the sensors will be chosen to monitor those environmental and operational impacts on the structure. If an offshore wind turbine is to be monitored, the main load profiles will be as a result of the operational condition and also the environmental loading on the structure. Considering an offshore wind turbine, the vibration analysis can be done. To be able to do so, the sensor type, location and number of them will have to be decided. In this case very often, accelerometers can be used and those are placed at different locations chosen by the presence of the dominating loads. For instance, there will very likely be one in the tidal regions, wave regions, current regions, at the top and bottom of the tower for the wind and operational loads. The operational conditions will be also assessed to make sense of the spectrum at a later stage, meaning that the rotor speed and blade passing speed will have to be monitored, and based on the position of the nacelle, the sideways and fore aft frequency can be determined. In the data acquisition phase, the sampling frequency needs to be cautiously decided. This is usually done based on the Nyquist sampling frequency[57]. For field projects though, the sampling frequency can be up to ten times the frequency of interest. Filtering and cleaning the data is also fundamental in that phase.

- *Feature extraction:* This is the extraction of the damage. Considering that the sensor is being used for fatigue purposes, then the data is processed to compute the fatigue damage. Feature extraction deals with the processing of the raw data and transforming it through mathematical models to extract valuable information that gives the state of the structure.
- *Statistical modelling:* Usage of machine learning and other tools for damage evolution and predictions. Once the damage is extracted, it is possible to compare the states of the damage under similar operating conditions for instance. If they are not matching, then a closer inspection of the structure is required to understand the reason behind that change.

1.8 Sensors

1.8.1 Electrical Resistance Strain Gauge

1.8.1.1 Working Principle

The electric resistance strain gauge is the most commonly used strain gauge due to its maturity in the field of strain measurement.

When there is a change in strain, the electric resistance varies proportionally[58]. Numerous resistance strain gauges of different sizes and shapes and various electronic devices that are used to measure small voltage changes are commercially available[59]. Measurements with resistance strain gauges can be performed over a wide range of temperatures[60].

A common type of strain gauge is the grid metallic foil. The reason behind the grid format is it maximises the amount of metallic foil with respect to the strain in the parallel direction. This, in turn, reduces the cross sectional area and the grid is minimised reducing the effect of shear strain[61]. A schematic of an electric resistance strain gauge is shown in figure 1-15.

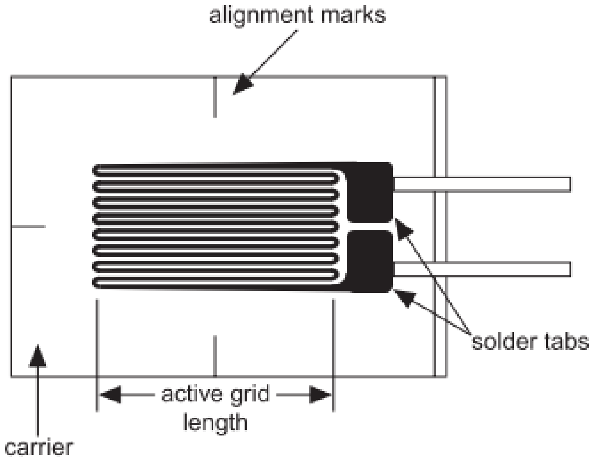

Figure 1-15: Strain gauge [58]

Proper bonding of the strain gauge to the test specimen or part is fundamental for proper transferring of strain from the test specimen to the strain gauge.

A fundamental parameter of the strain gauge is its sensitivity to strain, expressed quantitatively as the gauge factor (GF). Gauge factor is defined as the ratio of fractional change in electrical resistance to the fractional change in length (strain)[58].

The resistance is affected by the temperature. Monitoring of the temperature is crucial for proper measurement of the strain. A correction factor is introduced based on the temperature recorded to factor in such effects depending on the strain gauge connection.

1.8.1.2 Advantages and Disadvantages

Resistance strain gauges can be time consuming to install as the surface requires preparation. This involves polishing the surface, gluing the gauge, soldering the wires and protecting the gauge from damage[62].

The strain gauge, even if not costly, is a single-use element. When glued, it must stay in the same place. Strain gauges are affected by the environmental conditions, like humidity, a corrosive environment and high temperatures[60].

The advantages and limitations are listed as follows[63]:

Advantages

- Mature technology
- Low cost
- Commercial instrumentation readily available
- Very accurate (down to 0.1μmicro-metre/meter)
- Small mass and volume
- Remote monitoring possible, including wireless instrumentation
- Measures tension and compression
- Capable of elastic and post yield measurements
- Good frequency response
- Easy to attach
- Usable on a wide range of materials

Limitations

- Measures at a point (user must know where to place the gauge)
- Some skill needed to install and interpret result
- Strain averaged over grid length of gauge
- Three measurements required for complete stress state

1.8.1.3 Applications of Electric Resistance Strain Gauge for SHM

Having maturity on its side, electric strain gauge is by far the most common type of sensor used for SHM applications. A few of these are reviewed below.

To show the flexibility of electric resistance strain gauges, non-isotropic material was monitored and the damage investigated on the fibre polymer matrix[64]. It was possibly due to the change in conductivity as the carbon fibre gets fractured in the composite matrix. Notable results came from fatigue testing where it was observed that de-lamination began to occur at 30% of the fatigue life and the fibre breakage happened at 50% of the fatigue life. The paper concludes that the electrical strain gauge is an important contribution to SHM and can be used effectively for the monitoring of composites and joints as long as the materials are electrically conductive in nature. Other composites, like cement matrix and carbon fibre polymer matrix, were investigated and the measured strains were positively conclusive based on damage detection[65]. Different joints were also analysed where focus was laid on the de-bonding process. In that particular case, electrical measurements were found to have an accurate response. Different joints geometry was tested with a beneficial output.

Aircraft structures have also been monitored using strain gauges[66]. Several points were highlighted to improve on the robustness of the SHM approach employed, as listed below:

- Damage criticality ranking of components
- Benefits resulting from load monitoring
- Accuracy of damage location
- Robustness of sensing system
- Optimisation of sensor location

Monitoring of repairs was also carried out using strain gauges[67]. Patches were used for repairs and monitored with strain gauges for any dis-bonding. It was deduced after trials on aeroplane wings where patches were used for repair that, in the short and medium term, the electric strain gauge had excellent potential for monitoring of the patch for operational conditions of the aircraft.

Strain gauges have commonly been used in bridge monitoring[68]. A comprehensive study was from what was successfully carried out on the strain of the Tsing Ma Bridge and from the strain-time history obtained; the fatigue life was estimated near the toe welds[68]. A Rainflow count was carried out and through the application of the Miner’s rule, the damage was estimated.

Tower monitoring for wind turbine structures

Strain gauges were used for monitoring of the towers for wind turbines with the main purpose in finding the fatigue damage, the vibrational traces from the modal strain and load and stress monitoring to test against the design codes[69]–[75]. Modal analysis is the field of measuring or calculating and analysing the dynamic response of structures and/or fluids or other systems during excitation using strain data[104].

Radial arrangement of the stain sensors at the same height was carried out at the base weld joint[76]. The presence of a crack was detected using the strain difference method, which involves the comparison of the strain under the same operational and environmental conditions tested at different periods. The data collected was then used to find the residual life of the tower, which was achieved by using a frequency based method for crack propagation with the loading time history and fatigue crack growth rates. The method was extended to set up an inspection schedule[76].

Wireless strain gauges were successfully implemented to capture vibration strain data at the base of offshore wind structures[74]. As the offshore wind farms are being located further away from shore, wireless sensing systems will seem to be the solution for the future of SHM of the industry, which offers less installation effort when compared to the wired counterpart[74]. One of the major limitations is strain gauges are operated with battery power and often this can result in the battery being drained. This will require replacement and the cost effectiveness of the whole system will then be put into question as the cost incurred for such replacements can outweigh the economic benefits. That said, wireless sensors can be connected to the auxiliary power supply of the wind turbine that ensures that the Supervisory Control and Data Acquisition (SCADA) data, for instance, is being collected even in the case of no power production by the wind turbine.

Blade monitoring

The certification process for wind turbine blades requires strain gauges for extreme load monitoring for accelerated fatigue tests[233].Those tests were set up to check the ability of the blade to cope with the extreme conditions.

30, 1000-Ohm metal foil strain gauges were placed on the surface of a blade and the flap-wise tare load for fatigue monitoring was investigated[77]. Noticeable cracks were detected at 4million cycles when the test was stopped. The axial strain was measured by placing more than 100 strain gauges on a full scale 25m length blade under maximum design static load[78].

A study proved that at present value, strain gauging for blades is the cheapest solution for fault detection, lifetime forecasting and protection against high stresses in blades[79]. It also pointed out that the strain gauges tended to have a tendency of having low reliability behaviour and, thus, might be susceptible to damage and errors for field testing rather than laboratory testing.

The aim of this thesis is to explore and develop a model used for compiling the bending strain data from different sensors on the turbine as part of a SHM campaign and its application to the offshore wind monopile to evaluate the effects of fatigue and pitting corrosion. To do so, an extensive literature review has been undertaken to have a general overview of the offshore wind world and the necessity for applying SHM to monitor the health of the structures whilst being linked to fatigue in monopiles foundations and pitting corrosion.

Based on the work depicted in the literature, the gaps in knowledge were identified and comprised of using the strain gauge sensors and mapping the strains across the whole structure rather than at point loads. The technique consisted of using the cosine fit for circumferential interpolation and a linear fit for the longitudinal one.

This logic was extended to include pitting corrosion and characterise the growth of the pits with respect to seawater depth. Due to the lack of information in the literature on the distribution of pits with respect to water depth, a field experiment was done with the goal of characterising the corrosion types in steel of grade S355 which is currently employed for monopiles construction and corrosion rates ultimately used to calibrate the pitting corrosion model accordingly.

A substantial amount of new analysis was derived from the field experiment listed below:

1. To characterise the pit distribution and aspect ratio with respect to depths from plates set up at different locations for a period of 3 months.
2. To monitor the dominating environmental effects for pitting corrosion in the tidal region.
3. To use novel techniques from the optical toolbox to characterise and extract pit properties.
4. To employ the current modelling technique to try to predict the topological changes in the coupons/plates - Chapter 6.
5. To predict the pit count on a structure from simple coupon tests.
6. The mass loss and corrosion rate.

1.9 Summary of Chapters

Chapter 1: This chapter introduces the wind industry and explains the necessity for SHM, which is further described in the chapter looking at the various industries using it and how it is currently employed in the offshore wind industry.

Chapter 2: The chapter provides with an extensive literature review on fatigue and pitting corrosion. It explores the fatigue life estimation in detail and the factors affecting it. The chapter continues and explores the various corrosions in the marine world and focusses on pitting corrosion, which is then analysed in detail.

Chapter 3: The interpolation techniques were developed and the appropriate SN curves employed to capture the fatigue damage caused by the complex environmental and operational loading captured by the strain gauges on a monopile/tower. The work was also extended to increase the confidence in the sensor readings and also a sensitivity test to find out if there is oversampling. The data was drawn from a real structure. The data used was from a bending strain from an offshore wind turbine.

Chapter 4: The idea of the interpolation technique was applied to a structure where pits were grown with respect to time on a monopile and the pit to crack transition characterised. The model needed some further information to improve it, such as the aspect variation with respect to depth. Again, the bending strain data was used in this case; the same as in Chapter 3.

Chapter 5: A field experiment was set up and Chapter 5 details the process of the experiment from design to deployment and recovery and finally delves into the analysis phase consisting of visual inspection, mass analysis, chemical test, image analysis for capturing the number of pits, and 3D laser scanning for depth measurement.

Chapter 6: A topological analysis was performed to find out how a coupon surface varies with respect to time by applying three growth models for the pits, namely the uniform corrosion model, Melcher's model, and the Artificial Neural Network, and comparing them.

Chapter 7: Conclusion of the work overall with suggestions for future research.

2 Literature Review on Fatigue and Pitting Corrosion in Offshore Wind Turbines

2.1 Introduction

Fatigue analysis is a fundamental aspect to design for and monitor against in an offshore structure. The structure is expected to sustain a large number of cyclic loads the wind, wave and current and be fit for purpose for that design life. In the case of offshore wind foundations, the fatigue damage is compounded by the operational characteristics that add more loads on the structure, such as aerodynamics.

In general, fatigue cracks grow from defects that are initiated from manufacturing, transportation, installation or material defects. Those defects in offshore structures have to be detected and sized accordingly and generally inspection is carried out using non-destructive testing to determine whether further actions are required.

Fatigue damage is caused by cyclic loading and the damage increases in a cumulative manner which may lead to fracture. It has to be mentioned that the nature of those stresses are smaller compared to the yield stress of the material. The cyclic loads initiate cracks, very often at the hot spot stress locations, and under this type of loading the cracks grow, after a number of cycle will experience fracture. This is commonly referred to as a fatigue failure. Most materials have inherent defects. Therefore, it can be considered that the material already has some small cracks, thus increasing the chance of propagation of the crack under cyclic loading. In the process of the propagation, there are several factors affecting the crack growth but the two most influential ones are the cycles and the stress ranges. It has to be pointed out, though, that environmental conditions like a corrosive one can have substantial impact in accelerating the failure.

In this section, a review from design to monitoring is assessed with regard to the aforementioned form of damage.

2.2 Fatigue Life Estimation

The fatigue life estimation is based on various aspects going through the amplitude and number of cycles for different environment such as in air or sea water, complex geometries with varied stress distributions and also the presence of flaws and cracks that could have manifested in the processes of manufacturing, installation and also operational. When considering a welded structure, the damage propagation tends to be mostly fatigue crack driven. The imperfections in the welds contribute to substantial reduction in the fatigue life of the structure that can grow instantly unintentionally introducing cracks.

When dealing with the SN (Stress-Life) approach, it is assumed that there are no initial cracks and that the loads are subjected to a constant frequency and constant amplitude loadings.

2.3 SN Approach

Regions of higher stress ranges are more prone to fatigue failure. The fatigue curve is a measure of the damage experienced by the region of the hot spot stress[80]. This curve is developed empirically and shows the material failure process and is referred to as the SN curve where the S signifies the stress amplitude or stress range and N the number of cycles the material is subjected to at that respective stress[80]. There is a strong correlation between the higher stress ranges with the number of cycles to failure where the latter decrease with increasing stresses. In short, the SN curve represents the material resistance to failure.

The SN curve though is not fool proof. The tests are generally conducted under high stress ranges and is the contrary to the stresses on an offshore structure, which is subjected to random loading. Even though there are some tests that are carried out in artificial seawater to have a better representation of the corrosive effects of the marine world, it has to be mentioned that it is far from being reflective of the actual situation as it neglects the biological perspective of corrosion, e.g. Sulphate Reducing Bacteria. Coupled to that, the high frequency tests mask the effect of corrosion, which will have a far greater impact on low frequency structures. The last point can be assessed in terms of the loading sequences. In the development of the SN curve, the stresses alternate within defined constant amplitudes represented by a sinusoidal curve. In reality, marine structures experience random loads. This becomes a problem when dealing with inelastic material behaviour in the high stress regions where it is highly influenced by the load sequence. This becomes a complex problem making the analysis difficult to attain.

Regarding the applications of the S-N curve in the offshore wind energy sector, a particular study makes citations of 3 gaps that require to be filled[81]. The first comes down to the material properties geared more towards the Steel S355, which has seen changes in the manufacturing methods than the material tested before on which the S-N curve is based. As a second point, the S-N curve does not take into account the load sequence [81]. This is important as it has a major impact on the growth rate of the crack. In other words, the load cycles variations must be examined separately rather than computing the linear cumulative damage.

The S-N curves are categorised in three different classes depending on the environment of deployment of the steel. Those three categories are: air, water and free corrosion[82]. Comparing the SN curves, the steel in air has the highest fatigue life implying the least damage propagation and the one subjected to free corrosion has the shortest fatigue life and the most damage propagation. It has to be mentioned that for each of those conditions, there are 14 different SN curves[82]. They have to be carefully applied to their respective geometries to ensure that the design or monitoring is appropriately done.

2.3.1 Factors affecting SN Curve

2.3.1.1 Material Factors

There are two material factors that are taken into consideration and have major influence on the design of the foundation. The first one is the material safety factor (MSF), which is used to counter the uncertainty in some of the materials' defects. This is generally applied across the whole stress profile of the structure depending on the locations before the number of cycles to failure is determined from the SN curve[44].

The other safety factor is known as the design fatigue factor (DFF). This is applied in different regions of the structure (atmospheric, splash, submerged, scour or below scour zone). It is used to calibrate the inspection schedule, as shown in the table below[44].

Table 2-1: Design fatigue factor [44]

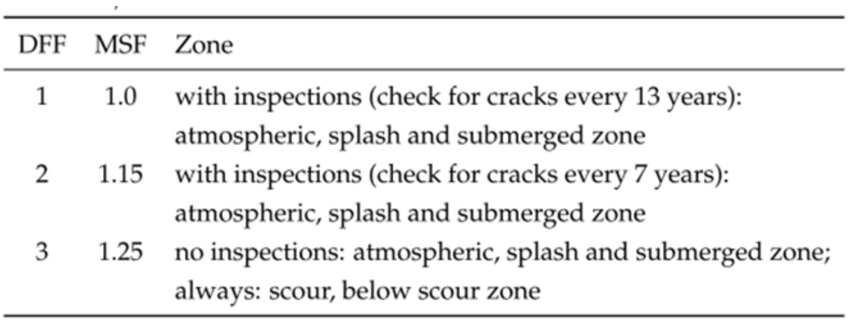

DFF	MSF	Zone
1	1.0	with inspections (check for cracks every 13 years): atmospheric, splash and submerged zone
2	1.15	with inspections (check for cracks every 7 years): atmospheric, splash and submerged zone
3	1.25	no inspections: atmospheric, splash and submerged zone; always: scour, below scour zone

The DFF being 3 and MSF being 1.25 is a more conservative approach and thus it reduces significantly the inspection visits compared to a DFF of 1 and MSF of 1.T[82]

2.3.1.2 Geometry-Thickness

Another highly influential factor is the size effect that accounts for the difference in thickness of the structure's geometry to that of the test specimen.

The wall thickness takes precedence in this analysis as the likelihood of failure from a thicker section is higher than thinner ones in the SN curve. To account for this effect, a thickness component K is employed. The reference thickness according to the DNV J101[44] Standards is 25mm. The correction factor is shown below:

$$SE = \left(\frac{t_w}{t_{ref}}\right)^K$$ Equation 2-1

2.3.1.3 Cathodic Protection(CP)

The region between the mud line and the mean water level is usually protected against corrosion using cathodic protection. It does have an important impact on the SN curve as it considerably retards the effects of corrosion on the fatigue life and, for a certain length of time, can be viewed unaffected by corrosion. This means that the fatigue life is considerably extended[82].

Some regions usually use CP rather than paints as it is easier to monitor the protective potential.

2.3.1.4 Structural Geometrical Considerations

To account for this effect, which is not found in the SN curve, a stress concentration factor has to be applied to correct the stress as a result of that effect[82]. The structural details are related to the thickness, eccentricities, concentricity and ovality[44].

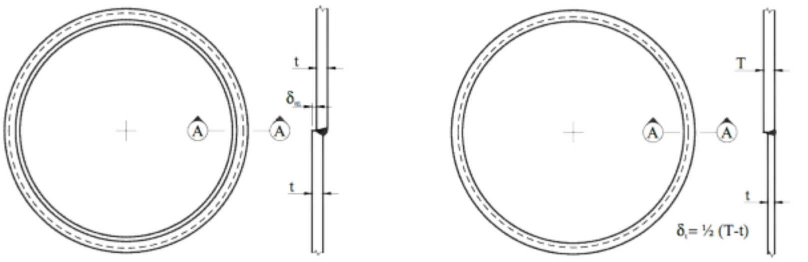

a) Concentricity Section A-A b) Thickness Section A-A

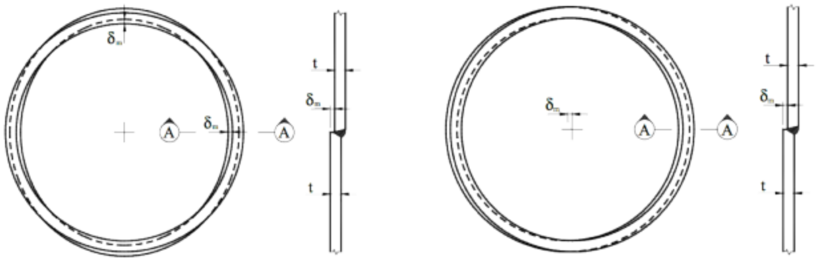

c) Out of roundness Section A-A d) Center eccentricity Section A-A

Figure 2-1: Eccentricity effects [82]

The equations for the SCF are given as:

$$SCF = 1 + \frac{6(\delta_t + \delta_m + \delta_0)}{t} \cdot \frac{1}{1 + (\frac{T}{t})^{\beta}} \cdot e^{-\alpha}$$

$$\text{with } \alpha = \frac{1.82\,L}{\sqrt{Dt}} \cdot \frac{1}{1 + (\frac{T}{t})^{\beta}}$$

$$\text{and } \beta = 1.5 - \frac{1}{\log(\frac{D}{t})} + \frac{3}{(\log(\frac{D}{t}))^2}$$

$$\text{for thickness transition: } SCF = 1 + \frac{6\delta_t}{t} \cdot \frac{1}{1 + (\frac{T}{t})^{\beta}} \cdot e^{-\alpha}$$

Equation 2-2

2.4 Variable Amplitude Fatigue

Loading of an offshore structure is stochastic in nature. To get a fine representation of the stress acting on the structure derived from the monitored strain gauges, an equivalent stress needs to be determined. In order to achieve the goal, a counting method needs to be determined and then used to compute the equivalent stress, which will ultimately give the number of cycles to failure. This is shown in the figure below.

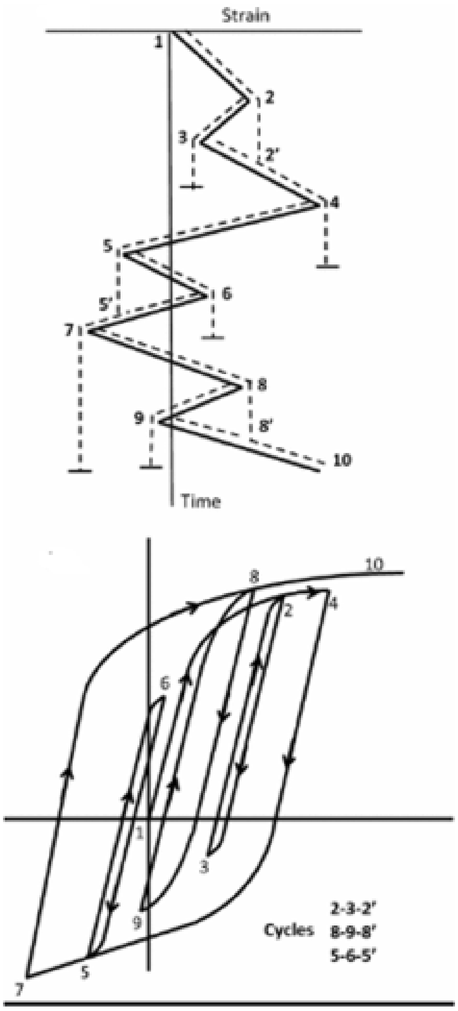

Figure 2-2: Hysteresis loops from fatigue damage [2]

Cycle Counting Methods

The Rainflow count has been the corner stone of the counting methods. Closed hysteresis loops are picked up from the response of the structure based in the cyclic loading[83]. There are different iterations of the Rainflow count as suggested below:

---

[2] https://www.nafems.org/publications/knowledge-base/hysteresis-in-fatigue/

Level Crossing Counting

The count is activated each time the positive or negative slopes do cross passes at a pre-set level. The reference load crossings are accounted when there is an identification of a positive slope portion of the strain history[84].

Peak Counting

In this algorithm, the maximum and minimum load values are identified and when there is the crossing of a peak above a reference point, there is count and if it goes below, there is another count[84].

Simple Range Counting

The definition of the range is crucial and is the difference between two successive reversals, the range being positive when a valley is followed by a peak and negative when a peak is followed by a valley. In the case there are both positive and negative ranges, then it is accounted as one-half cycle[84].

Damage Models

There are various damage models being used even though the most common one employed in the offshore wind business and inscribed in the Standards is none other than the Palmgren-Miner (PM) rule[85]. Different iterations have been proposed to counter the shortcomings of the PM rule, which will be further discussed below.

From the Rainflow count, the equivalent stress can be easily determined and from the SN curve the number of cycles to failure determined. To assess the damage, the PM rule is applied that assumes that the damage accumulation is linear. The PM rule mathematically states that the fatigue life is inversely proportional to fatigue damage occurring at various stress range levels.

It can be represented as:

$$\boldsymbol{D} = \sum_{i=1}^{k} \frac{\boldsymbol{n_i}}{\boldsymbol{N_i}}$$

Equation 2-3

Where n is the number of cycle for the equivalent stress and N is the total number of cycles to failure.

When D is larger than one, the component has exhausted its design life.

The downsides of this method are load level independence, load sequence independence and lack of interaction accountability.

2.5 Fracture Mechanics Approach

One of the limitations of the SN curve approach is due to the fact that it assumes no prior cracks. The presence of a crack changes the philosophy and the concept of fracture mechanics fills that void. The theory was presented by Griffith who looked at the problem from an energy perspective. He proposed two conditions[86]:

1. The crack tip must be stressed to the failure point. The stress at the crack tip is a function of the stress concentration factor that depends on the ratio of its radius of curvature to its length.
2. For an increment of crack extension, the amount of strain energy released must be greater than or equal to that required for the surface energy of the two new crack surfaces. This can be represented mathematically as:

$$\frac{dU_s}{dc} \geq \frac{dU_\gamma}{dc} \qquad \textbf{Equation 2-4}$$

Where U_γ is the surface energy and U_s is the strain energy and dc is the crack length.

Griffith applied the stress field equation for a narrow elliptical crack and the equation for the strain energy can be shown as:

$$U_s = \frac{\pi \sigma_a^2 c^2}{E} \qquad \textbf{Equation 2-5}$$

Where E is the Young's Modulus. This quantity must be carefully treated depending if it is plane stress or plane strain.

The surface energy for two surfaces created by the crack of length 2c and unit width is accounted to be:

$$U_\gamma = 4\gamma c$$ **Equation 2-6**

For crack growth to be existent, the following condition needs to be met:

$$\frac{\pi c \sigma_a^2}{E} \geq 2\gamma$$ **Equation 2-7**

2.5.1 Linear Elastic Fracture Mechanics

The stress field in the vicinity of the crack was expressed mathematically by Irwin who contributed immensely to the field of fracture mechanics[87].

The expression is with the stress direction detailed in figure 2-3:

$$\sigma_{yy} = \frac{K_1}{\sqrt{2\pi r}} cos\frac{\theta}{2}\left(1 - sin\frac{\theta}{2} sin\frac{3\theta}{2}\right)$$ **Equation 2-8**

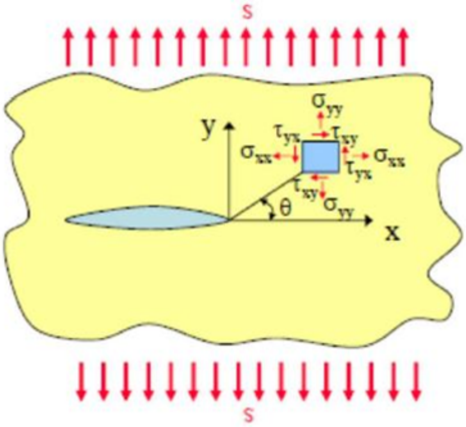

Figure 2-3: crack and stress orientations[88]

K_1 is referred to as the stress intensity factor and can be formulated as:

$$K_1 = \sigma_a Y \sqrt{\pi c}$$ **Equation 2-9**

Where σ_a is the applied stress, Y is the geometric factor and c is the half crack length.

The value of one associated to the Stress Intensity factor (SIF) is representing the loading type. In total there are 3 loading types as shown:

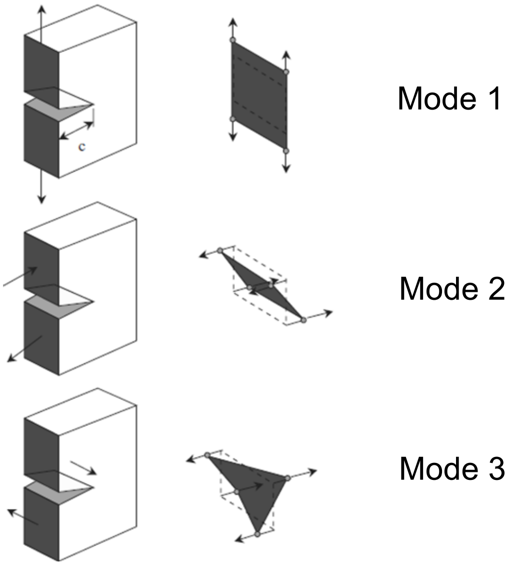

Figure 2-4: Different modes of fracture [86]

Mode 1 loading is also known as the opening mode and is the most commonly employed one to characterise brittle failure. In that case, the crack surfaces moves directly apart.

Mode 2 commonly identified as the edge sliding mode where the crack front moves normal to the crack surfaces.

Mode 3 or shear mode. In this case, parallel motion of the crack surfaces relative to the crack front.

Fracture is connected to fatigue as it considers that there is a crack that is propagating under fatigue load whereas in fatigue it is assumed that the material is defect free.

The crack is modelled from LEFM.

LEFM is a branch of fracture mechanics that used the stress around a crack tip to estimate the propagation of the crack.

LEFM used the elastic stress analysis of a cracked body, particularly the stress field surrounding the crack tip to estimate the conditions under which the pre-existing crack would propagate. An important assumption was that the material was a homogenous isotropic one where stress was proportional to strains[89].

The figure below shows the most widely used LEFM model for fatigue crack growth that has been developed [90].

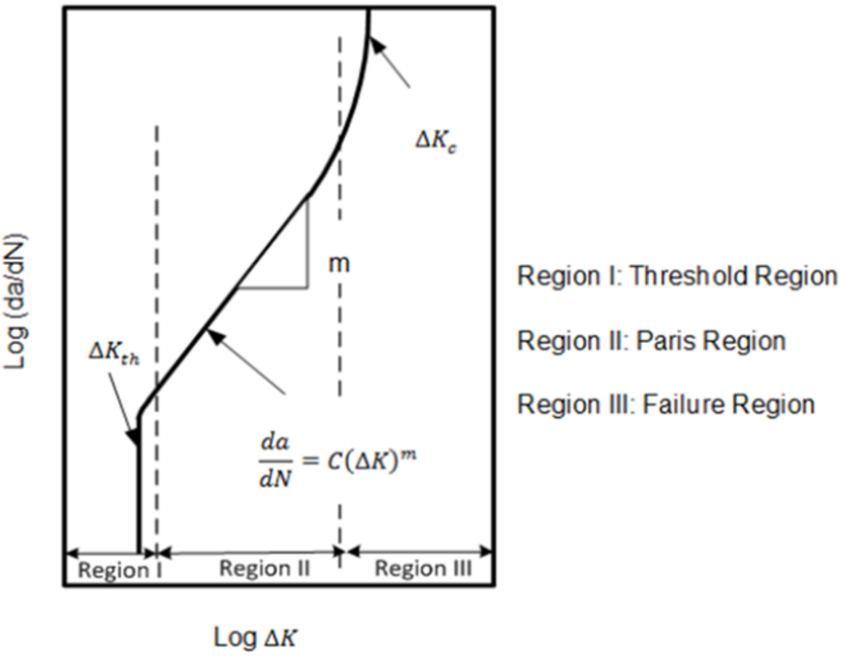

Figure 2-5: Paris region

In the equation, C and m are generally derived from testing and are dependent on the loading condition and the environment.

The differential equation could be solved to find the size of the crack from a known number of cycles. By substituting ΔK and sending dN on the right hand side of the equation, the final equation resulted as:

$$\int_0^N dN = \int_{ai}^{ac} \frac{da}{C[K_t \Delta\sigma Y\sqrt{\pi}]^m}$$

Equation 2-10

$$a_c = \sqrt[\frac{2-m}{2}]{\frac{N(2-m)\,C[\Delta\sigma Y\sqrt{\pi}]^m}{2}} + a_i^{\frac{2-m}{m}}$$

2.6 Fatigue Limit State (FLS)

The Fatigue Limit State (FLS) corresponds to failure due to the effect of cyclic loading[91].

In that design phase, the structure is designed to sustain the various fatigue loads with the number of cycles acting on it and very often applying a safety factor for the material, for instance, of the design fatigue factor, which when increased can result in less inspection but a higher involved cost. All of those analyses culminate to the Miner’s damage for assessment of the life of the structure.

2.7 Corrosion General Perspective

Corrosion is considered as one of the most damaging mechanisms towards materials[92]. It can be defined as the degradation of material properties due to interactions with their environments. A common analogy comes in the saying ‘*corrosion is something we hope to avoid; but ultimately it is something we must learn to deal with just like taxes and death.’’*[93]

Looking at the etymology of the word, corrosion is derived from Latin ‘*corrode*’, which can be translated in simple English as *‘to gnaw to pieces’*. Historically, corrosion has been observed since the very early phase of human development and progressing from the Copper Age, transitioning to the Bronze Age and moving forward with stronger materials developed particularly for military ends but all having that lack of resistance to corrosion[94]. Nowadays though, the field of corrosion has developed immensely to try to counter the disastrous implications that can result from material deterioration. It is assumed that the economic costs associated to corrosion in developed countries vary between 2 to 4% of the Gross National Product (GNP)[95]. To put that in context, the USA’s bill amounts to $276 billion per year[93]. This sum can be broken down into various sectors but the one that takes the lion’s share is Utilities, as shown by the chart below.

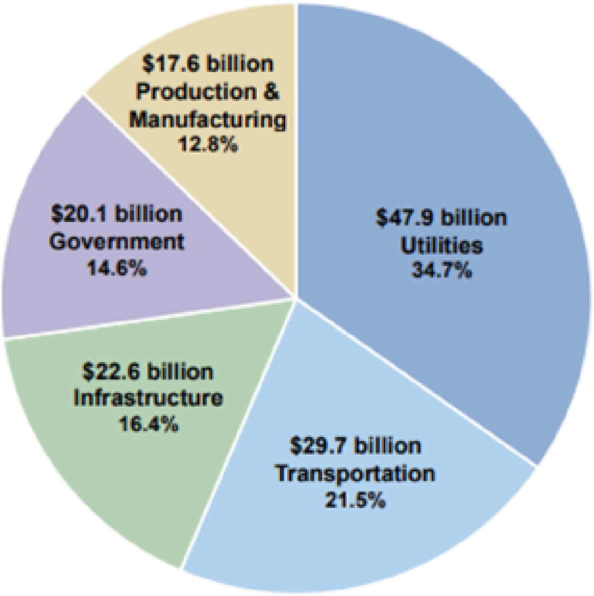

Figure 2-6: Expenditure on corrosion in the USA [93]

It is worth mentioning that the US army spends $20 billion per year to tackle the effects of corrosion[93].

At this point, it is fundamental to ask the question of why so much money is spent on corrosion. The answer is simple. Upon deterioration of a structure for instance, the strength of the material significantly reduces irrespective of the form of corrosion[96]. There will be a serious mass loss registered and this ultimately will put the integrity of the structure in jeopardy. The situation can then be considered critical if remedial measures are not appropriately taken, thus resulting in failure of the structure, which can put people's lives in peril[97].

A few common corrosion-related accidents are listed below:

The Bhopal incident that occurred on the night of 2nd to 3rd December 1984 where methylisocyanate(MIC) came in contact with water due to the corrosion of the stainless steel tank wall causing a rapid formation of gas that spread very quickly and silently into the neighbouring area. As a result, more than 3000 people lost their lives and it is roughly estimated that more than 300000 people required medical assistance due to health-related problems from that incident[97].

The El Al Boeing 747 freighter that crashed in Amsterdam on 4 October 1992 claimed the lives of 54 people in total. Two of the engines detached from the wing, thus losing the controls required to steer the plane. Upon further investigation of the collectable debris, it was deduced that the structural failure leading to the loss of the two right engines came from corrosion pits, which contributed in weakening the fuse pins that held the strut to the wings. Due to the complex operating conditions, the pit transitioned into a crack which accelerated the growth rate and, thus, kept growing until it reached failure point. The crack discovered in one of the fuse pins retrieved was a staggering 14mm deep[98].

A common environmental disaster attributed to corrosion is the sinking of the Erika in December 1999. The tanker split into two 70km off the coast of Brittany, France carrying about 30000 tonnes of heavy fuel oils of which 19800 tonnes was spilled. No fatalities were registered for that incident but the resulting economic impacts were disastrous. There was a substantial drop in tourism and major loss of income from fishing-related activities, which was worsened for the local fishing communities as a result of the ban imposed on sea products, such as oysters and crabs[8] .

The cause of the accident is attributed to poor maintenance of the ship, which had various holes resulting from intense corrosion. Corrosion, as in many marine-related accidents, tends to be the usual suspect and, as seen, can damage people’s lives in an instant [9].

In the following sections related to corrosion, marine corrosion and the various forms of corrosion will be discussed before delving into the current problems facing offshore wind turbines. This will be further extended to look at the modelling sections of pitting corrosion in the marine environment. The material that will be investigated is carbon steel as it is the material used for the manufacture of an OWT, which the main theme of this thesis relates to.

2.7.1 Marine Corrosion of Carbon Steel

Corrosion is an electrochemical process. Thus, it involves the flow of electrons resulting from anodic and cathodic reactions. Regarding the corrosion of carbon steel, it can be viewed as the metal being non homogenous and anodic and cathodic sites are formed on the surface of the alloys. To complete the circuit, there needs to be the presence of an electrolyte that sets up small corrosion cells. In the anodic regions, iron dissolves in the solution to form iron cations and at the cathodic site under immersed conditions, hydroxyl ions are formed[101].

$$Anodic\ Reaction\ \ 2Fe\ \rightarrow 2Fe^{2+} + 4e^-$$

$$Cathodic\ Reaction\ \ O_2 + 2H_2O\ +\ 4e^- \rightarrow 4OH^-$$

The overall equation can be deduced as)

$$Overall\ equation: Fe^{2+} + 2OH^- \rightarrow FeOOH$$

Metals do corrode with the exception of a few as they want to reach a lower energy level and do so by reacting with other elements to form a more thermodynamically stable compound[96].

The Pourbaix diagram is an illustration that shows the different equilibria between the metal ions and non-metallic ones[102]. It is a very interesting construct as it indicates the various regions of corrosion, immunity and passivation. They are built from the Nernst equation and solubility data for several of the metal compounds[103].

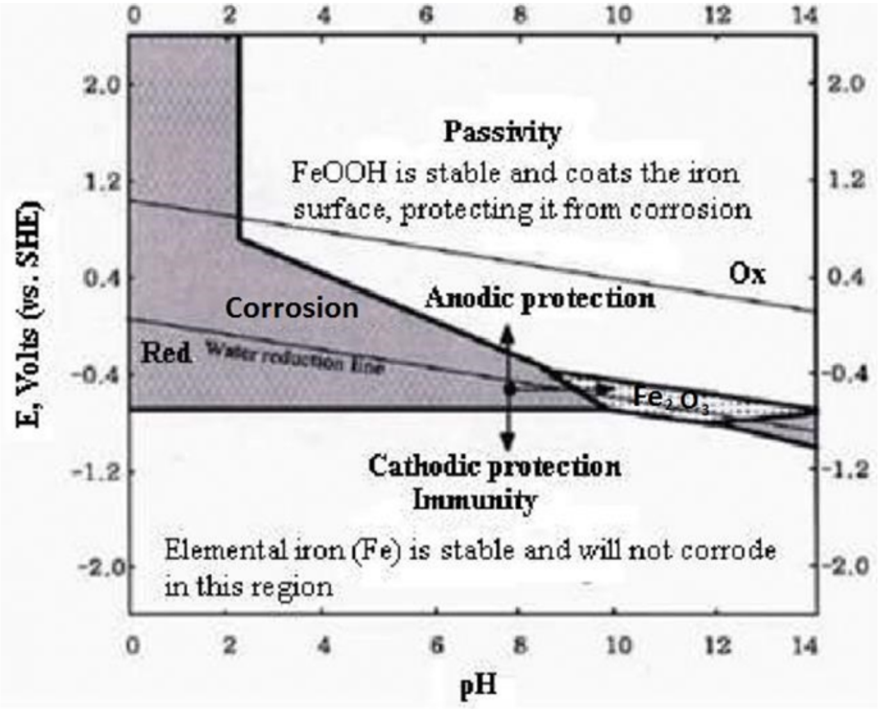

Figure 2-7: Pourbaix diagram[3] [104]

One of the problems with the Pourbaix diagram is that it does not give the rate of corrosion. To capture this effect, another clever diagram known as the Evan's diagram has to be mentioned[92]. This takes into account the cathodic current and the anodic current and the intersection of the lines gives the corrosion current. Based on the corrosion current and Faraday's law, the rate of mass loss can be determined[92]. The kinetics of the reaction can be significantly altered by changing the environment, such as increasing the velocity of the flow of the electrolyte or by changing the pH, or introducing ions like chloride ions or even hydrogen sulphide ions[92]. In the marine environment, those factors are always changing and, thus, determining those impacts on the corrosion current can be quite tricky to determine.

---

[3] Source: https://www.winmate.com.tw/anti_corrosion.asp

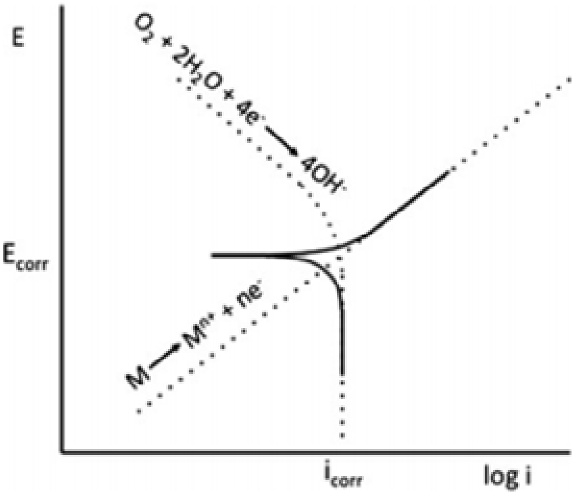

[4]

Figure 2-8: Evan diagram [103]

The Faraday equation is:

$$m = \frac{i_{corr}MTS}{nF}$$ **Equation 2-11**

Where m: mass loss

i_{corr}: corrosion current

M: molar mass (mol/kg)

T: time

S = surface area

n: number of moles of ion

F: Faraday's constant

2.7.2 Different Forms of Marine Corrosion

Marine corrosion can be split into four main sections[105].

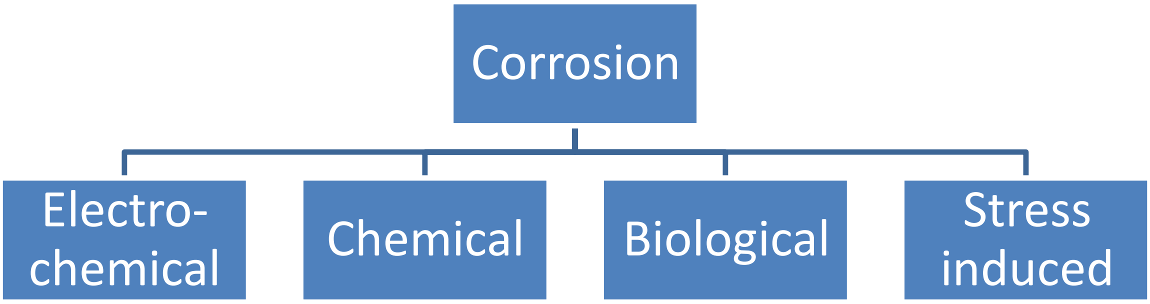

Figure 2-9: Marine corrosion forms

Each of these forms will be explored in this section to give an overview of the complexity of the marine environment and the behaviour of metals in these conditions. It has to be stated that very often different forms of corrosion can exist and, thus, tend to accelerate the failure of a component or structure.

2.7.2.1 Electro-Chemical Corrosion

This form of corrosion is very common in the aqueous environment and involves the transfer of electrons from an anodic to a cathodic environment[96]. The whole nature of this corrosion can be split in two sections. The first one involves anodic and cathodic regions being distributed steadily across the metal; it gives rise to uniform corrosion. In this case, the regions are localised in one region and is referred to as localised corrosion.

2.7.2.2 Uniform Corrosion

Carbon steel, due to its lack of a passive layer, preferably tends to undergo this form of corrosion. It deals with the constant thinning of the material and, hence, penetration of the metal tends to be limited and it can also be predicted based on the environmental set up, thus setting up a corrosion allowance for safe operation of the component or structure[96].

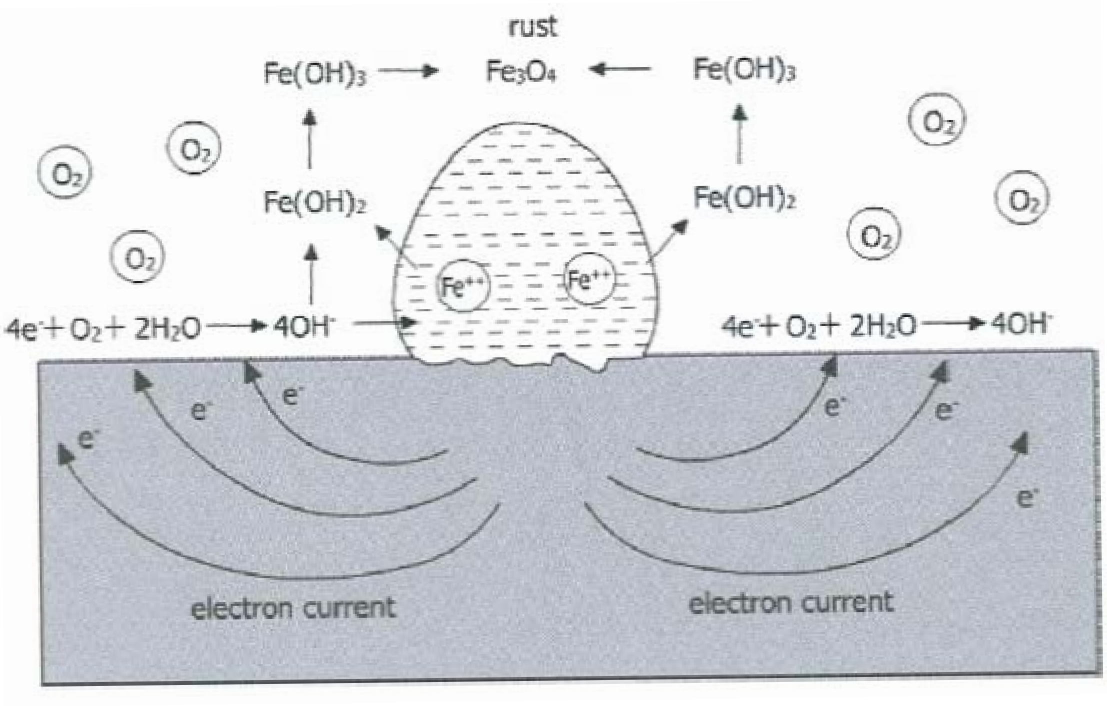

Figure 2-10: Corrosion cells formed [96]

In reality, under aqueous conditions, it is quite rare for a uniform condition to occur for complex structures as the distribution of the anodic and cathodic regions are far from being uniform[106].

2.7.2.3 Localised Corrosion

This form of corrosion may occur both at the microscopic and macroscopic scale and is considered as the most destructive form of corrosion. In the case of localised corrosion, the metal loss tends to be rather difficult to predict[96].

2.7.2.4 Pitting Corrosion

Pitting corrosion can be recognised by the fact that there are holes and cavities produced as a result of the breakdown of the passive layer or coatings of the metal[107]. Pitting corrosion is very much associated with marine corrosion as the environment tends to be rather rich in chloride ions. This ensures that the potential for pitting to occur stays within the pit potential[103]. It is considered as one of the most dangerous forms of marine corrosion as it is hard to predict and has a tendency to increase the stresses acting on the structure due to higher stress concentration factors.

Pitting corrosion tends to be very complex as it is dependent on the location, distribution and size of pits and the operational and environmental conditions, including the loading ones without forgetting the micro structure of the metal[101].

Pitting corrosion will be further detailed in the sections below.

2.7.2.5 Crevice Corrosion

Crevice corrosion is very similar to pitting corrosion except in the way it initiates. The initiation site for pitting corrosion is dependent on passive film ruptures and has more to do with the microstructure, whereas crevice corrosion deals with the differential aeration cells[96]. This will occur in different regions of the surface and oxygen reduction occurs in the regions of richer oxygen concentrations and the anodic region occurs at the crevice (lower oxygen levels) where the metal loss happens[105].

Other forms of corrosion do exist, like intergranular corrosion which will not be covered in this study.

2.7.2.6 Chemical Corrosion

This form of corrosion occurs under extreme conditions. For instance under highly acidic conditions, the metals will react and there will be eventual loss of metals[105].

Hydrogen sulphide is generally formed from biological effects on structures. When the H_2S is formed, it dissolves in the water to form a weak acid. Under certain conditions, such as in deep wells where the pressure is substantially reduced, the pH goes down and therefore the product is more acidic. At temperatures below 150 degrees Celsius, a scale is formed that acts as a barrier and reduces the corrosion rate but at a higher temperature, the conditions do favour hydrogen embrittlement[105].

2.7.2.7 Biological Corrosion

There are various forms of Microbial Induced Corrosion (MIC) and the most influential tend to be those generating H_2S[108]. The process is anaerobic where bacteria metabolise sulphate ions to form hydrogen sulphide[109]. When MICs come into the frame, they tend to influence the interface between the metal and the environment and, thus, change all the required requisites for corrosion to happen; for instance, concentration of oxygen, pH conductivity and redox potential[110]. The pH of the local environment due to some species of biofilms can change the pH by up to three units[101]. For MICs to exist, light is required, CO_2 and the electron donor and acceptor. In the process, iron sulphide is formed, which tends to be in the form of iron hydroxide and predicated causing the material loss[111].

2.7.3 Stress Induced Corrosion

There are various forms of mechanical corrosion but the most common are erosion-corrosion and corrosion fatigue

In mechanical corrosion, the component or structure is generally facing a corrosive environment and added to that are loads that accentuate the damage. This combination makes the failure more imminent[105].

2.7.3.1 Erosion Corrosion

This happens due to contact between high velocity fluids and the metal surface. This produces a shearing force at the surface that causes the solid corrosion products to be mechanically swept away by the moving fluid[105].

Very often, erosion removes the protective film and then the exposed metal becomes subjected to corrosion and the two distinct process act interactively

2.7.3.2 Corrosion Fatigue

This happens when a metal is exposed to alternating stresses in a corrosive environment. In doing so, the protective film ruptures and there is exposure of the metal to the environment, which allows localised corrosion to occur in the form of pitting corrosion[103].

The pit at some point turns into a crack and then the damage process becomes more driven by crack growth but with damage contribution due to the corrosive environment.

Corrosion fatigue is also very dependent on the structural geometries; for instance, bends and welds that tend to increase the stress concentration factors[105].

2.7.4 The Complexity of the Marine Environment

Sea water covers more than two thirds of the surface of the planet[101]. The offshore world tends to be more violent towards structures than its onshore counterpart. This is due to the environment but also more severe loading conditions that do accelerate the failure of the component or structure. To accentuate the complexity, the marine world is very dynamic with variations occurring in terms of constituency of the sea water depending on the seasons and man-made developments, amongst others[112]. One very important composition of sea water is chlorine. From this element salinity is derived, which gives the concentration of chlorine ions dissolved in sea water. In open sea water, the salinity measured as a percentage tends to hover in the region of 35%[113]. Those ions tend to combine with sodium to form sodium chloride, which is commonly found in kitchen salt. At deeper seawater levels, the chlorine does change quite significantly but does not have that much effect in the current shallow deployment zones of the wind turbines[114].

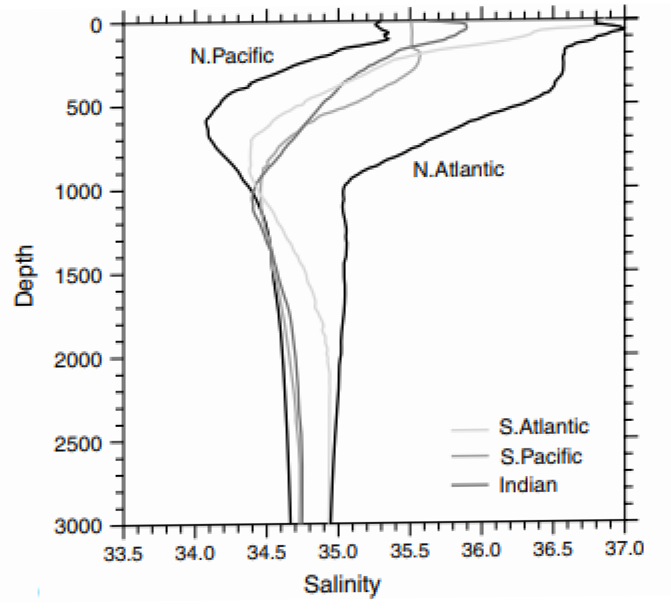

Figure 2-11: Salinity variation with depth [101]

The salinity is very important in pitting corrosion and will be discussed in further detail in the forthcoming chapters.

Temperature is another very important factor affecting corrosion in sea water. With depth, the temperature tends to decrease and at the sea surface there is a substantial increase from the surface temperature at the poles (-2°C) to the equator (35°C)[101].

Dissolved oxygen (DO) is one of the other factors that affect the corrosion rates in sea water. It varies from location to location where in the Arctic it tends to be 8ml/l but 4.5ml/l in the tropics[101]. It has to be noted that dissolved oxygen is affected by various other parameters. Temperature is one but another very important one is the transport effects, which are related to currents, waves and also the wind[115]. This increases the velocity profile of the sea water and the oxygen tends to increase. This is the reason behind the higher corrosion rate in the splash zones. Dissolved oxygen can also be heavily influenced by microorganisms that can absorb it, thus replacing it with carbon dioxide[107].

The pH of seawater lies between 8.1 and 8.3 in open sea conditions at sea surface. With depth, the pH is below 8 due to the effect of pressure reducing hydrogen dissolved[101]. Also, the pH reduces with increasing temperature[101].

Marine fouling is the growth of animal and plant life in the water that has an influence one way or the other on the corrosion process[116]. The marine growths can have also structural influences by changing the mass of the structure and in so doing might alter the natural frequency. In terms of corrosion, sulphate reducing bacteria can change the mechanism of corrosion from aerobic to anaerobic, thus increasing the corrosion rate[107].

In terms of corrosion for a structure, the corrosion rates recorded in the different areas are shown in the following diagram:

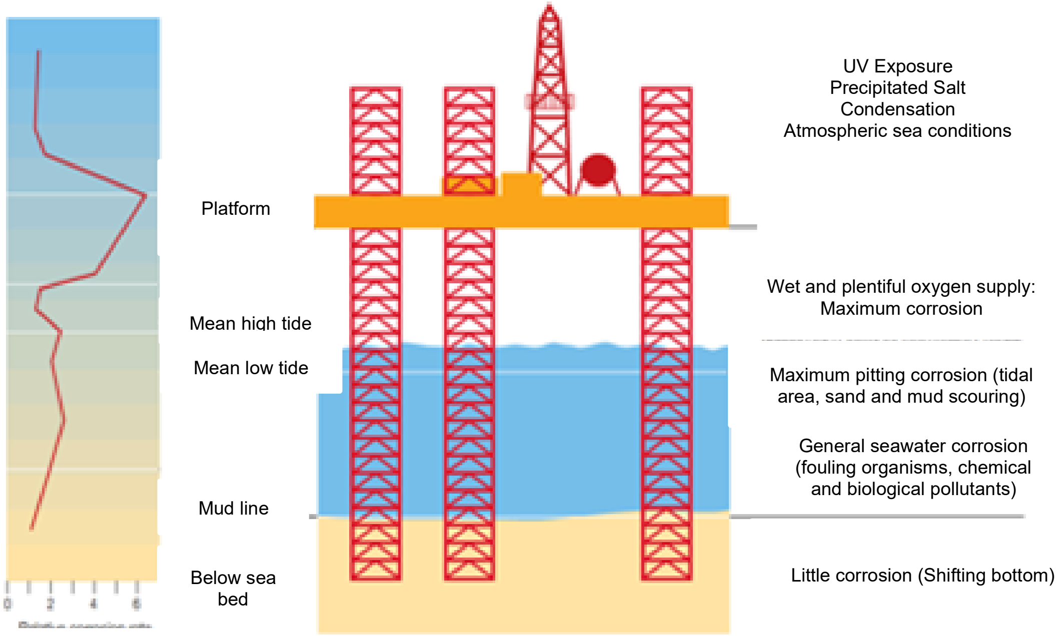

Figure 2-12: Profile of oil and gas corrosion [145]

The reason behind higher corrosion in the splash zone and the tidal zone is due to the circulation of more oxygen.

2.7.5 Corrosion in the Offshore Wind Industry

The offshore wind turbines being located in the marine world will suffer from corrosion[117]. The designers have borne this in mind and have been careful in the strategy for the corroding piles by including different corrosion protections especially in the immersed inner sections and splash zones of the monopile where in general it is considered to suffer more from corrosion[118].

If left unprotected, the structures are very likely to suffer from a myriad of corrosions going through corrosion stress, physical load and biological stress[119]. Very often, the offshore wind turbines tend to be compared to oil and gas platforms. Despite some similarities and standards being inspired from the oil and gas practices, there are some fundamental differences, particularly when looking at it in terms of accessibility and economics[120]. The OWTs are all unmanned structures with highly restricted access[119]. Therefore, the maintenance strategy is more complex and the evolution of corrosion in the structures can be rather difficult to gauge. Massive paint failures have been observed on OWTs after only two years in service[121]. The costs of repair are generally elevated costing about 1000 Euro per m^2, which is about 50 times more than the initial coating cost. Those costs pile up and cause a hike in the LCOE[122]. The economic perspective is important and worth mentioning. The breakeven time for an oil and gas platform and an offshore wind farm (OWF) is totally different, which is generally about 15 to 20 years for the latter compared to a few years more for the former[123]. So expensive maintenance is by no means a financial strain on the oil and gas platforms but takes a very different interpretation in the OWT portfolio.

The major problem with respect to corrosion took the industry by surprise[124]. It was meant to be non-existent and the design standards took a relaxed approach on this aspect[125]. It is related to the corrosion of the inner section of the monopiles[125]. To make more sense, it is crucial to understand the design of the monopiles and the connection of the various sections, like the transition piece (TP) and platforms and decks.

The monopile is a steel pile driven into the sea bed and showing above sea level by one to two metres. The transition piece is slotted on to the top of this free section with an overlap of about six metres. Brackets are used inside the monopile to orient the TP. The empty spaces left are then filled in with high strength grout to bond the two sections together. There are two other platforms that are then connected. The first one being the service platform located between the monopile and the TP and the airtight deck or platform that seals and secludes the upper section of the turbine from the lower one. The airtight platform usually has an opening which allows the J-tube to go through and exit the monopile in the seabed region through another opening at this section of the monopile[126].

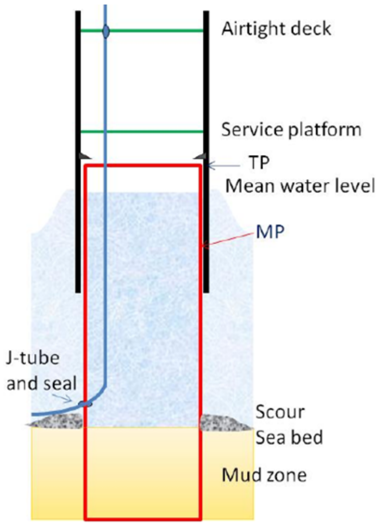

Figure 2-13: Corrosion in the inner compartments of monopiles [124]

There has been a considerable amount of grout failure in European wind energy projects. In addition to changing the load pattern and in the process increasing fatigue damage, there have been seawater leakages that have initiated corrosion sites. It has to be mentioned that corrosion at those regions were totally unexpected[126].

The fully sealed compartment has not been achieved and this has been revealed in the most brutal form upon routine inspection. A survey was set up in wind farms and it was observed that only 8% of the wind farms were corrosion closed compartment. 70% of them had water exchanges with oxygen levels being above 15% and the remaining showed immediate levels of oxygen transport. The seals and the airtight platform are to be blamed for contributing to this oxygen ingress[126].

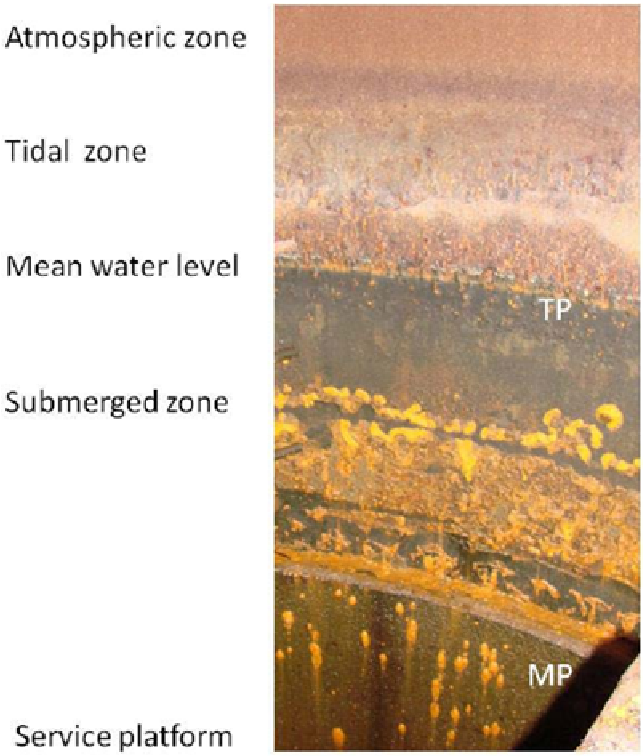

Figure 2-14: Different levels of corrosion in different regions [127]

The environment that this created is rather unique as it is highly dependent on the tides. During high tides, the water level in the column follows suit and when the tide recedes, the water level inside drops[124]. This creates a wetted area and an immersed one.

Corrosion in an OWT happens at different locations and it has to be specified that there are various corrosion mechanisms existing and thriving. The different regions can be broken down as[128]:

- Atmospheric zone
- Splash zone
- Submerged zone
- Mud zone

In a sealed structure, the dissolved oxygen is rapidly absorbed and the medium then transforms into an anaerobic one causing hydrogen sulphide to be released as a product of the new corrosion mechanism. This said, due to the closed environment, this form of corrosion is meant to die out as the environment does not support it anymore[126].

The reality though, with partial oxygenation, it affects corrosion in an unusual way and recently pits have been discovered[126].

To depict the multitude of corrosion mechanisms and impacts, the following diagram provides a comprehensive illustration:

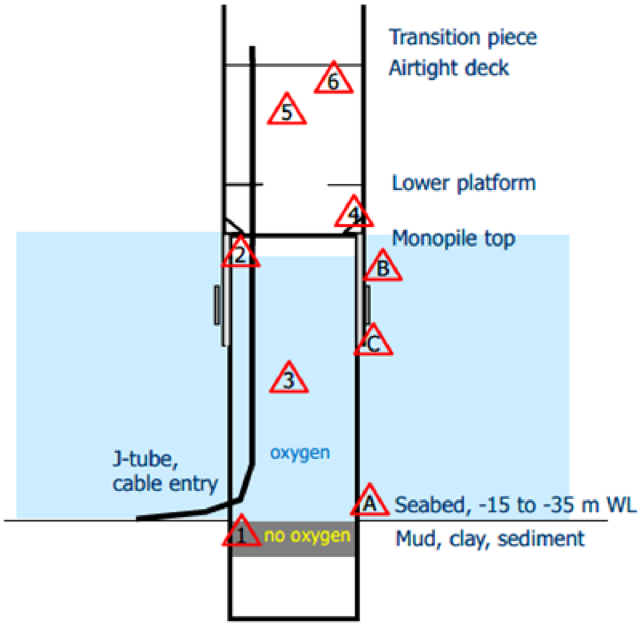

Figure 2-15: Regions of various corrosions [124]

Inner compartment[124]:

1. Mud zone: Differential aeration, MIC and HISC
2. Waterline: pitting corrosion due to differential aeration
3. Stagnant water causing important environmental discrepancies
4. Weld defects causing corrosion fatigue and SCC
5. Acidification if sacrificial anodes are installed
6. Gas accumulation such as H_2S, H_2 and CH_4

Outer compartment [165]:

A. Insufficient CP due to distance from anodes and high current demand
B. Splash zone, requirement for 20 years' lifetime of coatings
C. Grouted connection, possible ingress of oxygen or aerated water

2.7.6 Corrosion Protection (focussed towards offshore wind structures)

Corrosion protection exists to reduce the impact of corrosion on the structure. This can be achieved from the 4 points below that will be further illustrated[101]:

- Use of coatings
- Resistance of materials to a particular environment
- Cathodic protection
- Corrosion allowance

2.7.6.1 Coatings

The coatings used in OWT applications must be able to tolerate and protect the metals from humidity, salinity, UV lights and the mechanical loads fuelled by the wind and waves[129]. The coating regions are split in two, namely for atmospheric exposure and immersed exposure.

For atmospheric exposure, it involves a combination of 2-3 epoxy coats and a polyurethane topcoat. These follow the recommendations from general Standards such as EN ISO 12944, ISO 20340 and NORSOK M501[130].

The immersed section has coatings of epoxy followed by a polyurethane coat and tend to be generally thicker than the atmospheric ones[125].

The inner area of the monopile has been left uncoated, on the assumption that it will be sealed, and therefore is exposed to the full force of corrosion since there have been some leakages.

Future projects will incorporate an element of coating for the inner section[131].

Some problems have been identified, such as blisters, flaking of prime coats, and high dry film thickness, which caused the coat to crack[131].

2.7.6.2 Cathodic Protection (CP)

CP is used in regions that are in contact with seawater[132]. It exists in two iterations:

- Sacrificial anodes
- Impressed current

For both of them, important considerations are the protection potential and the protection current density. The table below gives the recommended values for protection.

Table 2-2: Corrosion protection voltage [119]

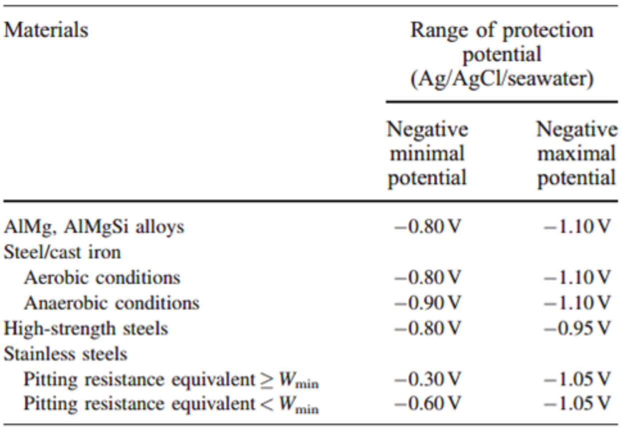

Materials	Range of protection potential (Ag/AgCl/seawater)	
	Negative minimal potential	Negative maximal potential
AlMg, AlMgSi alloys	−0.80 V	−1.10 V
Steel/cast iron		
Aerobic conditions	−0.80 V	−1.10 V
Anaerobic conditions	−0.90 V	−1.10 V
High-strength steels	−0.80 V	−0.95 V
Stainless steels		
Pitting resistance equivalent ≥ $W_{\min}$	−0.30 V	−1.05 V
Pitting resistance equivalent < $W_{\min}$	−0.60 V	−1.05 V

In the case of sacrificial anodes, it is the case of install and operate, whereas for impressed current it first requires power from the turbine to be activated[119].

2.7.6.3 Corrosion Allowance

Corrosion allowance is mostly applicable when uniform corrosion is considered.

The various sections of corrosion allowance can be seen in the table below[133]:

Table 2-3: Corrosion allowance [133]

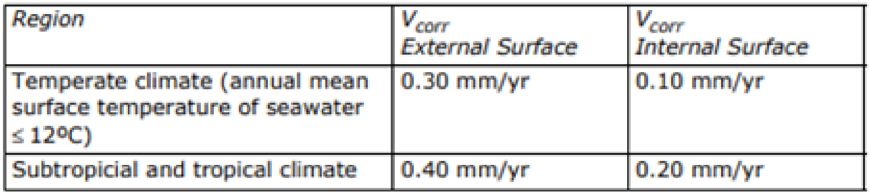

Region	V_{corr} *External Surface*	V_{corr} *Internal Surface*
Temperate climate (annual mean surface temperature of seawater ≤ 12ºC)	0.30 mm/yr	0.10 mm/yr
Subtropicial and tropical climate	0.40 mm/yr	0.20 mm/yr

According to a report by ORE Catapult, the annual corrosion allowance looks considerably low compared to the 2-3mm corrosion loss rate observed at the internal surfaces[134]. This is a scary thought acknowledging that the Standards underestimated the monitored one by a factor of 20. At this rate, the structural integrity of the structure might be compromised.

2.7.7 Monitoring of Corrosion for Offshore Wind

Coupons are traditionally a commonly used form of monitoring methods. They do provide reliable data and give a good notion of the various forms of corrosion existing[124]. The main drawback is the response rate as it takes time for the coupon to be retrieved and analysed. Real time data is not achievable[135].

Figure 2-16: Rusted coupons from wind farms [127]

Electrical resistance(LR) and linear polarisation resistance give real data and from those the corrosion current can be deduced and so will the corrosion rates[124]. It has to come with a red warning as those readings might be heavily influenced by a sulphide rich environment[124].

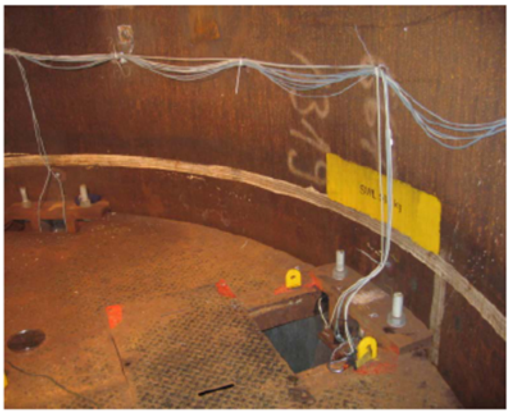

Figure 2-17: Monitoring of corrosion [126]

Environmental data sensors are generally installed in a water flooded compartment to gauge the levels of corrosion. This generally includes Dissolved oxygen (DO) sensors, temperature, salinity and pH sensors. A reduction in DO, for instance, might indicate the transition to an anaerobic form of environment[124].

2.7.8 Localised Corrosion and Pitting Corrosion

It has been mentioned that amongst all types of corrosion, pitting is the most common and damaging form in marine and offshore structures[136]. The ability to detect it is generally very difficult making it dangerous and it needs to be investigated in marine and offshore industries[137].

Pitting corrosion is defined as a localised dissolution of metals that occurs due to the breakdown of the protective passive film, notably the protective coating and paint on the surface[138][139].

For pitting corrosion to be initiated, the following conditions have to be met[140]:

- The protective film has to be broken either by chemical or mechanical effects
- The protective film can be attacked and frangible in an acidic environment; low DO concentrations and elevated chloride ions
- Localised damage with poor protection such as coating rupturing
- Non homogeneous metal with presence of impurities

The pits can exist in various shapes and some of the pits can form nodules and tubercles[141]. Wide pits and conical pits have been observed. The following diagram shows the various geometries observed.

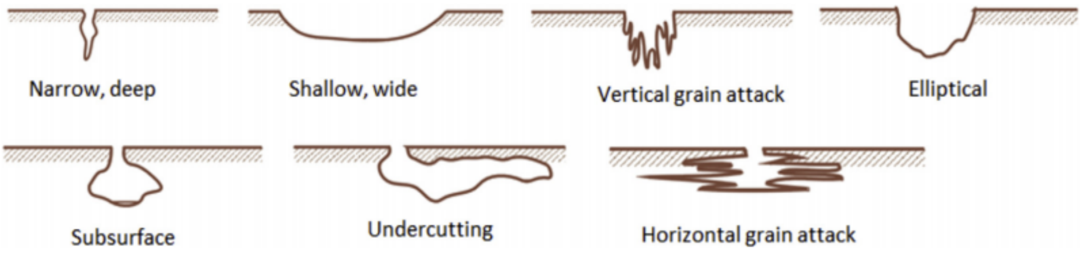

Figure 2-18: Different forms of pits [141]

The 5 stages below represent the formation of the pits.

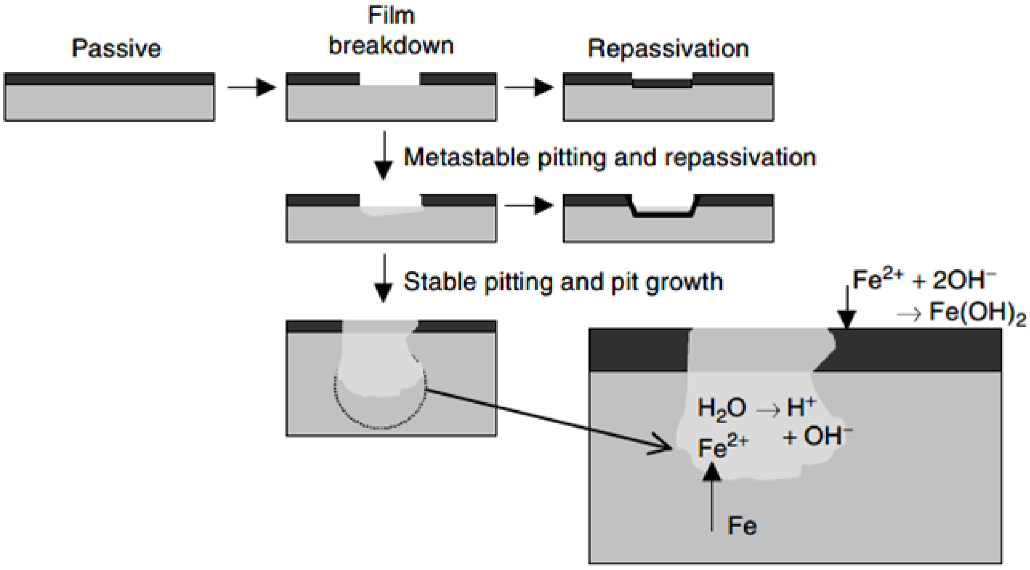

Figure 2-19: Breakdown of pits [103]

The passive film breakdown is the first stage and is the least understood of them all[142]. The passive breakdown theory states that there is adsorption of the damaging ions at the surface of the film, which results in mutual repulsion of the negative ions, thus causing the interfacial surface tension to be reduced which, in turn, weakens the passive film. Observing the breakdown happens very quickly at a nano-scale making it hard to detect[143].

For a metal to be susceptible to pitting, the potential needs to lie between the re-passivation potential and the pitting potential. Having a high pitting potential indicates that the material will have a high pitting resistance[137].

Pitting is highly dependent on the chemical compositions of the alloy and a pitting index is a quantitative way of indicating the resistance of a particular alloy from pitting.

It is expressed as

$$PREN = Cr + 3.3\,(Mo + 0.5\,W) + 16N. \qquad \text{Equation 2-12}^{5}$$

---

[5] https://www.nace.org/resources/general-resources/corrosion-basics/group-1/pitting-corrosion

PREN: Pitting resistance equivalent number

Cr: chromium percentage, Mo: Molybdenum percentage, W: Tungsten percentage, N: Nitrogen percentage

The pit initiation is a rapid process known to be only a few micro seconds. The pit initiation is said to have a factor of influence leaning towards surface effects, which can be picked during the manufacturing process. In that phase, there are mechanisms that have been suggested[142]:

- Penetration: seeping of aggressive anions into the passive layer that result in dissolution of the passive film
- Adsorption and thinning: reduction of film due to adsorption of halides in general at the surface
- Film breaking: involves mechanical stress that ruptures the passive film

Metastable pits are pits that initiate and grow and die and might be resurrected again[142]. They simply fall out of the pitting region and then based on environmental changes they grow again[142].

The stable pitting phase is the stage where the pit grows and rate of growth increases. In a marine set-up, the pit growth is defined as an autocatalytic process[138]. It does so when the iron cations and chloride anions react and through hydrolysis iron hydroxide is formed that covers the pit. The iron hydroxide is porous in nature. This arrangement causes the surroundings to change to become acidic, thus increasing the corrosion rate[138].

2.7.8.1 Factors affecting Pitting Corrosion

Pitting corrosion needs to have an appropriate environment to exist. In this section, the factors affecting corrosion will be discussed.

Temperature

There is a consensus in the research community that temperature is one of the most influential factors for pitting corrosion in sea water[144]. It has been observed that a higher temperature lowers the potential pit making it more accessible for the potential to fall in that region, therefore promoting pitting corrosion[145].

pH

The pH of the oceans fluctuates between 8 and 8.2[101]. Experiments carried out found that the pitting corrosion rate had minute fluctuations between a pH of 4 to 10 and is, therefore, considered as having little effect on pitting corrosion[146].

Salinity

Many authors reported that the salinity is of minor priority in marine pitting corrosion as the oceans do not experience a high fluctuation with respect to water depth [138]. This said the aggressive chloride ions are fundamental in the process of pitting corrosion.

Dissolved Oxygen

An increase in the levels of oxygen increases the corrosion rate. It can be extrapolated then that in regions with a high velocity of water where oxygen exchanges are more prominent, like splash zones, the rate of corrosion will increase. With increased pressure for greater depth of water, the DO in the water reduces with depth and again corrosion rates fall[138].

Bacteria

The Sulphate reducing bacteria (SRB) is well known to increase the rate of corrosion in the marine environment[116]. The mechanism that forms in offshore structures is referred to as the marine corrosion fatigue, which arises upon combination of the loads (wave and current) and the marine environment and with the combination of the SRB[107]. This accelerates the failure further and is rather challenging to inspect and monitor.

Table 2-4: Various factors affecting marine corrosion [147]

Environmental factors	Importance
Bacteria	Can be high throughout
Biofouling (marine growth)	mainly affects the initial phase
Nutrients	Increases effect of bacteria and biofouling
Temperature	Important as it affects rates of kinetic reactions of diffusion and of bacterial metabolism throughout
Oxygen concentration	Affects mainly intial and propagation phases
pH of environment	Affects mainly phase 1 i.e. before corrosion products build up
Carbon dioxide concentration	Not significant
Salinity	Affects model throughout but generally the practical effect is low. Its effect is moderated by carbonate concentration
Carbonate concentration	Builds less permeable rusts and thus reduces corrosion throughout
Pollutants	Little effect unless high
Pressure	Little effect
Stress	Higher stresses cause loss of protective rusts
Fatigue loading and stress	Ditto
Suspended solids	Little effect unless erosion involved
Wave action	Important if high
Water velocity	Important if high

2.7.8.2 Pitting Corrosion Modelling

The pitting corrosion model in a marine environment is complex as there are different aspects influencing it.

The modelling of a pit could be quite challenging as it involves a significant number of steps, as displayed in the diagram below.

Figure 2-20: Various steps for pit modelling

The electro-chemical perspective of the pitting model can be viewed in two parts, namely the pit initiation and pit growth.

2.7.8.1 Pit Initiation

The pit is initiated by the localised breakdown of the passive layer as a result of changing local conditions. The metal experiences metal dissolution and then metal loss and the pits start growing. The pitting initiation location has not been fully understood and is still an active field of research[138]. The initiation time generally has a very short lapse compared to the life of the pit[148]. Pit nucleation occurs and this is a process where the pits grow and sometimes stopped growing and then grow again cyclically as a result of the environment. This fluctuation is referred to as a metastable pit[142]. The pits are considered stable when they grow continuously and have been quantified to always be stable when they go above the threshold of 100µm[149]. At this stage, the pit is considered to grow continuously and is now out of the pit initiation but in the pit growth stage[149]. In some cases, the pit initiation is modelled as being instantaneous with respect to the observed time[150].

The section of the pit initiation stage was complicated to model as it involved a microscopic pit also known as micro pit that tended to have limited impacts at this stage of the stress acting on the structure.

The growth of the pits was defined by some models by the power law. Capturing the growth of a pit width and length data was unfruitful in the literature review exercise. Therefore, an experiment at sea was performed to capture those dimensions and the description is recorded in Chapter 5.

2.7.8.2 Pit Propagation

An important aspect to consider was the increase of the number of pits with time. The Non-Homogeneous Poisson Process was applied to find a general equation that characterised this effect and represented in figure 2-21[151].

$$E(N(t)|\lambda) = \lambda \int_{s=0}^{t} m(s) = \lambda M(t)$$

Equation 2-13

E(N(t)|λ): the expected number of pits at a certain time

λ : the pit intensity per metre square

m(s): the pit initiation time represented by a uniform random number.

λ M(t): arbitrary function for number of pits at a specific time where

$$\lambda\, M(t) \; = \lambda\, t^2$$

Equation 2-14

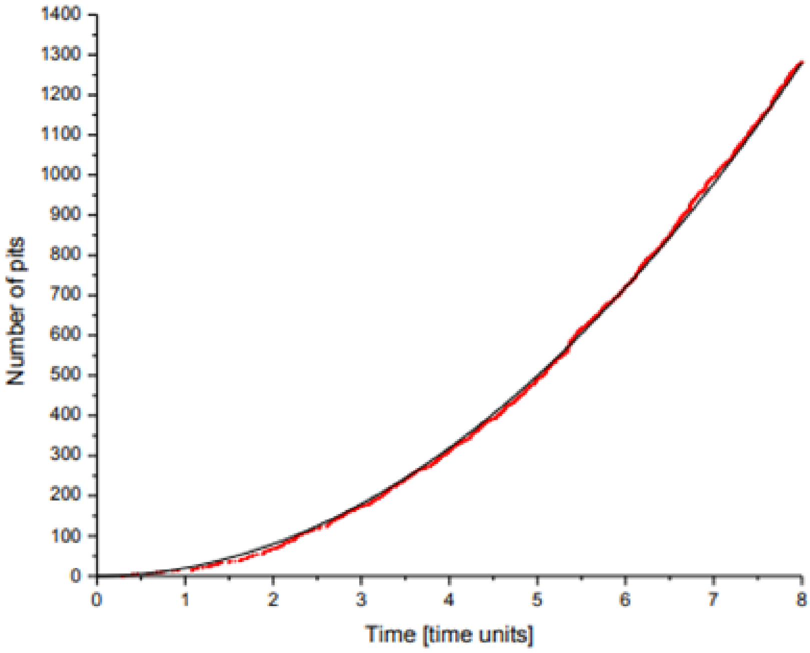

Figure 2-21: Increase in number of pits with respect to time in years [151]

2.7.8.3 Pit Growth Models

There have been various modelling techniques to characterise this very complex phenomena of pitting corrosion in the offshore world. The models can be characterised in three ways:

1. Deterministic: this is heavily geared towards short and long term corrosion observation on and in various structures including oil and gas platforms, ships including tankers and pipes. The models have evolved in complexity from simple linear estimates to bi-models showing transitions in the mechanism of the pitting corrosion. Some of the common models are the linear model, the power law and the Melcher's model further explored below.

The linear model is actually a very commonly used one, especially in field experiments or surveys where the initial and final states of the coupons are being observed. In this case, there are only two reference points and the only mathematical links can be a straight line going through the origin. The American Society for Testing and Materials (ASTM) Standards suggest this form of analysis[152].

$$t_r = c_1 T, \qquad \textbf{Equation 2-15}$$

Where t_r is the corrosion depth, C_1 is a constant and T is the structure age.

The Power model is very commonly used as it gives a good estimation of the mechanism of the building up of the rust with time, which reduces the diffusion rate of oxygen, thus limiting direct contact with the metal.

The equation for the pit depth is[153]:

$$c = At^B \qquad \textbf{Equation 2-16}$$

Where A is the coefficient of the power law and obtained in the field as 0.3, B is the exponent that lies between 0.3 and 0.8, t is the time, and c is the pit depth[153].

Melcher's model is probably the most advanced deterministic model currently in use today. It is built up of 4 different sections representing various corrosion mechanisms and taking into account both the environment and also the diffusion effects due to the rust layer at the surface that substantially reduces the corrosion rate[154]. The marine growth and the respiration mechanism involved due to this colonisation changes nature from an aerobic form to an anaerobic one when enough layers have grown[155]. This constitutes a different form of mechanism that needs to be reflected in the model. The importance of this section is vital as it does have a considerable effect on the pit depth and its growth rate. When the pit is totally soaked in this anaerobic environment, it then finally evolves into a linear form.

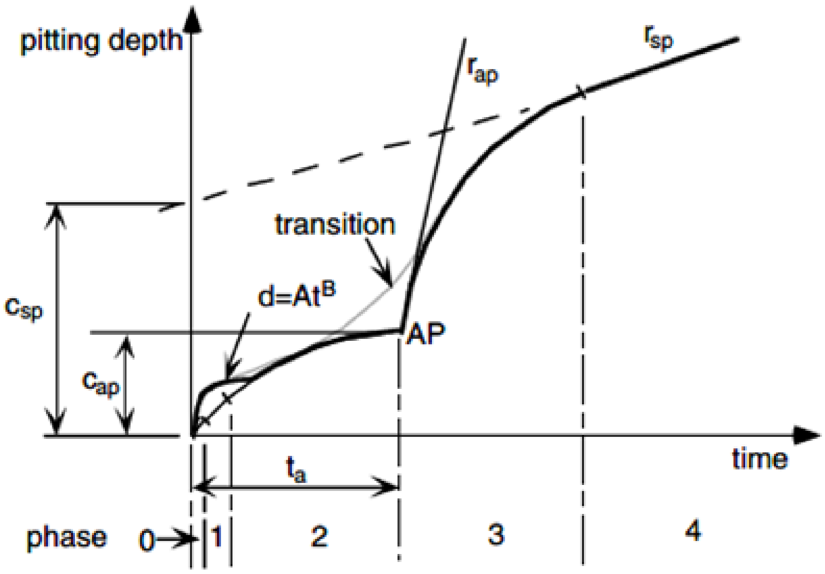

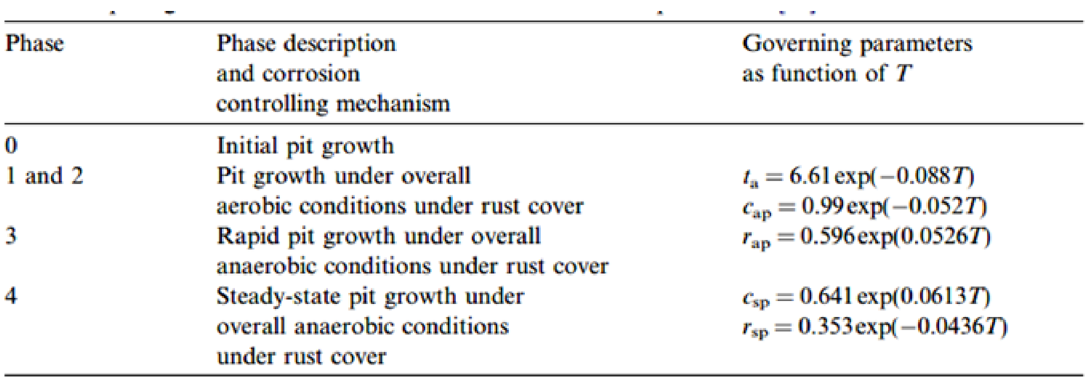

Phase	Phase description and corrosion controlling mechanism	Governing parameters as function of T
0	Initial pit growth	
1 and 2	Pit growth under overall aerobic conditions under rust cover	$t_a = 6.61\exp(-0.088T)$ $c_{ap} = 0.99\exp(-0.052T)$
3	Rapid pit growth under overall anaerobic conditions under rust cover	$r_{ap} = 0.596\exp(0.0526T)$
4	Steady-state pit growth under overall anaerobic conditions under rust cover	$c_{sp} = 0.641\exp(0.0613T)$ $r_{sp} = 0.353\exp(-0.0436T)$

Figure 2-22: Melcher's model [155]

t_a: exposure time under aerobic conditions

c_{ap}: depth of pit under aerobic conditions

r_{ap}: corrosion rate of pit under aerobic conditions

c_{sp}: depth of pit under anaerobic conditions

r_{sp}: corrosion rate of pit under anaerobic conditions

All the above terms are dependent on annual mean temperature (T)

AP: transition from aerobic corrosion to anaerobic corrosion

The transitions can be calculated as a function of the average yearly temperature.

2. Machine Learning (ML)

This has gained immense popularity across the research spectrum and pitting corrosion has not been spared from its grasp. With recent advancements and more powerful computational power, implementation of ML has been very accessible and many researchers are now heading in that direction to refine the models.

With the improvement of ML, the implementation of the application in the corrosion world was imminent and surely the trend towards its usage will go one way, meaning it will only increase[156].

The author of this paper captured the environment of corroding specimens of steel A106B and trained the input data with respect to the concentration, surface roughness and immersion duration with output as pitting density and pit depth for the Artificial Neural Network (ANN). The results seemed to have a great match with an R^2 value larger than 90%[157].

Other studies were carried out focussing heavily on the environmental effects such as concentration, pH and temperatures[158]. The ANN prediction was in good agreement with the results from the experiment with respect to the pit depth[158]. The Support Vector Machine (SVM) has also been employed with great accuracy for prediction of pitting behaviour accounting for environmental inputs, such as pH, temperature and chloride concentration giving the potential values as output[159].

Artificial Intelligence has been employed for prediction of pitting and determination of corrosion rates for concrete and steel. Different techniques of learning were employed, such as ANN, SVM, classification and regression tree (CART) and linear regression[160]. A second aspect of this study takes into account the hybrid metaheuristic regression model used to predict steel corrosion in which the smart fly algorithm was also employed for improving the accuracy of the models[160]. The authors are positive that this method can be used in the real world for informed decisions about risk management[160].

- Artificial Neural Network (ANN) model

  ANN is defined by Deboeck and Kohonen as described Neural networks (NNs) as a collection of mathematical techniques that can be used for signal processing, forecasting and clustering and termed as non-linear, multi-layered, parallel regression techniques[234].

  This has been applied previously in the field of pitting corrosion and their applications can be found in the following papers.

  The ANN model gives more flexibility compared to Melchers' model and the uniform models as more factors affecting the corrosion process can be included, such as the temperature, salinity, pH and dissolved oxygen. It has to be noted though that it fails to characterise the biological effect of corrosion on the steel. This will require data pertaining to this effect, which has not yet been found in the literature. The implementation of the ANN can be found in chapter 6.

2.7.8.4 Pit to Crack Transition

The pits with high fatigue load cycles would transform into a crack if the right conditions are met. This had been observed and the process had been documented with the cracks growing alongside the pit and eventually the crack taking over as the most damaging mechanism[161].

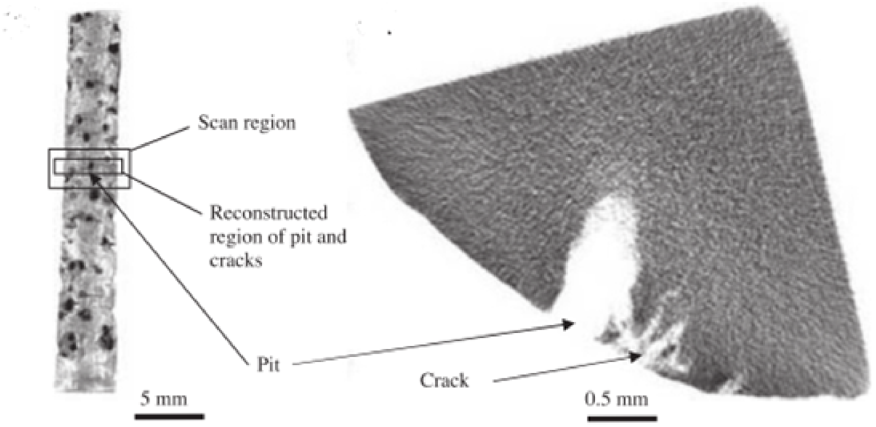

Figure 2-23: Scanning electron microscope of pit and crack interaction [161]

Over the years, different models have been employed to capture as accurately as possible the pit to crack transition. It has to be noted that those test have been run based on sinusoidal load curves and not representing the stochastic loading encountered by offshore wind turbines.

The models that were shortlisted for further analysis were all from steel due to the construction material of the OWT.

A comprehensive list of the models have been reviewed by Larossa and is summarised below[162].

The author Hoeppner developed a model that was used to determine the critical pit depth required to develop into a crack under fatigue loading conditions. The SIF Threshold was developed in this case using empirical means. Lindley was ransition was found using two methods[164].

ress intensity factor

growth and crack growth

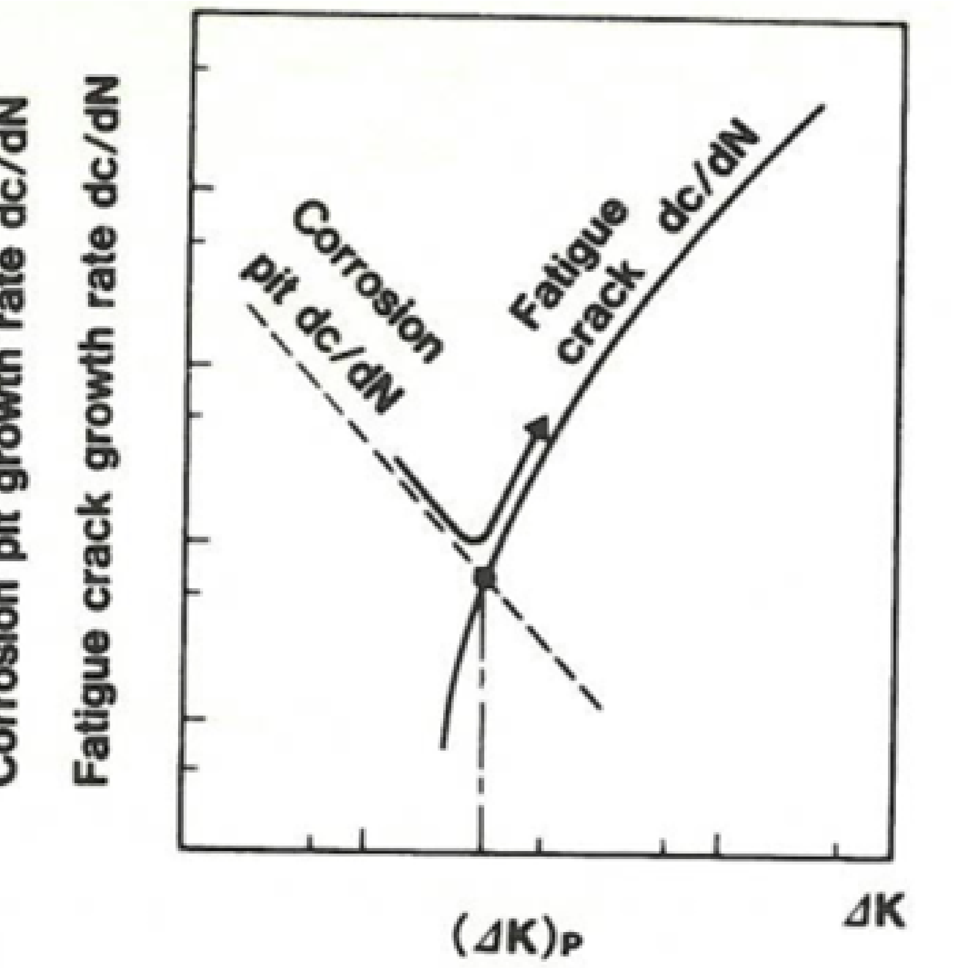

Figure 2-24: Showing pit to crack transition [163]

t to crack transition was analysed in conjunction with both criteria uired stress for the crack SIF to develop to the threshold level.

factor

nption of Kondo was to assume the pit to be a crack. At this point, d intensity factor) was found, which was challenging to calculate ding the critical depth size of the pit.

The SIF had been derived from the plates rather than a pipe/cylinder[165]. The reason lies in the size of the monopiles which have a larger diameter than the pipe and therefore the solution of Newman and Raju do not hold. Therefore a simpler solution has been adapted by using plates. The curvature is a key element and the larger the tube diameter gets, the less is the effect of the curvature on an elliptical deformation.

The equation below relates to the curvature of an elliptical deformation on a cylindrical shell[166].

$$\beta^2 = \frac{a^2[12(1-\nu^2)]^{0.5}}{8Rh}$$

Equation 2-17

Where β is the curvature, a, is the elliptical width, v the Poisson Ratio, R is the radius of the cylinder and h is the thickness of the cylinder. The numerator of the equation can be considered to be a constant in this analysis as bracketed mathematical symbols dealt with the material factor whereas a was the geometry which represented the major axis of the ellipse and, therefore, considered small compared to the structure.

Therefore, the above equation is simplified as shown below:

$$\beta^2 \alpha \, \frac{1}{Rh}$$

Equation 2-18

In a monopile, the values of R and h are significant and they are tending to grow larger with time in the manufacturing phase. This implied that the curvature at the surface decreased and the larger the denominator became, the flatter the surface was. A simple example would be, for instance, the value of the curvature using a radius of 0.1m and 10m for the same thickness of the cylinder. The value of β^2 would be proportional to 10 and 0.1, respectively. This just showed that the effect of curvature could be neglected.

The equations used are as those for the computation of ΔK. Where Kt was the SCF due to the pits and was equal to 5, Y_{NR} was the geometry factor and is estimated from [163]:

$$SIF = YK_t\sigma\sqrt{\pi\frac{a}{Q}}$$

Equation 2-19

The solution held for the following condition and represented in figure 4-6:

a/c = 0 to 1

a/t = 0 to 1

c/b = 0 to 0.5

And φ = 0 to 180 degrees

Where a, b, c and t are shown below:

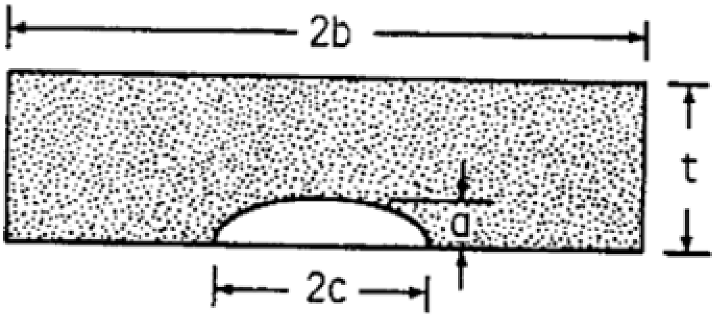

Figure 2-25: surface crack schematic

The lack of solutions for the SIF for cylinders the size of monopiles had proved problematic to correctly identify and quantify the value of the SIF. For instance, when Newman and Raju dealt with the SIF for pipes, the ratio of R to t (where R is the radius and t the thickness) are not calibrated from the monopile dimensions. The goal of this study was not to find the new SIF but, instead, demonstrated the feasibility of applying SHM to find the pit to crack transition. From the reduced curvature as displayed above, the crack on the cylinder will be simulated as a plate. The size of the crack when compared to the width would be so small that the finite plate width factor, f_w, can be neglected.

Where a is the crack depth, c is the crack width, t is the thickness and w is the width of the plate, but in that study assumed to be discretised to the width of the crack to represent this flat surface. Y was referred to as the geometry factor and Q as the shape correction factor. It should be noted, the loading was considered as only under bending. The following set of equations is from Newman and Raju for a semi elliptical crack on a plate surface [212]:

$$Y = \frac{F_b \sigma_b}{Q}$$

$$F_b = [1 + G_1\left(\frac{a}{t}\right) + G_2(\frac{a}{t})^2][M_1 + M_2(\frac{a}{t})^2 + M_3(\frac{a}{t})^4]\, f_w$$

$$Q = 1 + 1.464(\frac{a}{c})^{1.65} \text{ for a/c} \leq 1$$

$$M_1 = 1.13 - 0.09\left(\frac{a}{c}\right)$$

$$M_2 = -0.54 + \frac{0.89}{0.2 + (\frac{a}{c})}$$

$$M_3 = 0.5 - \frac{1.0}{0.65 + \left(\frac{a}{c}\right)} + 14(1 - \frac{a}{c})^{24}$$

$$G_1 = -1.22 - 0.12\left(\frac{a}{c}\right)$$

$$G_2 = 0.55 - 1.05\left(\frac{a}{c}\right)^{0.75} + 0.47\left(\frac{a}{c}\right)^{1.5}$$

$$f_w = \sqrt{\sec\left(\frac{\pi c}{w}\right)\sqrt{\frac{a}{c}}}$$

Equation 2-20

The value of the local stress range will require to be calculated for the pits. This is done using the SCF. The global stress is obtained using the

The value of σ_b that represented the global stress needed to be converted to the local stress. It was achieved by:

$$\sigma_{rf} = K\sigma_{\infty}$$ **Equation 2-21**

K: SCF

σ_{rf}: local stress

σ_{∞}: global stress

The SCF could be computed in various ways but a study was done with the variation of pits aspect ratio to the Stress concentration factor for a single pit and then compared to a surface that accounted for 20 pits[167].

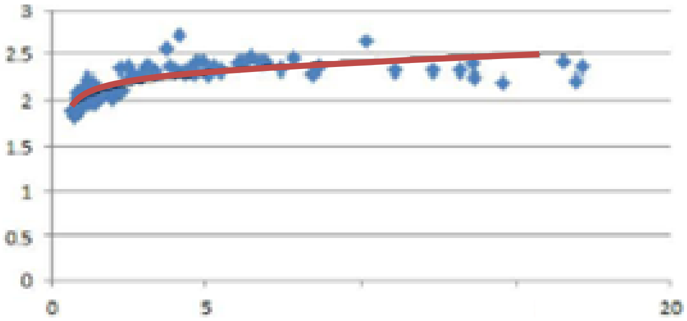

Figure 2-26:SCF vs aspect ratio for only smooth surface[167]

The above graph only considered one pit and not multiple pits. For multiple pits, the SCF did not increase quite as significantly as indicated by the graph below.

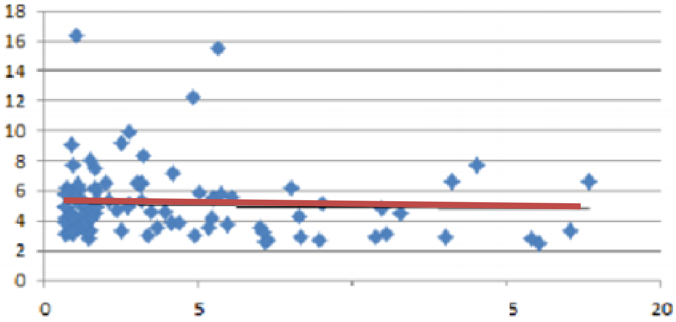

Figure 2-27: SCF vs aspect ratio for rough surface [167]

In this study, the SIF_{pit} was calculated from a simplified methodology, which did not take into account the pit depth transitional value but the pit depth was verified at each iteration of varying equivalent stresses[168].

$$\Delta K_{th} = \frac{\Delta\sigma\sqrt{\pi \cdot a\left[1.13 - 0.07\left(\frac{a}{c}\right)^{1/2}\right]}}{\left[1 + 1.47\left(\frac{a}{c}\right)^{1.64}\right]^{1/2}}$$

Equation 2-22

The above equation would be used to characterise the transition with respect to the SIF of the crack.

During comparison, there were 3 scenarios that would surface and are described further below:

Case 1: Pit Growth

$$Kp > Kth$$

At this point, the mechanism continuing is still corrosion based and the power law is still applied for the growth of the pit.

Case 2: Pit Depth = Crack Depth

$$Kp = Kth$$

This is defined as the critical pit size; at this point the pit turns into a crack and the prediction of the depth of the defect is done with LEFM.

Case 3: Crack dominant

$$Kp < Kth$$

At this point, the mechanism of failure dominating the scene is clearly due to the crack. Again LEFM is applied.

Pit Growth and Crack Growth Rates Comparison

It is important to imagine that the crack has the same dimension and aspect ratio as the pit for comparison purposes.

The Paris law from LEFM is employed to characterise the value of the crack growth. .

The comparison is based on the rate of growth of the pit with the rate of growth of the crack with respect to the number of cycles.

There are two scenarios that can occur depending on this comparison:

1. $\frac{dc_{pit}}{dN} > \frac{dc_{crack}}{dN}$

   In this case, the pit was the winning mechanism and, hence, the most prominent damage mechanism was still the pit and the growth is, therefore, following a corrosive one. It has to be mentioned that it is assumed that the pit can be also a crack and the competition is won by the mechanism with the highest rate.
2. $\frac{dc_{pit}}{dN} \leq \frac{dc_{crack}}{dN}$

   When the above condition was met, it was implied that the dominating mechanism was actually the crack at which point LEFM was employed to govern the growth of the crack.

   The mathematical set up needed to be modified slightly to accommodate the number of cycles.

   The time can be expressed as:

$$\boldsymbol{t = \frac{N}{f}}$$ **Equation 2-23**

The pit depth was therefore:

$$\boldsymbol{c_{pit} = A\left(\frac{N}{f}\right)^{B}}$$ **Equation 2-24**

The pit growth per cycle is found by differentiating the previous equation:

$$\boldsymbol{\frac{dc_{pit}}{dN} = AB\ N^{B-1} f^{-B}}$$ **Equation 2-25**

And can be re-written as:

$$\frac{dc_{pit}}{dN} = \frac{B}{N} c_{pit}$$ **Equation 2-26**

For the crack growth, according to the Paris law:

$$\frac{dc_{crack}}{dN} = C\Delta K^{m}$$ **Equation 2-27**

Where C and m are the intercept and gradient of the Paris region

2.7.8.5 Crack growth

Refer to section 2.2.6

2.7.9 General Overview of Pitting Corrosion and Topological Observation

The observations carried out on the topological changes by Melchers and Jeffrey on coupons plates for a period of two years and can be summarised by the following processes:

(A) Initiation of micro pits
(B) Coalescence of smaller pits
(C) Growth of pits
(D) Formation of benches in pits

The diagram below illustrates those four steps providing a visual of its journey.

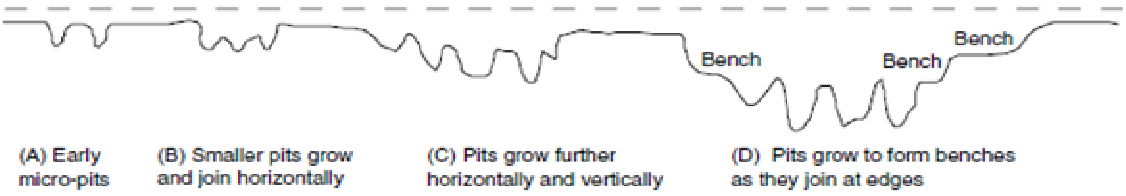

Figure 2-28: Evolution of pits[169]

2.7.10 Pit Definition

The question as to what defines a pit is not related to the comprehension of a corrosion pit as a theoretical exercise. It is regarded instead in a more practical term and asks the questions of what constitutes a pit? and What are the dimensions required for a pit to qualify as a pit? This is a more complex question than it sounds and tends to have more far reaching consequences for inspection.

As a rule of thumb, pits and general corrosion are taken to be[170]:

- Pitting corrosion, which refers to corrosion with length and width less than three times that of the un-corroded wall thickness.
- General corrosion (wastage), which refers to corrosion with length and width more than three times the un-corroded wall thickness

This value should be viewed with a critical mind-set and the following questions have to surface: Why 3 times, why not 2 or 5 in that regards? What is the impact of this definition of pit on a thin walled structure and thick walled structure? Where does that value derive from? Another important point is that pits are very rarely characterised based on their length and width but instead the depth. No studies have been done relating, for instance, to the extreme value of length and width of a pit. To shed light on that point, it is fundamental to think of a piece of steel of thickness 60mm, which is currently employed in offshore wind structures. If there is a surface defect as a matter of corrosion that is 150mm in length and width but only a few microns in depth, can that really be defined as a pit? The problem compounds itself in the case there is pit coalescence with one just smaller than 180mm and the other 50mm with depth of 1mm and the other 5mm, as an example. Is it general corrosion or is it pitting corrosion? This situation causes a serious increase in the SCF, which general corrosion cannot emphasise [235].

2.8 Summary

This chapter looks in detail at both fatigue and corrosion. In each case, an extensive literature review is given to ensure a proper understanding but also capture the various models and tools available in the literature that will be applied in the future chapters. It also allows identifying the gaps in knowledge that can be summarised as:

- A methodology to connect SHM to fatigue for the whole structure from a data-driven approach
- A methodology to connect SHM with pitting corrosion

3 Application of SHM techniques to Fatigue for Tower/Monopiles

3.1 Introduction

The field of SHM is a relatively recent one as it is highly dependent on various interlinked fields including sensor technology, computational processing power, data analysis, and structural and mechanical engineering. There are various sensors that are being used in this field, notably accelerometers, load cells and strain gauges. The most commonly used is still the electrical resistance strain gauge that has the advantage of maturity on its side and can be used to determine the loads, the fatigue damage and even the modal strain.

In offshore wind structures, the bending strain provides the most dominating form of fatigue damage. The strain gauges deployed are used to measure and capture this data but, unfortunately, they do so at point location. This is where the problem lies and is expressed below.

The region that experiences the most damage as a result of fatigue is at the welded parts. Due to the high stress gradients, the strain gauges are placed far from the welds, therefore, capturing of the damage at such locations is not performed. A number of strain gauges are used in general to be able to capture the different regions where the loads are applied i.e. the splash zone(which is wave dominated), the tidal zone(dominated by currents) and the atmospheric zone (dominated by wind loads).

SHM must not be thought only as point problems. This approach might prove to be uninformative as the damage very seldom happens in the non-welded part. The current practice of data analysis is an ironical one and fundamentally flawed and can be summarised as:

“The assessment of the OWT monopile is based on the region where it is less prone to damage and the health of the whole turbine is technically diagnosed at its point of lower damage.”

The very common phrase can be analogous with this practice as being the strength of the chain is measured by its strongest link rather than the weakest link. It is not only wrong but also misconceived and expensive. The development of this tool provides a leap of improvement in the field but one needs to be always aware of garbage in, garbage out.

The analysis in the thesis employed the data from the strain gauge at the same height and the techniques of data fusion are applied to create a mathematical correlation between them. The strain gauges, at the same height, employed the cosine fit, whereas for vertical ones the linear interpolation was used.

The bending strain data used for this analysis was sampled at 20Hz and for three hours across four channels, each one representing a strain gauge placed at the same height but at different circumferential placements. A Rainflow analysis was carried out to find the number of cycles and corresponding stress ranges and mean stresses. Once completed, the equivalent stress was derived and using the appropriate SN curves, the number of cycles to failure could be found at each extrapolated point. The damage was calculated using the Miner's rule.

3.2 Methodology

Different techniques were applied with the aim of providing the fatigue damage.

An important part of this data analysis would be the way the data is saved. Since a cylindrical object was considered in this analysis, it was logical that the damage was saved in a three dimensional matrix but from the start to the finish it varied, from a two dimensional matrix to a three dimensional and then a four dimensional matrix and, finally, the damage data saved in the 3D one.

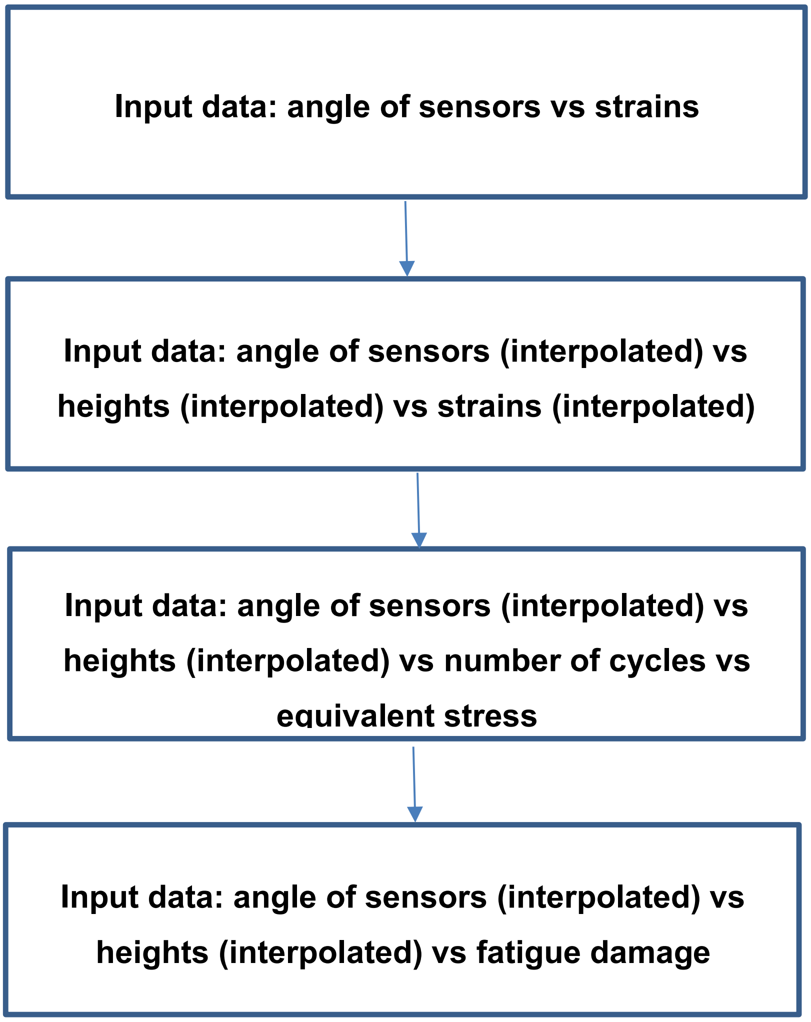

Figure 3-1: data storage evolution from input data to final step in processed data

The method consisted of nine different steps before the Save Damage Block was reached, as shown below.

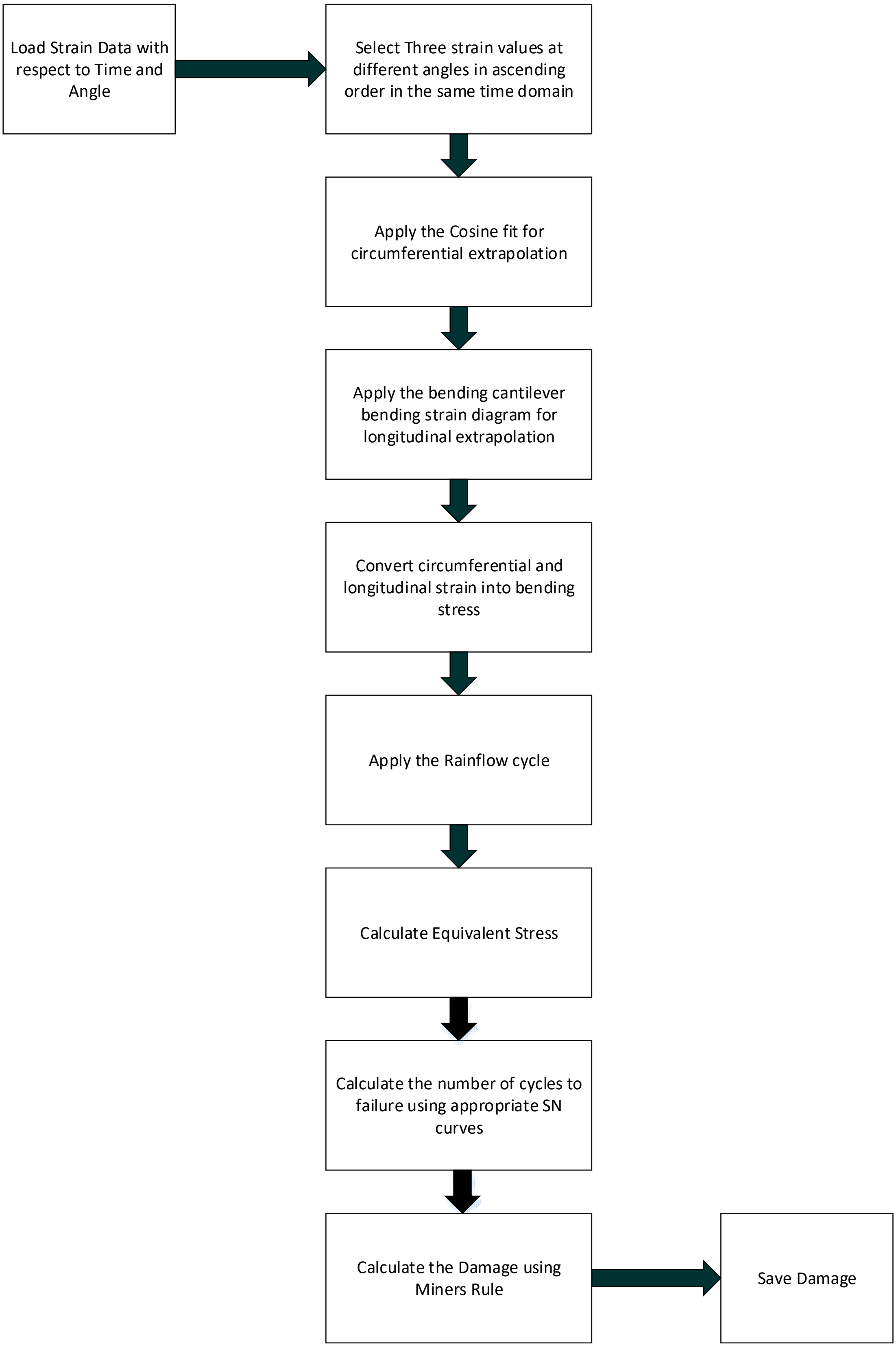

Figure 3-2: Methodology for interpolation techniques

3.2.1 Loading the Data

The data analysed was for an actual offshore wind turbine tower where the bending strain gauges were placed at a distance of 1m from the root of the tower. The data is stored in situ and then transferred wirelessly to a processing station. The data is then batch processed for further analysis as part of a desk study. At this height, four strain gauges with circumferential placements of 0, 120, 180 and 300 degrees, respectively, were used. This system of strain gauge location followed a simple logic and meant to improve on the redundancy aspect of those strain gauges. There was a difference of 180 degrees between a pair of sensors. In theory, the strain gauge pair would read the same magnitude but the direction would be different indicating if one region was in tension implying the other would be in compression. If one of the sensor pairs was damaged, the other pair could still be used for monitoring. It could also be used effectively to check any damage in the strain gauge.

The data analysed was recorded at a frequency of 20 Hz for 3 hours, meaning that for each strain gauge there would be 216000 data points per channel for a wind turbine tower.

This data had to be anonymised for this study.

3.2.2 Geometry of the Tower

The geometry of the tower was taken to be a cylinder with a diameter of 5m and height of 50m. This is not from an imagined structure

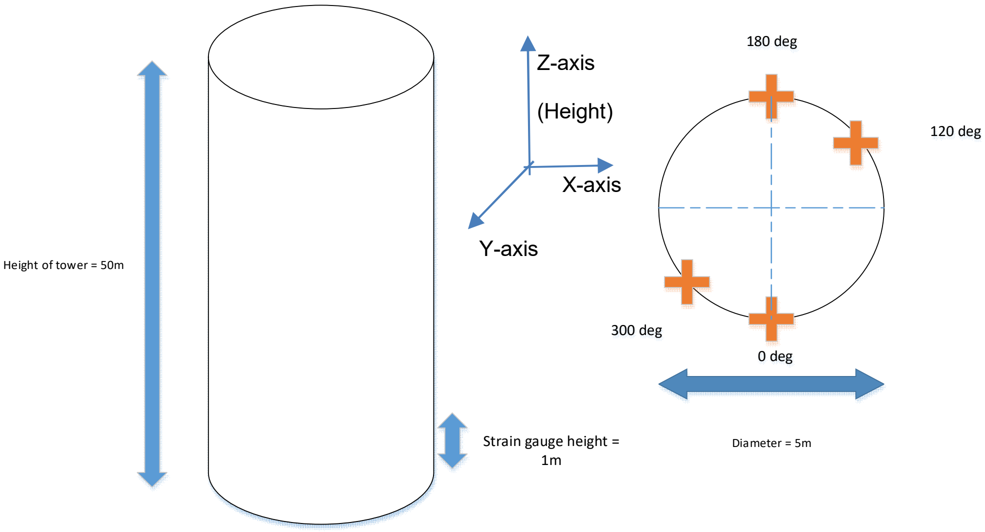

Figure 3-3: Tower/monopile definition

The crosses in the above diagram represented the bending strain gauge installed circumferentially. The angles of the sensors are actually from the real structure.

The material employed for the analysis was Steel, S355 grade commonly employed in the manufacture of wind turbine structures and towers.

3.2.3 Cosine Fit

The cosine fit was chosen as a method of data fusion(is the process of integrating multiple data sources to produce more consistent, accurate, and useful information than that provided by any individual data source)for the circumferential strain values at the same time series[171]. This followed the logic of the redundant strain gauge. If the strain gauges had the same magnitude but different direction and separated by 180 degrees and this logic extended across the whole circumference of the deployment; then it would follow a cosine curve.

This curve would have to be calibrated at each time stamp and this would be demonstrated below as there was a significant variation from one form to the other with common changes in the minimum and maximum points. The three strain gauge values located at 0, 120 and 180 degrees were taken for that analysis and the one at 300 degrees was used as the redundant one and not used in this analysis.

The cosine fit represented a realistic scenario as it clearly displayed the regions of tension (positive values) and compression (negative values). Also, a finite element analysis of a tubular structure is done to validate the cosine fit in this section.

A tube of 25 m long and outer diameter of 50m and inner diameter of 45m was modelled. The boundary condition set was that of an encastre and a load of a concentrated force applied at the top.

The data plotted at 50m outer diameter once the simulation was done under bending stress was plotted as shown:

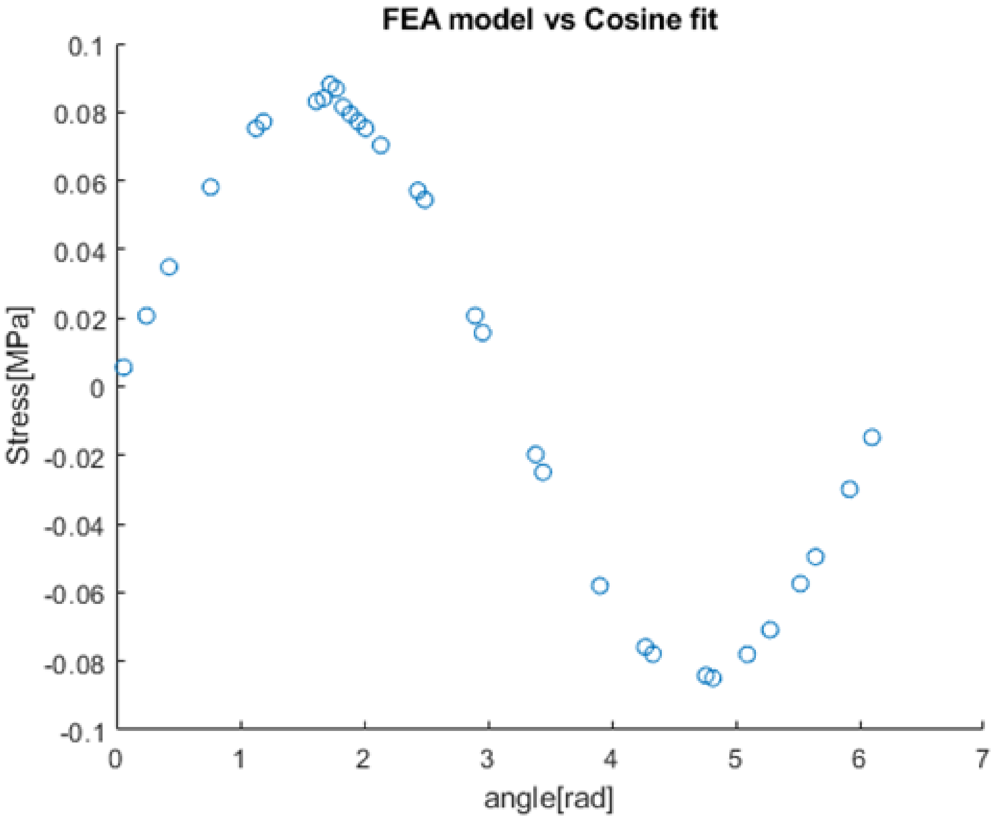

Figure 3-4: cosine fit from FEA model

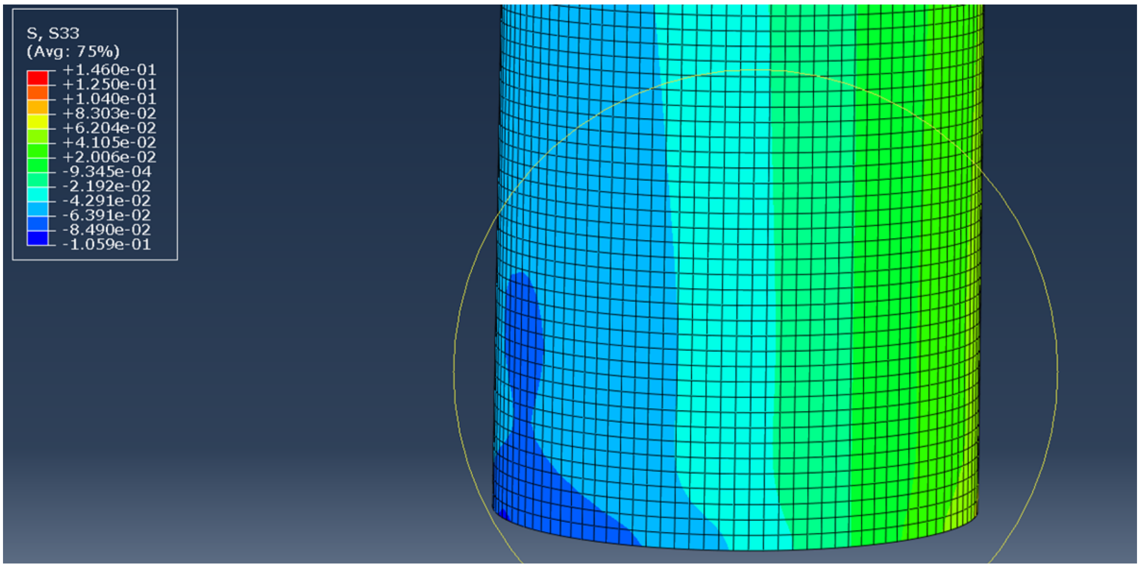

Figure 3-5: FEA results showing region of tension and compression

The above diagram shows the results of the bottom of the tube and the variation from tension to compression on both sides.

This clearly represents a cosine fit.

Mathematics behind Cosine Fit

The general form of the cosine fit can be expressed as:

$$F(\theta) = A - B\cos(n\theta - k) \quad \textbf{Equation 3-1}$$

In the above Equation 3-1, the letters and symbols represented:

- F(θ): the strain value at the respective chosen angle
- A: constant showing the translation along the Y-axis
- B: stretch in the Y-direction
- n: number of cycles in one revolution(where one revolution was between 0 and 360 degrees). In that case, n=1 as there was only one region of tension and compression.
- k: translation in the x-axis

The cosine fit would have to be applied for each set of strain values for the respective time.

The three equations are indicated below for the values of 0, 120 and 180 degrees when applied:

$$F(0) = A - Bcos(0 - k)$$

$$F(120) = A - Bcos(120 - k)$$

Equation 3-2

$$F(180) = A - Bcos(180 - k)$$

Expanding the brackets yield the equations to:

$$\mathbf{F(0) = A - Bcos(k)}$$

$$\mathbf{F(120) = A - B[\left(-\frac{cos\,(k)}{2}\right) - \left(\frac{\sqrt{3}}{2} sin\,(k)\right)]}$$

Equation 3-3

$$\mathbf{F(180) = A + Bcos(k)}$$

Solving those equations simultaneously, the value of A could be found.

$$\mathbf{A = \frac{F(180)+F(0)}{2}}$$

Equation 3-4

For the sake of simplicity, the equation 3-4 obtained and would be renamed as D.

D was replaced as A in the three equations yielding the set:

$$\mathbf{F(0) = D - Bcos(k)}$$

$$\mathbf{F(120) = D - B\left[\left(-\frac{cos(k)}{2}\right) - \left(\frac{\sqrt{3}}{2} sin(k)\right)\right]}$$ **Equation 3-5**

$$\mathbf{(180) = D + Bcos(k)}$$

B was made subject of the formula:

$$\mathbf{B = \frac{F(180)-D}{cos\,(k)}}$$ **Equation 3-6**

The expression of B was then substituted to find an expression for k. It had to be noted that finding k could be challenging between the ranges of values from 0 to 360 degrees as two values of k can exist. To circumvent this problem, the denominator and numerator signs were taken into account and plotted in a quadrant:

$$\mathbf{\tan k = \frac{2\times F(120)-D-(F(180)-D)}{-\sqrt{3}(F(180)-D)}}$$ **Equation 3-7**

In general:

The definition of the function *tan* can be expressed as:

$$\mathbf{tan(\beta) = \frac{\Delta y}{\Delta x}}$$ **Equation 3-8**

This can be seen as:

$$\tan(\beta) = \frac{\text{numerator}}{\text{denominator}}$$ **Equation 3-9**

To evaluate the key angle, the absolute value of the ratio had to be used:

$$Numerator = 2 \times F(120) - D - (F(180) - D)$$

$$Denominator = -\sqrt{3}(F(180) - D)$$

Equation 3-10

To determine in which quadrant the angle would fall, the signs of the numerator and denominator were required. The diagram below shows the quadrant where the range lies.

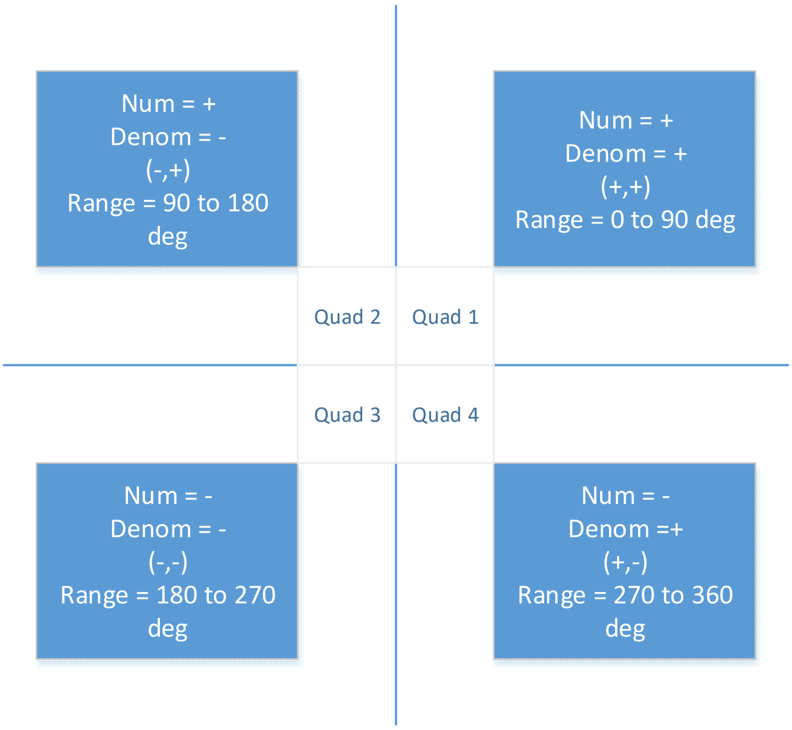

Figure 3-6: Quadrant checks

Once the quadrant is known, the angle could be adjusted to give the value of k as follows:

Table 3-1: Angle correction

QUADRANT	**<u>ADJUSTMENT TERMS</u>**
Quad 1	$k = critical\ angle$
Quad 2	$k = \pi - critical\ angle$
Quad 3	$k = \pi + critical\ angle$
Quad 4	$k = 2\pi - critical\ angle$

The critical angle is the angle calculated from the absolute ratio of the numerator and denominator of equation 3-9.

All the unknowns were now found and from this the strain values could be easily extrapolated for various angles by just substituting them into the equation, which were 0 to 360 degrees with a 30 degree interval. The data processed were stored in a 3D matrix consisting of strain, angle and time. The time had been omitted as the time stamp could be easily redeveloped. At this stage, the data was back to a 2D matrix of angles and strain.

Flowchart for Cosine Fit

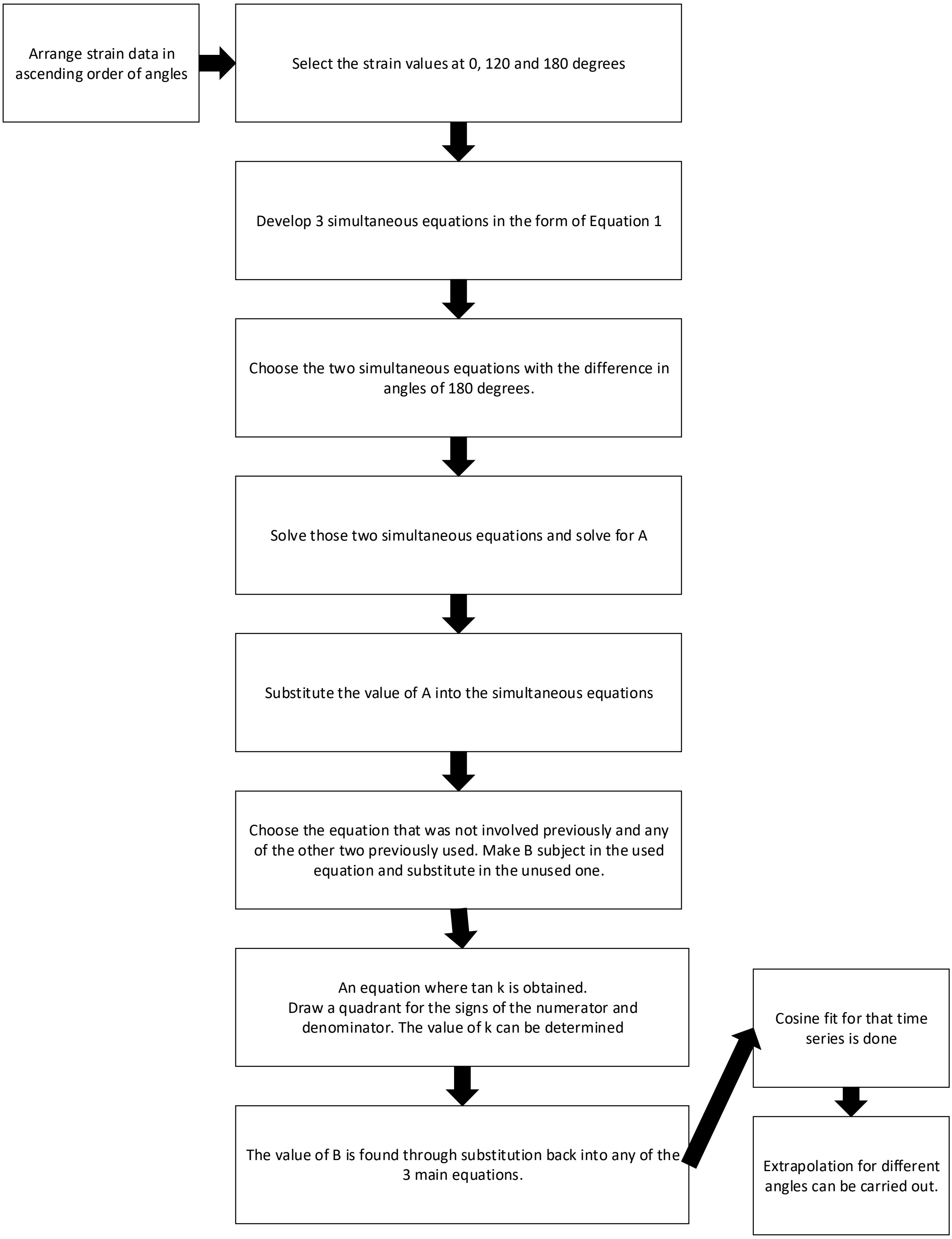

Figure 3-7: Interpolation for circumferential methodology

Bending Interpolation for the Longitudinal Strain Values

The tower could be considered as a cantilever structure. Since the bending strain was known at the 1 metre mark from the root of the tower, the strain values could be linearly interpolated with the top section where the strain was zero. Since there were only two points, the linear fit seemed the more appropriate.

The linear extrapolation from the strain value at the one metre mark to the free end, which was at 50 metres, could be done to find the respective strains at different height intervals. In this case, a height increment of one metre was used starting from 0 to 50metres.

This stage deals with the global stress only.

The saving matrix was transformed from a 2D to a 3D one.

The weld material is different to that of the parent metal. In this study, the heat affected zone is not taken into consideration due to the complexity of this region. The Young's Modulus of welded steel material is generally in the order of 200GPa which is similar to the parent metal[172]. The major difference is in the yield point where the weld tends to have higher strength than the parent metals and a deviation in the plastic region.

In this study, the yield point is considered not to be reached in any case due to the high safety factors incorporated in the design procedures. Therefore the difference will lie in the SN curves employed for the welded and non-welded region.

Mathematics behind Longitudinal Strain Fit

The mathematical derivations were developed as shown below:

($\left(\theta_{1,1}, G(\theta_{1,1})\right)$) where $\theta_{1,1}$, was the first angle at 1 m and $G(\theta_{1,1})$ was its respective strain value.

($\left(\theta_{50,1}, G(\theta_{50,1})\right)$) where $\theta_{50,1}$, was the first angle at 50m and $G(\theta_{50,1})$ was the respective strain value.

Using those two sets of data, a linear equation can be formulated.

The gradient of the line, m is first calculated:

$$\mathbf{m} = \frac{\mathbf{0} - \left(\mathbf{G}(\boldsymbol{\theta}_{\mathbf{1,1}}\right)}{\left(\boldsymbol{\theta}_{\mathbf{50,1}} - \boldsymbol{\theta}_{\mathbf{1,1}}\right)} \qquad \textbf{Equation 3-11}$$

The value of y-intercept, c would be assumed to be zero due to the cantilever effect..

This process was done for the different angles obtained in the cosine fit extrapolation and from that the strain for the simulated angle and height could be determined.

Flowchart for Linear Interpolation

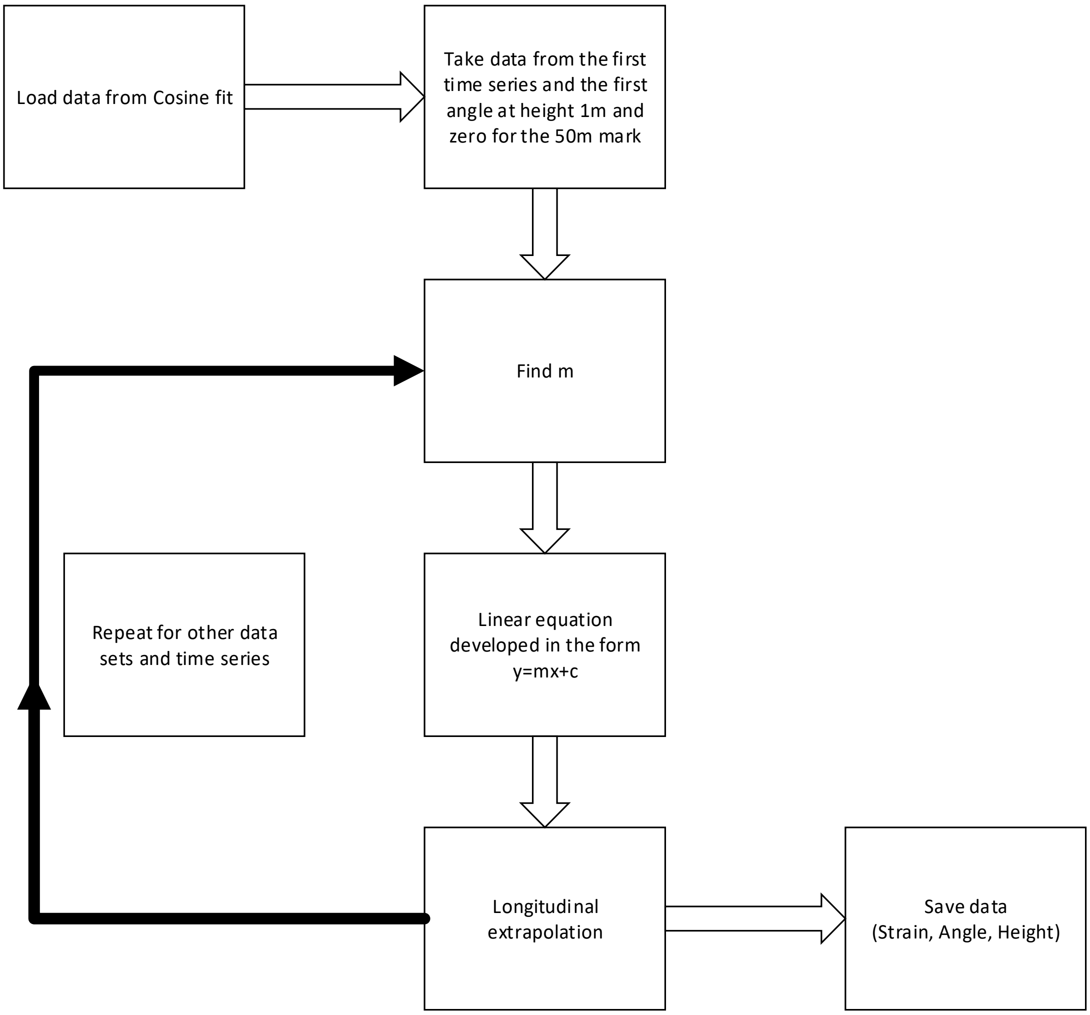

Figure 3-8: Longitudinal interpolation method

3.2.4 Conversion from Strain to Stress

The bending strain was converted to bending stress using the equation below:

$$\mathbf{Youngs\ Modulus} = \frac{\mathbf{stress}}{\mathbf{strain}} \qquad \textbf{Equation 3-12}$$

The stress was calculated for each of the points on the cylinder. The value of the Young’s Modulus was taken as 200 GPa for the grade of steel defined.

3.2.5 Rainflow Count

The Rainflow algorithm used was from the MathsWork toolbox on signal processing based on the ASTM Standard[173]

The Rainflow was carried out for each data set per time series extrapolated from the previous methods. The Rainflow cycle reduced the time series into a set consisting of the stress range and number of cycles. The dimensions saved in that case are in the form -Stress Range and mean, Number of cycles, Angle, Height creating a 4D matrix.

Equivalent stress

The equivalent stress was calculated based on the gradient of the SN curve obtained from DNV C203:

$$\Delta\sigma_{eq} = N_i \left[\sum_{i=1}^{n} (\Delta\sigma)^m\right]^{\frac{1}{m}} \qquad \textbf{Equation 3-13}$$

Where:

- $\Delta\sigma$: stress range
- N_i: the number of cycles in the range of $\Delta\sigma$.

The data was saved in this format: (Equivalent stress, Angle, Height)

SN Curve calculation

The SN curve was used to estimate the life of the structure based on the actual equivalent stress values.

For the purpose of this particular study, the SN curves chosen were obtained from the DNV design of offshore structures for welded and non-welded sections[44].

- B1 – Non welded sections
- B2 – Longitudinal weld
- C1/3 – Circumferential Butt weld made from both sides dressed flush i.e. Automatic fillet or butt welds carried out from both sides but containing stop- start positions.
- F3/7 – Circumferential Butt weld made from side without a backing bar(used for additional connections like ladders)

The schematic indicates where the welds were applied:

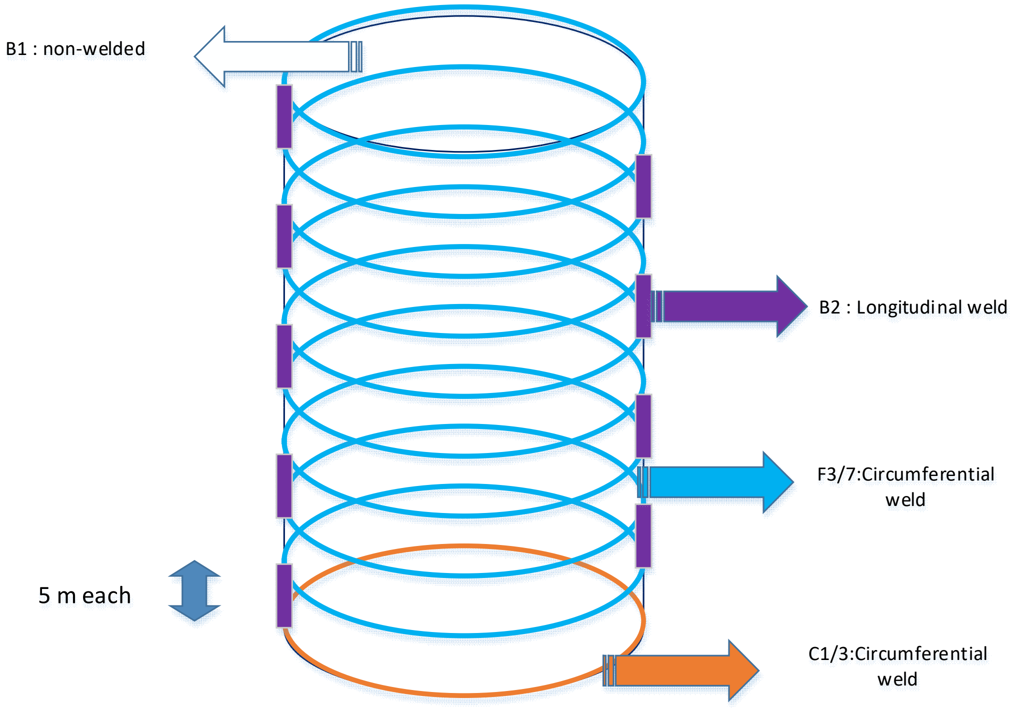

Figure 3-9: Welds locations and SN curves used on tower/monopile

Damage

The damage was evaluated from the Miner’s rule described in chapter 2

N can be found to be 9.46E6 cycles. If the value of D is lower than one, then the structure will survive else it will not.

3.3 Results and Discussion

3.3.1 Cosine Fit

There were two main types of extrapolation before the results from those processes were further processed to get the damage. The first aspect of this section was to demonstrate the capabilities of the cosine fit in extrapolating the data.

Various plots were undertaken for different time series and are displayed below. It should be noted that the data plotted was for sensors deployed at a height of one metre from the root of the tower.

Those graphs are important as they are displaying the variation of the bending strain with varying environmental and also operational conditions. For instance under high wind speeds, the bending strains will be higher than under low wind speeds.

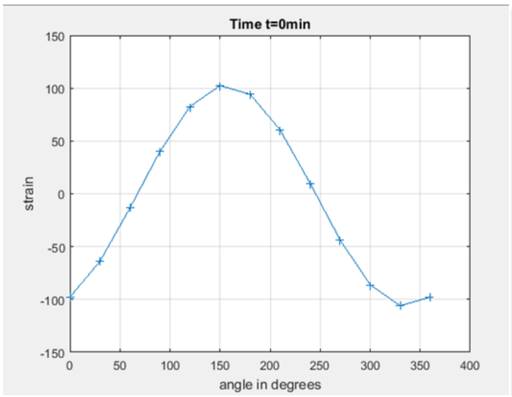

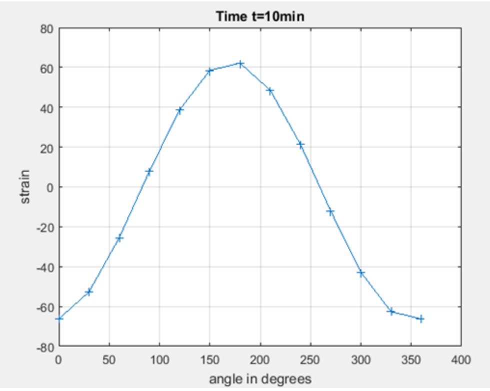

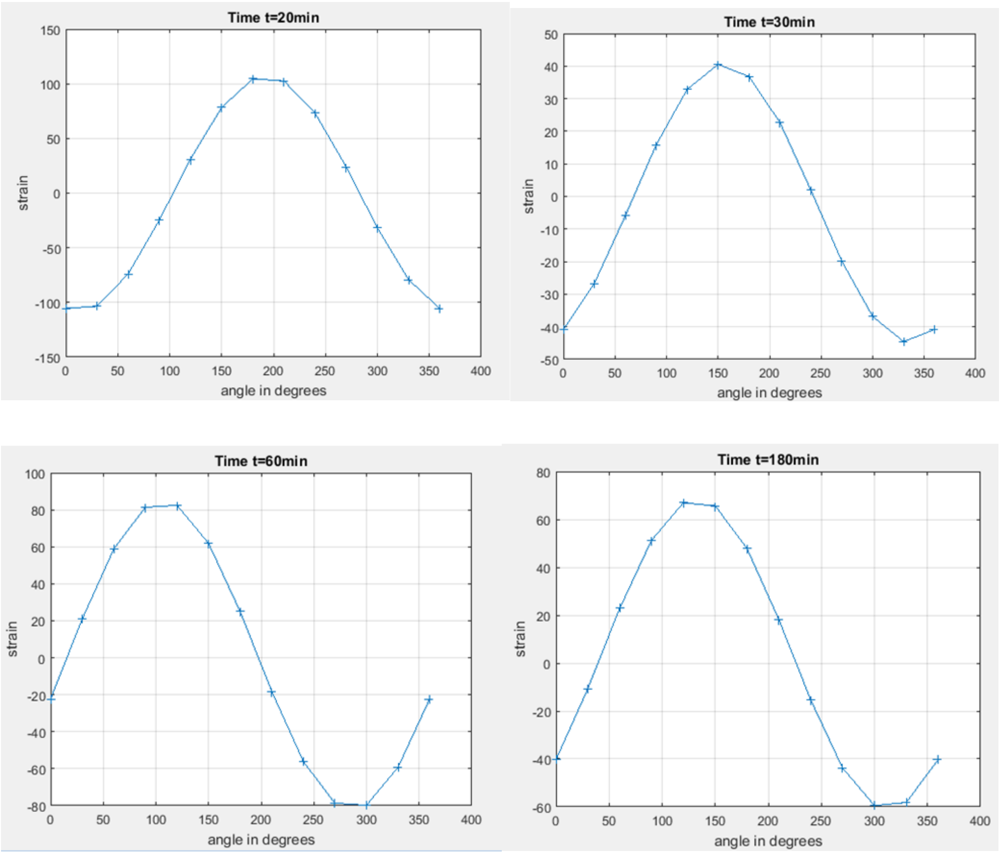

Figure 3-10: Variations of cosine fits in terms of amplitude and shape

The resolution of the graph can be achieved by increasing the angular intervals. The downside of increasing the accuracy would be the time taken for processing the data and the increase in data storage.

A problem with the cosine fit was it did not take into consideration the effect of eccentricity. For ageing structures there might be some errors with regard to the data processing using this technique as it assumed that the geometry on a horizontal planar level was circular.

3.3.2 Longitudinal Interpolation and Rainflow Count

The data set analysed using an iterative loop took more than 10 hours to generate the interpolated values but those using matrix multiplication took less than 3 minutes. It is highly recommended to take this approach while coding.

The processed data was increased by 50 fold generating a matrix storing 216000 X 13 X 50 data points. This must not be a problem, though, as at a later stage the matrix would be reduced and the 216000 rows of data for each angle and height would be converted to one after the Rainflow count. The parameters stored were the stress range and number of cycles. The stress range consisted of the difference between the maximum and minimum values. The matrix saved was expressed as stress range, number of cycles, angles, heights. This data was smaller than the previous longitudinal strain data which can be discarded at this stage.

3.3.3 Conversion of Strain to Stress, Equivalent Stress, SN Curve and Damage

The estimated equivalent stress (obtained from the conversion of the strain to stress) was calculated with each of the values of the gradient attributed accordingly based on the SN curves in the DNV C203 standards..

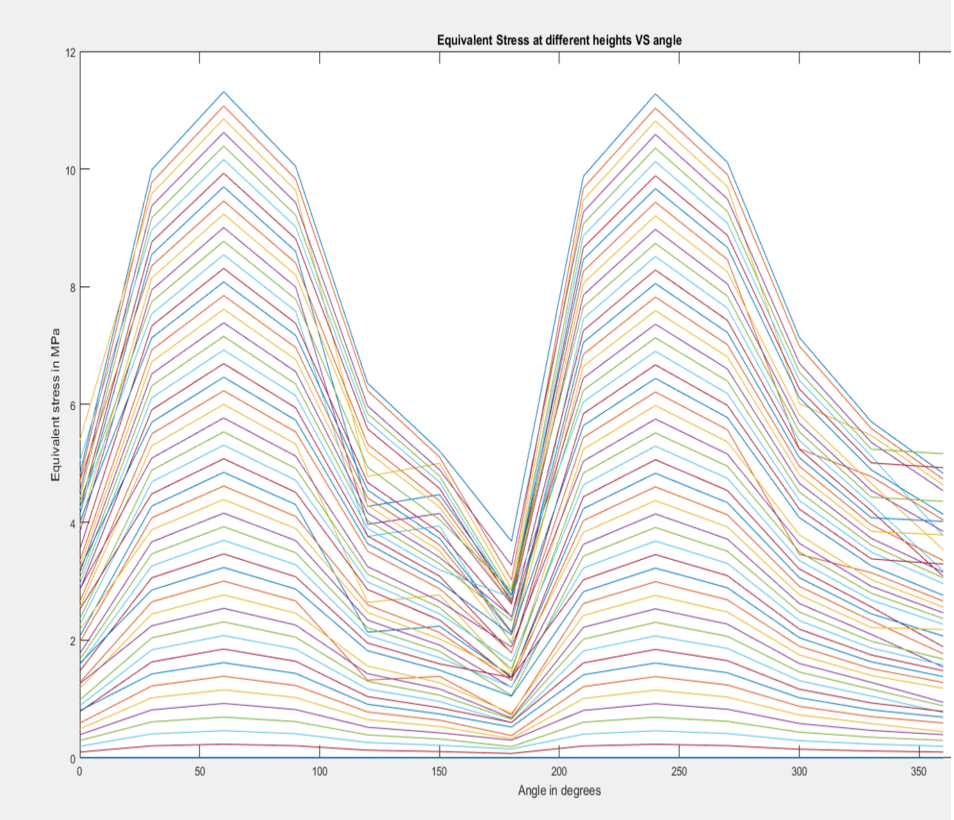

Figure 3-11: Equivalent stress

It could be seen from this graph that the peaks for each graph were consistent and this was a good indication of the algorithm working. In that case, the maximums are at two specific heights. The graphs are almost symmetrical due to the nature of the cosine fit. .

The graph below shows the computed damage. It was important to note that the highest damage was not at the root of the tower as this weld section used the C1 curve that has its SN curve proving to be more resilient to fatigue loading even though the stress range is higher. The damage vs. angle graph actually indicates the variation and the damage across the structure.

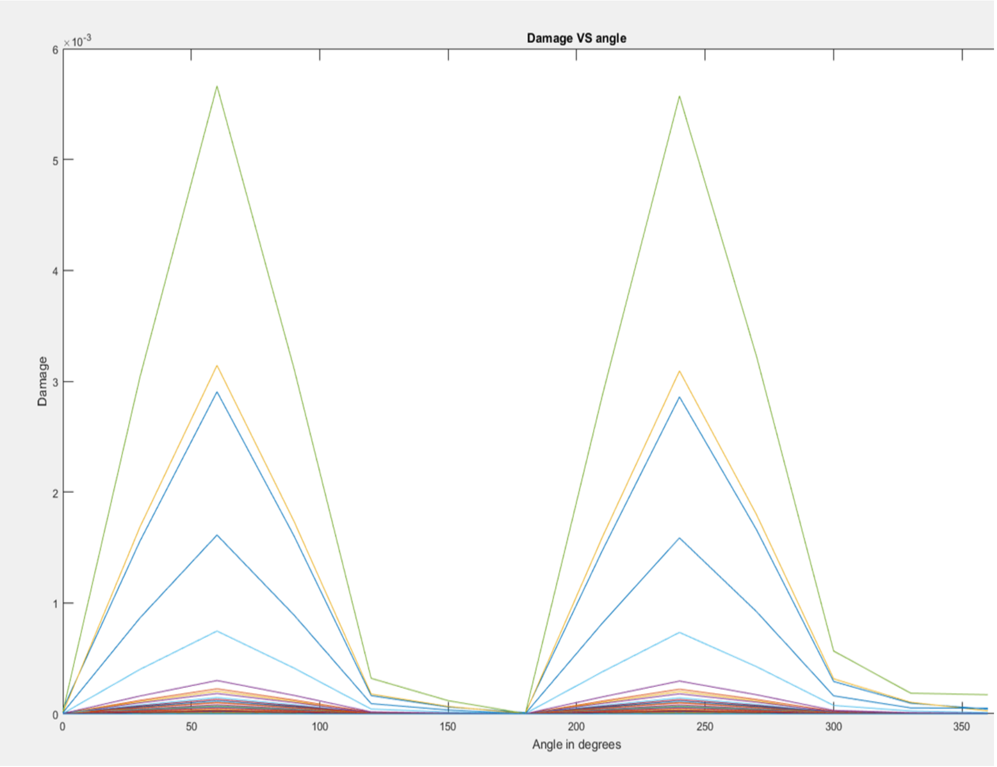

Figure 3-12: Damage vs angles at various heights

It can be observed that above 25 metres in height from figure 3-13, the damage was negligible and at first sight any kind of inspection was not really valid considering the low level of damage in those regions. Obviously, this analysis assumed that there were no prior defects in the structure, for instance pitting corrosion or manufacturing defects that could cause a change in the damage graph.

The visualisation at this stage was still confusing and a better model had to be represented showing the damage on the structure.

The welded regions, as expected, were the regions that required more attention both for design and inspection, as represented below. The welds had been assumed to have a Young's modulus of 200GPa and only the elastic region has been considered. The base metal could be neglected for inspection provided that the manufacturing requirements had been met and good corrosion controls had been established.

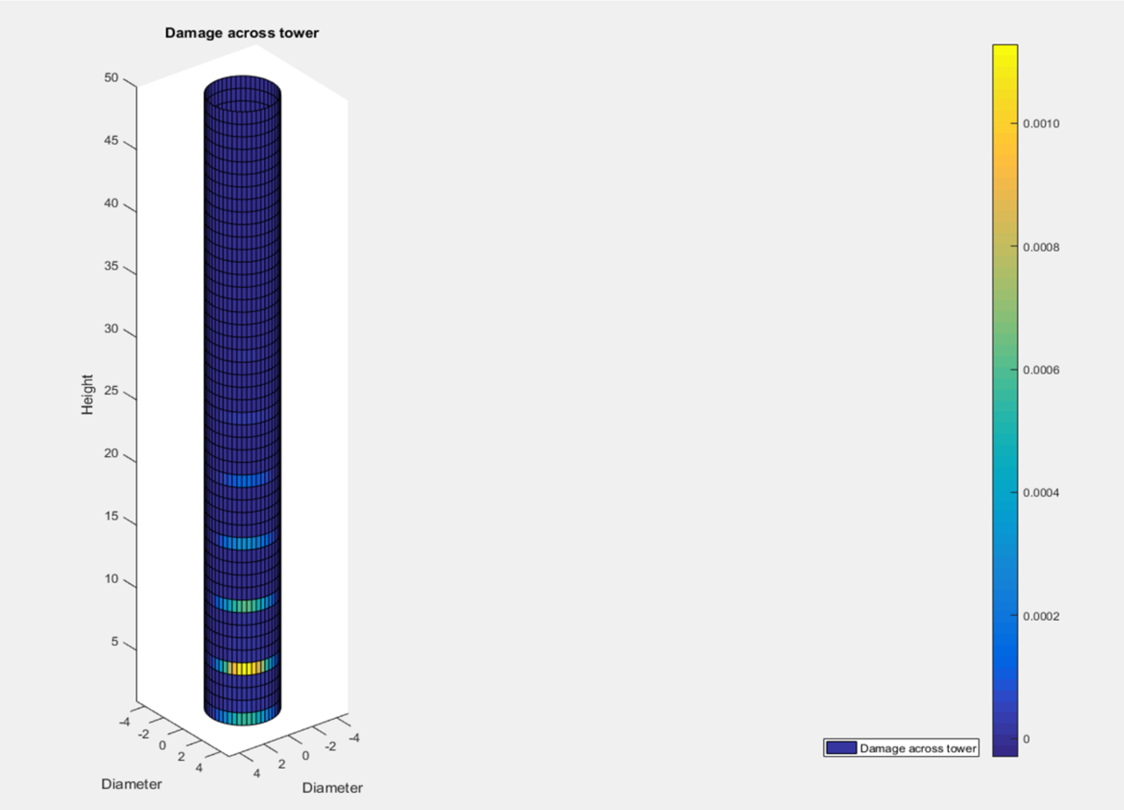

Figure 3-13: Damage representation

3.4 Summary

The interpolation technique provided a new perspective in the data analysis of offshore wind structures with strain and fatigue damage accessible on the structure. Using this technique and applying the right SN curves, the improved fatigue damage had been calculated and visualised. The processing speed and stored data could be problematic but with parallel computing and large capacity multicore computers with online storage, those problems can be avoided even though the implementation cost can be quite high.

This method had to be used carefully and a data check was required before any attempt to extrapolate the data.

If more sensors are deployed at different heights on the structure, the linear interpolation can be refined in using a more appropriate model fit.

4 Application of SHM to Pitting Corrosion for Tower/Monopiles

4.1 Introduction

The marine world is complex and unforgiving towards structures. Even giant structures like wind turbines are damaged by the environment in different forms. There are various forms of marine corrosion varying from general corrosion, to pitting, crevice, corrosion fatigue and others but pitting corrosion is considered the most damaging.

The inspection of the internal part of the monopiles brought to light the presence of pits, a problem that was not foreseen by the designers as it was assumed that the internal section would be water tight. This happened due to the leakages of the J-tube seal, which had encouraged water exchanges that created quite a unique environment for corrosion to thrive. The water movement had been mainly a result of the tidal changes implying that during low tides the water level inside the monopile lowered and during high tide the water level went up. This alteration created two regions, namely a wetted one and another section that is basically immersed inside the monopile. It is worth mentioning the effects of splash zone corrosion were non-existent in this actual case as the structure's internal components were shielded from the wave loads and the rich oxygen environment synonymous with that region. The inner section of the monopiles was not protected and since the corrosion problem had been flagged, wind developers had been trying different techniques of corrosion protection with varying levels of success. For instance, covering the surface with marine coatings had proved to be beneficial but the problem of inspection became more challenging; also, the process of coating on site at sea was usually an expensive feat costing around £3000/m^2. The other strategy was connecting sacrificial anodes to the inner surface of the monopile. This strategy did not work but due to the design of the monopiles, which comprise an air tight platform, there had been releases of hydrogen and hydrogen sulphide gases (flammable gases) that accumulated at the top section of the inner platform. Also the pH of the environment changed immensely and became more acidic with respect to time. This meant that the sacrificial anodes would consume themselves and their effectiveness towards protecting the structure became questionable in the long run. As a matter of fact, when the pH increases it also implies that more hydrogen will be evolved at a faster rate in the process, thus making the situation more risky. Corrosion allowance was another strategy used. The design standards provide a degree of corrosion allowance but this must be carefully assessed in terms of cost and effectiveness. The corrosion allowance applied was taken as uniform corrosion, which meant that stress raiser effects were neglected. Also, the non-uniform corrosion allowance needed to be observed in the fatigue limit state, which was omitted in the design code. The important question related to the inspection of the damage as a result of the corrosion. This needed to be viewed in the form of frequency of inspection and also time spent on inspection, which were all strongly correlated to the operational expenditure of the project.

The pitting mechanism is complex as in its evolution it goes through different phases. It can transit from a chemical effect to a mechanical one implying a transition from pitting corrosion to a crack. Once the mechanism shifts to a crack, the damage accelerates significantly and, therefore in practice, the need for an inspection becomes more pressing to assess fully the structural integrity of the foundation.

The aim of this study is to develop a tool that would allow the wind developers to make an informed decision for the inspection with respect to pitting corrosion of monopiles. SHM, using bending strain gauges, had been employed and married with the current pitting model to assess the stress raisers as a result of the pits, the pit to crack transition and finally the crack growth. According to the literature, no such study has ever been performed where the combination of a data-driven approach is linked to a pitting corrosion model. The pit model included the increase in the number of pits with time and also the growth in the dimension of those pits. The marrying part comes in the form of the cosine interpolation technique, described in Chapter 3, for finding the global stress at the pits. The stress concentration was applied to compute the local stress based on the aspect ratio of the pits. Once this was done, the pit to crack transition was calculated to determine the relevant growth mechanism and to also establish whether the growth mechanism would be corrosive or crack driven or it can be both such as stress corrosion). The instant it transformed to the latter, linear elastic fracture mechanics (LEFM) would be applied to capture the evolution of the crack with respect to time or number of cycles. Finally the damage had to be calculated to make the inspection decisions easier and more quantifiable.

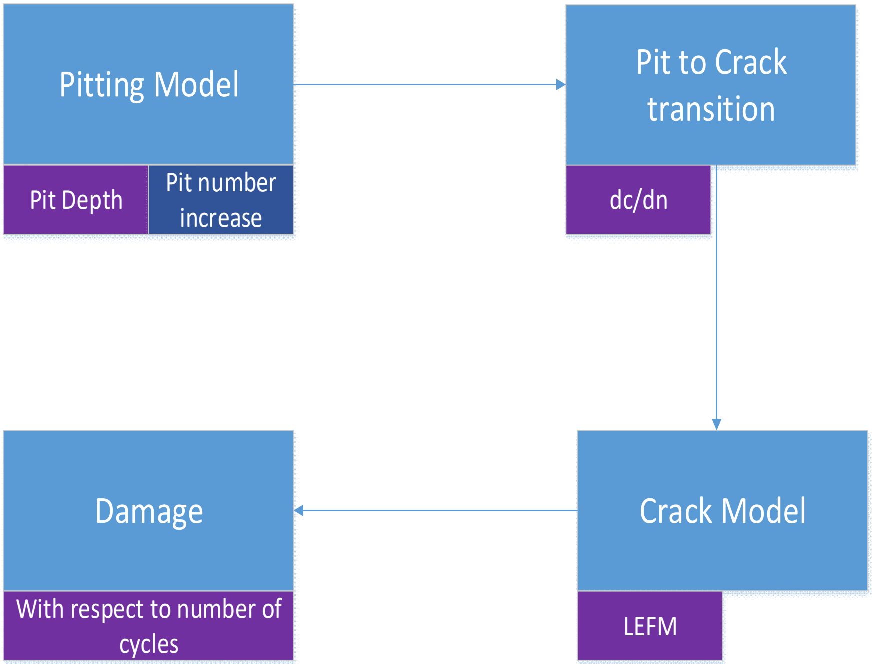

Figure 4-1: Schematic of models used in this study

4.2 Methodology

The main idea of this study was to link the bending strain data to pitting corrosion. This required a careful assessment of the electrochemical and mechanical effects to determine which damage mechanism was the dominant one and, thus, taking precedence in the algorithm developed.

1. **Load the Bending Strain Data**

   The data for the bending strain gauges for the wind turbine was loaded. The strain gauges were placed at an angle of 180 degrees between each pair to characterise the region of tension and compression and had the same lay out as the one used in the previous chapter on fatigue analysis. The difference was instead of finding the strain history for each section defined by the angle and height of each can (pre-set with constant intervals), in that case it was being used to find the bending strain and eventually the equivalent stress at each pit.

2. **Load the Geometry of the Monopile**
   The geometry of the monopile was taken to have a diameter of 5m, a height of 10m and thickness of 50mm.
3. **Load the Strain Gauge Location**
   The strain gauge locations had to be included in the analysis. This would include the height where they were positioned and also the respective angles. Failure to do so would result in the cosine fit interpolation being not applicable. The angles were at 0, 120 and 180 degrees.
4. **Increase the Number of Pits with respect to Time (year)**
   For the coefficient of the quadratic term from equation 2-15, a random integer was generated between one and another random generated integer to represent the pit intensity.
   The unit of time in that case is in years. Therefore, the number of pits is increased on a yearly basis.
   When adding those pits, care was taken into taking away the pits from the previous year. For instance if the equation generated was simply t^2 where $\lambda = 1$, the first year would have one pit and the second year would have four pits, meaning that the newly added pits for the second year was three.
5. **Location of Pits**
   The pits were generally considered to have a random distribution at their initiation sites as no spatial correlation has been found in the literature and has not been considered in this study[143]. The locations of the pits have not been characterised yet inside the monopiles. Therefore, the pits were randomly distributed across the structure and the methodology had been provided below.

The monopile was a cylindrical structure. To locate the pits required a 2D geometrical interpretation of the monopile, which was simply a rectangle that has been curved.

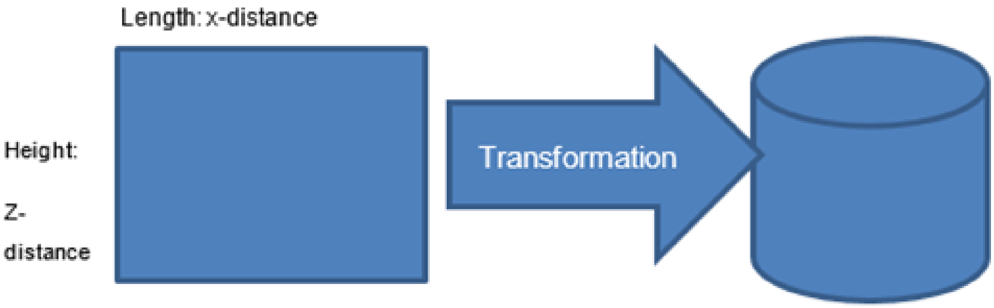

Figure 4-2: Coordinate transformation

The height of the pit location stayed the same upon transformation to a cylinder but the length required a mathematical transformation into polar coordinates.

The radius was constant and for the study it had been chosen to be 2.5m.

The total length represented the circumference of the circle. Using this fact and knowing the distance of the pit in the x-direction, the angle for the polar coordinate was computed as:

$$L_X = r\theta \qquad \textbf{Equation 4-1}$$

From this equation, the angle was found and the pit locations were changed to cylindrical coordinates as (r,θ,h_z).

The values of the x-distance and z-distance were randomly generated in Matlab for the yearly pit intensity before being converted into cylindrical coordinates.

6. Pit Strain History

There were four strain sensors at the bottom of the monopile and there was a linear interpolation done assuming that the monopile was cantilevered and the top section has no strain acting on it.

For each pit location, using the z-distance of each pit, the longitudinal strains from the 4 sensors could be mapped and using the angle for the pit and applying the cosine fit, the strain history was derived for each pit.

The strains at the pits were extracted using the following procedure:

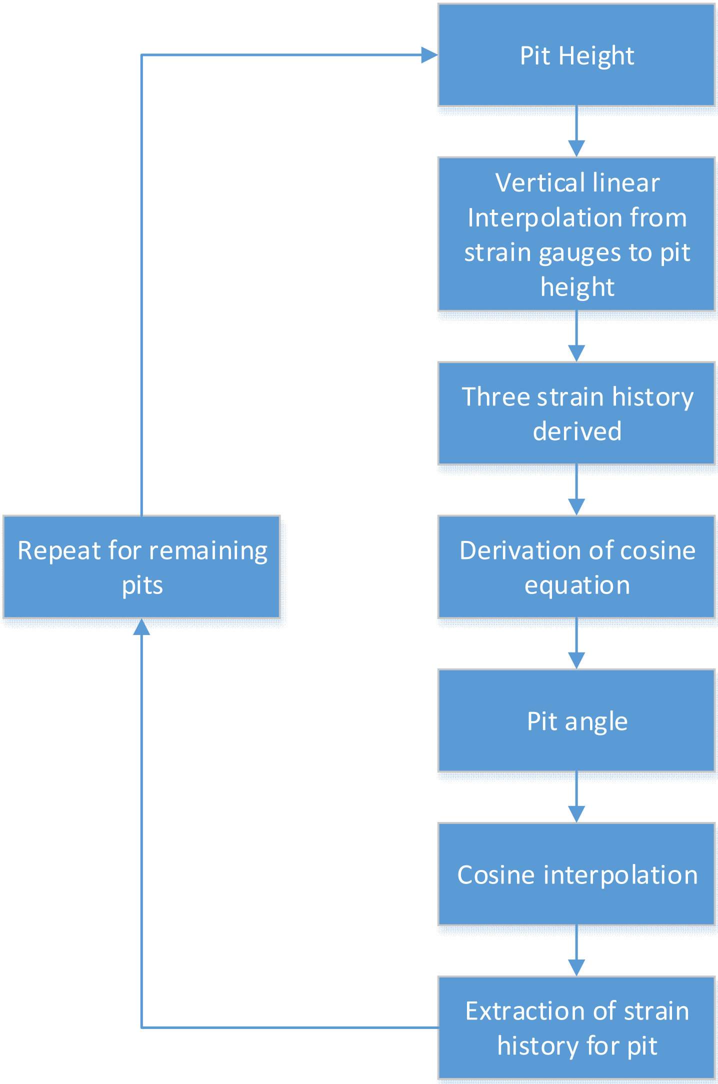

Figure 4-3: Flowchart for pit strain history

7. **Pit Growth**

   The pit's dimensions were made to increase with respect to time. The pit's depth has been observed to follow a power law[148]. The reason behind its application is that the model for pitting growth in sea water has been calibrated and this is more representative of the actual problem.

   The equation for the pit depth was:

$$c = At^{B} \qquad \textbf{Equation 4-2}$$

   Where A was obtained in the field as 0.003 and B was the exponent that lay between 0.3 and 0.8 and, for each pit available, this value was randomly generated in Matlab where t is the time and c is the pit depth[153]

   .

   For the pit width, the equation is employed:

$$\frac{c}{2a} = aspect\ ratio$$

$$2a = \frac{c}{AR} \qquad \textbf{Equation 4-3}$$

   c: pit depth

   2a: pit width

   T

8. **Stress at Pits**

   The strain was converted to stress by multiplying with the Young's Modulus of Steel S355 (200MPa) and the Rainflow count was done and, thus, the equivalent stress computed. This stress represented the global stress and did not take into account the effect of the pits. The stress concentration factor was taken to be five, as demonstrated in Figure 4-7.

9. **Rainflow Count and equivalent Stress**

The Rainflow count was the method used to calculate the equivalent stress for a stress history[174].

The sections defined in this study only take into account the B1 curve.

The equations for the equivalent stress is then[175]:

$$\Delta\boldsymbol{\sigma}_{eq} = \left[\sum_{i=1}^{n} \boldsymbol{N}_i(\Delta\boldsymbol{\sigma})^{m}\right]^{1/m}$$ **Equation 4-4**

The values of C and m are those from the SN curve for B1 chosen to be m=3 and C = 12.436 under free corrosion[175].

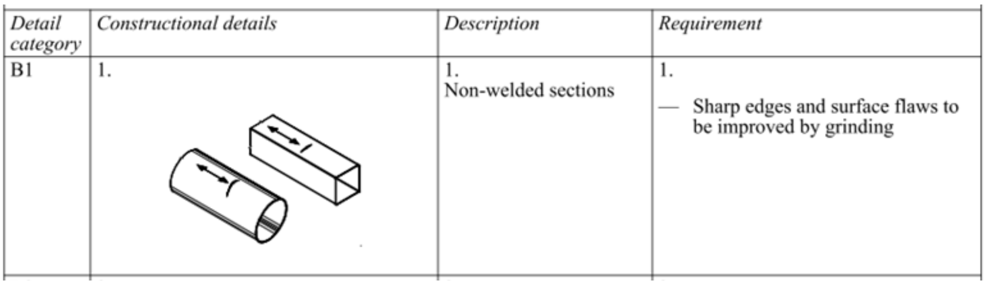

Detail category	*Constructional details*	*Description*	*Requirement*
B1	1.	1. Non-welded sections	1. — Sharp edges and surface flaws to be improved by grinding

Figure 4-4: Non-welded section B1 used to define Paris region[175]

10. Pit to Crack Transition

The pit to crack transition was characterised from the change of depth of the pit and crack with respect to the number of cycles. To illustrate this section in a clearer manner, an example was set up. It consisted of looking, for instance, at 20 pits that were initiated by the algorithm for the first year. Coming to that section, the pits were tested to check if they had evolved into cracks or still growing into pits. Assume, for the sake of simplicity, that 5 of those pits had now turned into cracks. The moment the pits turned into cracks, they remained as cracks. This meant that the algorithm needed to sort the pits from the cracks as their growth was totally different. Thus, when the pit turned into a crack, a new matrix was set up to save the one that had turned to a crack with the others still behaving as pits and their growth mechanism for the second year following the power law.

The value for computing ΔK according to the Paris region is m=3.86 and C = 1.25X10^{-12} selected from the material base metal (BM) in sea water undergoing free corrosion[176].

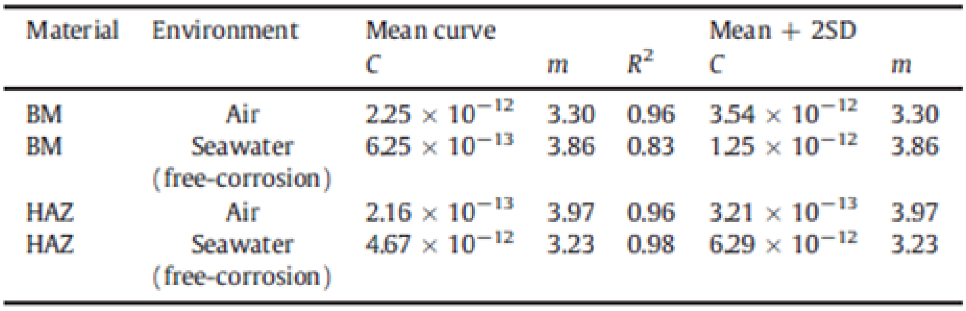

Material	Environment	Mean curve			Mean + 2SD	
		C	m	R^2	C	m
BM	Air	2.25×10^{-12}	3.30	0.96	3.54×10^{-12}	3.30
BM	Seawater (free-corrosion)	6.25×10^{-13}	3.86	0.83	1.25×10^{-12}	3.86
HAZ	Air	2.16×10^{-13}	3.97	0.96	3.21×10^{-13}	3.97
HAZ	Seawater (free-corrosion)	4.67×10^{-12}	3.23	0.98	6.29×10^{-12}	3.23

Figure 4-5: Non-welded section B1 defining Paris region[176]

11. Crack Propagation

For those remaining as pits, this section did not apply. The cracks only were now considered.

From the derived equation for the crack growth from the Paris law, the number of cycles needed to be calculated. As a rule of thumb, the frequency of a monopile can be considered to be 0.3Hz. This corresponds to the soft-stiff region, which tended to be ideal and out of the frequency range of the environment and the operation of the structure. This value of 0.3 Hz can be employed to determine the number of cycles experienced by the structure in a year.

$$\frac{10}{3}s = 1\ cycle$$

The total number of seconds in a year:

$$1\ year = 365.25X24X3600\ s$$

Now it can be said that:

$$1s = \frac{3}{10}cycles$$

$$1\ year\ = \tfrac{3}{10}X\ 365.25\ X24X\ 3600 = 9467280 \text{ cycles}$$

The values of C and m were taken to be the same as the previous section[176].

12. Damage due to Pit and Crack

The damage for the pits can be calculated using the stress concentration factor and the stress range(obtained from the strain gauges and the rainflow count) and the SN curve B1. The number of cycles obtained can be used to calculate the Miners Damage.

In case of the pit transforming to a crack, the Paris law is used. Here a through crack is assumed and the Paris equation 4-5 is used to calculate the number of cycles to failure. Again using the Miner’s damage, the damage can be calculated.

$$N = \frac{a_c^{\left(1-\frac{m}{2}\right)} - a_c^{\left(1-\frac{m}{2}\right)}}{Q^m\left(1-\frac{m}{2}\right)c(\Delta\sigma)^m}$$

Equation 4-5

Pit growth size using power model

Crack growth prediction using SHM and LEFM.

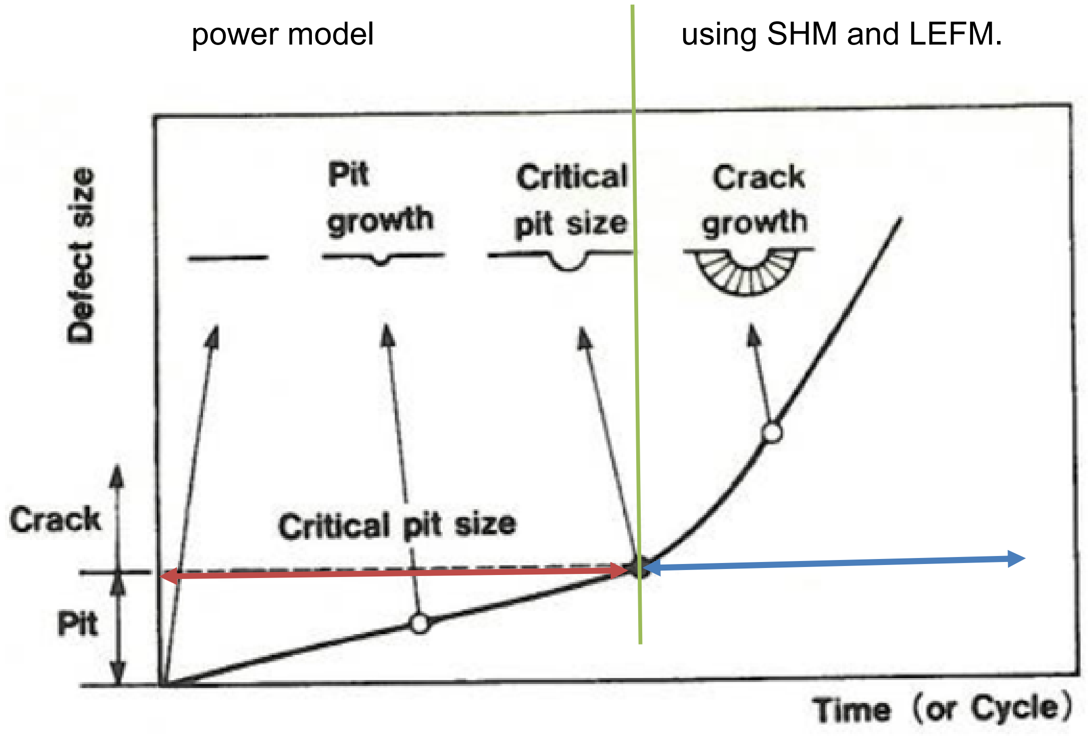

Figure 4-6: pit and crack growth and application of SHM

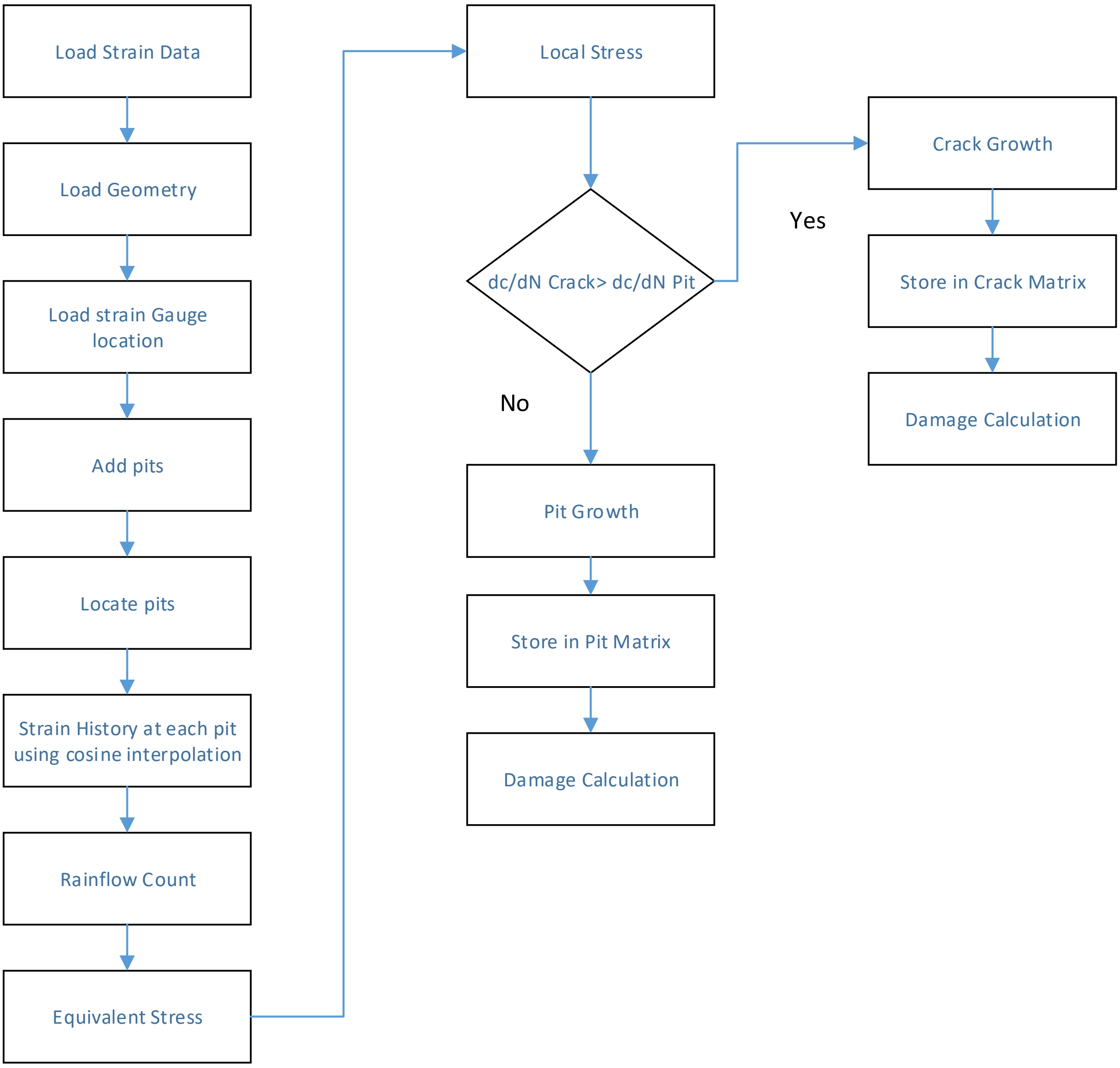

Figure 4-7: Methodology of pitting corrosion with SHM

4.3 Results and Discussion

The pit location was first computed and it was distributed over a height of 10 metres. The number of pits were then increased under the equation as shown in the pitting corrosion model with the value of $\lambda=28$. This value was randomly generated.

The simulation ran over a period of 3 years and the following graphs demonstrate their distribution in the monopile.

It had to be denoted that the number of pits varied according to the section, as shown in section 5.10 of this thesis.

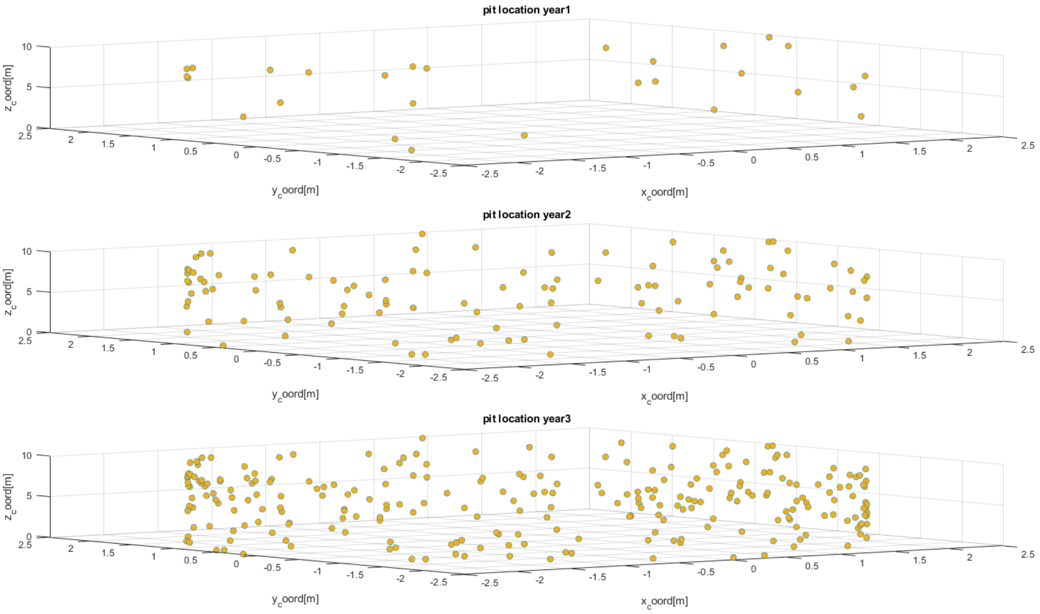

Figure 4-8: Pits distribution from 1 to 3 years

They were all in a cylindrical coordinate and the thickness chosen was 50mm.

At the start, the pit dimension was set to vary from 0 to 1mm and then distributed accordingly with the statistical distribution obtained from Section 5.10.3. It has to be mentioned that the results in that section tend to be for 3 months exposure to pitting but at this stage no other data was obtained for such profiling of the aspect ratio and also the depth. The pits were taken to be 2 dimensional rather than 3 dimensional as the solutions would be complex and require a finite elements model to address that which defeats the purpose of a SHM-data-driven approach model. The most conservative of the aspect ratios was used meaning the sharper one was considered between the x-z and y-z aspect ratio of the pit.

Concerning the approach of Kondo and applying it from a SHM perspective could give challenging results[163]. The SIF did not exist for a pit. It is a myth and Kondo applied it and assumed that the pit was a crack and, therefore, SIF can be applied. A stress concentration factor exists for a pit but not the SIF.

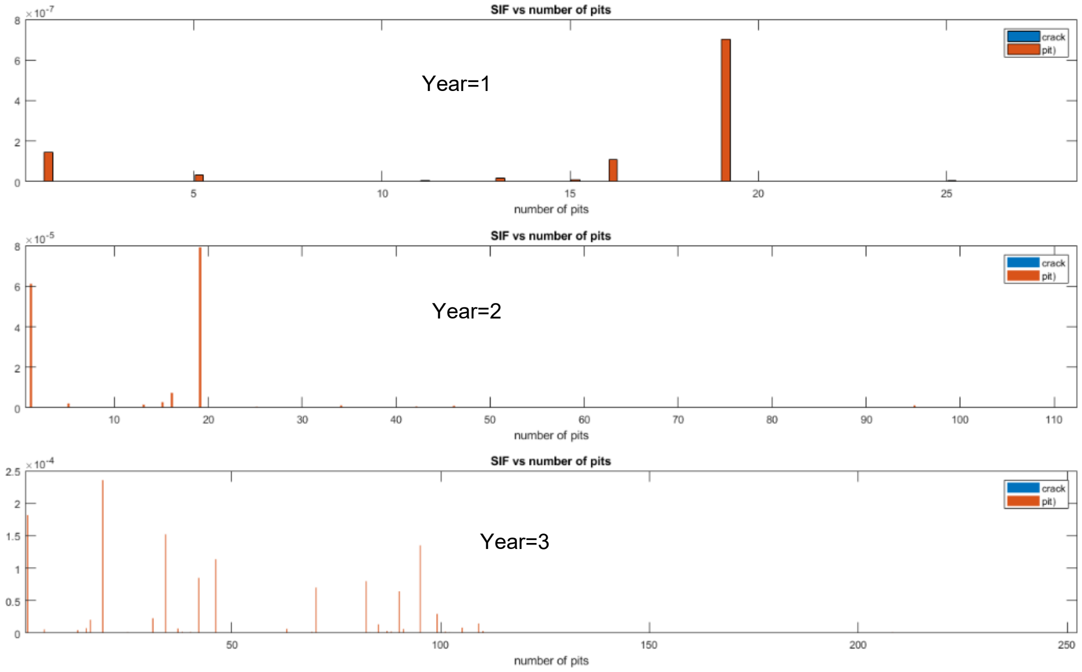

Figure 4-9: da/dN of crack vs pits for year 1 to 3.

For the three years simulated, the pits were the dominating mechanism but the rate decreased over the years, which implied that there might be a change to the crack over the years provided that the equivalent stress was maintained. The figure 4-16 represents the competition of pit vs crack in terms of their growth rate and it is clear that the pit is always the winner for the 3 years with the new pits added.

The new depth was calculated to ensure the growth of the pits.

The damage was then found and none of them after three years proved to be considered problematic.

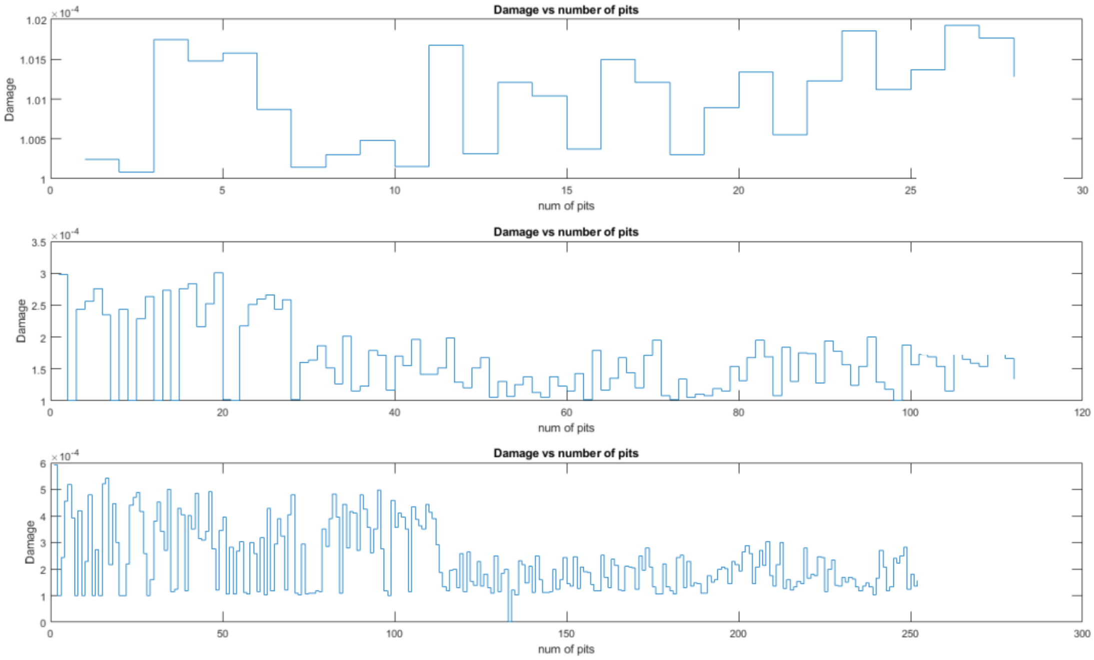

Figure 4-10: Damage as a result of the pits

4.4 Summary

- Identified and compiled a suite of models that allow a data-driven SHM approach to be applied for the monitoring and assessment of cracks initiated from pits.
- This is the first time that this type of approach was undertaken with data based SHM being married to pitting corrosion and even extended to capture the crack effects in case the pit to crack transformation happens.

5 Field Experiment and Deployment for Pitting Corrosion in the North Sea

5.1 Introduction

The field experiment stems from the development of the algorithm in Chapter 4. The incorporation of pitting corrosion to a data-driven structural health monitoring system changes this approach but the pitting model needs to be carefully adopted to reduce the uncertainties in the model. The problem at hand can be summarised as follows. Corrosion at the initial stage is highly dependent on the levels of oxygen. In other words, the more oxygen is present, the more corrosion attack is prevalent. If the profile of oxygen is considered with regards to depth in the ocean, it can be observed that the oxygen level decreases accordingly. In short, the probability of having a pit initiation with reduced oxygen, for instance at the mudline, is lower than having the probability of having a pit in the tidal zones where the oxygen concentration is more abundant. Even in terms of development or propagation of the pit, the richer oxygen content of the tidal regions or splash zone will ensure a higher growth rate of the pit in those regions. The size of the pits is expected to be larger at the higher concentration of oxygen regions and also more populous than the lower concentrations.

This idea needs to be also viewed in pit to crack transition terms. There is a major influence of the pit size and aspect ratio with respect to the stress concentration factors. A deep pit with a small aspect ratio is more likely to turn into a crack at the same stress than a shallower one. There is another major factor in this and it has to do with the bending stress. Consider a pit in a wind turbine foundation closer to the mud line and one that is in the tidal region. In that case, the pit at the mudline is shallower than the one in the tidal region but the global stress is much higher. So now the pit to crack transition becomes quite challenging to determine.

To have a better understanding of this pit distribution, the decision was taken for a field experiment to be undertaken.

This chapter looks at the reason for deployment and how, where and why it was deployed at the location selected. The mass analysis and a brief explanation of the topology pre- and post immersion and the characterisation of the pits are also carried out.

5.2 Motivation

It has to be stated that various field experiments have been done to characterise the pit growth rate but, unfortunately, not the distribution of aspect ratio and pit depth with respect to sea depth. The literature tends to have a bias for the deeper pits and considers the failure as the thickness loss rather than regarding it as a crack transition, which is more relevant in structures. The first solution to this problem was to create a sea environment in the laboratory with real sea water but there was a major downside and it was related to the effects of oxygen on corrosion. Simulating the various regions will be challenging as the pressure will have to be changed to capture the effects of dissolved oxygen, i.e. the higher the pressure, the lower is the DO levels. To counter, this problem a field experiment was thought through that involved accompanying Mr Paul Causon who, in scope of his research, is looking at marine growth effects on structures. The idea is to have the coupons/plates mounted to Mr Causon's experimental set up with minimal risk of influencing any of the two experiments during the connection and data collection phase. Further explanation will be given at a later stage regarding the technical aspects of the experiment.

5.3 Field Experiment

This section will go into the detail of how the experiment has been designed, set up and deployed.

It has to be mentioned that the main design of the array has been done by Paul Causon and this is a summary of his work.

The whole experiment will consist of five arrays, each containing four frames. Each of those frames will hold one plate. The whole set up will be moored to the seabed by anchors and held under tension by the buoyancy offered by a submerged buoy. The idea of using a submerged buoy rather than a floating one boils down to the impracticality and viciousness of the North Sea. In case of adverse weather conditions, the North Sea transforms to an unforgiving monster. The wave heights (from crests to troughs) can attain up to 10m+.The force generated by those waves is immense and will carry or displace large objects lying on the sea surface without any difficulty. The submerged buoy will be situated under the minimum tidal height so it is not influenced by those effects. Operating the experiment under the tidal zones tends to provide a shield from this effect. It should be said, as a result of this, a region had to be compromised, which is the splash zone.

Between the topmost frame (closest to the sea surface) and the submerged buoy and the bottommost frame and the anchor, there is an interesting device known as a spacer. For each array there is a pair of spacers. The reason for the introduction of that extra device is to prevent the ropes from twisting.

The frames are made of two materials; one of plastic and the other of Steel S355, which marine structures are usually from. The attachment of the plates to the frames, depending on the materials of the latter, is quite different. For the metal frames, at each corner, a triangular bracket with a through hole of 10mm diameter was drilled. This allowed the marine cable ties having a breaking strength of more than 150kg to connect the plates to the frame. The plastic frame is connected simply to the plates directly by cable ties.

An overarching look at each array will consist of (from seabed to sea surface) the following components:

Table 5-1: Components for field experiment set up

Component	**Function**	**Quantity per array**
Anchors	To keep the array in place and prevent it from drifting away	2, each of 125 kg.
Spacer 1 (bottom)	To prevent ropes from twisting	1
Frame 1 with plate 1	For data collection and connecting the plates for corrosion	1
Frame 2 with plate 2	For data collection and connecting the plates for corrosion	1
Frame 3 with plate 3	For data collection and connecting the plates for corrosion	1
Frame 4 with plate 4	For data collection and connecting the plates for corrosion	1
Spacer 2 (top)	To prevent ropes from twisting	1
Submerged Buoy	To provide the buoyancy necessary to keep the array taut in the water	1
Marker Buoy	To indicate ships/boats of a deployment	1
DO sensor (only one array)	Monitoring environment across depths. Sensors include temperature and dissolved oxygen	3

The connectors used are as shown:

Table 5-2: Connectors for field experiment

Connectors	**Function**	**Quantity per array**
Ropes	High strength nylon ropes of breaking strength of 2 tonnes to connect the whole array together	4
D-Clamps	**Smaller ones:** To connect the metal frames to the ropes **Larger ones:** to connect bottom section of rope to the anchors	Smaller ones: 32X Larger ones: 1X
Connecting ring	Connect top section of ropes to the submerged buoy	1X
Cable ties	Connect plates to frames	32

5.3.1 Coupons/Plates

In the offshore environment though, specific coupons are employed. They are generally made of the same material as the structure or component to be investigated and the largest dimensions are usually employed to have better representation of the corrosion environment. The following diagram shows the effects of choosing a smaller dimension coupon. It is advised to use the largest one possible to capture the corrosion effects in a more accurate form. Generally, it is the tidal region that suffers the most from this effect[177].

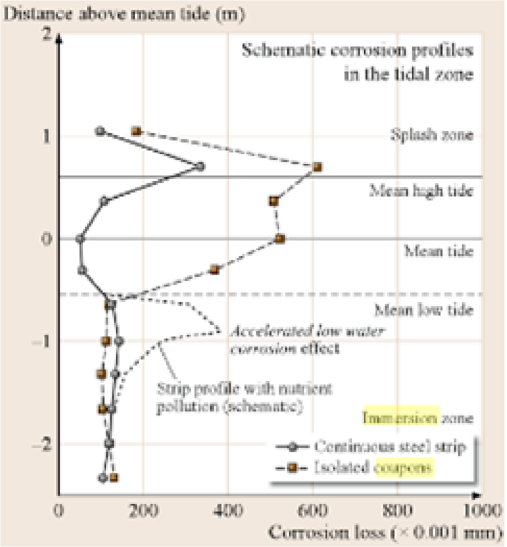

Figure 5-1: Coupon vs plates [177]

One of the logical steps to take in this experiment is to use the same material from which offshore wind turbines are manufactured. Therefore, Steel S355 will be used. Some experiments have been carried out in the past using coupons. The one most relevant in the literature was carried out in the North Sea for offshore wind turbines. The coupons used had dimensions of 400X90X6 mm^3[178]. The same dimensions are going to be used in this experiment. It has to be mentioned that there are no commercially available coupons of that size and they have to be tailor made requiring some engineering drawings. Four holes will have to be drilled into the coupon during manufacturing for attachment to the frame. It will have to be kept to a minimal size as this region will have to be excluded in the study.

The exposure time for the experiment for pit formation should cover a 3 month period.

From the ASTM Standard, the number of replicates advised for the field experiment ranges from 5 to 10 samples[179]. Due to financial constraints, it was agreed to have five replicates at each height making a total of 20 plates being deployed.

The engineering drawing is shown below:

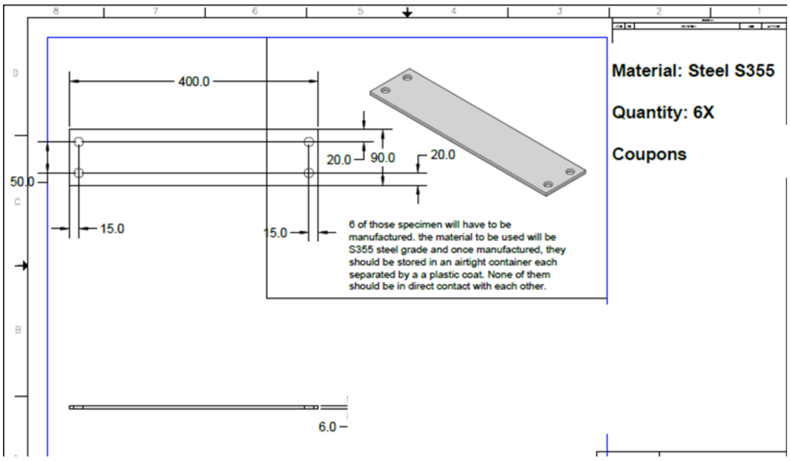

Material: Steel S355

Quantity: 6X

Coupons

6 of those specimen will have to be manufactured. the material to be used will be S355 steel grade and once manufactured, they should be stored in an airtight container each separated by a a plastic coat. None of them should be in direct contact with each other.

Figure 5-2: Drawings of coupons

5.3.2 Dissolved Oxygen Sensors

The dissolved oxygen sensors have been chosen to survive in a rugged environment. The duration of the field experiment has been targeted to be ongoing for three months. This means that the data logging should operate for a minimum of three months.

The logger chosen is the Hobo U26-001. It also has a temperature sensor incorporated within the casing. This type of sensor requires calibration of the dissolved oxygen before usage and the dissolved oxygen tip has a shelf life of 6months.

Figure 5-3: Hobo sensor - DO sensor

Calibration is done with pure water and the gain is adjusted on the Hobo interface software until the value of the saturated oxygen is constant. Once this has been adjusted, the tip has a shelf life of six months. It is advisable to do this procedure a day before the experiment to maximise on the data logging. The data was logged at a sampling rate of one per hour. Corrosion tends to be a rather slow process and 1 hour sampling gives ample data for an environmental understanding.

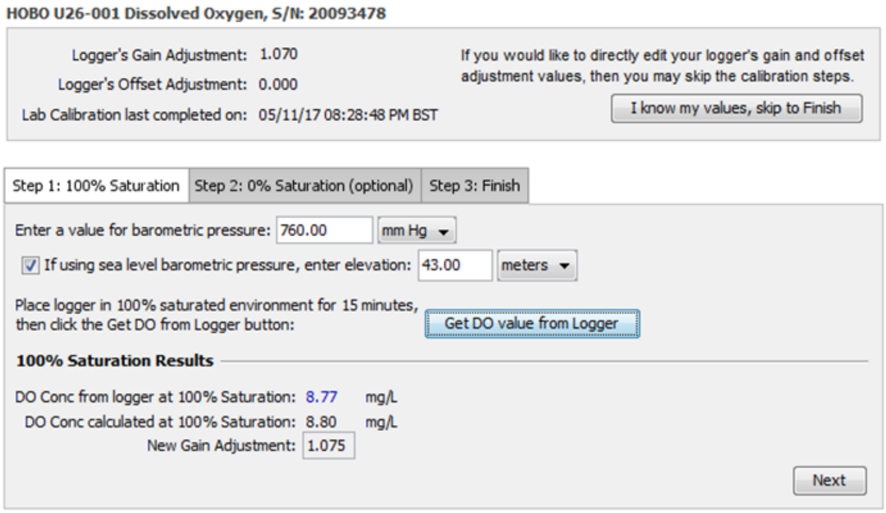

HOBO U26-001 Dissolved Oxygen, S/N: 20093478

Logger's Gain Adjustment: 1.070
Logger's Offset Adjustment: 0.000
Lab Calibration last completed on: 05/11/17 08:28:48 PM BST

If you would like to directly edit your logger's gain and offset adjustment values, then you may skip the calibration steps.

Enter a value for barometric pressure: 760.00 mm Hg

☑ If using sea level barometric pressure, enter elevation: 43.00 meters

Place logger in 100% saturated environment for 15 minutes, then click the Get DO from Logger button:

100% Saturation Results

DO Conc from logger at 100% Saturation: 8.77 mg/L
DO Conc calculated at 100% Saturation: 8.80 mg/L
New Gain Adjustment: 1.075

Figure 5-4: Calibration of sensor

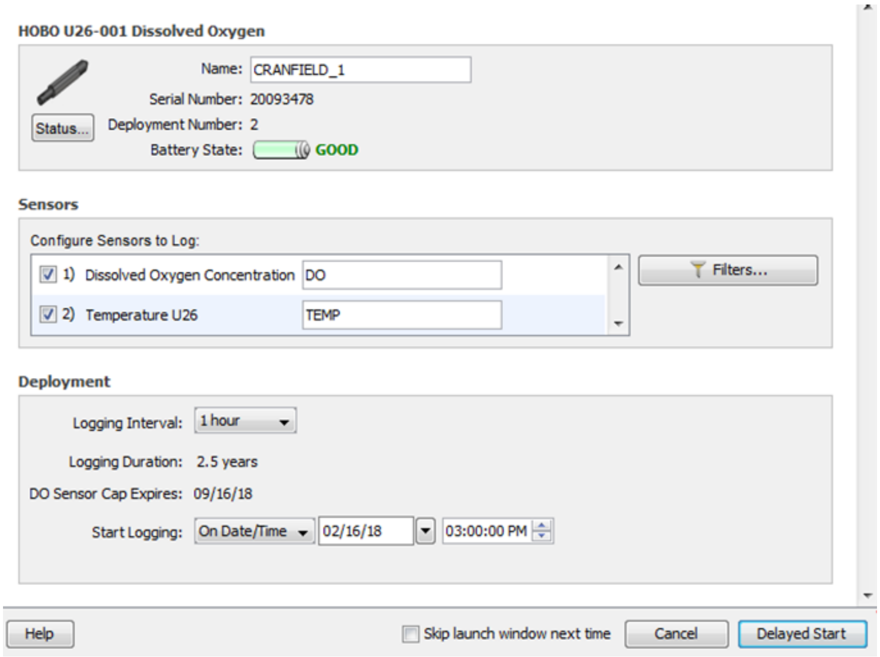

HOBO U26-001 Dissolved Oxygen

Name: CRANFIELD_1
Serial Number: 20093478
Deployment Number: 2
Battery State: GOOD

Sensors

Configure Sensors to Log:
☑ 1) Dissolved Oxygen Concentration DO
☑ 2) Temperature U26 TEMP

Deployment

Logging Interval: 1 hour
Logging Duration: 2.5 years
DO Sensor Cap Expires: 09/16/18
Start Logging: On Date/Time 02/16/18 03:00:00 PM

☐ Skip launch window next time

Figure 5-5: Set up for sensor

Three of the sensors are placed on one of the arrays to characterise the oxygen concentration and temperature profile. The depth of the sea bed from the mean water tide height is 20 metres. The location of the sensors with respect to the sea bed is approximately at 1, 4, 10 and 16 metres from the seabed respectively. They are attached using marine circlips and provide extra security by attaching high strength Dynema ropes and cables to the attachment hole in the sensor to the main rope.

There were cost cutting measures that were applied on the connecting ropes. The Dynema tend to be very expensive and they were replaced for the full deployment by high strength Nylon ropes.

5.3.3 Deployment Location

The location of the deployment was in the vicinity of the Westermost Rough Wind farm, as shown on the diagram. Due to restrictions imposed, the deployment must be at its closest point 1 mile from the boundaries of the wind farm.

Figure 5-6: Deployment location

The close proximity of the wind farm to the deployment site will provide a great opportunity to explore the effects of corrosion and marine growth in wind farms in such environments.

This region of the sea tends to be very rich in marine life, such as lobsters and crabs which are rich in nitrates. Due to their high population, there is a lobster farm and setting of lobster pots is a common practice by local fisherman. This nitrate content will have a serious effect on the pit growth rate especially in the seabed area where the excrement from the lobster is found.

5.3.4 Pre-Processing and set up of Plates

The plates were firstly cleaned using the following procedures set in the ASTM G1 Standard[177].

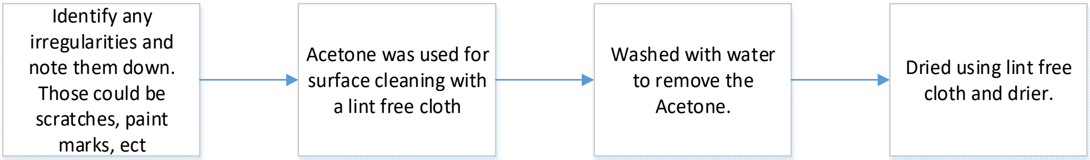

Figure 5-7: Steps for cleaning

They were deployed as such using the seabed as the reference:

Table 5-3: Deployment heights

Plates number	Height[m] (distance from sea bed)
4	1 (deepest deployment)
3	5.5
2	10.5
1	16

The sea depth is 30m with the tidal depth being at 20m.

The marine tape in the corners is used as references in case 3D point subtraction is employed for 3D scanning. There is a problem that can arise with this; the water can flow beneath the layer of the tapes and introduce a limited amount of oxygen resulting in differential oxygen concentration causing crevice corrosion. So each of the spots where the tapes were applied were also glued on with extra strong marine glue usually used to patch holes in hulls of boats.

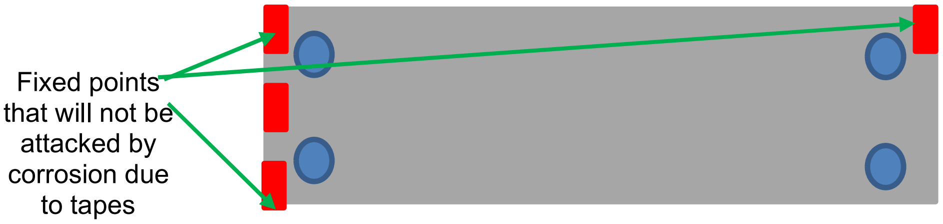

Figure 5-8: schematic of coupon and labelling

The plates were colour coded based on the array where they were to be deployed; the colours were grey, black, blue and green. For the trial, the plates were colour coded with red. Strips of marine tape were cut out and placed at the top of the front section, as shown in figure 5-8.. The corners of each plate were protected with a layer of marine tape, which is meant to be the reference in gauging the level of corrosion when using the optical methods.

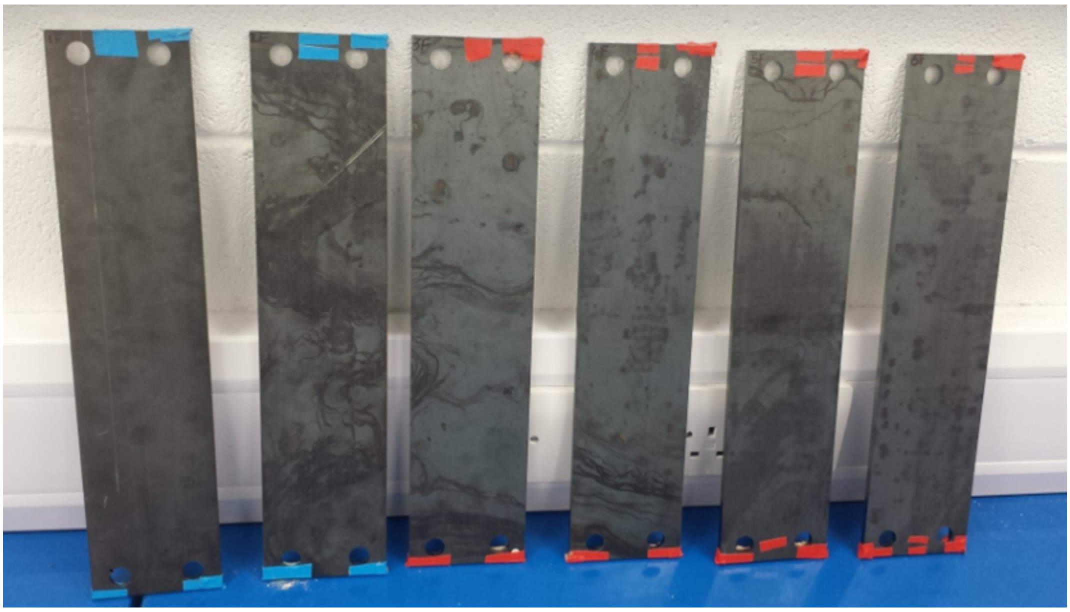

Figure 5-9: Some of the plate samples

To differentiate between the plates at the top section and bottom section, the corners at the top were fully covered whereas the ones at the bottom had only one of them covered with the left one exposed and right one covered with marine tape. Each colour of the corner stickers were the same colour of the deployed arrays to give added visibility. It should be mentioned that when retrieving the plates, it is very likely that the plates will be covered with marine growths. For retrieving them, sealed bags will be used that have been numbered, for instance 1 blue meaning that this is the topmost plate in the blue array.

For further identification, small marine plates going from 1 to 20 have been attached to the frames.

The dissolved oxygen sensors were placed on the black deployed array. The one closest to the sea surface was marked with one stripe, the one in the middle with two and the one closest to the seabed with three.

There was a codename attached to each of them. For instance 1bb would read as plate placed at height 1(16m), blue coded and the second b is back. Red would be 1rb, green, 1gb, black 1kb and grey 1grb.

The front section for blue would be 1bf, for instance.

5.3.5 Mass Measurement

The initial mass of each of the samples were weighed in after being dried up. This was repeated three times and averaged.

The first instance was to measure the mass with and without the tapes and there was no difference at all as the sensitivity of the scale was not high enough to depict

The scale had a reading resolution of 0.1g. The Standard does mention a higher resolution scale but since the plates were way larger than the ones mentioned, the upper limit of the prescribed scales would have been exceeded.

Despite this limitation in that method, the readings were archived. Each plate had a minimum of three readings taken depending on the variations. The larger the variations, the more readings were taken and then a plot was created to see if there was a convergence on the new recorded readings. No variations were present in the results.

At each measurement, the scale was set to zero and then the plate added on. The plates mass are tabulated, as shown below:

Table 5-4: Mass measurements

Mass[g]					
Plate number	**Black**	**Green**	**Blue**	**Grey**	**Red**
1	1668.8	1655.3	1629.9	1659.3	1663.2
2	1661.4	1650.7	1647	1658	1652.8
3	1666.9	1654.8	1661	1669.4	1665.4
4	1657.4	1640.2	1667.1	1667	1668

5.3.6 Trial or Proof of Concept Deployment

One of the arrays was meant to be tested as a proof of concept in the North Sea in the whereabouts of the Westermost Rough wind farm on the 20 September 2017. The assembly was done at sea and took a lengthy time to achieve the required standards for the deployment.

Figure 5-10: Set up for deployment

This specific assembly was coded the red assembly.

The codename number red-one plate was at the top or closest to the floating buoy and the one codename number red-four plate was at the bottom of the anchors. This array was not the instrumented one for obvious reasons.

The following procedures were used for the assembly section:

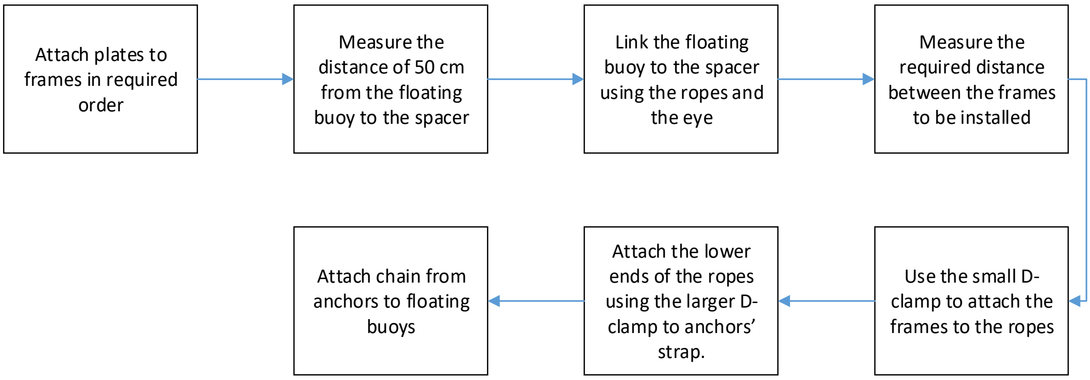

Figure 5-11: Set up for field experiment

The deployment required a crane to lift the anchors and drop it in the sea. Through the force of gravity the rest is pulled down. The coordinates of the deployment are noted for easy retrieval.

5.3.7 Full Deployment

Some amendments to the trial deployment had to be met to ensure that less time would be spent on the boat. This was achieved by connecting most of the assembly offshore. The plastic frames were connected to the rope assembly and wrapped for transport to prevent any misplacing or tangling of the ropes.

The deployment of each assembly was a success taking approximately 30 minutes each.

The dissolved oxygen sensor was placed on the third array – the green one.

5.3.8 Experiment challenges

Due to the nature of the experiment, there were numerous challenges that had to be overcome.

First and foremost it was the timing of the deployment. It was crucial that we did not miss the weather window (from March to October) or the experiment will have the potential to be delayed by a few months. So the design and procuring periods were carried out from November to March. Unfortunately, due to unforeseen circumstances, the location of the deployment had been changed. In that respective location, a concrete block was fixed to the sea bed. The setup of the experiment was simple and required the experimental array to be tied to the concrete block. This set up would have ensured the profiling of every aspect of the sea depth from the seabed, tidal zones and finally the splash zone. It was simple and more importantly cheap and this allowed seasonal checks and retrieval. The setup of the array was simple and required marine ropes and cables to be attached to the concrete block and the coupons would be tied directly to the ropes.

As a result of the change of location, the designs had to change as there were no concrete blocks. So the design had to be reviewed and it was decided that the old design was inadequate. The whole set up would now be held by tension provided by a submerged buoy.

The first deployment happened in October 2017 and the set up was done on the boat. The setup lasted more than 6 hours. Despite it going well, it was clear that modifications in the deployment had to be done in the set up so that minimal time is spent at sea for the full deployment. To achieve this, the set up was done on land. They were packed tight and transported for the full deployment in February 2018.

On this deployment, the boat engine unfortunately failed and as a result the deployment was unsuccessful.

On March 2018, a replacement boat was chartered and the deployment went on fully without any glitch. The deployment time got reduced to 30 minutes preparation which was basically untying the whole array.

5.4 Post-Processing of Plates

The winter of 2017-2018 was a very peculiar one with two very strong storms. This meant that the assemblies were expected to sustain some damage. Actually, three assemblies were lost and the other two were recovered by the Ports authorities as they had snapped from their anchors. Experiments do have their challenges but marine field experiments, especially in the open sea, are really tough where every aspect needs to be thought throughout to the smallest details.

The two recovered arrays were collected on 20 July 2018 and were found to be in a bad state. In those two arrays, the 2 and 4 Black and the 4 Blue was lost.

The plates were cut from the respective cubes and placed in sealed bags.

The next step was to measure and photograph the plates. On first inspection, the rust layers formed were thick and from this point onwards it was clear that marine corrosion on bare steel of S355 grade is vicious.

With care, the plate was removed and the mass measured. This was referred to as the mass of unclean plates.

The chemical cleaning of the plates this time involved some rather hazardous chemicals. According to the ASTM G1 Standard[177], to carry this out, 1000mL Hydrochloric acid, 20 g of Antimony Trioxide and 50g of sodium hydroxide were mixed for a period of 25 minutes until the rust had been dissolved. The solution should be gently brushed so that the acid effectively attacks the rust and dissolves it. The whole point of the Antimony Trioxide is to act like an inhibitor to the bare metal when it is exposed to the acid, thus protecting it from further reaction.

The Plates are then washed under water and dried out using a drier. Finally, the plate was cleaned again with acetone to dissolve all forms of organic materials. The plates were then locked in a hygroscopic environment to prevent any further reactions.

5.5 Visual Assessment

The visual assessment was to determine the types of corrosion encountered using the human eye and under a laboratory magnifying glass.

Different forms of corrosion were identified.

In some cases, there were no localised corrosion observed with the naked eye but under the laboratory magnifying glass, clear micro-pits were observed. The study though is not related to the initiation stages of the pits and, therefore, the micro pits were neglected and efforts concentrated on the macro pits.

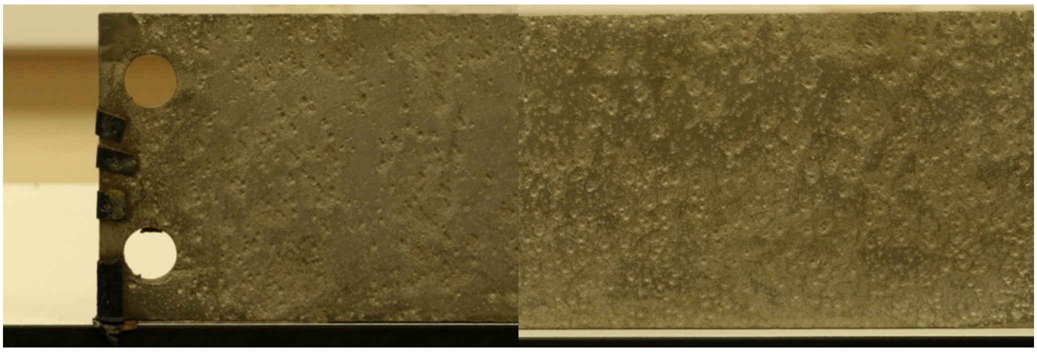

Figure 5-12: Plates and pitting variations

The pitted region of the 3 black plates was dense. It has to be mentioned that the pits were shallow with the exception of a few that tended to be larger.. Pit coalescence was also observed.

This is the case where two or more pits join together to form a new pit profile, which is wider than each individual pit. This means that in structural terms, the SCF is reduced significantly when that process happens.

Figure 5-13: Pit coalescence represented by the red circles(each showing a pit) that are now joined to form a new pit.

It can be seen from the above image that there are three pits joined together. There are a few similar cases to this one on the other plates.

There is another case which involves a pit inside pits. This is a case that can be detrimental to the structure as it tends to increase the SCF significantly.

The marine tape was used for colour coding and there was always a risk in this case of introducing crevice corrosion.

This happened only once out of all the plates. For the difference between pitting corrosion and crevice corrosion refer to chapter 2.

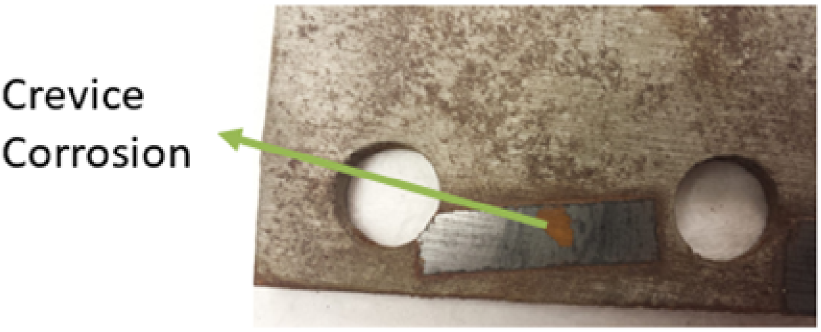

Figure 5-14: Crevice Corrosion

The visual inspection is good way to assess the various forms of corrosion but a more detailed interpretation is required to quantify the corrosion.

5.6 Mass Loss and Corrosion Rate

The mass loss and the corrosion rate are important parameters to design against corrosion. The mass loss can change the natural frequency and the corrosion rate can be used to predict that mass loss in a model.

The mass loss is derived from the following equation:

$$mass\ loss = original\ mass - final\ mass\ after\ acid\ cleaning$$

The units measured are in grams.

Corrosion loss is derived from the mass loss and related to the density.

$$\boldsymbol{Density = \frac{Mass}{Volume}} \qquad \textbf{Equation 5-1}$$

The volume of a cuboid (the volume is the approach taken to calculate the thickness loss):

$$\boldsymbol{Volume = Area\ X\ thickness\ loss} \qquad \textbf{Equation 5-2}$$

The thickness loss can be calculated as:

$$\boldsymbol{thickness\ loss} = \frac{\boldsymbol{Mass\ loss}}{\boldsymbol{Area\ X\ Density}}\ \textbf{[mm]} \qquad \textbf{Equation 5-3}$$

The corrosion rate or corrosion loss is the ratio of thickness loss to coupon exposure time in years.

$$corrosion\ loss\left[\frac{mm}{yr}\right] = \frac{thickness\ loss}{Number\ of\ exposure\ days}\ X\ 365.25$$

Equation 5-4

The DNV J101 Standard mentions a corrosion rate of 0.2 mm/yr in the splash zone. The results provided proved much higher than mentioned by the Standards. This can have some really bad consequences for the structures.

The mass loss was calculated in two ways:

1. Chemically uncleaned
2. Chemically cleaned

The scale used was the same as that used in the pre-processing section.

Figure 5-15: Cleaned plate mass measurement

The figure below shows the difference between clean and uncleaned plates:

Figure 5-16: Difference between clean and dirty plates

The graphs below show the results in terms of corrosion loss and mass loss.

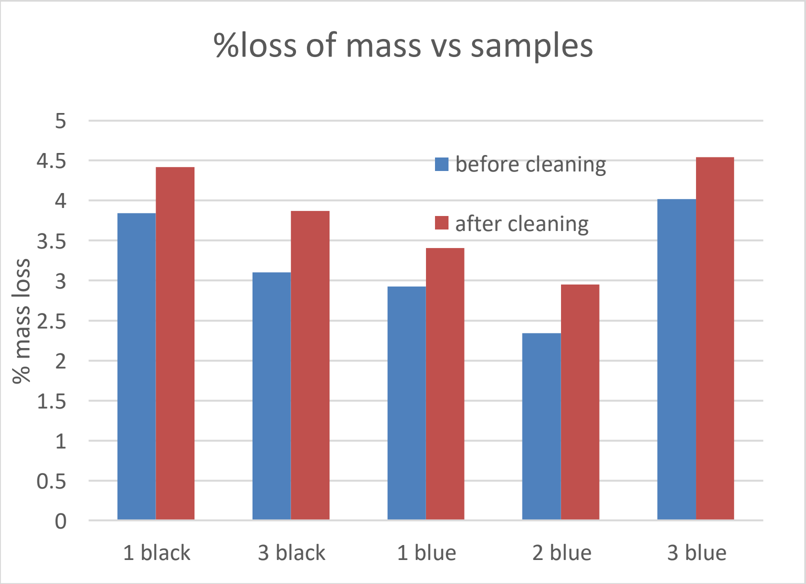

Figure 5-17: Mass loss

The mass loss in 1 black is way more than 1 blue by quite a margin.

However, it can be said as a trend that for corrosion observed from the black plates decreases from the high oxygen corrosion region to the lower oxygen level of corrosion. The story is totally different where there is an increase in corrosion loss with respect to depth. The reason for this difference is unknown and might be related to the location of deployment.

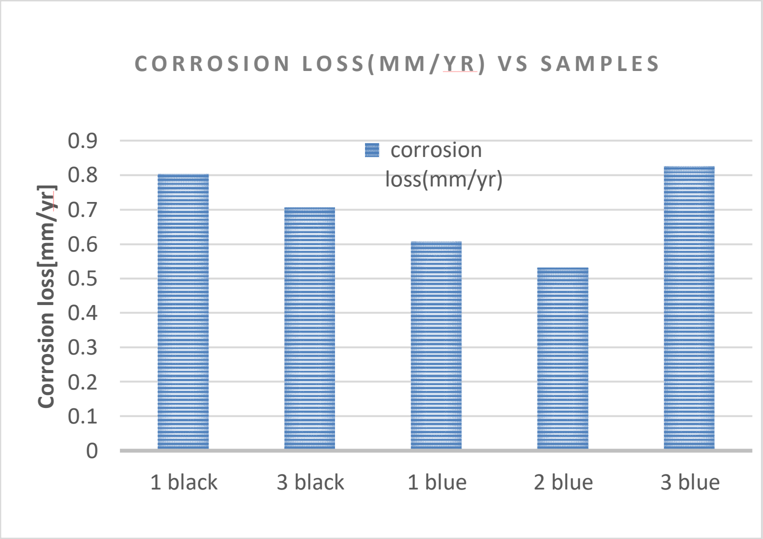

Figure 5-18: Corrosion rate

The same phenomenon is reflected obviously in the corrosion loss/yr. The density is obtained from the ASTM G1 standard.

Here though, those values tend to be way more than anticipated. The 3 blue at nearly 0.81 mm/yr is nearly 4 times more than what the Standard anticipates where generally the opinion on marine corrosion stipulates that this should be lower than 1 blue. Serious questions about those numbers provided by the Standards will have to be asked. The first one would be when and where were those values deduced? Which depth or relative depth? How long has the exposure been? Corrosion is a non-linear process. What were the impacts of the SRB on those values? Which grade of steel was it subjected to? Which environment and when as due to global warming, there has been an increase in temperature? Image Processing and Pit Depth

The goal of this study is to extract features fundamental in the assessment of a pit, which are described below from the coupons of a field experiment in the North Sea for a period of three months. After an acid bath, the pits revealed themselves and were clear to be visually assessed. A first stage was done by shading the surface of the coupon using a pencil on paper, which was then scanned and provided some great results for pit detection. The image was then scanned using a high definition scanner and converted to a JPEG format before being processed in the code developed in the Matlab environment.

In the literature, there is a major absence of study on pitting corrosion with respect to depth of the sea but it can be viewed in different perspectives based on the characteristics of a pit, defined as:

1. The pit major length.
2. The pit minor length
3. The orientation
4. The area
5. The number of pits
6. The centroid

One aspect that cannot be extracted in 2D is the pit depth. A pit gauge will be used to extract that very important information and a statistical fit will be fitted to the data.

Due to its stochastics nature, the most appropriate statistical distribution will be captured from each of those features extracted from each coupon deployed in the field experiment. The field experiment has been described previously and the goal of this chapter is to fill the gap in knowledge for distribution of pits with respect to depth in a marine environment.

The area of the pit can seem quite unnatural to capture at this point. In reality, when measuring the pitting potential, the area of the pit is required and this can be used as a good estimate to get the depth loss and vice versa. Also, the probability of pitting found in the ASTM G4 Standard also employs the area. It is to be noted that the image processing is 2 dimensional, meaning if looking at the plate from a top view, it represents the top view surface area measured in pixels^2.

To make this process more comprehensible, the following steps have been employed and are summarised in the flowchart below:

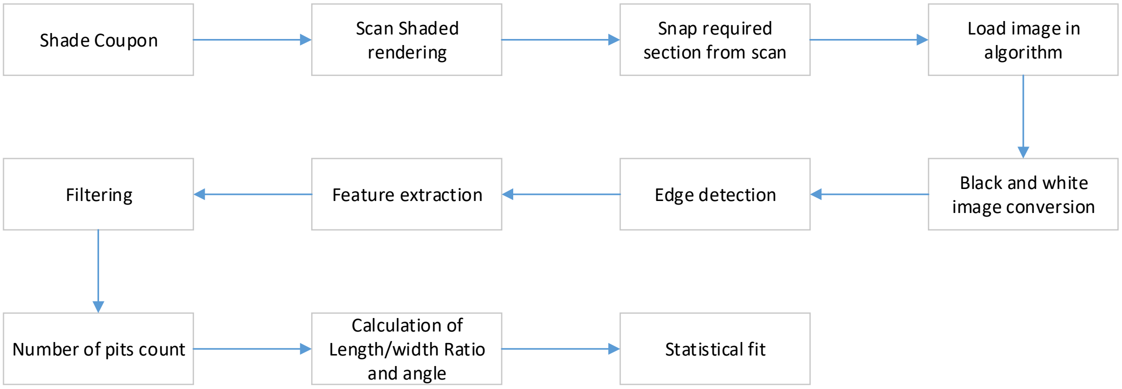

Figure 5-19: Processes for image processing

Once all the images have been duly processed, an average image will be characterised to find the average number of pits and also the associated characteristics for the North Sea environment.

5.6.1 Methodology

The process of this algorithm starts not with taking a picture of the corroded surface of the sample but instead shading it with a pencil. The reason is that it has been observed that the rendering of the pits is clearer using this method compared to a picture of the plate. There is another reason for this process to be used. Very often, there is a slight curvature in the plates or coupons that might be incurred during its deployment for corrosion monitoring. The curvature will introduce some errors in the measurement of even the plate itself if an image is taken as it is representing the projected area of the plate. Shading it helps to remove that effect and the total length of the plate is finally measured as a result and the pits can be characterised in a more realistic manner. The effect of curvature of the plates has been an unexpected one, as discussed in the previous chapter.

Once the shading has been done, the image is digitised using a high resolution scanner. The image is scanned as a black and white format at the highest resolution available by the scanner. There are unwanted white sections of the paper that are edited using the appropriate software, such as Microsoft Paint or even the SnippingTool. This is an important process as this is the picture that will be fed into the algorithm.

The algorithm firstly requires the image to be loaded. The first aspect of the algorithm is to convert the image into a proper black and white image. The actual loaded one is in grayscale. Now a rather challenging process appears. It is the case of thresholding; T where the grey value is measured and compared with respect to T which is user defined. It runs as follows:

When the value of T > than the grey value, the binarising process turns to zero else it is one. Zero represents white, one represents black.

Following this step, the case of feature extraction is required. It first requires the process of edge detection. In this case, the zeros that form a closed process are extracted.

5.6.1.1 Pit Count

The number of pits is simply the number of closed loops there are. There is a count of those closed white regions and those characterise the pit count.

5.6.1.2 Area

The features extracted are firstly the area which is simply the count of pixels inside each of the extracted features multiplied by the area of each pixel. The conversion is now defined by the area scale factor. The mathematical expressions are shown below:

$$\boldsymbol{A} = \sum_{\boldsymbol{n}=\boldsymbol{1}}^{\boldsymbol{n}} \boldsymbol{P}_{\boldsymbol{n}} \qquad \textbf{Equation 5-5}$$

Where A is the area and P is the pixel area and n is the number of pixels.

The area scale factor is dependent on the length and width of the plate or coupon and the conversion from pixel to length is explained on the next page.

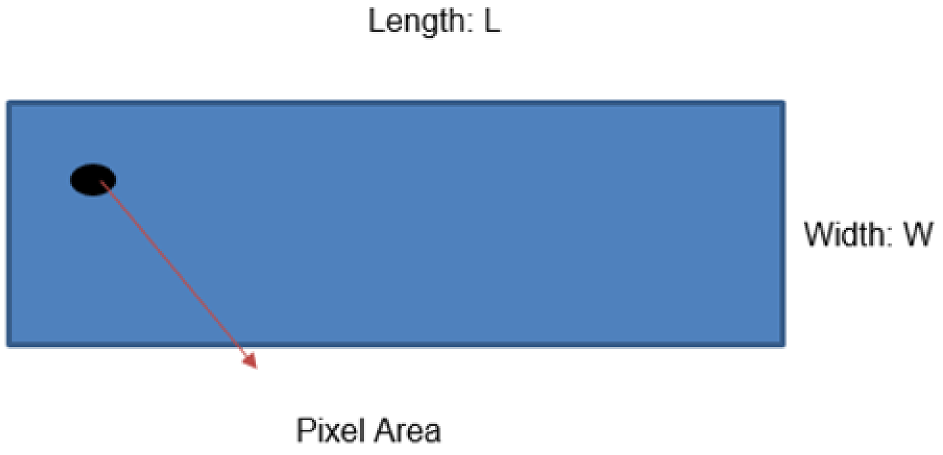

Figure 5-20: Schematic of plate

The geometrical area of the plate is:

$A = Area = Length\ X\ Width$

$\boldsymbol{PA = Pixel\ Area = \ P_l X\ P_w}$ **Equation 5-6**

Where PA, in this case, is the pixel area of the whole plate determined in the properties function of the image.

The area scale factor:

$\boldsymbol{\frac{A}{PA} = \ K}$ **Equation 5-7**

The actual area is calculated as:

$\boldsymbol{Area\ of\ feature = \ K\ X\ pixel\ area\ of\ feature}$ **Equation 5-8**

5.6.1.3 Minor & Major Length and Aspect Ratio

The minor and major length of the zeros clusters are extracted.

For each feature that has been selected, the minor and major length is characterised. The major length is simply the longest distance and the minor length the shortest distance between two points across the pit. The distance measured at this current stage is in pixels.

There requires a conversion and this is slightly more complex than the area.

It requires the x and y coordinates that characterises the length. From there, the difference in the x and y coordinates can be found.

$$\Delta x = Difference\ in\ x\ coordinates = x_{max} - x_{min}$$

$$\boldsymbol{\Delta y = Difference\ in\ y\ coordinates = y_{max} - y_{min}}$$ **Equation 5-9**

The length scale factor, LSF, now needs to be measured in the two axes.

$$\frac{L}{P_x} = LSF\ x$$

$$\boldsymbol{\frac{W}{P_y} = LSF\ y}$$ **Equation 5-10**

The length L_x and L_y are representing the corrected length and are calculated as:

$$L_x = \Delta x\ X\ LSF\ x$$

$$\boldsymbol{W_y = \Delta y\ X\ LSF\ y}$$ **Equation 5-11**

The actual minor and major length in millimetres can be found using the Pythagoras theorem:

$$\boldsymbol{minor\ or\ major\ length = \sqrt{L_x^2 + W_y^2}}$$ **Equation 5-12**

The aspect ratio is far simpler as it is dimensionless and this can be found as:

$$\boldsymbol{Aspect\ Ratio = major\ length/minor\ length}$$ **Equation 5-13**

The angle between the major length and minor length is also found as:

$$\boldsymbol{\tan\theta = \frac{\Delta y}{\Delta x}}$$ **Equation 5-14**

The depth of the pits were measured using a pit gauge.

5.6.1.4 Filtering

The process of filtering is fundamental as it is required to remove all the unnecessary noise in the picture. Rather than going through an elaborate filtering process, the area and major length were used to remove the unwanted points. If a standalone feature with a length of less than 5 pixels and more than 2 pixels are captured as the major length, then this is deleted from the collection of pits. In addition to that, there is a second filter laying, stating if the area is larger than 20 pixel square, then the pits are deleted.

5.6.1.5 Pit Depth

The pit gauge is used to measure the depth of the pit. To extract this information using manual labour is time consuming. Only three of the most pitted plates were used to do so. For each of them only 20% of the pits' depth was measured by Miss Carole Liao in a random manner and an average found and the extreme pit extracted.

5.6.1.6 Statistical Fit

For the area, aspect ratio, angle, major and minor length, the most appropriate statistical fit was chosen from a list of the following statistical distribution from Matlab.

They were evaluated against the Akaike Information Criterion (AIC) to determine which fit is the most representative. As a reminder, the AIC assesses the bias versus the precision of the fit. The more parameters there are, is the higher the penalty.

$$AIC = -2log_e(L) + 2q \qquad \textbf{Equation 5-15}$$

The likelihood L, is calculated as:

$$L = \prod_{i=1}^{n} f(x_i) \qquad \textbf{Equation 5-16}$$

The flowchart below summarises the various steps involved:

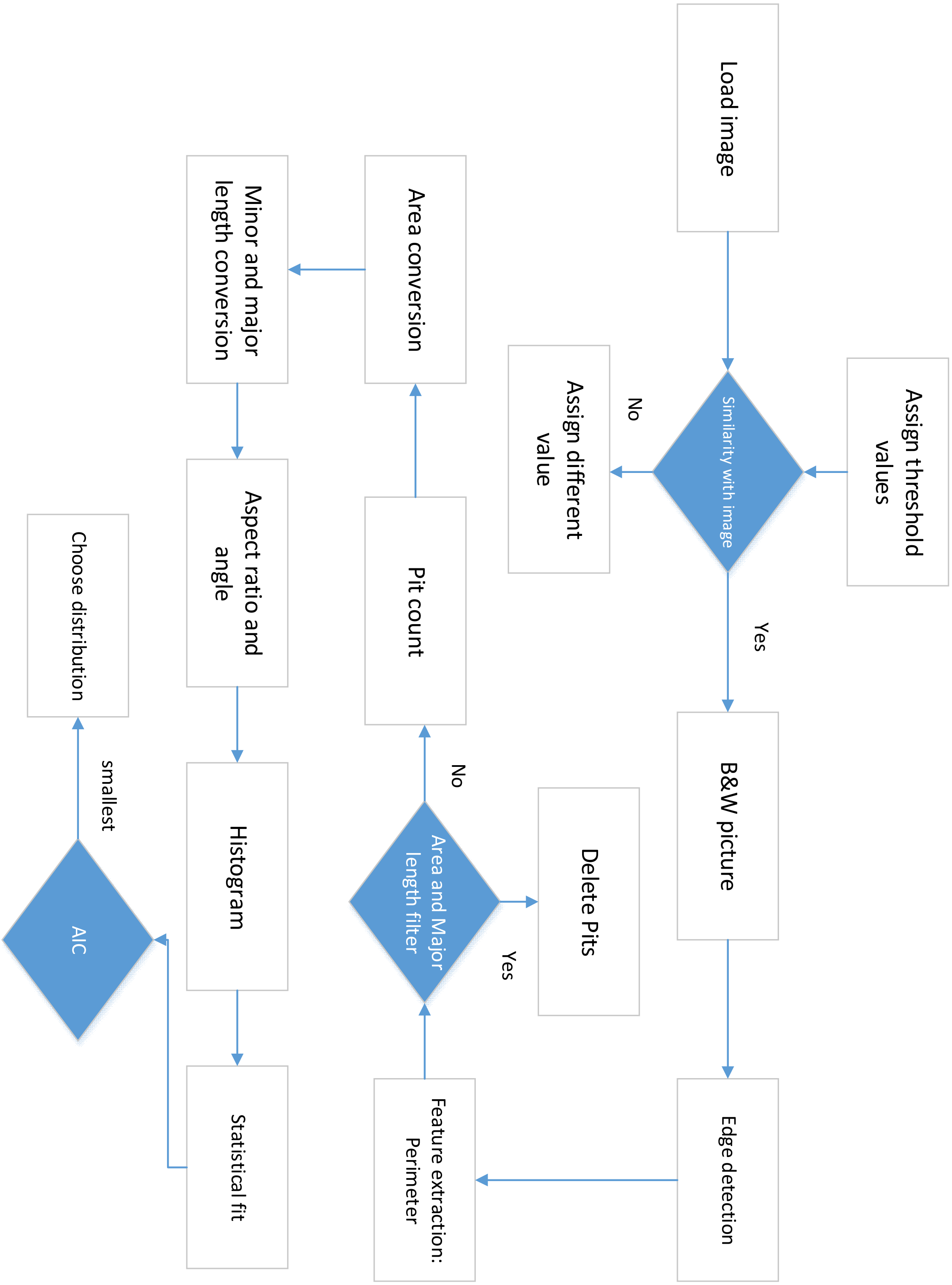

Figure 5-21: Flowchart for image processing

5.6.2 Results and Discussion

5.6.2.1 Pit Detection and Sizing

The coupons were all shaded and the surficial conversion of one coupon is shown in the following diagram. The original on the diagram shows the shaded and scanned one. It is then transformed into a grayscale to remove the colour dimensions of the image. It is inverted for easier viewing of the pits and ultimately binarised through the thresholding process.

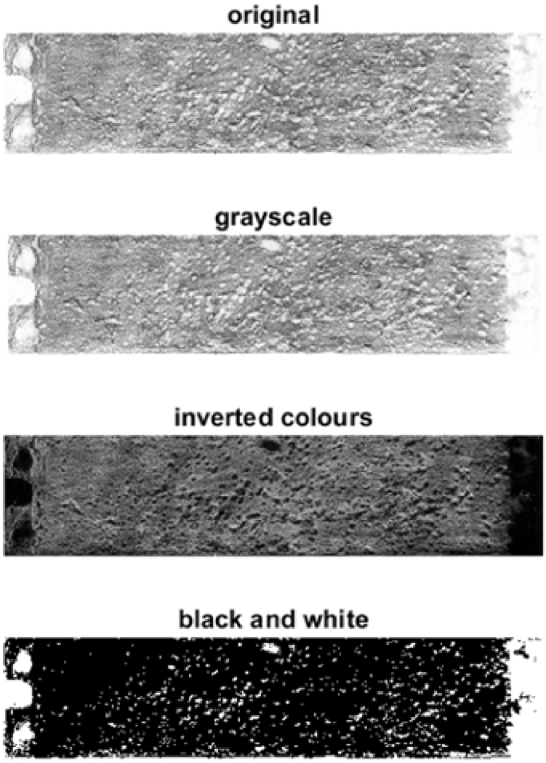

Figure 5-22: Image conversion

In this case, it is crystal clear that there are pits from a basic visual inspection. The image processing algorithm was used to extract information about the pits but before doing so, the image had to be re-characterised as a black and white one. The threshold levels had to be adjusted and compared from a value of 0.75 to 0.95 going through steps of 0.025. Visually it was observed that comparing the plate to the image that the most appropriate threshold value is 0.875. The black and white image is as shown below with the thresholding procedure. It is to be noted that the thresholding is highly dependent on the conditions of the shading and the scanning.

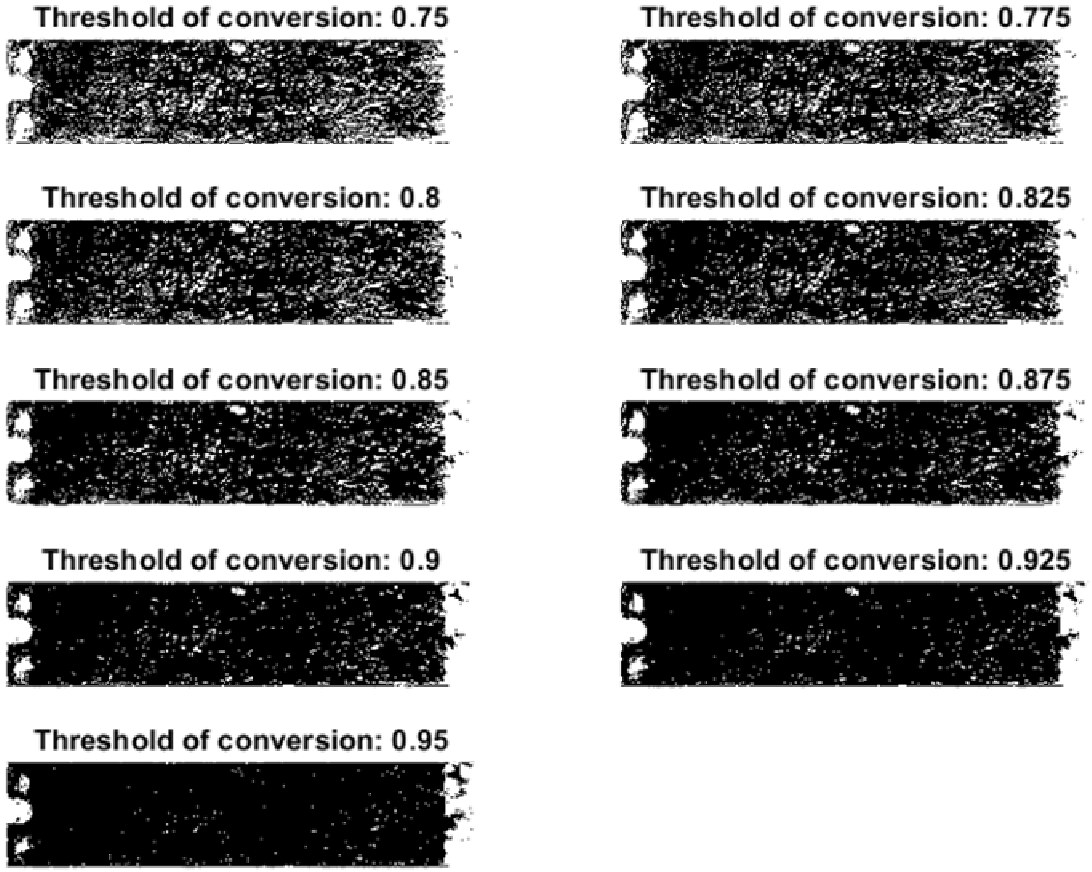
Threshold of conversion: 0.75

Threshold of conversion: 0.775

Threshold of conversion: 0.8

Threshold of conversion: 0.825

Threshold of conversion: 0.85

Threshold of conversion: 0.875

Threshold of conversion: 0.9

Threshold of conversion: 0.925

Threshold of conversion: 0.95

Figure 5-23: Effect of thresholding

The other aspect that had to be done once the white regions had been identified and picked out was to extract the features and count the number of objects. At this stage, despite the thresholding, there was a high level of noise that had to be removed.

The regionprops function in Matlab was used and in so doing, the pixel counts were affected.

The features were extracted and sized up. The smaller pits were up to a size of 0.1mm, which corresponded to the size of 1 pixel. To be able to refine it further, a higher spec scanner can be used, in which case the dimensional representation of the pits can be significantly improved (more pixels to represent 1mm) and, therefore, be used to eliminate the objects. The filtering allowed those singular pixels to be removed and finally the number of pits obtained can be tabulated, as shown below.

After the filtration, the maximum number of pits obtained was 545 and the minimum 67.

The pit intensity has also been calculated as:

$$\boldsymbol{pit\ intensity = \frac{number\ of\ pits}{Area[m^2]}}$$ **Equation 5-17**

Validation of the plate 3 black back for the number of pits was essential.

Three individuals counted the pits and this was used as a benchmark to also calibrate the thresholding value for the binarising process.

The number of pits counted by the three people produced the following format:

Table 5-5: Number of pits counted

	Number of pits counted
Individual 1	498
Individual 2	462
Individual 3	514
Average	**491**

The closest one is 545 from the results obtained, which are tabulated below with different thresholding values.

Table 5-6: Number of pits calibration

Threshold	Number of pits	% Error
0.75	1216	142.55319
0.775	928	85.106383
0.8	884	76.329787
0.825	695	38.630319
0.85	623	24.268617
0.875	545	8.7101064
0.9	407	-18.81649
0.925	203	-59.50798
0.95	75	-85.03989

The positioning of the pits can be plotted with respect to the centroid.

The probability of pitting as a ratio of the area of the projected pits to the area of the plate is as displayed below.

Table 5-7: Display of pit data

Coupon	Probability of pitting[%]	Number of pits	Pit intensity [pit per square metre]	Depth from seabed[m]
1 blue back	0.18	274	3.97E+03	16
1 blue front	0.23	200	5.56E+03	16
1 black back	0.36	311	8.64E+03	16
1black front	0.59	424	1.18E+04	16
2 blue back	0.66	533	1.54E+04	11.5
2 blue front	0.054	63	1.75E+03	11.5
3 blue back	0.54	459	1.28E+04	5.5
3 blue front	0.069	67	1.86E+03	5.5
3 black blue	0.67	545	1.51E+04	5.5
3 black front	0.63	514	1.43E+04	5.5

The variation for the number of pits for each coupon is displayed below:

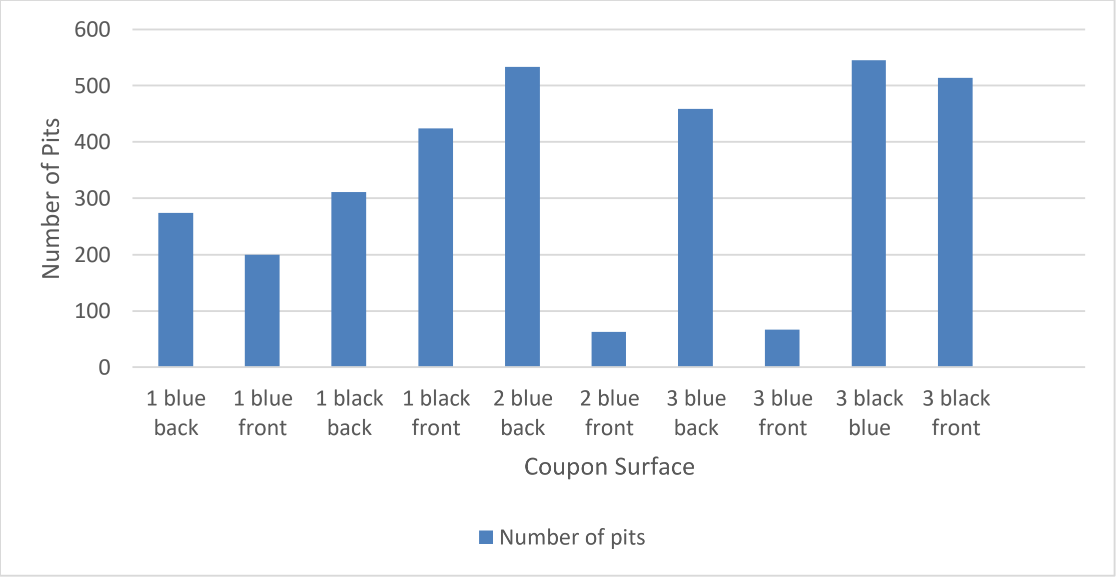

Figure 5-24: Number of pits for each plate

It is very difficult to fully understand the reason behind this variation, first between the same plates but different sides and also between the plates. One hypothesis is that the marine growth has a greater impact closer to the surface, which tends to incubate more pits than the ones exposed with more corrosion. In marine corrosion the biological corrosion is also a major issue and when the corrosion mechanism shifts to anaerobic, the corrosion rate increases. This is a theory but needs to be proved with careful monitoring of various plates. Another explanation might be due to the microstructure of the coupons. Even though the plates are manufactured from the same batch, they might have potential variabilities in the micro structure, which will tend to increase the number of pits. This is a tedious process and will require a microstructural analysis before and after the coupon id deployed.

Two statistical dimensions were looked at, namely the maximum number of pits for each height when compared one another and finally the average.

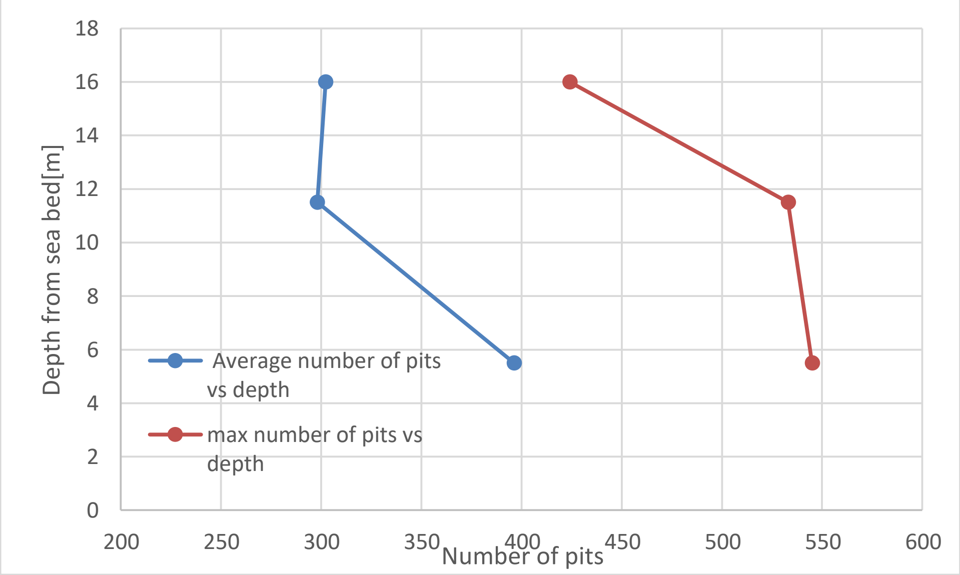

Figure 5-25: Number of pits with respect to depth

In light of this, there is a pattern that can be viewed and that with respect to depth there are more pits. This is usually counter to the gut feeling that with depth there is less oxygen and ultimately corrosion is less. It can be said that with depth, there is more localised corrosion as also shown by the probability of pitting in the above table.

Another perspective is to look at the problem with the number of pits and the probability of pitting to estimate the number of pits on a surface.

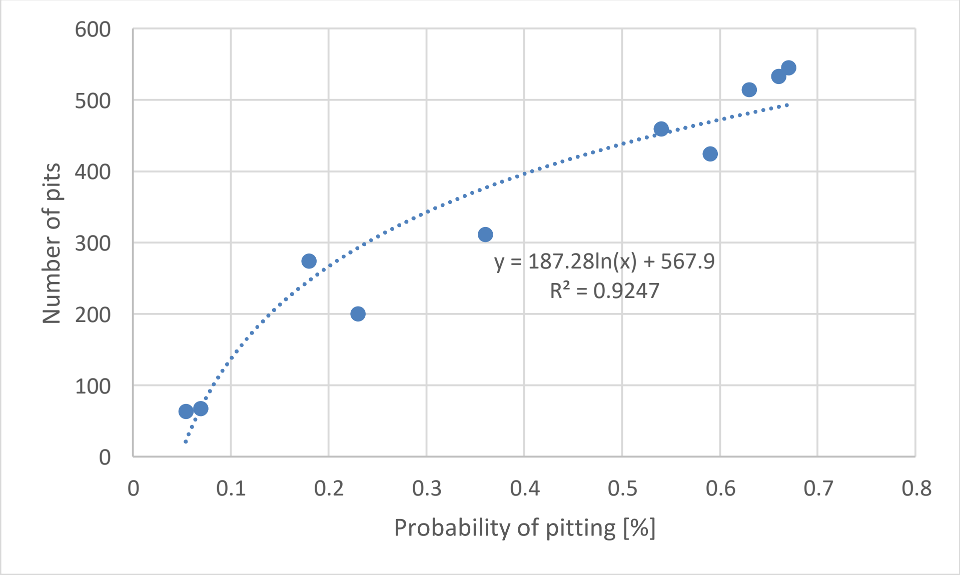

Figure 5-26: Probability of pitting

This case has a bit more of conclusion and a logarithmic fit giving a total of 1430 pits that can be formed on this plate based on this current distribution of pits

5.6.2.2 Statistical Fits for Features extracted

The plates used for finding the most appropriate statistical fit were those with the most pits at each height. This might prove to be rather conservative but the difference is so substantial that is better to go with a conservative philosophy rather a more relaxed one on pitting corrosion.

The ones chosen for the fits are:

- 1 black front
- 2 blue back
- 3 black back

The best fit for each of them with the parameters describing the most appropriate distributions assessed by the AIC is given below.

Table 5-8: AIC values

Distribution	Area			Aspect Ratio			Major Length			Minor Length			Orientation		
Plates	*1kf*	*2bb*	*3bb*	*1kf*	*2bb*	*3bb*	*1kf*	*2bb*	*3bb*	*1kf*	*2bb*	*3bb*	*1kf*	*2bb*	*3bb*
Normal	11.21	39.7	34.3	26.50	36.0	27.9	8.75	10.1	9.35	9.36	12.4	10.3	18.92	23.5	20.5
Exponential	25.44	16.4	12.1	37.1	50.7	40.6	14.5	18.7	15.9	19.52	25.1	21.7	23.25	29.6	25.4
Extreme Value	15.86	15.9	3.9	20.02	25.5	19.2	10.2	12.4	11.2	9.57	12.9	10.43	20.80	25.9	22.3
Gamma	25.96	25.6	48.2	26.92	35.8	28.8	81.40	9.24	8.67	94.60	12.3	10.40	18.1	22.5	19.7
Log normal	30.94	30.9	52.7	25.62	33.5	27.4	80.05	9.07	8.52	95.74	12.4	10.5	17.9	22.8	19.5
Poisson	Inf	Inf	Inf	Inf	Inf	Inf	Inf	Inf	Inf	Inf	Inf	Inf	Inf	Inf	Inf
Rayleigh	12.88	37.02	32.1	9.40	10.9	9.66	0.939	12.5	10.9	141.68	18.1	15.5	14.17	24.1	20.9
Kernel	N/A	N/A	N/A	N/A	N/A	N/A	N/A	N/A	N/A	N/A	N/A	N/A	N/A	N/A	N/A
Weibull	15.99	43.7	37.5	27.39	101.9	28.6	8.711	10.2	2.86	92.97	12.4	10.2	18.5	23.2	20.2

The distributions chosen for each of the heights are as follows:

Table 5-9: Best distribution chosen

	Chosen distribution				
Plates	**Area**	**Aspect Ratio**	**Major Length**	**Minor Length**	**Orientation**
1 black front	Extreme Value (μ=0.5521, σ=0.2116)	Extreme Value (μ=0.6526, σ=0.1694)	Log Normal (μ=1.2729, σ=0.2068)	Normal (μ=2.0143 σ=0.4235)	Log-Normal (μ=1.6464 σ=0.3668))
2 blue back	Extreme Value (μ=0.5233, σ=0.2311)	Rayleigh (β=0.4304)	Log-Normal (μ=0.1.2451, σ=0.2152)	Gamma (A = 12.1669 B=0.1651)	Log-Normal (μ=1.6060, σ=0.23657)
3 blue back	Extreme Value (μ=0.5151, σ=0.2382)	Rayleigh (β=0.4251)	Log-Normal (μ=1.2977, σ=0.2095)	Normal (μ=2.0926, σ=0.6736)	Log-Normal (μ=1.6980, σ=0.3739)

5.6.2.3 Pit Depth

The depth was measured using a pit gauge (shown in the figure below) for each of the chosen plates' distribution.

Figure 5-27: example of pit gauge[6]

---

[6] https://utmss.com/category/utm-gauges/page/4/

There were five individuals involved, each one measuring 20% of the total number of pits, approximately, in a random fashion. They were then tabulated and the data presented in a histogram for extreme value evaluations. This process might not be the most accurate but clearly indicates an approach of automatic pit detection and sizing.

The task required some approximation as the resolution of the pit gauge is 0.1mm. A lot of the pits could not be measured as the sensitivity of the gauge was too low to fully characterise it.

It is logical that at this stage that the most appropriate fit for the pit depth will be the exponential as there are pits at 0.1mm.

They are seen below for each of the selected coupons:

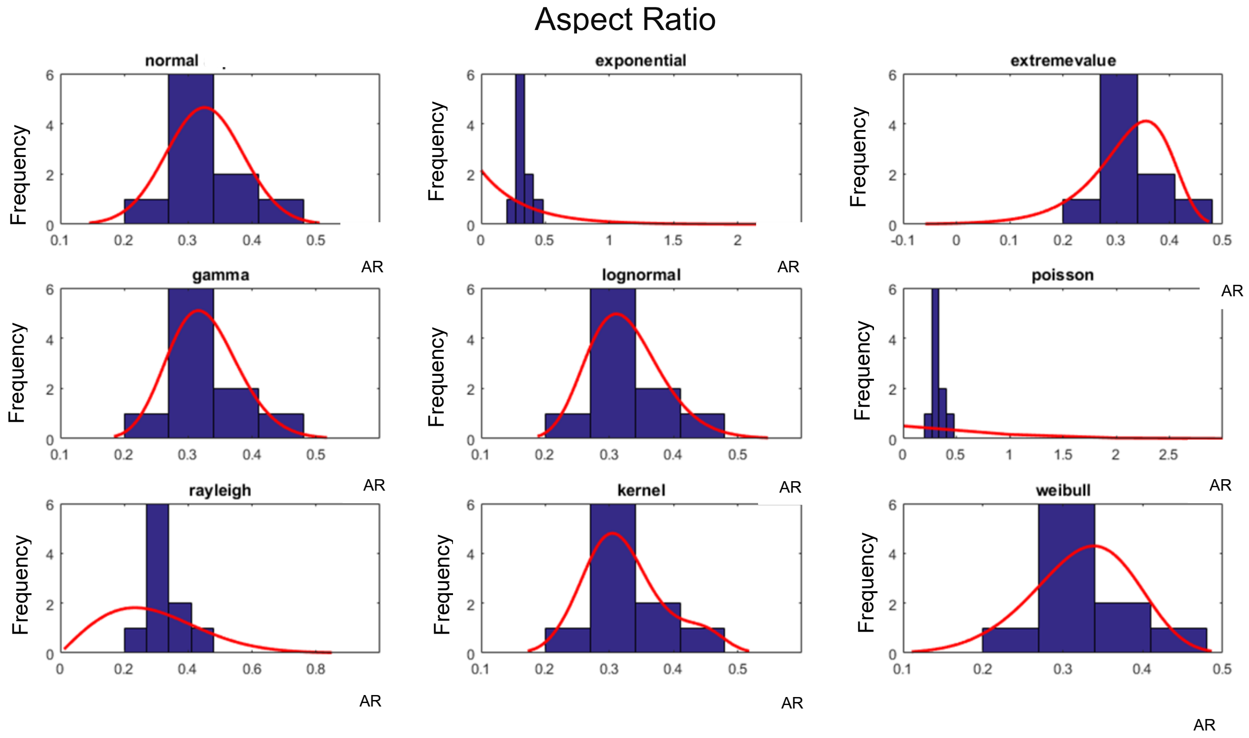

Figure 5-28: Pit distribution vs aspect ratio

The AIC for each of the plates chosen proved to have three of the distributions chosen to be the extreme value one.

Table 5-10: Best distribution parameters

Plates	**Depth[mm]**
1kf	Extreme Value (μ=0.2343, σ=0.1197)
2bb	Extreme Value (μ=0.2417, σ=0.1652)
3bb	Extreme Value (μ=0.2341, σ=0.1440)

The maximum pit depth recorded across the whole range was near to 0.6mm.

It cannot be fully emphasised how challenging this process was and it is clear that a more realistic method needs to be developed, at least for extracting pit information.

5.7 Image Processing and pitting corrosion

Digital Image Processing is a technique that employs digital images and extracts information from those pictures. In the case of pitting corrosion, the easiest way to do so is to have the image converted into a black and white image as the colours introduce another layer of complexity that might not be necessary in the case detection of the pits and the extraction of information from those.

There have been a number of studies of pitting detection from image processing even though the depth effects have to be measured differently, unless there is a cross-sectional section in which case, this is a possibility. This gives the advantage to also categorise the shape which has already been researched[180]. In this particular paper, the author extracts the information of the pits from the cross sections of the location of the pits and the shapes are then determined as a result. The dimensioning of the pits is done using digital image processing. That said, attaining the cross section can be a lengthy and rather expensive process, especially in the case of a heavily pitted specimen. Another interesting paper is the digitalising, filtering and thresholding of the image and from that point the pits were identified using the algorithm[181]. Using the pixel area and converting it to the actual area, the real area of the pits can be found [182]. This is used to find the probability of pitting according to ASTM G4 Standard.

The MATLAB image processing toolbox provides the necessary tools for this type of image processing. The processes of image segmentation are included as a function for thresholding and edge detection, which can ultimately be used for feature extraction and object counts[183].

5.7.1 Summary

- It is clear that in the tidal region from the North Sea, that the number of pits does not necessarily decrease with increasing water depth. The reasons for this have to be further investigated and to improve the confidence on the experiment. It is unfortunate only 5 plates were recovered from the 20 installed.
- The pitting probability can be easily deduced by the projected surface area and can be fitted to determine the number of pits required to fill a full plate.
- The statistical distributions have been fitted and do not show a specific tendency for favouring any one of the distributions.
- The pit depth is a slow process using the pit gauge but a distribution was able to be fitted for each of the plates taken into consideration.
- The average plates using averaging methods in the grayscale format have been realised with the distributions fitted for a possibility of the recreation of the plates.

5.8 Laser Scanning

3D laser scanning is a very effective tool and has a track record that was established in the engineering field. It has been used effectively in various fields, from automotive to aerospace for inspection and also reverse engineering. The spectrum of its application is wide and the resolution is continuously improving with time. Also, with better computing and processing power this technology ensures smaller defects can be detected. The idea is to use this technology and carry out fine resolution detection of the pits and characterise them accordingly.

The laser scanning was used both on the plates from the field experiment and from coupons inside the monopile.

The characterisation process involves:

- Pit detection and isolation
- Pit depth
- Pit major length and minor length
- Pit aspect ratio: AR-XY, AR-XZ, AR-YZ can be deduced from the major length and minor length easily.
- Area
- Orientation

The coupons/plates were scanned accordingly. A calibration error has been removed, the data was cleaned to obtain only the points on the plates. The average depth of the plate is calculated and used as a threshold to define the pits. The pits were then manually extracted and defined and for each one, the deepest point is extracted. The pit depth was then calculated as a result of a region of 2mm from the pit extreme x-y coordinates. The major and minor lengths were calculated as a result of the extreme coordinates extracted. The aspect ratios were computed respectively.

Unfortunately, the coupons collected from the field experiment had been curved and this changed the laser scanning procedure significantly as the reference is hard to pick to obtain the characteristics of the pit including the pit depth (further explained in the methodology section). Some coupons were obtained from the internal section of the monopile and had been exposed for 528, 538, 560, 590, 600,600, 802, 1049 days (those are different to the field experiment carried out in this thesis). The analysis of picking the pit characteristics was executed using a grey image formed from the 3-dimension laser scan, which is then analysed using the image processing tool box in MATLAB.

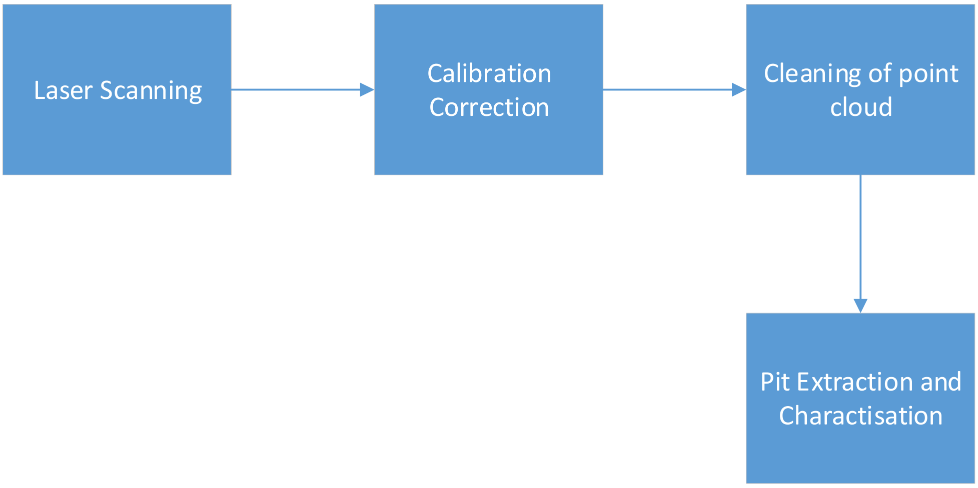

Figure 5-29: Flow process

5.8.1 Methodology

This analysis will require a few important steps before generating some concrete results.

5.8.1.1 Laser Scanning

Laser scanning is a tool for capturing 3D coordinates from a reference point. It requires the equipment and data acquisition software, which is usually installed on a portable computer. The main parameter is the resolution of the scan and this has been set to 0.2mm. This particular scanner has the capability to capture data points to a finer resolution to 0.04mm. Unfortunately, the computer could not cope with this level of high resolution and, therefore, the second best option had to be chosen, being 0.2mm.

Before the scans, the calibration plate was employed to correct any calibration issues with the machine.

The scan was made and it is obvious that some data from the surroundings was captured.

The point cloud would require some digital cleaning before effective usage.

Figure 5-30a & b: Laser scanning tool and raw data cloud

5.8.1.2 Cleaning Cloud Point

The cleaning of the unnecessary data was automatic.

The points to be removed had to fall inside the bracket defined as:

$$Z = 4 < Z < 6\ [mm]$$

The extreme ends of the coupons was also selected. The logic is demonstrated below:

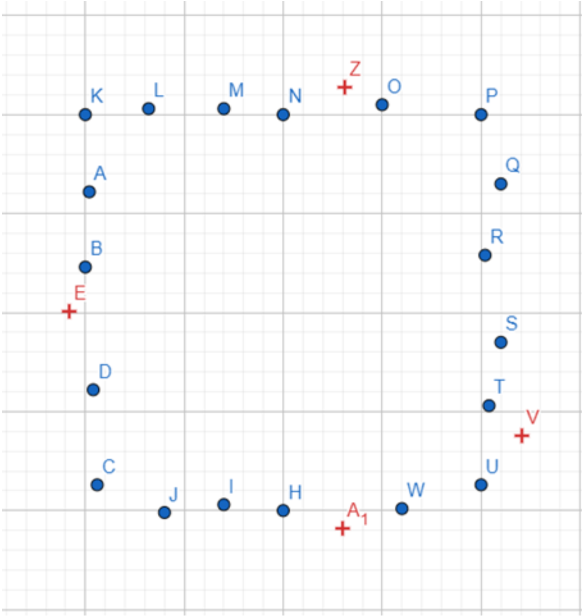

Figure 5-31: Boundaries of plate

From the left edge, E seemed to have the lowest x value and V the highest value and likewise A1 and Z had the corresponding y values.

The region defined by the coupon could be mathematically expressed as:

$$region = \{\min(x)\,, \max(x)\; and\; \min\,(y), \max\,(y)\}$$

Any coordinates lying in this region passed the test and, thus, constituted the plate, else they were discarded.

This gave a plate and was shown below.

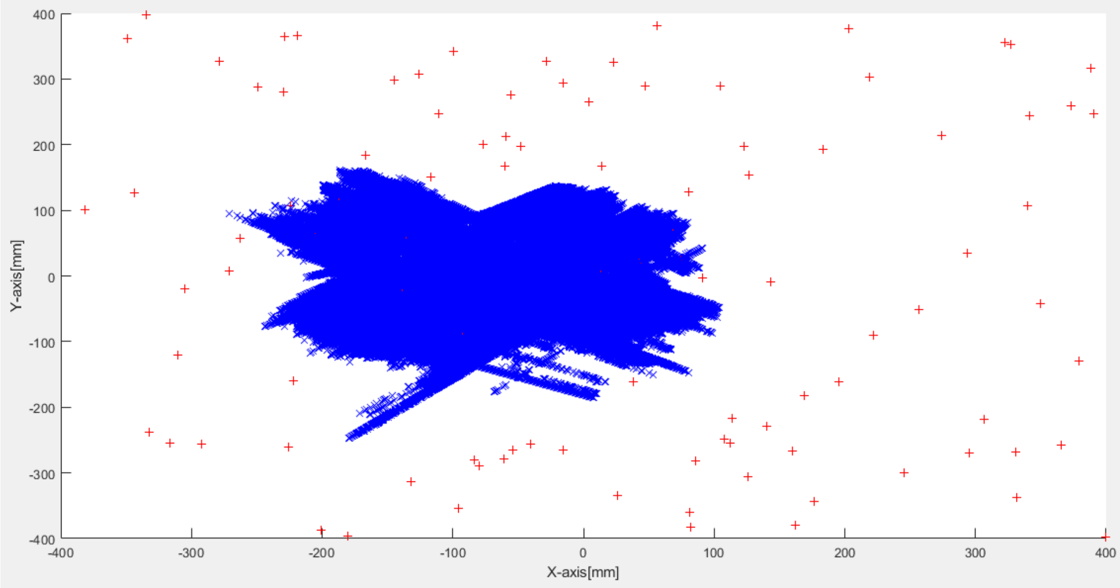

Figure 5-32: Plane visualisation parallel to coupon

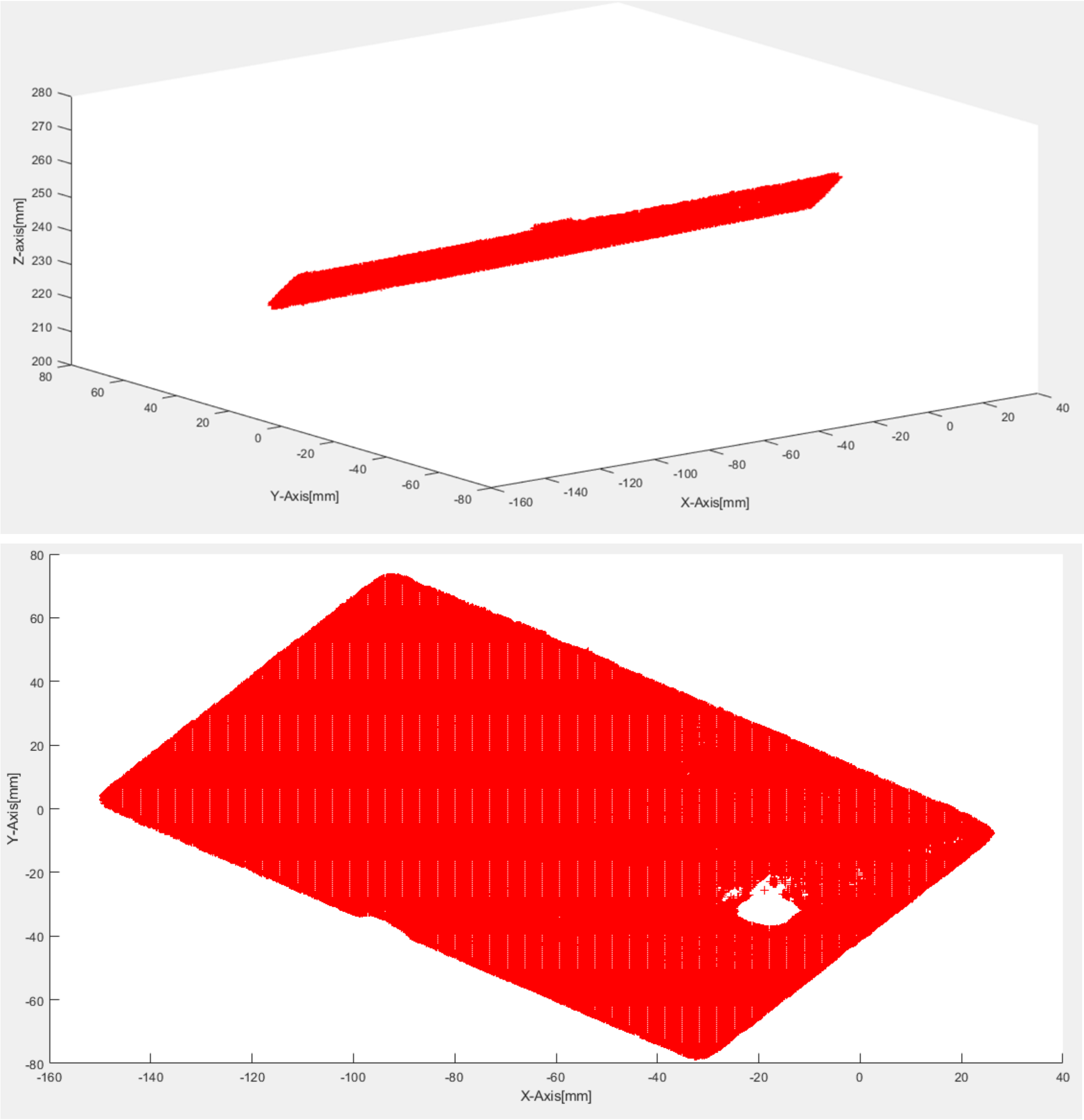

Figure 5-33a & b: Removal of inclination effects

5.8.1.3 Calibration

The data have been observed to have a tilt. This means that any point cloud analysis will be difficult and this cloud will require to be flattened.

There is a major assumption that the table is entirely flat and there are no differences in the depth at all. It is implied from that hypothesis that the table can be represented by a plane and the coupon surface for the same x and y coordinates will remove the Z inclination with respect to the global axis coordinate system, i.e. the plate is parallel to the plane.

To define the plane, three points at least are required from the table to let those coordinates be A, B and C. The position vectors can be calculated **AB** and **BC.** The cross product of **AB** and **BC** will give the normal. The equation of the plane is then easily found by substituting **n** into the Cartesian equation of a plane. To reduce errors in the calculation of the normal, more than a hundred combinations from various points have been employed to calculate an average normal.

$$\boldsymbol{n} = \boldsymbol{AB}\ \boldsymbol{X}\ \boldsymbol{BC}$$

$$\boldsymbol{n}.(x, y, z) = \boldsymbol{n}.\boldsymbol{AB}$$

Equation 5-18

The difference between the depth of the coupon and the plate helps to flatten the coupon on the X_Y plane. The angle between the global zero and the corner coordinate is computed and a rotational matrix is applied in a 2D plane(only x-y).

$$R = \begin{pmatrix} \cos\theta & -sin\theta \\ sin\theta & cos\theta \end{pmatrix}$$

Equation 5-19

The depth is associated to each of the rotated x and y coordinates.

5.8.1.4 Pits Extraction and Characterisation

The pits were characterised manually and, using the coordinates, the major length and minor length were calculated using the distance formula. A contour fill plot was employed from the Matlab plotting toolbox. The purple regions are indicative of the deeper pits but, on first analysis, it is interesting to observe the effect of general corrosion in the turquoise, yellow and green regions.

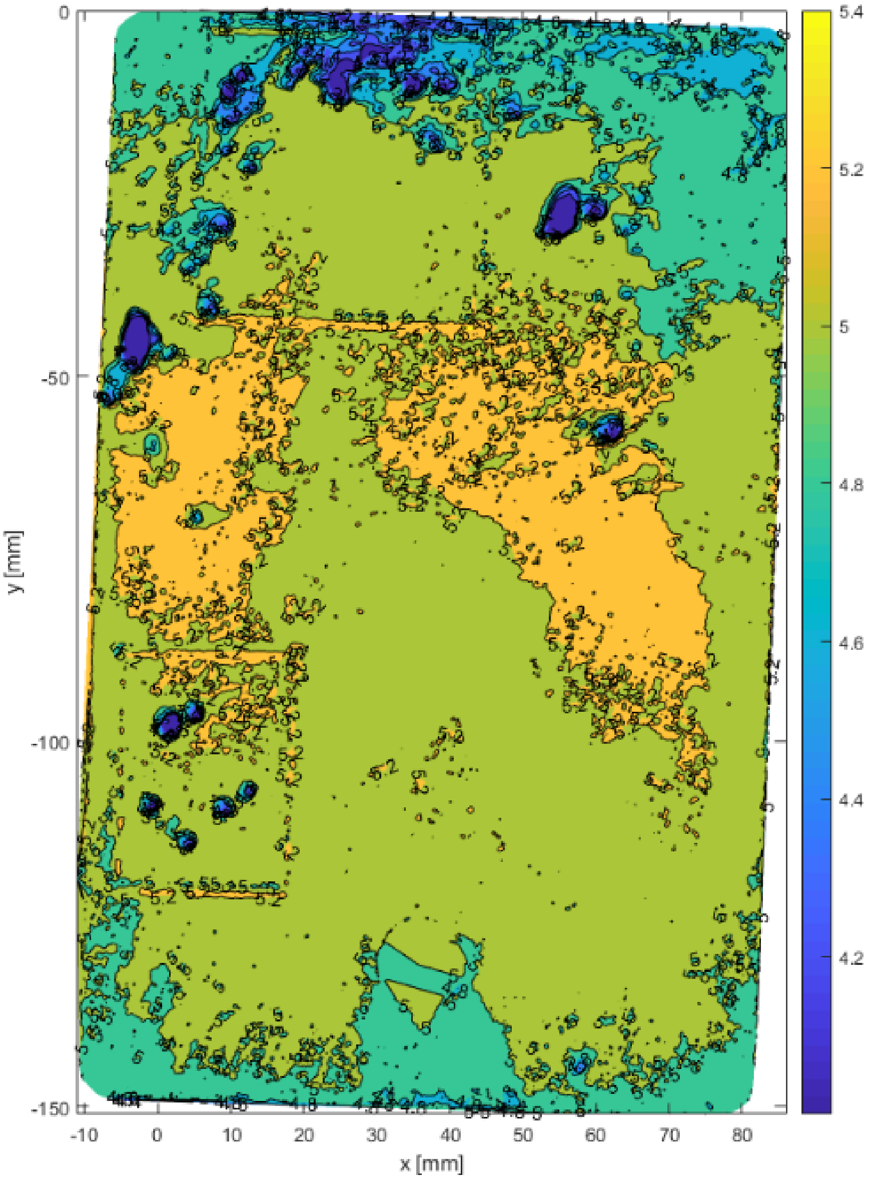

Figure 5-34: Pits present

As a recap, the pits were extracted in terms of their major length, minor length, orientation, area and centroid coordinates in the x-y plane.

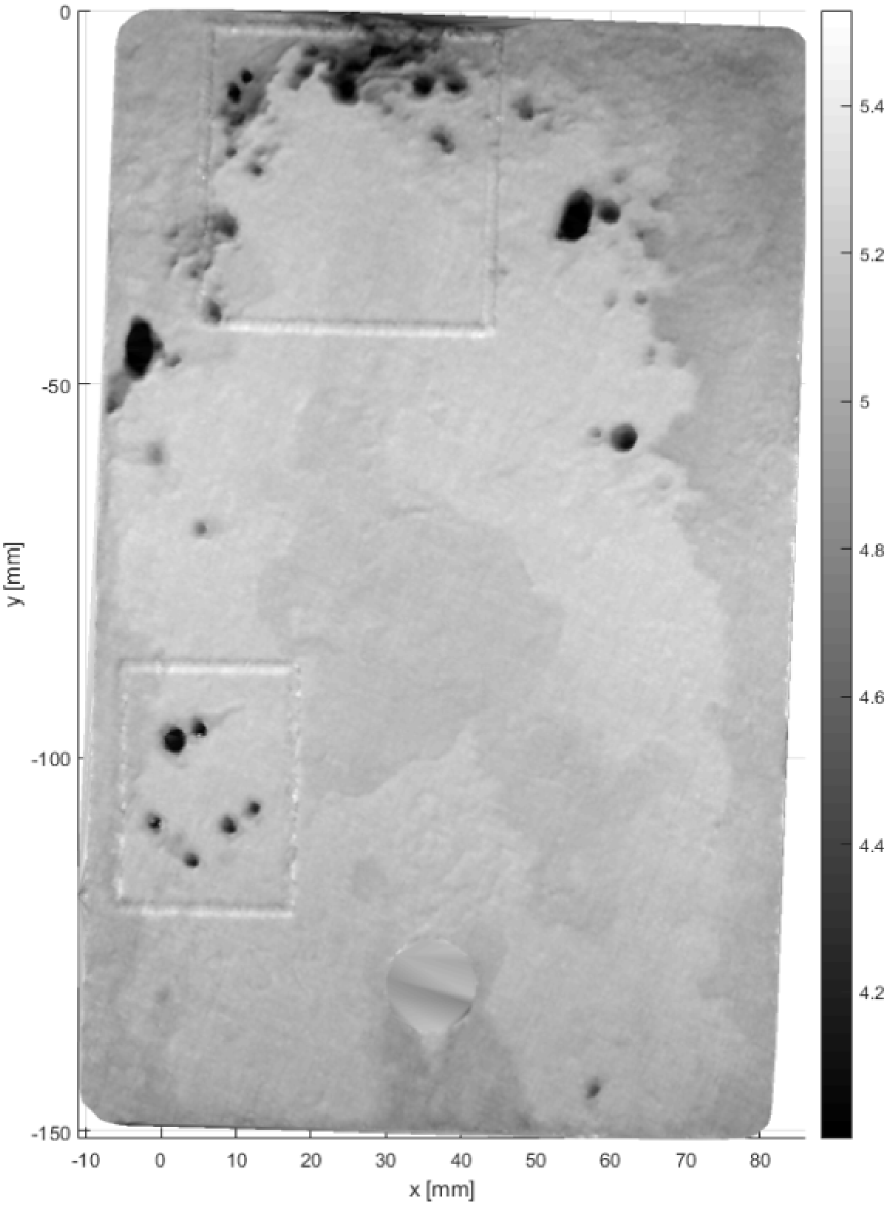

Figure 5-35: Change to an image

A few conditions were employed to choose the pits and were as follows:

- The areas registered smaller or equal to 0.5mm^2 were neglected(smaller than that has proved to capture some noise).
- The depressions smaller or equal to 0.2mm are neglected and were considered as general corrosion rather than pits.
- The pits that were located 2mm from the edges were not taken into consideration due to edge effects.

The filters are important or else it is difficult for depressions/valleys detected that do not correspond to pits, which are considered as macro pits rather than micro pits.

To capture the actual pit's depth, it needs to be measured from a reference, which was chosen as a region just outside the pit and around it in a rectangular fashion. It is calculated as the region 1.0 to 1.2 times the length of the major length. This creates square region and the average is computed to determine the average depth of the reference to that region.

In some cases, the regions tend to be outside the plates and those regions are neglected whilst calculating the average reference depth. An example of the selection of those regions is shown below:

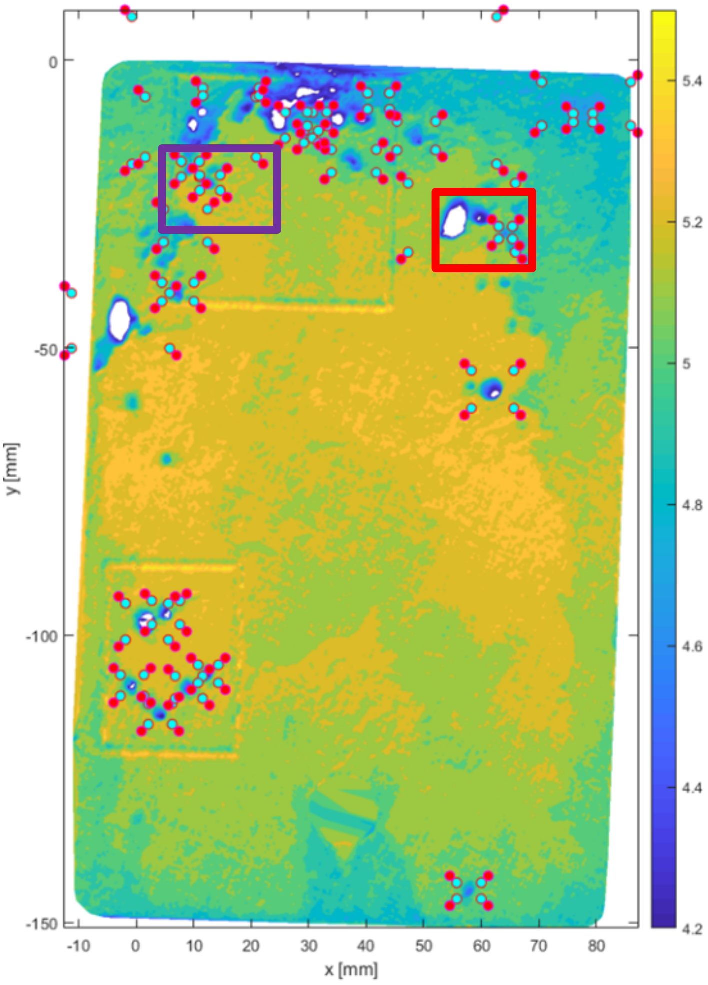

Figure 5-36: Pits' depth references

Considering the red square, the region between the cyan dots and the red ones provide the region of the pit enclosed in that square. The purple square provides another case where the regions to the left, right and down are not accounted for in the calculation; only the one to the right of the pit is accounted for. This is because the left section is outside the edge part of the top and bottom one too which are partially lying outside.

$$Pit\ depth\ =\ average\ reference\ of\ pits - minimum\ point\ of\ pit$$

Equation 5-20

The aspect ratio is calculated as:

$$AR_{xy} = \frac{(Major\ length)}{Minor\ Length}$$

$$AR_{yz} = \frac{(Minor\ length)}{depth}$$

$$AR_{xz} = \frac{(Major\ length)}{depth}$$

Equation 5-21

5.8.1.5 Curved plates

The plates had a curvature and it was deemed best to generate a surface that is curved that fits the bottom of the curve. This would have the same exact curvature and a mathematical function will be available and correspond to the x and y points from the plate. From this, the z coordinates could be extracted and the difference will remove the curvature effect.

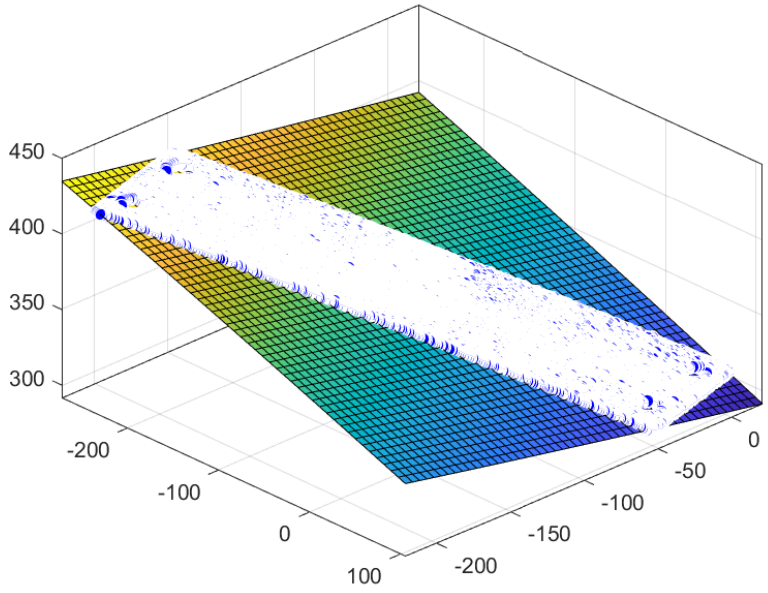

Figure 5-37: Curved fit to curved plate

This was tried but, unfortunately, the results were far from being great, as shown below when it was attempted to extract the pits.

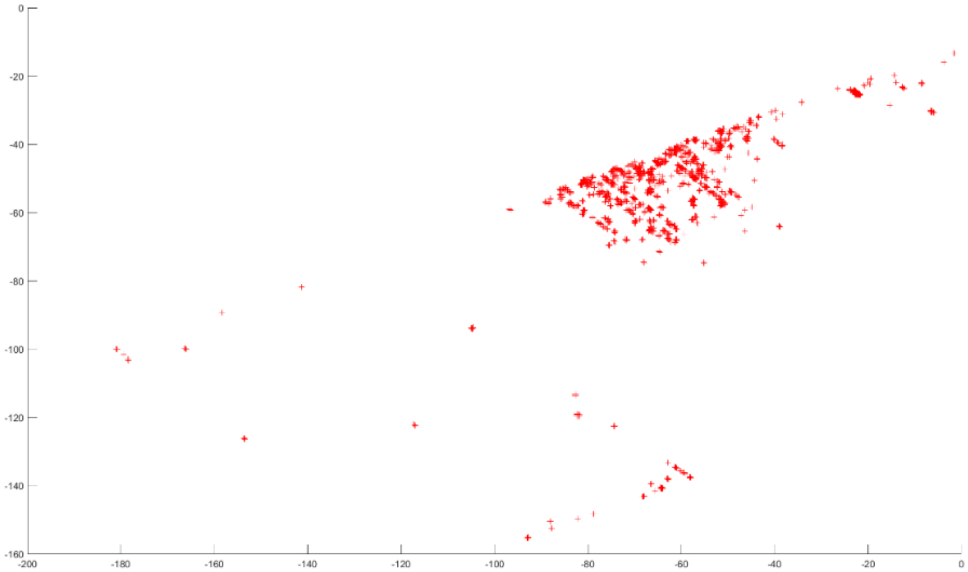

Figure 5-38: Errors from subtraction

The scatter points looked nothing remotely close to the location of the pits and the proceedings were shelved. This is another project that will be worked on in the future.

5.8.2 Results and Discussion

In this section and onwards only the coupons from the monopiles have been used.

The various characteristics including the area, aspect ratio, minor length and major length, and the depth were extracted from the cloud of data captured by the laser scanner.

The diagram shows the various pits defined and extracted and the values obtained as a result for each plot on the side graphs.

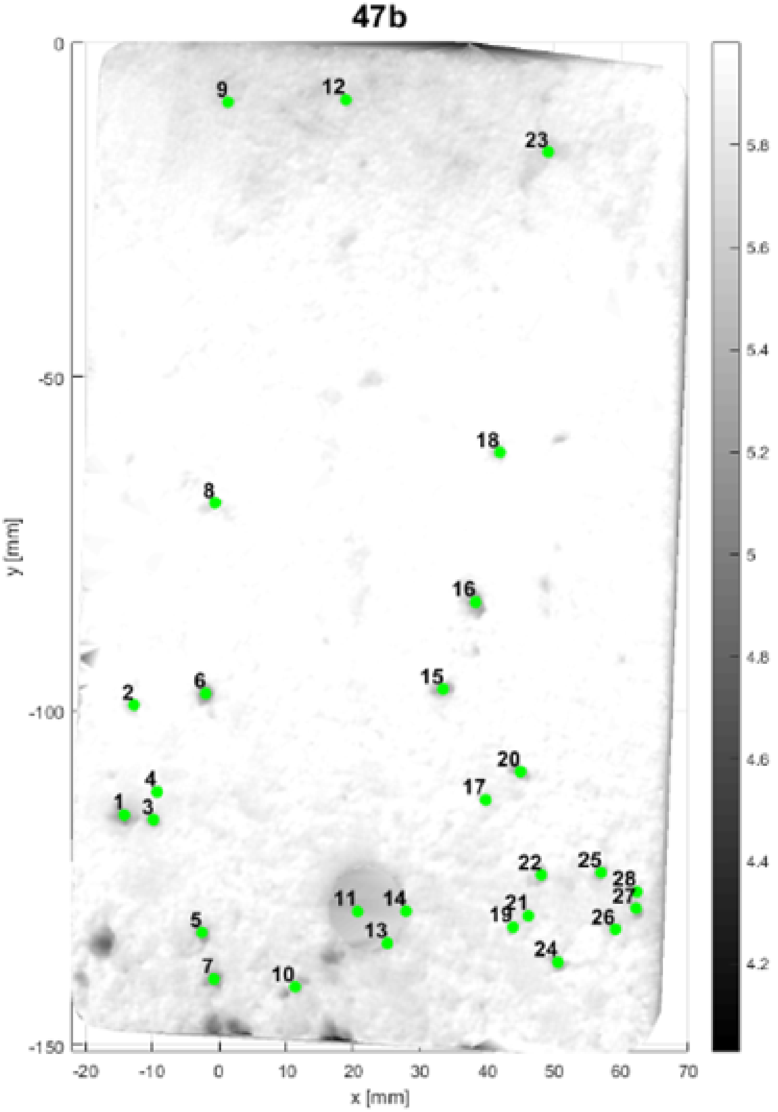

Figure 5-39: Pit labelling and pit data extraction

It is clear that within the analysis the number of pits decreased with respect to time, from 1 to 3 years. The reason is that is could be assumed that the pits were coalescing. In so doing, the total volume increased and could be demonstrated by the following graphs.

The volume increases meaning that the pits were growing in size and that was followed by a quadratic equation.

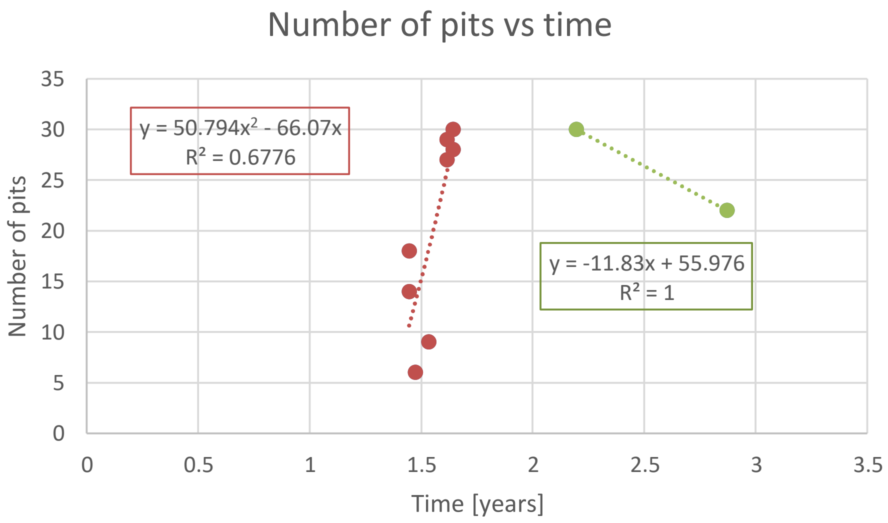

Figure 5-40: Number of pits vs. time

Solving the two linear equations result in a maximum number of pits of 36 at a time of 1.7 years. After that point, the number of pits decreased according to the analysis undertaken.

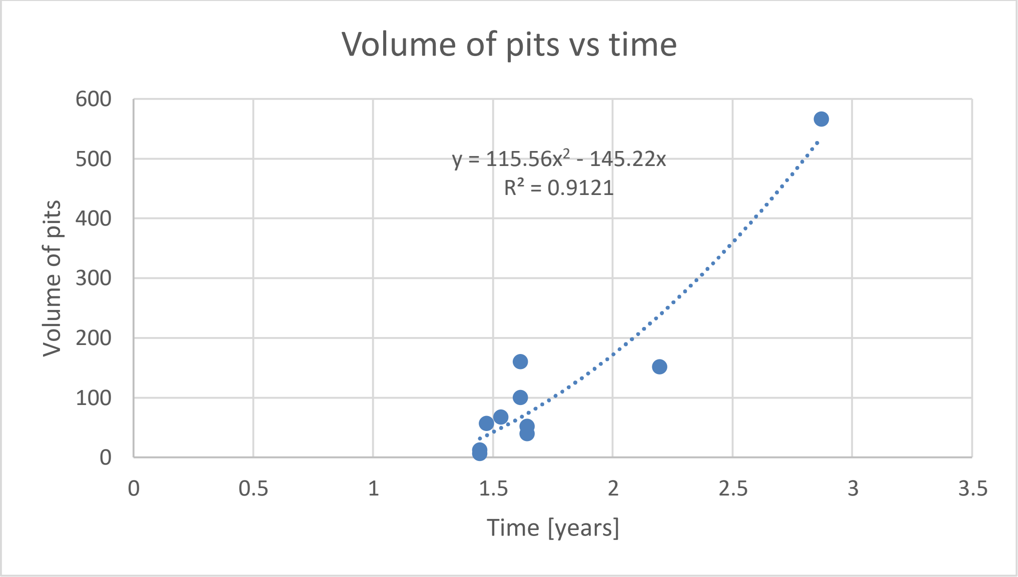

Figure 5-41: Volume of pits vs. time

Each of the plates was characterised as a statistical function, similar to the image processing section in this chapter.

Table 5-11: Depth fitting

	depth				
time[years]	parameter value		name of parameter		name of distribution
1.45	0.42	0.00	'mu'	[]	'Exponential'
1.45	0.31	0.00	'mu'	[]	'Exponential'
1.62	0.45	0.00	'B'	[]	'Rayleigh'
1.62	-0.73	0.53	'mu'	'sigma'	'Lognormal'
1.64	0.55	0.21	'mu'	'sigma'	'Extreme Value'
1.64	0.39	0.00	'B'	[]	'Rayleigh'
1.53	0.43	0.00	'mu'	[]	'Exponential'
1.47	0.50	0.00	'B'	[]	'Rayleigh'
2.87	-0.85	0.69	'mu'	'sigma'	'Lognormal'
2.20	0.79	2.57	'A'	'B'	'Weibull'

Table 5-12: Minor length fit

	minor length				
time[years]	parameter value		name of parameter		name of distribution
1.45	0.40	0.36	'mu'	'sigma'	'Lognormal'
1.45	0.62	0.62	'mu'	'sigma'	'Lognormal'
1.62	1.12	0.50	'mu'	'sigma'	'Lognormal'
1.62	0.98	0.77	'mu'	'sigma'	'Lognormal'
1.64	0.50	0.64	'mu'	'sigma'	'Lognormal'
1.64	0.57	0.51	'mu'	'sigma'	'Lognormal'
1.53	6.90	1.50	'A'	'B'	'Weibull'
1.47	1.24	0.86	'mu'	'sigma'	'Lognormal'
2.87	0.76	0.79	'mu'	'sigma'	'Lognormal'
2.20	0.76	0.68	'mu'	'sigma'	'Lognormal'

Table 5-13: Major length fit

	major length				
time[years]	parameter value		name of parameter		name of distribution
1.45	1.08	0.44	'mu'	'sigma'	'Lognormal'
1.45	1.40	0.46	'mu'	'sigma'	'Lognormal'
1.62	1.54	0.62	'mu'	'sigma'	'Lognormal'
1.62	1.50	0.71	'mu'	'sigma'	'Lognormal'
1.64	0.91	0.83	'mu'	'sigma'	'Lognormal'
1.64	1.06	0.58	'mu'	'sigma'	'Lognormal'
1.53	11.90	2.20	'A'	'B'	'Weibull'
1.47	1.70	0.96	'mu'	'sigma'	'Lognormal'
2.87	1.28	0.95	'mu'	'sigma'	'Lognormal'
2.20	1.26	0.81	'mu'	'sigma'	'Lognormal'

Table 5-14: Minor length fit

	growth rate minor length				
time[years]	parameter value		name of parameter		name of distribution
1.45	0.02	0.44	'mu'	'sigma'	'Lognormal'
1.45	0.34	0.46	'mu'	'sigma'	'Lognormal'
1.62	0.37	0.62	'mu'	'sigma'	'Lognormal'
1.62	0.33	0.71	'mu'	'sigma'	'Lognormal'
1.64	-0.28	0.83	'mu'	'sigma'	'Lognormal'
1.64	-0.13	0.58	'mu'	'sigma'	'Lognormal'
1.53	3.88	2.20	'A'	'B'	'Weibull'
1.47	0.62	0.96	'mu'	'sigma'	'Lognormal'
2.87	-0.47	0.95	'mu'	'sigma'	'Lognormal'
2.20	-0.22	0.81	'mu'	'sigma'	'Lognormal'

Table 5-15: Growth rate fit

	growth rate Minor length				
time[years]	parameter value		name of parameter		name of distribution
1.45	-0.66	0.36	'mu'	'sigma'	'Lognormal'
1.45	-0.44	0.62	'mu'	'sigma'	'Lognormal'
1.62	-0.06	0.50	'mu'	'sigma'	'Lognormal'
1.62	-0.19	0.77	'mu'	'sigma'	'Lognormal'
1.64	-0.69	0.64	'mu'	'sigma'	'Lognormal'
1.64	-0.62	0.51	'mu'	'sigma'	'Lognormal'
1.53	2.25	1.50	'A'	'B'	'Weibull'
1.47	0.16	0.86	'mu'	'sigma'	'Lognormal'
2.87	-0.99	0.79	'mu'	'sigma'	'Lognormal'
2.20	-0.72	0.68	'mu'	'sigma'	'Lognormal'

Table 5-16: Growth rate depth

	growth rate depth				
time[years]	parameter value		name of parameter		name of distribution
1.45	-1.9989	0.374571	'mu'	'sigma'	'Lognormal'
1.45	-2.27352	0.315436	'mu'	'sigma'	'Lognormal'
1.62	-1.76359	0.395551	'mu'	'sigma'	'Lognormal'
1.62	-1.90712	0.529558	'mu'	'sigma'	'Lognormal'
1.64	-2.08195	0.451621	'mu'	'sigma'	'Lognormal'
1.64	-1.92685	0.426966	'mu'	'sigma'	'Lognormal'
1.53	0.158018	3.419028	'A'	'B'	'Weibull'
1.47	-1.66286	0.51869	'mu'	'sigma'	'Lognormal'
2.87	-2.59482	0.6851	'mu'	'sigma'	'Lognormal'
2.20	-1.94375	0.509744	'mu'	'sigma'	'Lognormal'

When testing them against the Akaike Information Criterion-AIC, the log normal seems to be the most commonly used one for the growth rate for depth, minor length and major length but the picture is somehow different for the depth.

The variations in the distributions of the depth should be associated to the changing environment and this is interesting as the other parameters measured are rather fixed. This will require some further investigation to determine this change.

When plotting the various parameters, coefficients for the log normal, there seems to be a cyclic change of the location and scale. The pits are telling a story through those distributions but it seems to be an alien language that still needs to be deciphered. Corrosion is never straight forward.

5.9 Summary

- Methodology and instrumentation/analysis for design/deployment of site specific corrosion coupons.
- Corrosion rates of up to 0.8mm per year.
- Pit intensity of up to $1.54X10^4$ was observed.
- Large variation of pits and pitting numbers observed.

6 Surface Topography Evolution under Corrosion within Offshore Structures

6.1 Introduction

Offshore structures are prone to exist in hostile environments and are designed to survive for a period of at least 20 years. This environment consists of high wind speeds and waves combined with biological and chemical influences coming from the sea water that tend to be a catalyst for structural damage.

One of the most damaging mechanisms to those structures comes in the form of corrosion, which is known to be an electro-chemical process. The consistency and chemistry of the sea water is always a fluctuating one, with varying pH, dissolved oxygen, temperature and other elements that are considered to have important consequences on the rate of corrosion. Another aspect is the biological impacts where the nature of the corrosion changes from an aerobic to an anaerobic scenario. In so doing, this accelerates the corrosion rate that results in greater losses and, therefore, reduces the integrity of the structure drastically.

Corrosion exists in different forms and from the reference 1, pitting corrosion is considered as the most damaging form of marine corrosion. The reason for its notoriety lies in its random nature in spatial distribution and aspect ratio, thus making it difficult to design and inspect. The impact on the structure appears in the form of stress raisers, which when high enough under adequate fatigue loads, can transit to a crack. This process is referred to as the pit to crack transition and is highly dependent on the pit depth, aspect ratio of the pits and the stress range.

Predicting this change is a non-trivial one, especially for complex offshore structures. The evolution of those pits with time does create a significant change on the stress distribution of the structure and to characterise this effect, the topology needs to be understood.

The goal of this paper is to replicate this effect of corrosion and observe on a longer time horizon, as proposed by Melchers, the topology of a steel plate. This phenomenon occurs due to the varying topological changes as a result of the evolution of the pits where new pits are formed and old pits keep growing. This results in quite a few different scenarios; there is a potential of a pit growing inside another pit or pits coalescing or even both happening.

This study consists of a few techniques to allow the future to be foreseen in terms of pitting on a coupon. The first aspect is to simulate a coupon surface with initial pits. The pits are then defined as a function of the average corrosion depth, and from this the pits can be detected and extracted using the hierarchical cluster analysis. From that point, they have to be re-characterised in a semi-ellipsoid geometry to make it mathematically robust to grow. The number of pits increases each year and this was characterised using the Non-Homogeneous Poisson Process. The pits need to grow in dimension and three methods have been employed for pitting growth rate predictions and comparison; the methods are: the uniform corrosion model, Melchers' Model and, lastly, the Artificial Neural Network. A summary of the various stages are illustrated in the flowchart below:

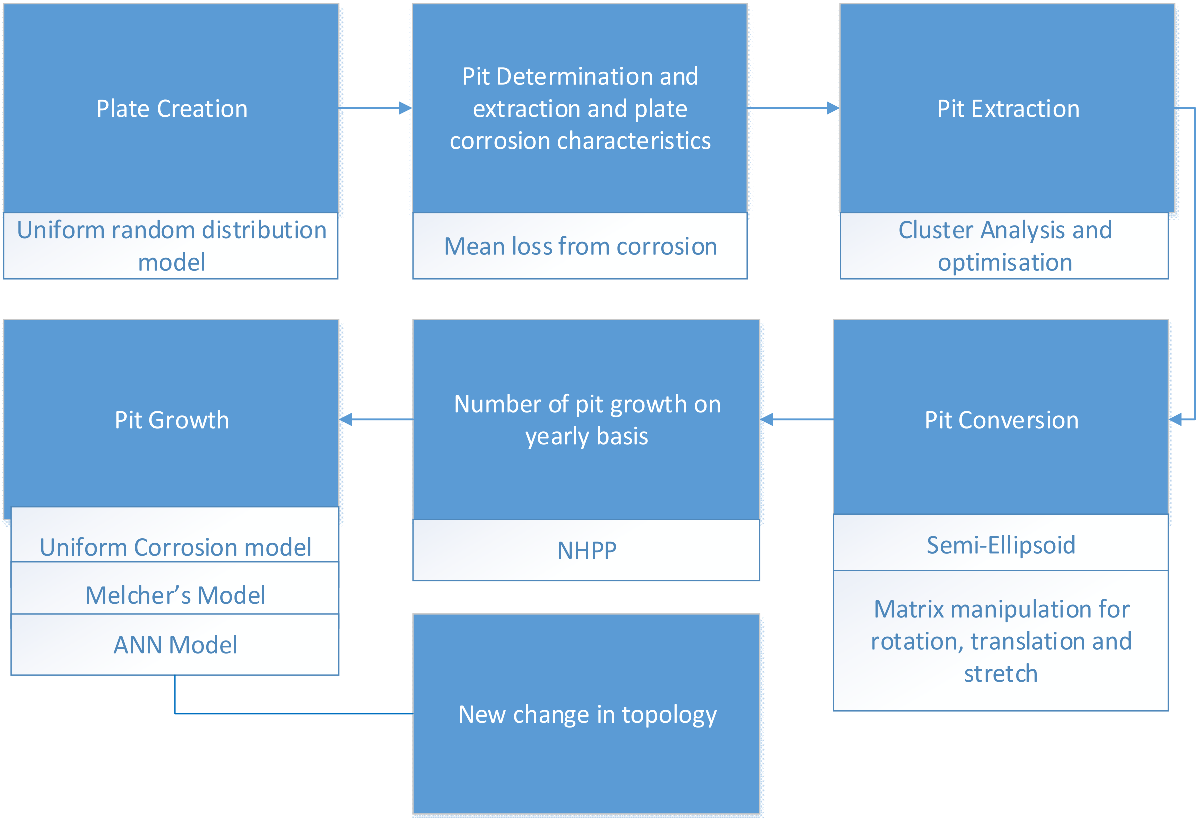

Figure 6-1: models used for modelling the future plate topology

6.2 Methodology

6.2.1 Size of Coupons

The plate creation was rectangular in geometry and was gridded to allow for ease of pit growth. The size of the plate selected was 400X90 mm [178]. The initial depth with its x and y coordinates, as a result of the occurrence of localised corrosion, has been simulated as a uniform random distribution; the reason is that no data is available yet for this phenomenon.

The depths have been distributed to form a depth with a maximum value of 0.2mm, which can be found as a corrosion rate heavily employed in the offshore wind design environment on a yearly basis [91]. The plate is estimated to have been exposed to marine corrosion for one year. The depth set is referred to as Z_1.

The plate will also be created before corrosion in which case it is just a flat surface with depth of zero. This is a grid and is referred to as Z_0.

6.2.2 Pit Geometry and Mathematics behind Geometry

Various pit geometries have been observed in the field and consist mainly of those geometries listed below:

In terms of simulation though, there has been a tendency to use hemispherical and semi–elliptical pits[138].

The pit shape chosen in the scope of this study is semi elliptical as it provides three degrees of growth with differing values compared to the hemisphere, which needs to have the growth happening with only one value for the three directions.

6.2.3 Cloud Comparison

The cloud comparison is a result of the cloud of coordinates before and after corrosion. The grid, before and after corrosion, has the same x and y values, which correspond to the length and width of the plate.

The depths, coincident to the same x and y coordinates, are then subtracted from one another and finally the depth loss due to corrosion for a surface is obtained.

In that cloud comparison, there is a word of warning that comes to mind. If the points are not coincident, the algorithms, like interpolation between points, can be used or even the nearest neighbour to predict the losses. This might be the case for real data obtained from optical methods.

$$\boldsymbol{\Delta Z = Z_0 - Z_1} \qquad \textbf{Equation 6-1}$$

ΔZ is representing the depth loss as a result of corrosion.

6.2.4 Average Loss due to Corrosion

The corrosion depths can be averaged to represent the average corrosion loss:

$$\boldsymbol{average\ corrosion\ loss} = \frac{\sum \Delta \boldsymbol{Z}}{\boldsymbol{N}}$$ **Equation 6-2**

Where N is the number of data points.

By dividing the average corrosion depth loss by the number of years, the corrosion rate can be found in mm/year:

$$average\ corrosion \frac{loss}{year} = \frac{Average\ corrosion\ depth\ loss}{number\ of\ years}\ [\frac{mm}{yr}]$$

Equation 6-3

6.2.5 Hierarchical Cluster Analysis for Pit Extraction

In this analysis, the Matlab toolbox for cluster analysis has been employed. The importance of this analysis is to isolate the pits and extract their coordinates.

The threshold for the cluster analysis was set to be 30% with regards to the average depth of the pit as it provided the best results for isolation of the pits.

6.2.6 Pit Change to Semi Ellipse

From the corrosion pit section, it can be seen that various pit geometries have been observed on steel. However, the geometries that are generally mostly simulated for numerical analysis tend to be the semi sphere or semi ellipsoid. The semi ellipsoid offers a better degree of manoeuvrability as the pit upon growth can be associated with three different values rather than only one for a semi sphere. There are also conic pits that have been observed but they tend to be found in special cases, like in cast iron. This does not mean that this rule of pit geometries in cast iron exempts conic pits in other types of steel but in the scope of this study they will be neglected and also the aspect ratio with regard to the depth might be very steep, thus simulating the conic shape to a certain level even if a semi ellipsoid is used.

The conversion of the pit to a semi ellipsoid firstly requires the coordinates of the data to be extracted from the cluster analysis. Four sets of coordinates are pulled from each data set and they represent the extreme data points. It is to be noted that the data points extracted are only in the x and y direction at this stage.

$$Extreme\ data\ points\ = \left\{ \begin{matrix} (minimum\ x, Y(\ minimum\ x)), \\ (X(minimum\ y), minimumy), \\ (X(maximum\ y), maximum\ y), \\ (maximum\ x, Y(\ maximum\ x) \end{matrix} \right\}$$

Equation 6-4

Y(minimum x) means that the minimum value of x from the pit is indexed and attributed to its corresponding y coordinates. As can be seen, the ellipse will be formed within the rectangle formed from the extreme coordinates.

The following diagram shows a representation of the points on a grid of a cluster.

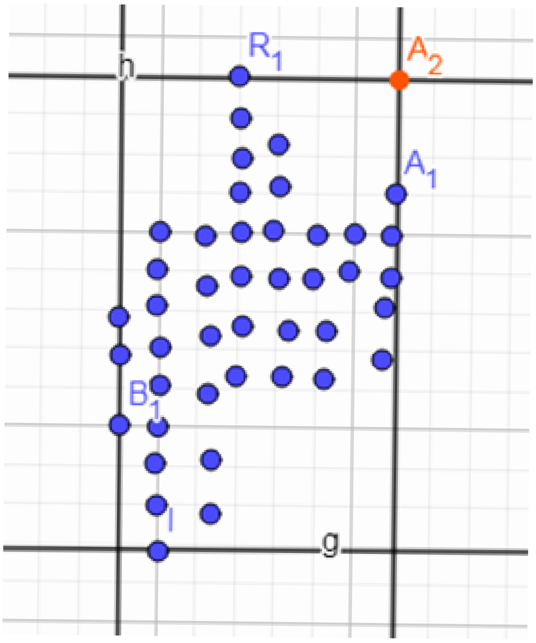

Figure 6-2: Points on grid representation

$$Extreme\ data\ points\ = \left\{ \begin{matrix} Point\ B1 = (minimum\ x, Y(\ minimum\ x)), \\ Point\ I = (X(minimum\ y), minimumy), \\ Point\ R1 = (X(maximum\ y), maximum\ y), \\ Point\ A1 = (maximum\ x, Y(\ maximum\ x) \end{matrix} \right\}$$

Equation 6-5

From those extracted points, the centroid in the x and y direction can be computed easily.

It will simply be:

$$(X\ Centroid, Y\ Centroid) = (\frac{minimum\ x + \ maximum\ x}{2}, \frac{minimum\ y + \ maximum\ y}{2})$$

Equation 6-6

It is noted that the centroid geometrically represents the centre of the enclosed rectangle. The ellipse will be built from that enclosed rectangle now and will be referred from that point onwards as the test area.

6.2.7 Minor and Major Axis Calculation

The minor and major axis are crucial for the mathematical definition of an ellipse.

The major and minor axis will be firstly considered as the distance only in the x and the y direction between the two extreme points. Again, the reference is the test area.

The definition of the major length is the longest length going through the centroid of the ellipse, whereas the minor length is the shortest length going through the centroid of the ellipse. They are at an angle of 90 degrees to one another and they represent the backbone of the ellipse.

It is first required to test which of the two combinations is longer. It is crucial to emphasise that the distance of the minor and major length are the distances from the test area, which are always represented as a rectangle.

There can be two candidates for the major and minor length and to distil which one is the major or minor one, a test needs to be carried out.

The two possibilities for the test-major length are:

$$test\_Major\ length_1 = (maximum\ x - minimum\ x)$$

$$test\_Major\ length_2 = \ (maximum\ y - minimum\ y)$$

Equation 6-7

The two possibilities for the test-minor length are:

$$test\_Minor\ length_1 = (maximum\ x - minimum\ x)$$

$$test\_Minor\ length_2 = \ (maximum\ y - minimum\ y)$$

Equation 6-8

The logic for the selection is:

If test_Major length$_1$ is larger than test_Major length$_2$, the minor length chosen will be Minor length$_2$. The other case will be the inverse.

The minor and major length is now established and the next important characteristic of an ellipse can be determined, which is the focal length.

The major and minor length equation can be calculated as

$$Major\ length_1 = \frac{(maximum\ x - minimum\ x)}{2}$$

$$Major\ length_2 = \frac{(maximum\ y - minimum\ y)}{2}$$

$$Minor\ length_1 = \frac{(maximum\ x - minimum\ x)}{2}$$

$$Minor\ length_2 = \frac{(maximum\ y - minimum\ y)}{2}$$

Equation 6-9

U_1 represents the centroid. F_2G_2 represents the major length whereas I_2B_2 represents the minor length.

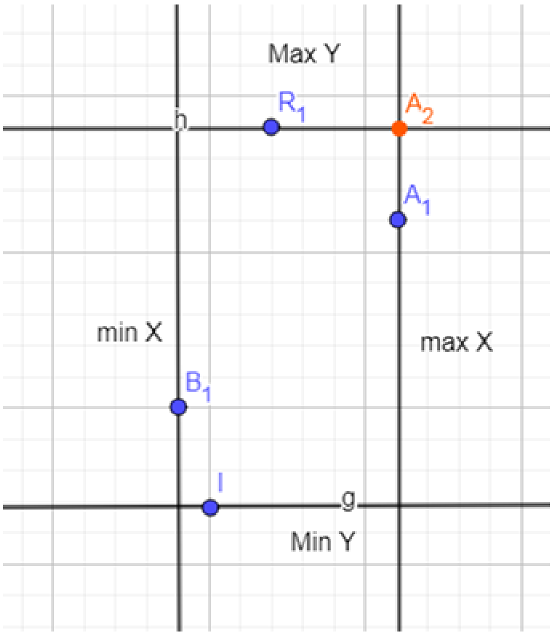

Figure 6-3: Extreme point selection

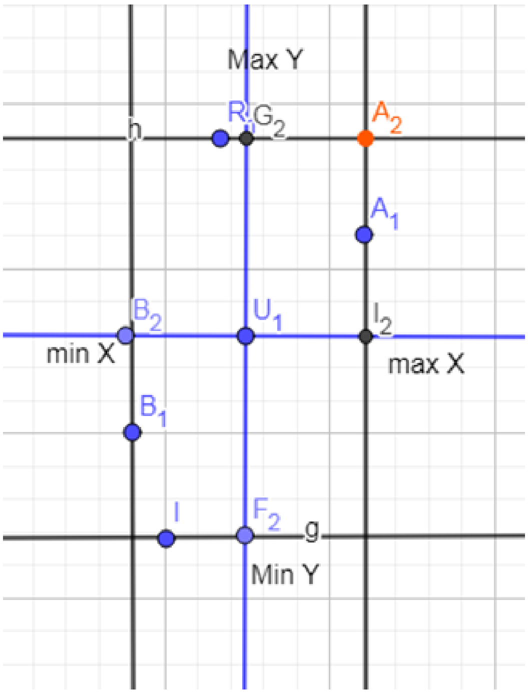

Figure 6-4: Centroid location

6.2.8 Calculation of Angle of Rotation

The ellipse will now be rotated to be more representative of the pits' coordinates obtained from the cluster analysis. The maximum Y and maximum X is used. If the major length is in the Y direction, then maximum Y will be the numerator in the equation below, else maximum X will be the numerator. To calculate the angle required for rotation, the equation needs to be employed:

$$larger\ maximum\ Y;\ tan\theta = \frac{maximum\ Y}{maximum\ X}$$

$$\boldsymbol{larger\ maximum\ X;\ \tan(90-\theta) = \frac{maximum\ X}{maximum\ Y}}$$ **Equation 6-10**

6.2.9 Focus and Focal Length Calculation

For two given points, the foci, an ellipse is the locus of points such that the sum of the distance to each focus is constant[184].

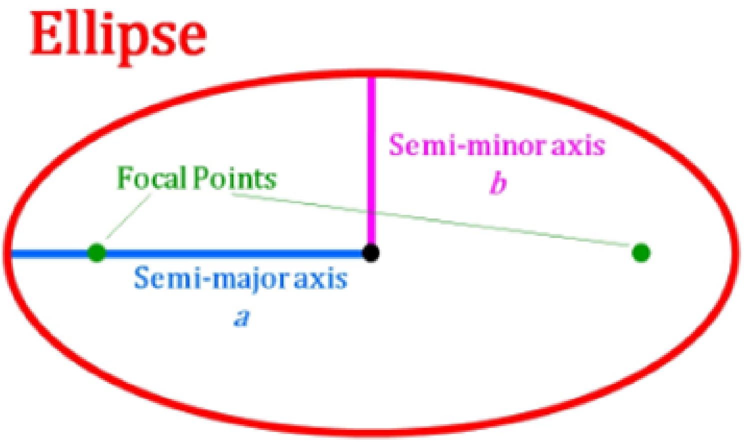

Figure 6-5: Ellipse[184]

The equation for the focal length is calculated as:

$$\boldsymbol{f = \sqrt{a^2 - b^2}}$$ **Equation 6-11**

The focal points can be calculated by using geometry:

$$focal\,point_1 = (x_{centroid} - f\cos(\theta), y_{centroid} - f sin(\theta))$$

$$focal\,point_2 = (x_{centroid} + f\cos(\theta), y_{centroid} + f sin(\theta))$$

Equation 6-12

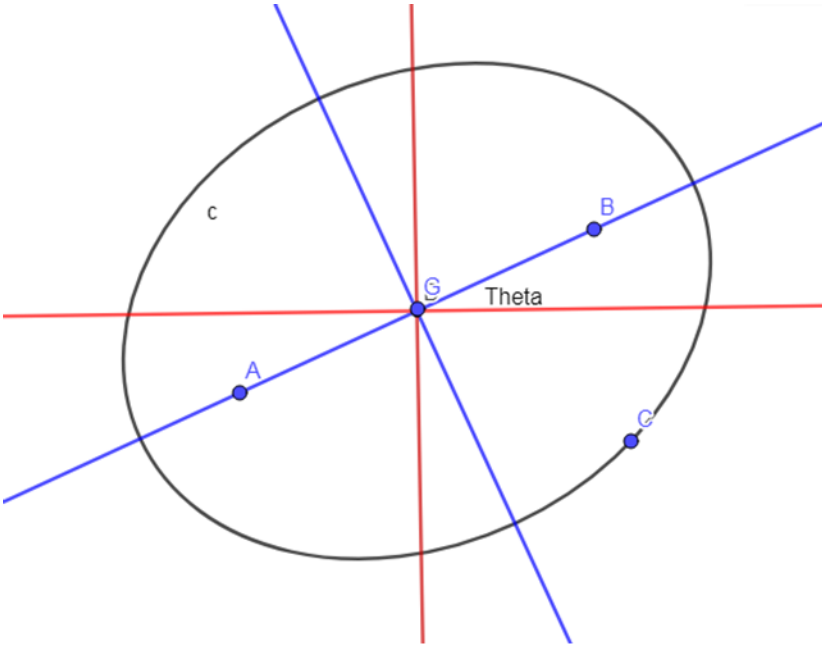

Figure 6-6: Ellipse focal points

6.2.10 Test Area

The set-up of the minor and major length coordinates all lie within a test area that is gridded. As seen, the test area is a rectangle and contains coordinate points at regular intervals. The test area can be refined by decreasing the seed size. As default, the seed size has been chosen to be 1mm.

6.2.11 2D Ellipse Formation

The definition of the focal length will be used at this point on the coordinates of the test area.

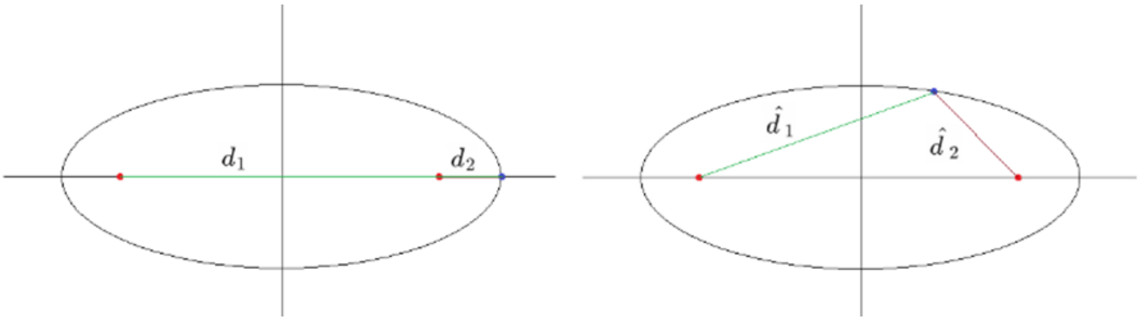

Figure 6-7: Ellipse formation

The sum of d_1 and d_2 need to be equal to twice the semi major length.

All the points in the test area will be tested with respect to this criterion. If the value of the distance of focal point 1 to the test point, which is d1, and the distance of the focal point 2 to the test point, which is d2, is less than twice the major length, then they form part of the ellipse, otherwise they are not.

This causes the formation of the ellipse.

At this point, it is good to take a step back and realise the reason behind not using the equation of the ellipse. The logic is that it directly comes down to a mathematical problem.

The major axis and minor axis are used to create the ellipse. This ellipse is also rotated meaning that it requires an adjustment based on a global coordinate system. Each ellipse derived from the pit clusters has a different angle of rotation and will require one reference coordinate system to allow them to grow over time. This is where the problem arises.

Considering the following diagram explains the problem.

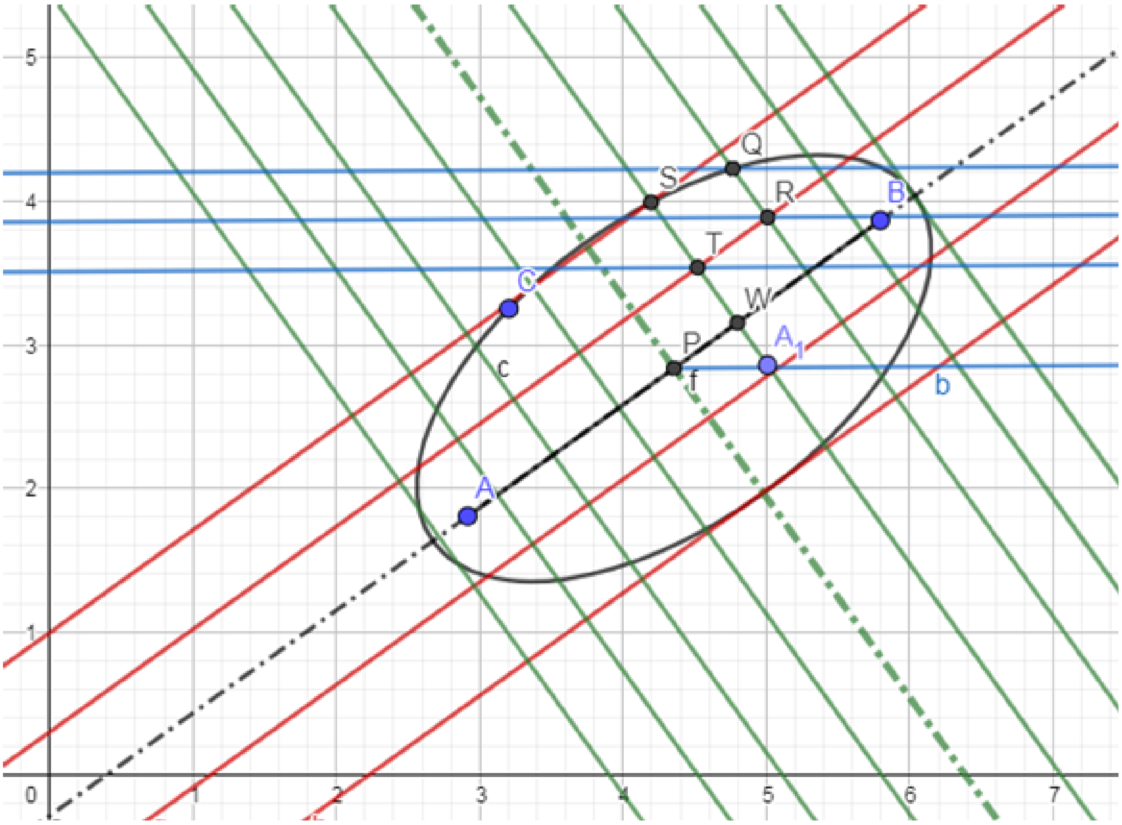

Figure 6-8: Gridding problems

A and B are the focal points.

The centre lines represent the location of the minor and major axis, respectively.

The red lines are all parallel to the major axis and the green ones to the minor axis. They constitute the grid and this will be referred to as the local grid system. The global grid system is the reference Cartesian coordinate system.

The ellipse is developed from the major and minor length and is done very similarly as the previous sections. All the local grid points are tested by rearranging the equation of the ellipse and making the y value subject of formula for an x value. If it does not exist or turn to infinity, those values are neglected as they fall outside the bounds of the ellipse.

The equation of the ellipse is:

$$\frac{x^2}{a^2} + \frac{y^2}{b^2} = 1 \qquad \textbf{Equation 6-13}$$

Rearranging it:

$$\boldsymbol{y} = \boldsymbol{b}\sqrt{\mathbf{1} - \frac{\boldsymbol{x}^2}{\boldsymbol{a}^2}} \qquad \textbf{Equation 6-14}$$

At this point, the coordinates are still adjusted to the local coordinate system and the first problem arises here. The points that form do not fall on the grid system for the y coordinate. It exists as a coordinate cloud instead. This has to be projected on a grid system to simplify the topological changes. The global grid system is used to do so. This is where the mathematical problem arises.

For the projection to happen there needs to be a trigonometrical projection of the line on the global grid. This requires the length of the triangles and an angle known as α.

From the above diagram, considering the angle θ and constructing parallel lines at T, R and Q, with respect to the global x-axis, the exterior angle from the geometry will be θ too. This can be seen clearer in the figure below.

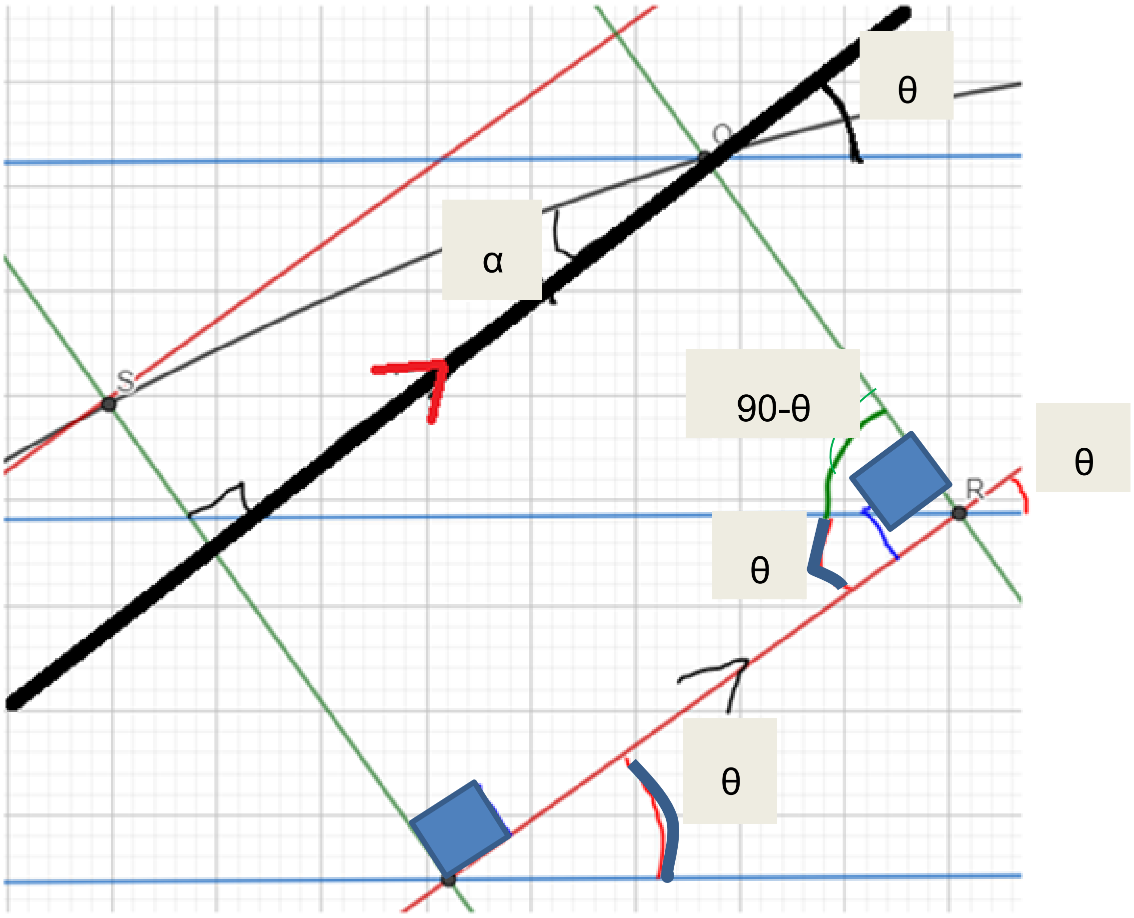

Figure 6-9: Problems with mathematical representation of ellipse

It can be shown that the value of α cannot be found and, thus, the global grid will not work.

There is the possibility to solve it with coordinate geometry but this becomes quite a tedious computational task and was ditched.

6.2.12 Semi Ellipsoid Formation

From the 2 dimensional ellipse, the semi ellipsoid can be done quite easily. It is assumed that the maximum depth of the pit is at the centre of the 2 dimensional ellipse. From this, the values of the depth can be calculated from the equation for each ellipse from the ellipsoid equation. Only the negative values will be taken to represent the semi ellipsoid.

The equation for the ellipsoid is:

$$\boldsymbol{\frac{x^2}{a^2}+\frac{y^2}{b^2}+\frac{z^2}{c^2}=1}$$ **Equation 6-15**

The associated coordinates of z for the known values of x, y, a, b and c can be calculated as:

$$\boldsymbol{z = c\sqrt{1-\frac{x^2}{a^2}-\frac{y^2}{b^2}}}$$ **Equation 6-16**

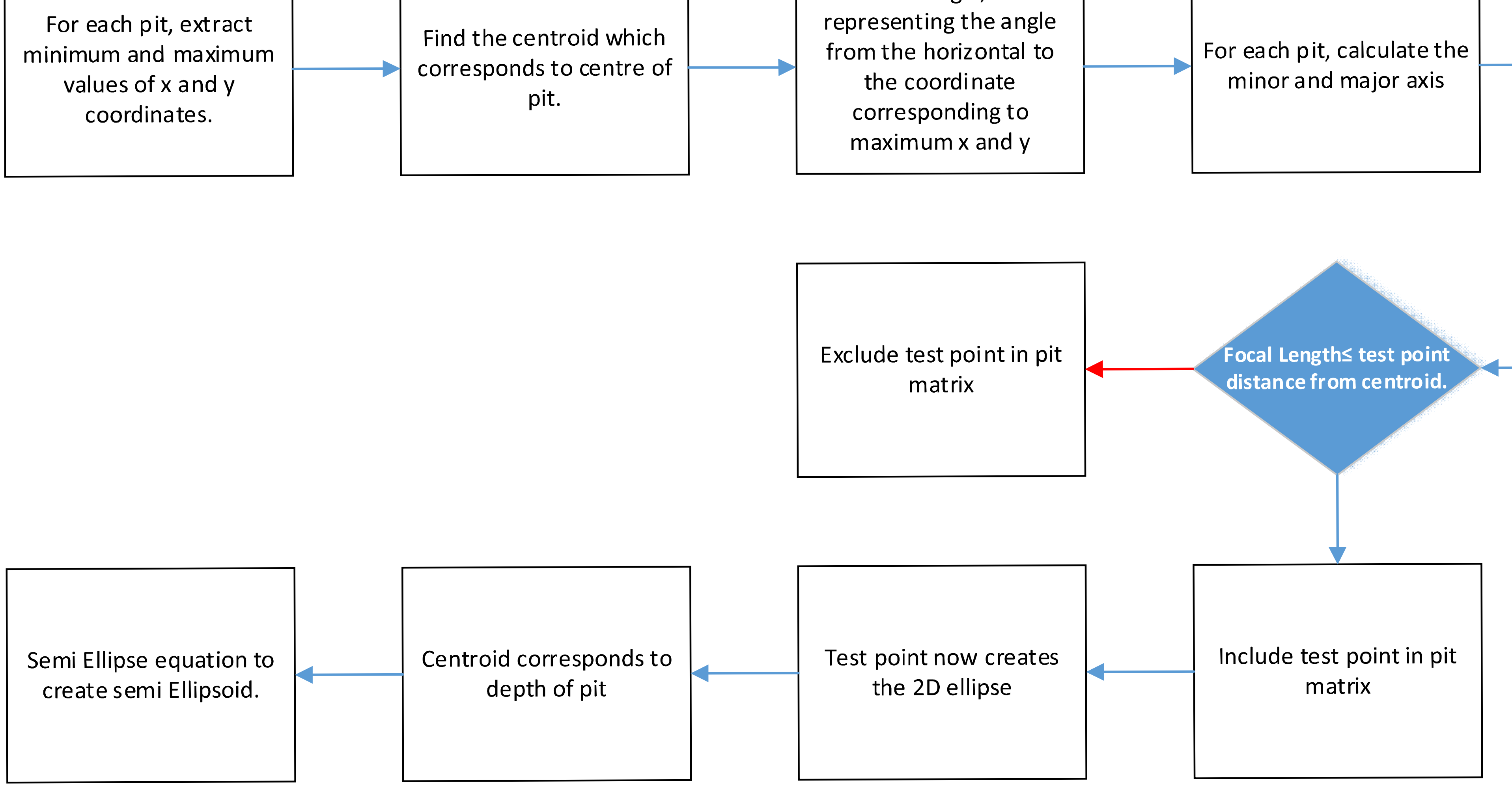
For each pit, extract minimum and maximum values of x and y coordinates.
Find the centroid which corresponds to centre of pit.
representing the angle from the horizontal to the coordinate corresponding to maximum x and y
For each pit, calculate the minor and major axis
Exclude test point in pit matrix
Focal Length≤ test point distance from centroid.
Include test point in pit matrix
Test point now creates the 2D ellipse
Centroid corresponds to depth of pit
Semi Ellipse equation to create semi Ellipsoid.

6.3 Methodology for Pit Growth and Topological Changes

The conversion of the surface pits to a semi ellipsoid requires the growth of those pits but also the growth of the number of pits with respect to time. To do so, the following steps have to be employed to complete the topological changes.

Translation of semi ellipse

Each of the semi ellipsoids are now translated across the x-y plane to the global zero coordinates. This is achieved by taking away the semi ellipse coordinates from the centroid of the pit. It causes the pit to be centred at (0,0). The reason this is done is to simplify the growth operation of the pit found at a later stage:

$$x\_centered = x_{semi-ellipse} - x_{centroid}$$

$$\boldsymbol{y\_centered} = \boldsymbol{y_{semi-ellipse}} - \boldsymbol{y_{centroid}} \qquad \textbf{Equation 6-17}$$

It should be mentioned that the pits are also rotated to an angle of –θ so that the pit is aligned to the x and y coordinates.

6.3.1 Number of Pits Growth

6.3.2 Pit Growth Models Application

The pits have to be grown in the x, y and z coordinates. They are highly dependent on the aspect ratio. The models that have been developed are all related to the pit depth. The reason for which is the literature has more information and models developed for the growth of the pits with regard to depth. It is a shame that the aspect ratio or dimensions are not measured and it is highly encouraged that this practice becomes standard practice as the planar aspect ratio is also very important for the health of the structure or component.

The pit growth models used are not linked together as the environment of each of the samples differs substantially. Therefore, they are not meant to be there on a comparison basis but rather to indicate the flexibility of the model to accommodate different models.

The aspect ratio has been taken as random and is taken to be constant throughout the whole process.

Before the length and width of the pit can be determined, it is fundamental to estimate the depth of the pit. To do so, three models have been employed that cover the deterministic, but also the machine learning, perspective of the pit growth.

A summary of each is described below:

- Uniform Growth/linear model - refer to Chapter 2.

  The equation defined by Melchers for this transition is given as a differential equation and the transitions are highly dependent on the annual mean temperature.

  $$\frac{dC_p}{dt} = 0.596e^{0.0526T}$$

  $$\int dC_p = \int 0.596e^{0.0526T}dt$$

  $$C_p = 0.596e^{0.0526T} + K$$

  K: integral constant.

  Conditions for finding K are:

  - t=t-1, provided t≠0
  - $C_p = A(t-1)^B$

  Therefore, the final equation is:

  $$C_p = 0.596e^{0.0526T} + A(t-1)^B$$

  To find the time, it requires for the transition:

  $$ta = 6.61e^{-0.088T}$$

  This will have to be compared with the actual time.

  The following flow chart shows the algorithm implemented to determine the depth of the pit using the Melchers bimodal.

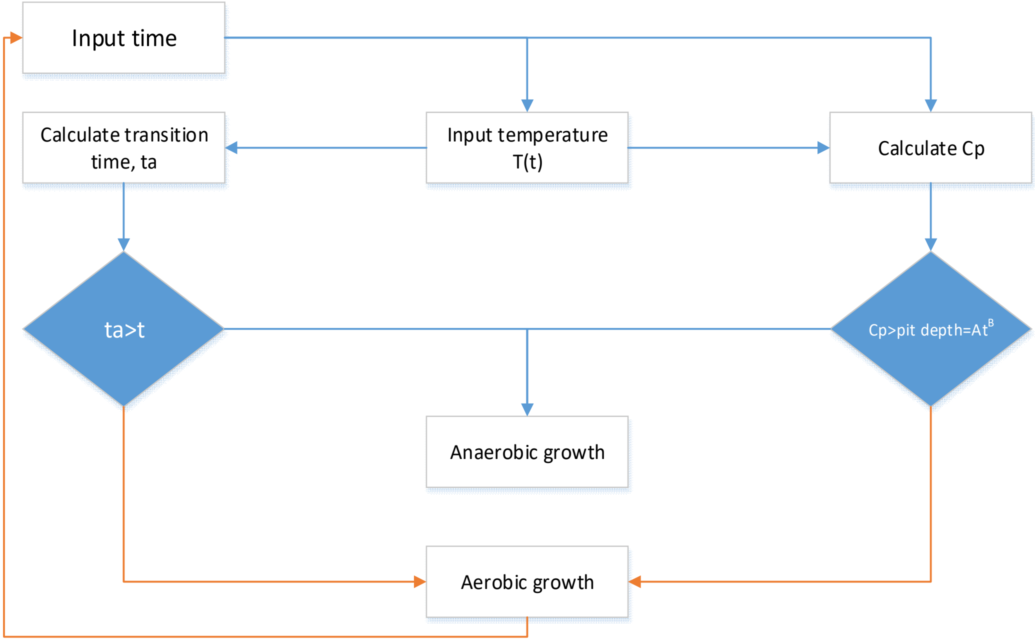

Figure 6-11: Melchers' model implementation

It has to be stated that as soon as there is anaerobic corrosion, the state of corrosion stays as such but for aerobic corrosion with each coming year, it has to be tested to observe any mechanism change.

- Artificial Neural Network (ANN) model

The methodology for the ANN for prediction of the pitting of the corrosion rate is as shown below:

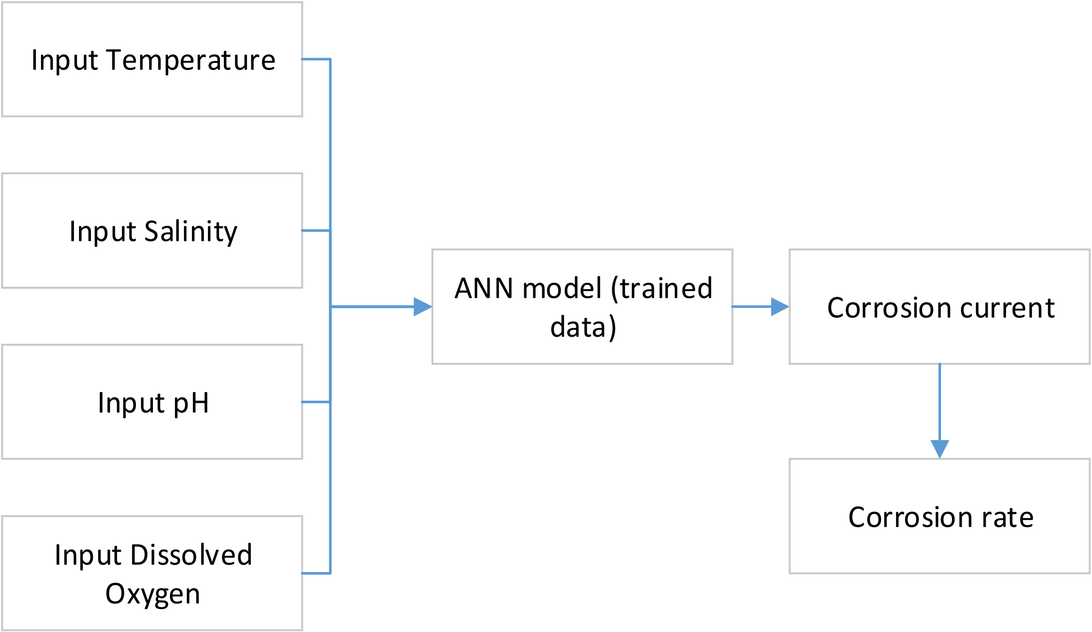

Figure 6-12: ANN model implementation

The ANN model was trained in the Matlab ANN toolbox and data used was from the paper, which gives the output as a corrosion current, based on the input shown for each year (1980-2010). This has to be converted to a corrosion rate and the following equation was used to do so:

$$CR = Icorr\ K\ EW\frac{A}{d}$$

Equation 6-18

CR	The corrosion rate. Its units are given as the unit of K
I_{corr}	The corrosion current in amperes
K	A constant that defines the units for the corrosion rate.(3272 mm/(A cm Yr)
EW	The equivalent weight in grams/equivalent
d	Density in grams/cm³
A	Area of the sample in cm²

6.3.3 Topological Evolution with Respect to Time

The topological evolution is the last section of the methodology and takes into account the growth of each of the pits but renders the corroded section as the ones that have the biggest depth. To achieve so, it is required to have a grid. The points on the grid are a representation of the actual geometry of the pits in the x-y plane.

For each of the points, all the sets of data points that represent the pit depth- Z coordinates are compared and the one with the smallest value is used to represent the pit depth at this point.

6.4 Results and Discussion

From the simulations explained in the methodology, the various results have been obtained and are shown in this section.

The first aspect of the study is to create a plate. The x and y coordinates' limits have been randomly chosen to lie between 400 and 90mm respectively and 100 data points have chosen to do so. The z coordinates are then associated to coordinates to create the coordinate system. The value of the delta z, which represents a change in depth as a result of corrosion, is basically the value z defined earlier on. The z values chosen were randomly chosen between 0.5 and 2mm, to represent the corroded plate.

The plots shown are as shown:

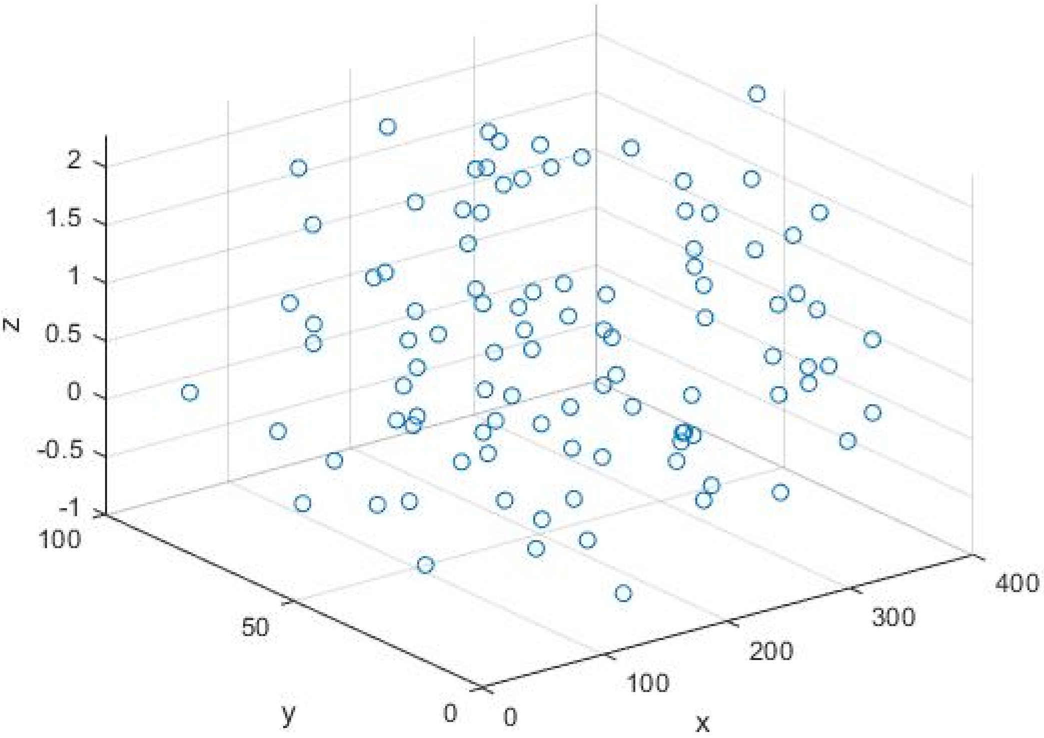

Figure 6-13: Points distribution

From this point, the mean can be calculated that represents the average loss as a result of corrosion.

In this case, it was computed to be 0.7895 mm.

At this point, a grid needs to be formed to capture the data point. The z values in between the x and y grid were interpolated using a linear interpolation regression between the points. It is worthy to note, the finer the mesh, the more accurate the rendering of the surface will be but this has a considerable downside, as the immense computational power that will have to be dedicated to the task is quite impressive. Changing the size from 1mm mesh to 0.25 mm mesh causes the simulation to take at least four hours per model.

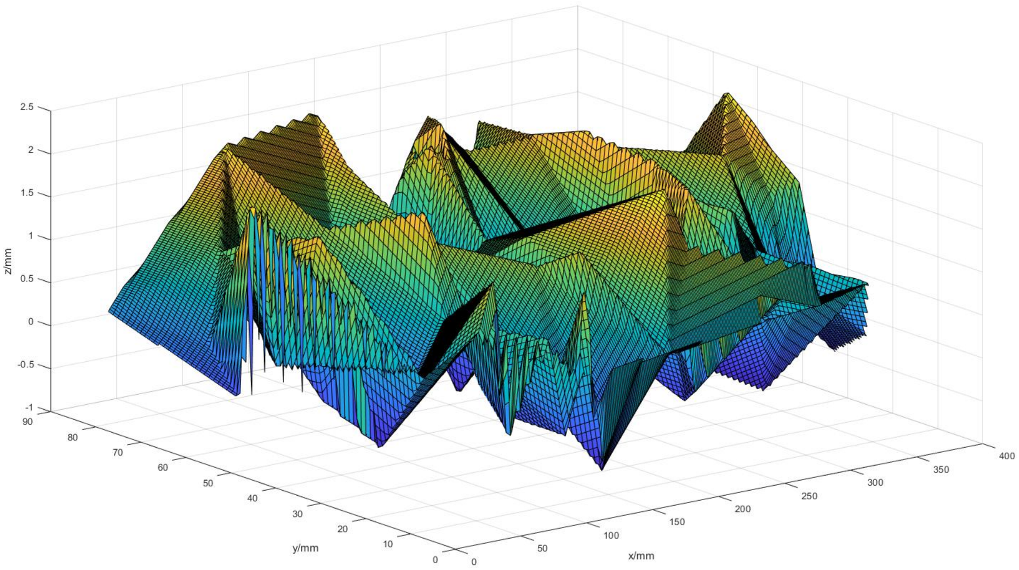

Figure 6-14: Grid

A top view is also shown to better represent the interested regions that define the pits. The topology at this point is representing a very jagged surface, which is due to the linear interpolation reasoning applied earlier. Due to the lack of information, the uniform random distribution methods have been used for creating such data. The reality is that those methods have been used in conjunction with optical methods. They will be capturing those data points and the data represented at this point will be more reflective of the situation.

This method is being used as proof of concept, or to put it in a more direct context ‘to think out loud’, to show that the topological changes can be simulated and demonstrated. The first model derived from the data, either optical or simulated randomly (like this case), is crucial in the determination of the topological changes. It is very likely that those first pits due to their time advantage will be dominating in growth and be the recipient of other inner pits growing within them or even coalescing. Emphasis needs to be given to its fullest on that aspect for proper prediction.

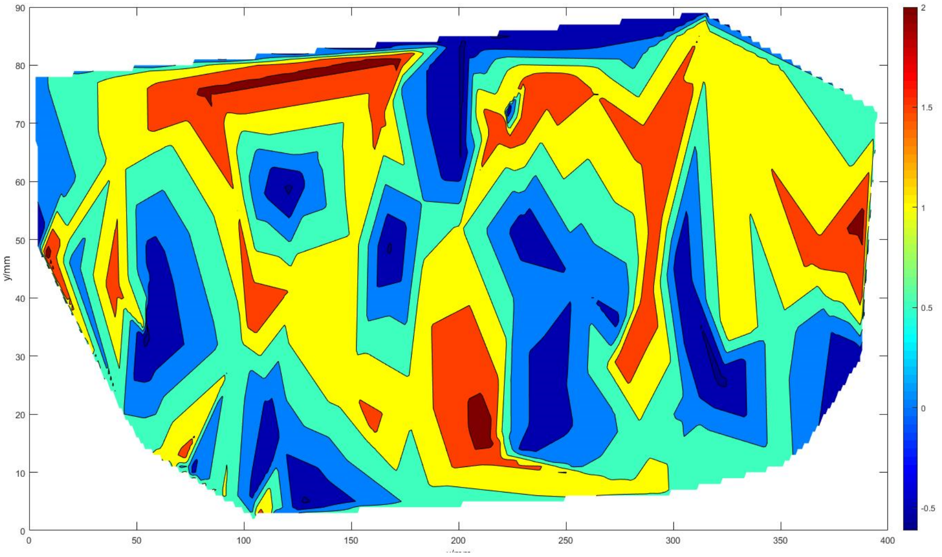

Figure 6-15: Top view of grid

The blue regions represent the pits and will have to be captured by the cluster analysis. The other regions can be removed from the analysis and to do so the definition of the pit is important at 30% of the average corrosion depth. For the sake of simplicity; this value can be defined as the K value. This K value is not set in stone but has to be varied to capture the lower peaks as much as possible. This will require some variations or, when needs call, some optimisation to define this value. It changes the whole definition of a pit and this method can provide this new interpretation.

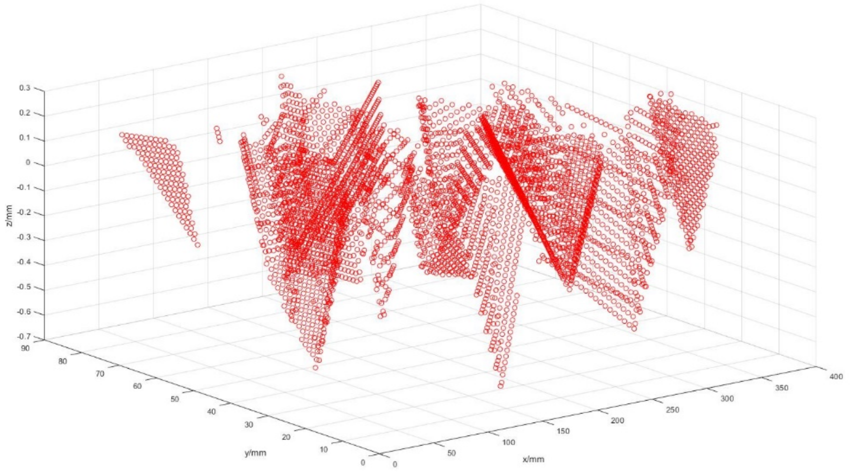

Figure 6-16: Pits detection

The cut off has been applied and to find if the local minimums have been captured properly, the following diagram proves to be the real assessor. It can be observed that 10 red regions have been formed and is an indicator of the number of clusters that will require extraction.

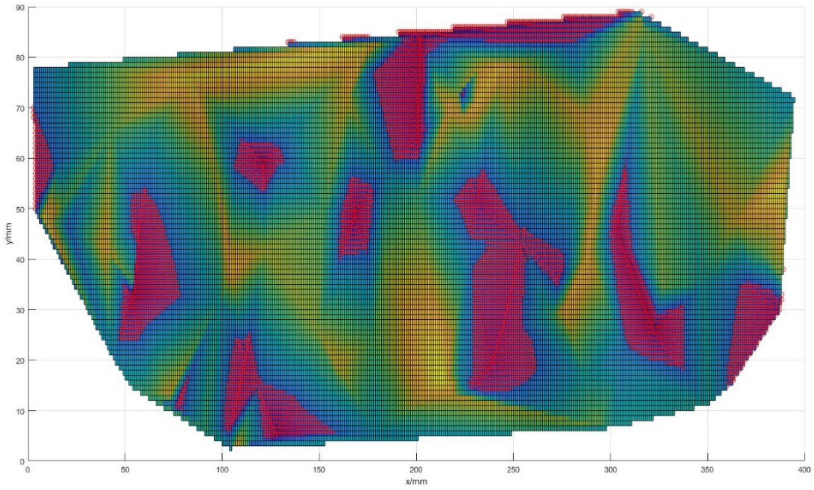

Figure 6-17: Pits detection on grid

As shown, the red regions have nearly fully covered and can, thus, be isolated for the extraction of pit information.

The cluster analysis isolated each of the clusters and in total at the initial point, 10 clusters were formed.

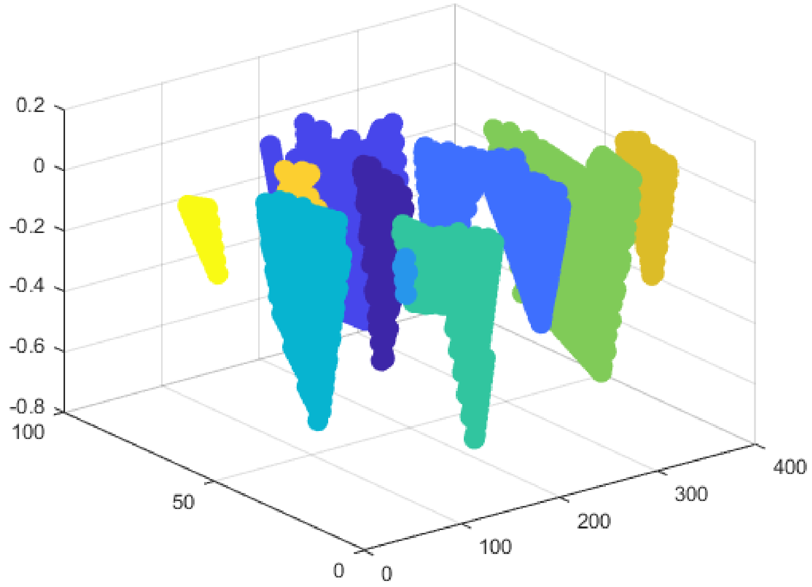

Figure 6-18: Pit isolation

Once the clusters are obtained, they need to be transformed into ellipses.

The following diagram shows the formation of the ellipses from their respective coordinates and also the matrix manipulation including the rotation and translation.

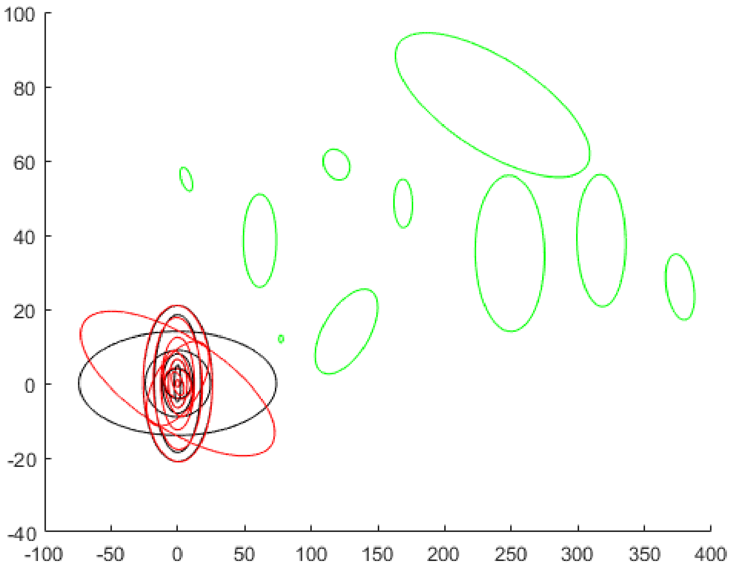

Figure 6-19: Pit transformation

At this point only the ellipse is formed and needs to be transformed into an ellipsoid.

The centroid of each ellipse is associated to the depth coordinates from which the other coordinates are easily calculated from.

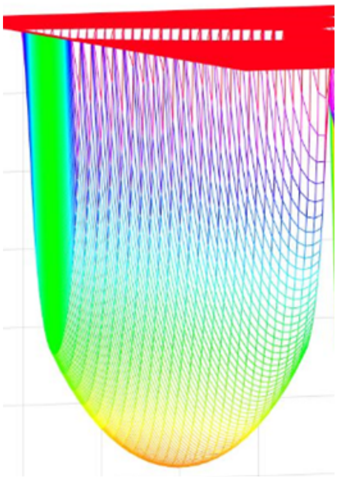

Figure 6-20: Isolation of pits

There is a problem related to the ellipsoid and this is due to the size of the seeds. Sometimes the edges are not captured and, therefore, the geometry is not fully constructed.

The level of refinement will put considerable stress on the computational capabilities and also the time taken to render the simulation. The mesh size in this case has been chosen to be 1mm in size on the x and y coordinates' grid system.

6.4.1 Uniform Growth Model

The uniform growth model is used very often to characterise the pit depth. In this case, this has been applied based on two aspects, namely the ORE Catapult report and the DNV GL report.

The aspect ratio has been attributed to a value of 0.025 to 10 based on the Cerit paper[235]. They are randomly attributed and once the pits are created, the three aspect ratios are kept constant for the remaining 25 years. In reality, this might not be the case and based on the lack of information, this is one the major assumption of this study. Feeding in a change of aspect ratio with respect to time in those three orientations can or will ensure an improvement in the model and a more realistic interpretation of the topological changes incurred. The same logic has been applied for the other two models.

The growth rates in the x and y direction has been computed from the aspect ratio previously defined. The idea is to know the depth and then the rest is rather trivial.

The first year will be exactly the same and so will the number of pits for the remaining years. The difference lies in the new added pits that are formed as a matter of uniform random distribution. The ellipsoid will be very different and so will be the depth.

The point that needs to shine out from this comparison study is that the DNV GL value is used as a matter of design of offshore wind structures. This is the bedrock to assess the corrosion allowance for designing the OWT. According to mathematics, for a structure to be in service for an estimated 25 years, the corrosion allowance for that period of time will be 5mm. The report from ORE Catapult tells a different story and is based on inspector reports. The corrosion reported was up to 2.5mm/year.

The difference is substantial and can have serious effects on the structure if no remedial actions are observed.

Each year, the number of pits do increase and get increased by 1Xtime^2; where the time is in years.

The results from the simulation for a 0.2mm/year and 2.5mm/year corrosion rate can be shown below[44], [134]:

<u>ORE Catapult</u>

The first year of the analysis will display the same results but then there will be a change, which will be quite substantial especially in terms of the topological changes as a result of the losses.

The aspect ratio is kept as a constant over the whole 25 years of the simulation, having similar x and y direction.

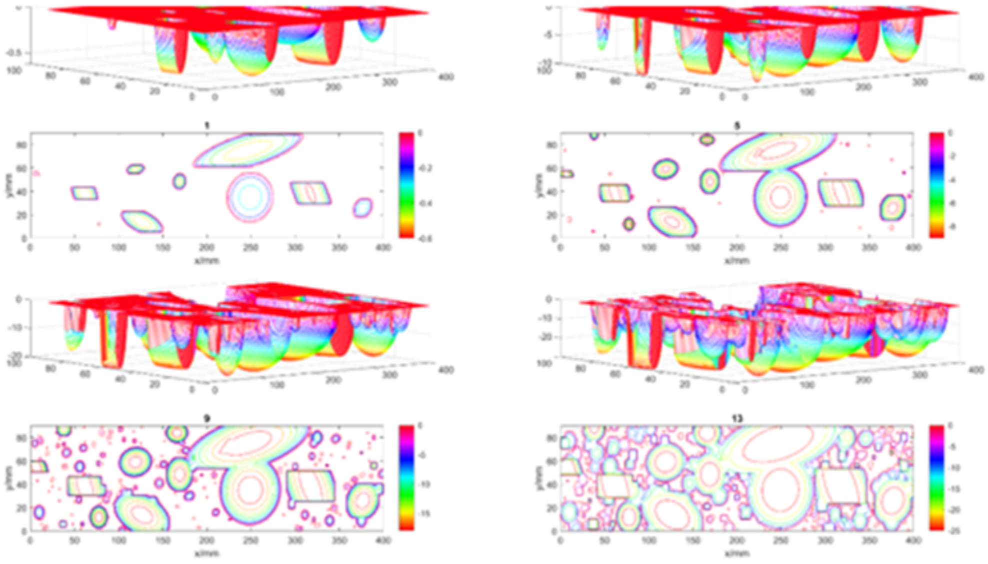

Figure 6-21 : evolution of pits

For the first 15 years, there is an increase in the number of pits governed by the quadratic expression. It is expected that the existing pits from year 1 grow more than the rest both in the x-y plane but also in terms of depth. At year 9, the pit coalescence can be observed and the dominating larger pit has a considerable impact. Upon inspection, another very important aspect is the formation of pits within a pit.

Year 13 shows a significant increase in pits and the topology is very jagged. There is still a smaller region of red representing the base and purple representing the base metal. This means that there is the potential of the removal of a layer as a result of pitting corrosion that is giving rise to a form of non-uniform corrosion.

The non-uniform corrosion can be observed from year 17 where there seems to be the beginning of a smoothing process.

This difference can be observed from year 17 to year 25, where it seems to be less jagged and where the pits are dominated by some of the larger pits and the smaller ones seem insignificant at this point. This means that there is the transition from pitting corrosion to non-uniform corrosion.

This model is far from being accurate but is the closest in terms of information provided by offshore wind turbines. The annual average corrosion rate does not take into account the effects of Microbial Induced Corrosion in the long run.

This according to Melchers' model will cause an increase in the corrosion rate and even more damage in terms of pitting corrosion.

Looking at the maximum corrosion, depth is indicative of more than 50mm over the period of 25 years.

Considering the design corrosion tolerance of 0.2mm/year from the DNV GL J101, this is a major deviation and an indication of the corrosion underestimation for the design. At such a rate of corrosion including the stress effects as a result of the pits, it is clear that the structural integrity of the offshore corrosion wind turbines will be jeopardised and failure will be a reality. Action calls for prevention, such as marine coatings or fixing of sacrificial anodes, and will be required to safeguard the structure from potential major failures as a result of corrosion.

The average corrosion depth with respect to time is given below with the standard deviation shown:

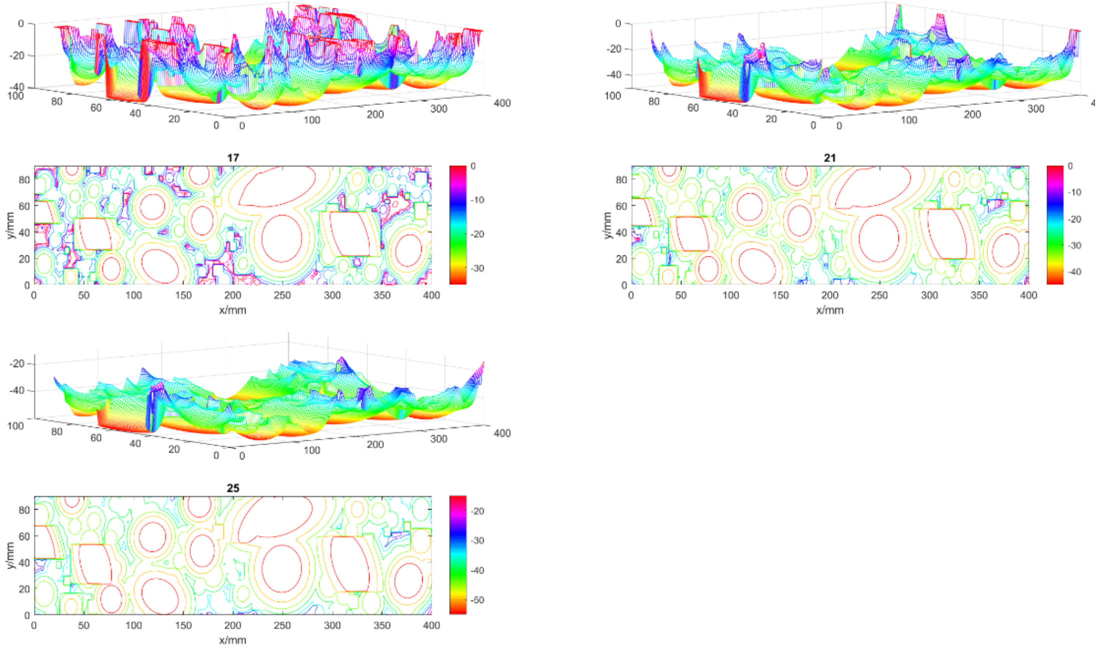

Figure 6-22: 17 to 25 years plate evolution

DNV GL results based on their corrosion rate

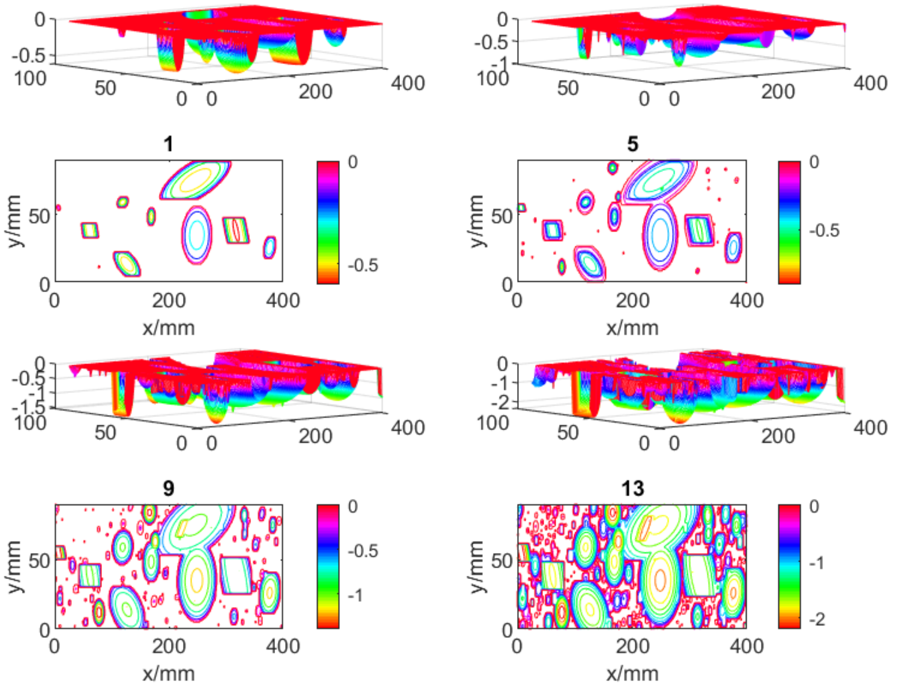

Figure 6-23: corrosion of plates from 1 to 13 variations

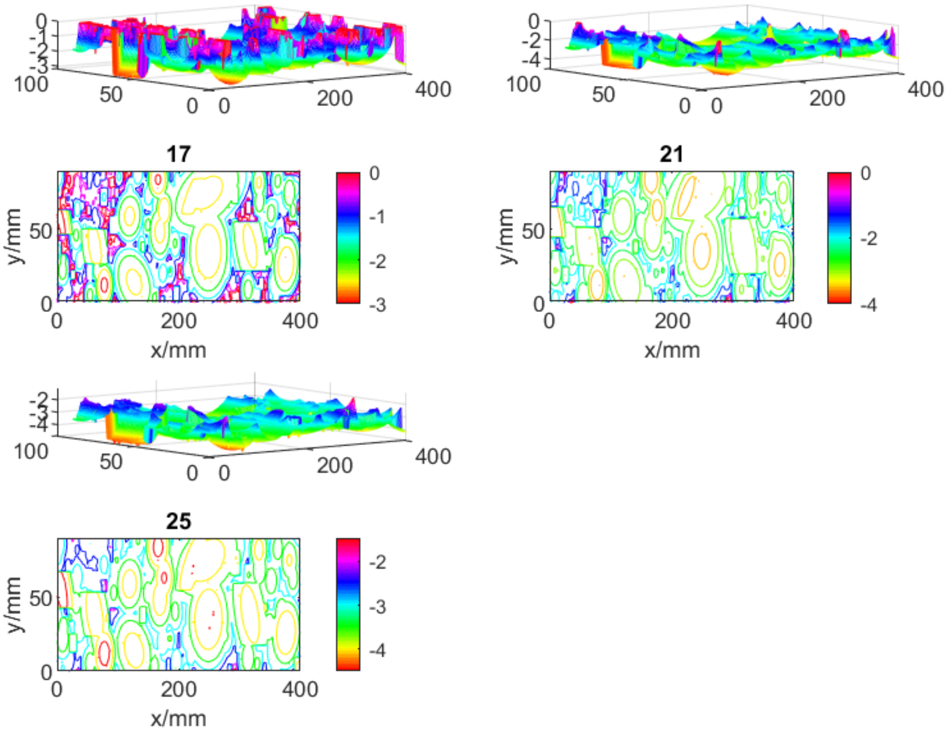

Figure 6-24: Pits evolution DNV GL J101

The DNV GL corrosion rate is purely a comparison between the two models to show the variations between the reality observed from inspections and the design criteria.

The DNV GL obviously is way below the inspection results by a factor of nearly 10.

6.4.2 Melchers' Results

The Melchers growth rate has to be computed from each of the pits as they show a time and temperature dependency. This model takes into account the transitional change occurring in marine corrosion from aerobic corrosion to anaerobic corrosion.

This said though, it is not reflective of the inner corrosion of the monopiles but can give an interesting estimation of the topology of the free corrosion that can happen in terms of the outer monopile corrosion loss.

The Melchers model is sensitive to the temperature and the temperature of the North Sea had to be used for the period of 25 years. The temperature in the equation represents the mean annual temperature and the data registered is measured on a quarterly basis. The data source taken is from the P4 data sets[7].

The choice of this data set is that it is more complete than others.

Figure 6-25: Buoys used for data collection on ferry routes [185]

---

[7] Data Source: https://www.cefas.co.uk/cefas-data-hub/sea-temperature-and-salinity-trends/presentation-of-results/ferry-route-data/

There were also gaps in the data as a result of missing data and they were found using a moving average.

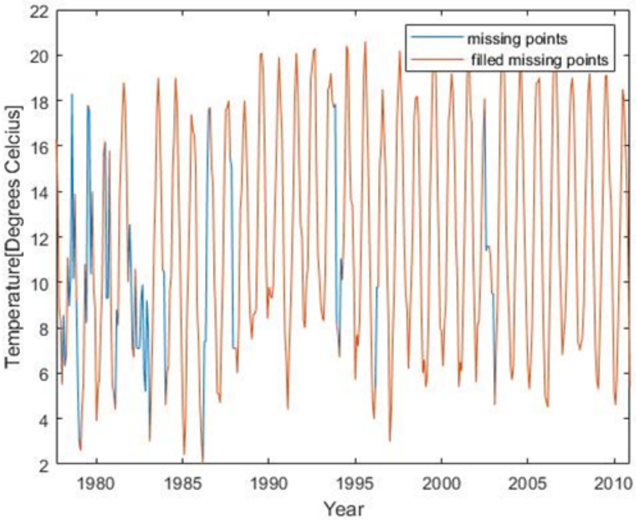

Figure 6-26: Missing data fill

Therefore, the mean for the four seasons for each year was computed and the result is as shown below:

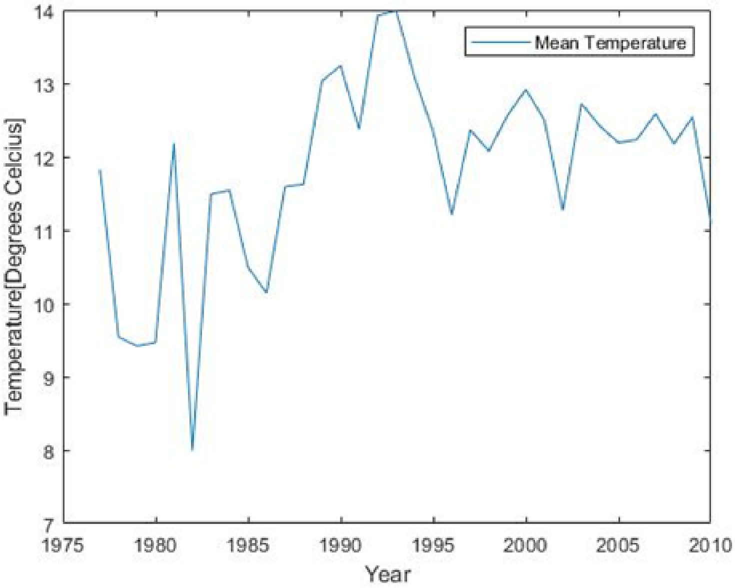

Figure 6-27: Annual average temperature

The temperature chosen was from 1985 to 2010 and applied to the algorithm for the pit growth.

This model is slightly more challenging than the pitting model as for each pit an interrogation is required if there has been an aerobic to anaerobic transition for the pit mechanism.

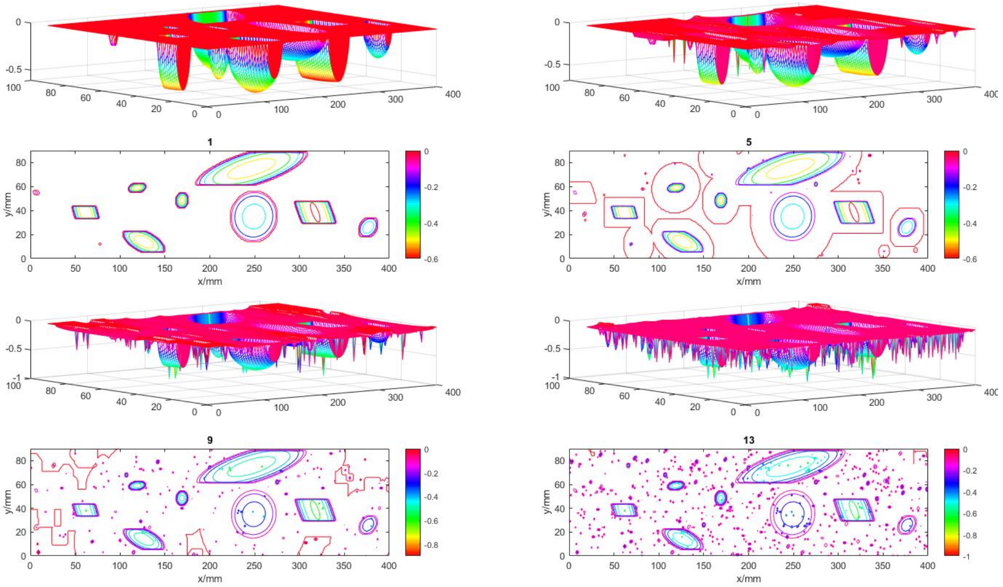

Figure 6-28: Melchers' model pit evolution

The Melchers model results show a much lower corrosion loss where after 25 years, the corrosion depth goes down to 1.4mm.

It is to be noted that the Melchers model is not reflective of the environment inside a monopile and has been used in this light for an indication of free corrosion surfaces.

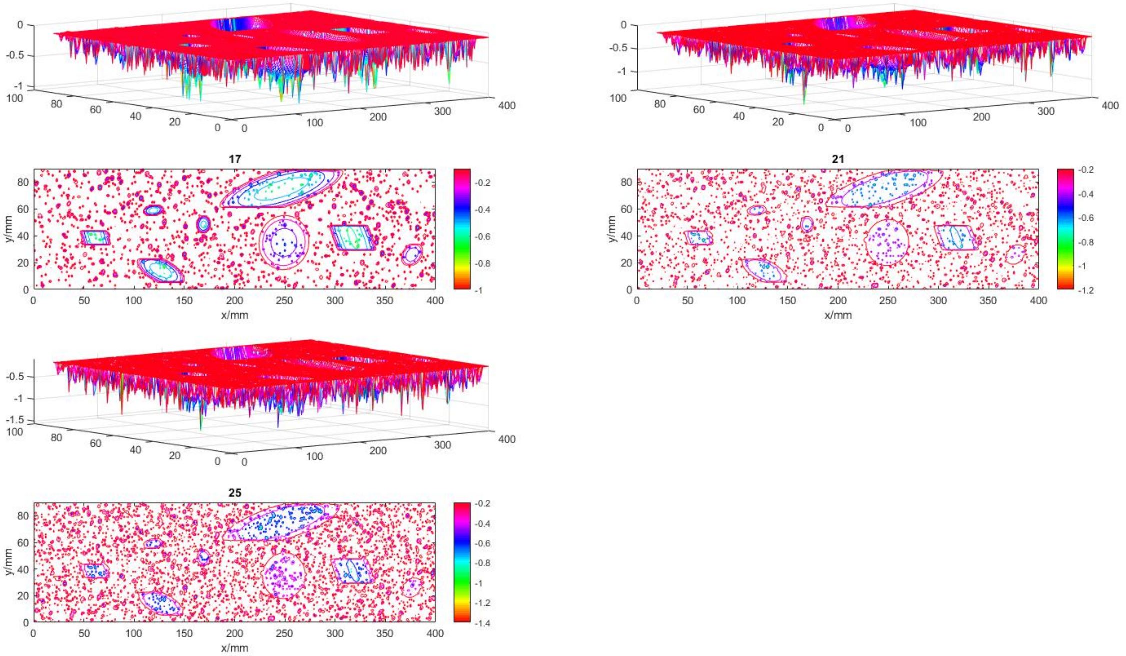

Figure 6-29: Melchers' model pit evolution from 17 to 25 years

After 25 years, there are important quantity of needle like pits rather than the broader pits found in the uniform corrosion models.

Nevertheless, the aspect ratio is from the same uniform distribution from the uniform distribution model.

6.4.3 Artificial Neural Network

The ANN uses data from the South China Sea and the results are given with respect to the corrosion current, which can give the corrosion rate on a yearly basis.

The data has then been trained using 10 neurons and the overall fit of 70%.

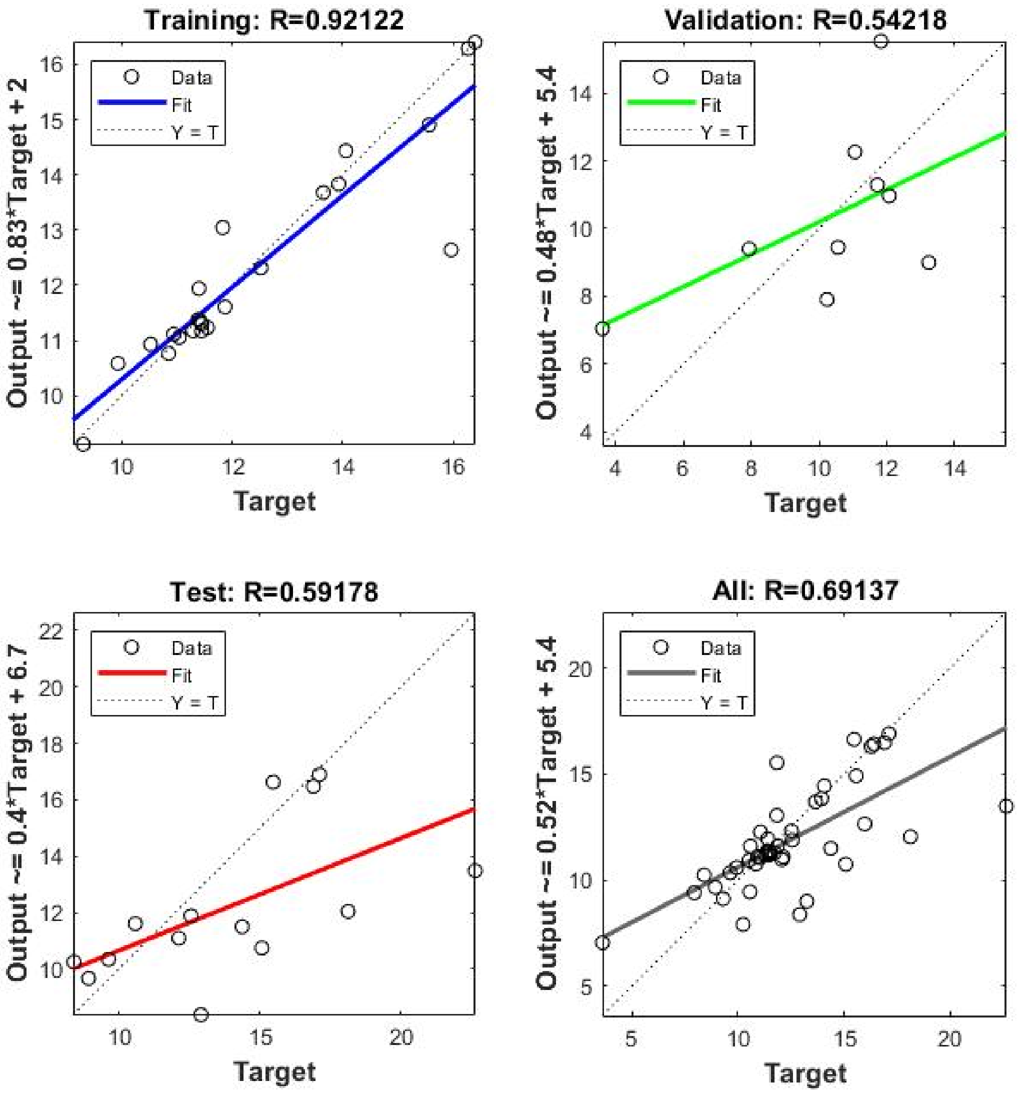

Figure 6-30: Training data regression

The North Sea temperature, salinity, DO and pH data were applied once the data are trained to give an output current, which is then used to calculate the corrosion rate[185].

The data for the salinity and temperature were obtained from the same source as the Melchers model with salinity missing points being filled using a 10 moving point average. The average for each year was then calculated as shown in the graph below.

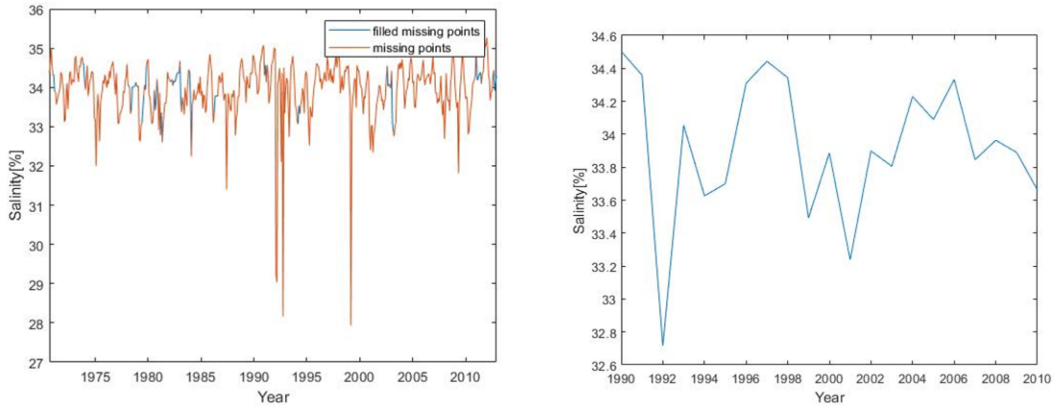

Figure 6-31: Salinity missing points

The DO[8] and pH[9] data were found for the North Sea but the span lasted only for 20 years.

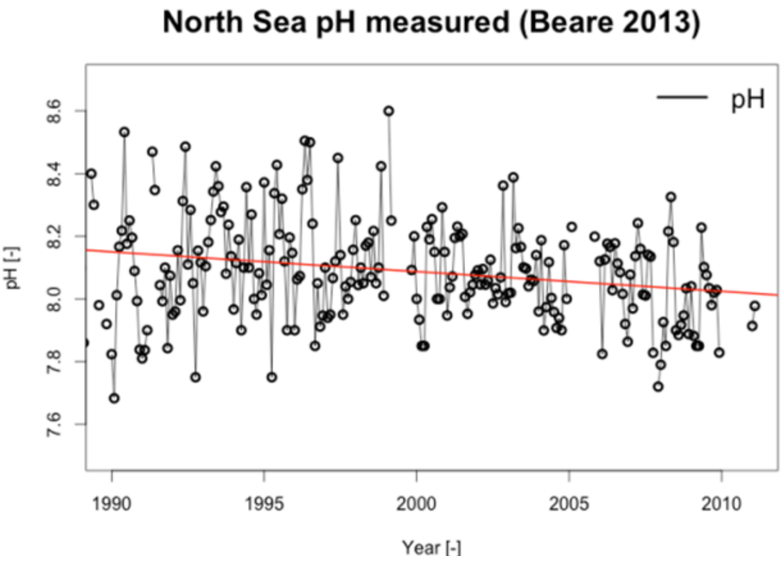

Figure 6-32: pH change over the years[186]

The dissolved oxygen graph with respect to time is shown below:

---

[8] Source: https://oap.ospar.org/en/ospar-assessments/intermediate-assessment-2017/pressures-human-activities/eutrophication/dissolved-oxygen/

[9] Source: https://core.ac.uk/download/pdf/38632499.pdf

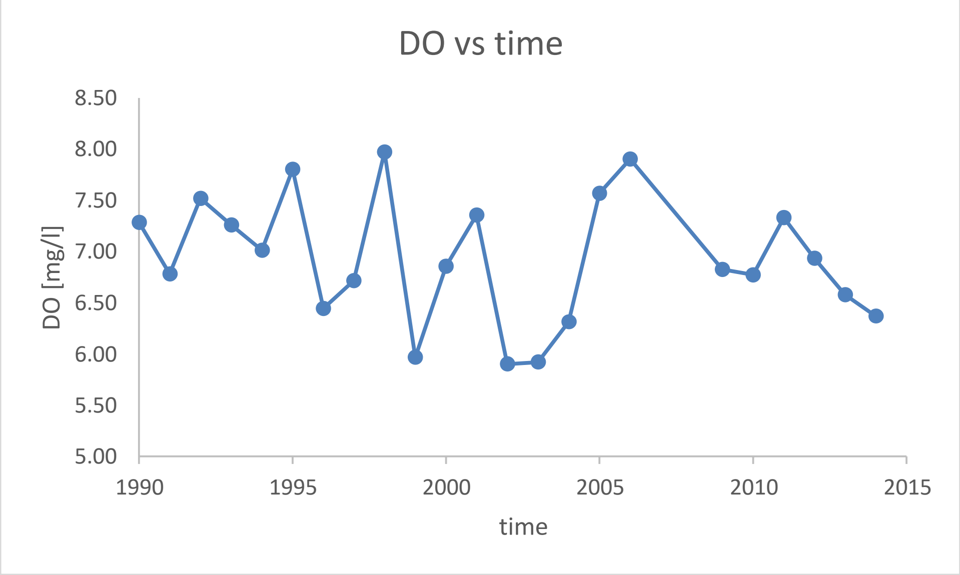

Figure 6-33: DO with respect to time[186]

Using those yearly datasets, the outputs for the depth were calculated and it has to be said that they were rather small compared to the other models employed for the simulation.

The graph below shows the maximum depth from the surface with respect to time and also the average corrosion depth for the plates.

Finally, using the same concept of aspect ratio as the previous depth models, the following topologies were obtained. In this case, as with the Melchers model, the x-y aspect ratio is defined as a result of the depth of the pit and, therefore, tends to be very sharp.

It can be seen, though, that the effect of pitting corrosion generates a surface that is more sharp and that there is no removal of layers as observed in the unform corrosion model, an observation that has been seen in the marine field experiment.

The ANN is a powerful tool but in this case it proves to be rather unrealistic in determining the corrosion rates. It would be advisable to have more training data for a longer period to establish the level of corrosions and also the type of corrosion. Also in this case, the data captured is from the South China Sea, which has totally different characteristics in terms of chemical/biological contents to the ones in the North Sea.

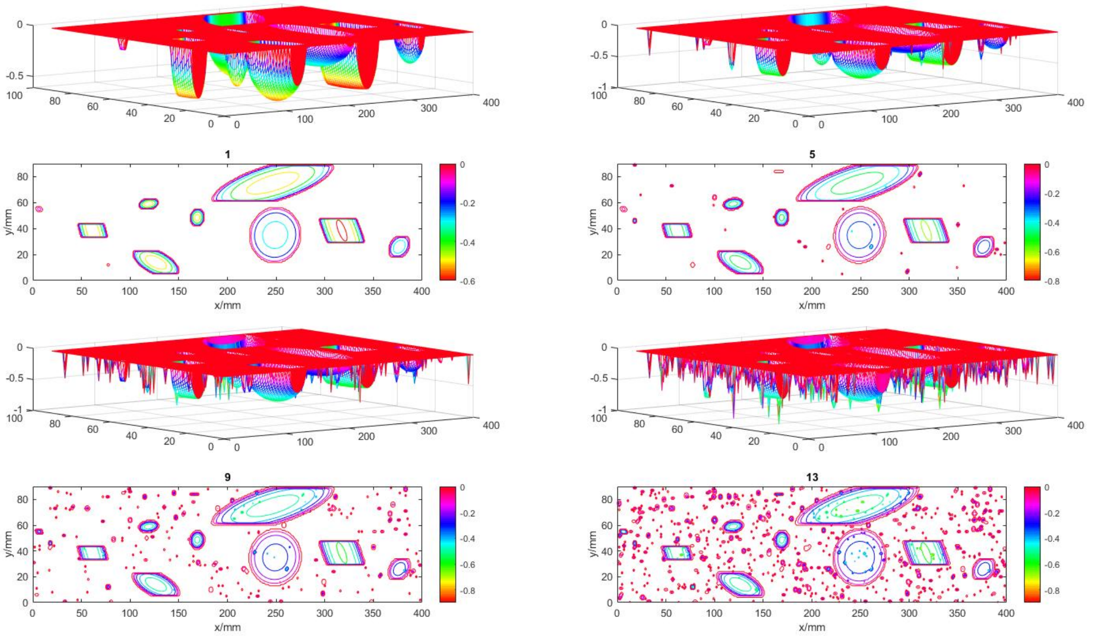

Figure 6-34: ANN results for topological changes

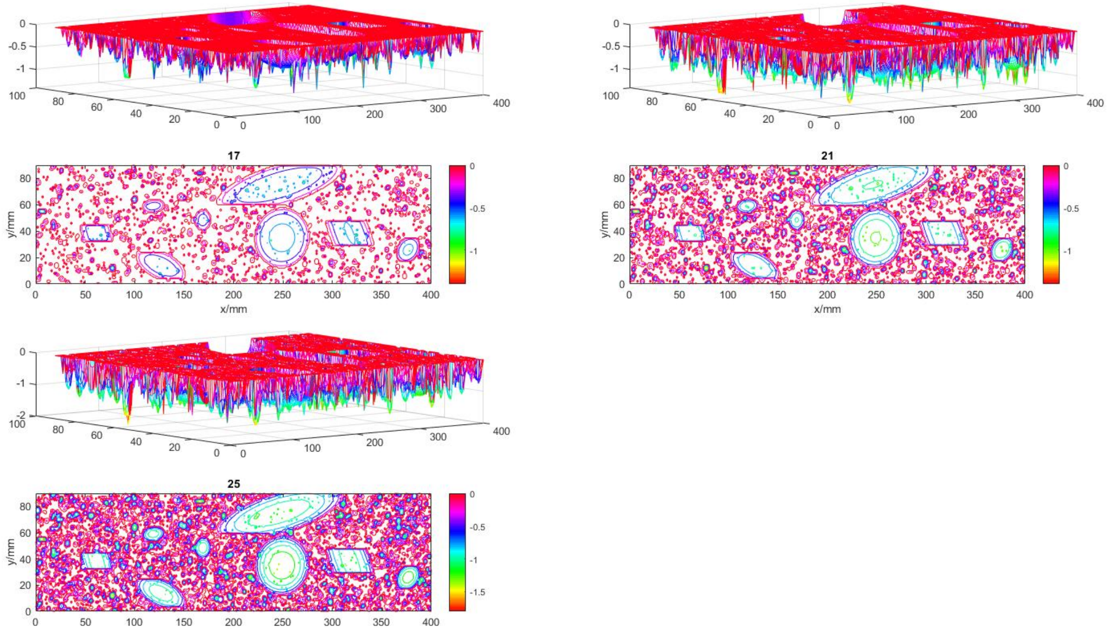

Figure 6-35: Topological changes for ANN

In this case, the maximum depth goes no more than 1.75mm for a 25 year period and as seen from the top view diagram, most of the region falls in the region of below 0.5mm with barely any patches above 0.5mm.

6.5 Validation

The results were validated using the plates from the coupons discussed in Chapter 5 in the laser scanning section. The growth rate in the x and y direction was taken as the largest number for the pits. The Melchers model and the ANN were not validated for the simple and good reason that the year of insertion of the coupons was not known and, therefore, the environmental characteristics are unknowns, which would have been required to be fed into the algorithm. Since the Melchers model is highly dependent on the temperature and the ANN for the pH, temperature, salinity and dissolved oxygen, without knowledge of the year of deployment, validation will be entirely futile.

The results of the validation proved to show strong correlation in terms of the volumetric loss as a result of the pit evolutions.

The volume loss was assumed to be semi ellipsoidal and the following equation was used:

$$\boldsymbol{V = \frac{\pi abc}{2}}$$ **Equation 6-19**

Where a and b are the half major and minor length respectively, c is the pit depth which was extracted from section 5.9-laser scanning from the experiment and extracted from the analysis

The following results are as shown below:

Table 6-1: Errors for validation

Volume[mm^3]			
year	simulation	experimental	% error
1	29.66	29.3087	-0.00351
2	128.8	122.4631	-0.49337
3	604.38	674.3018	0.699218

The comparison in a more graphical way is as shown below:

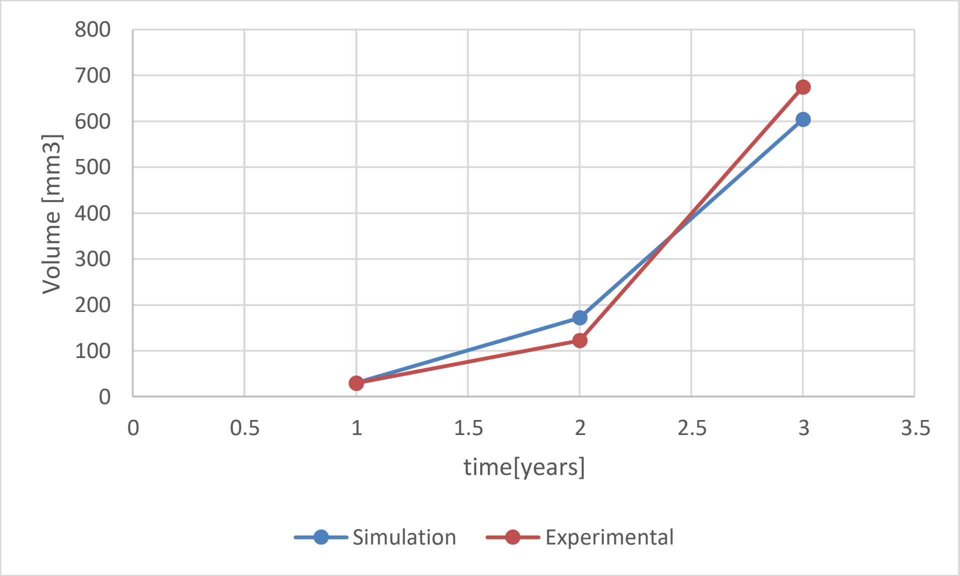

Figure 6-36: Volumetric differences

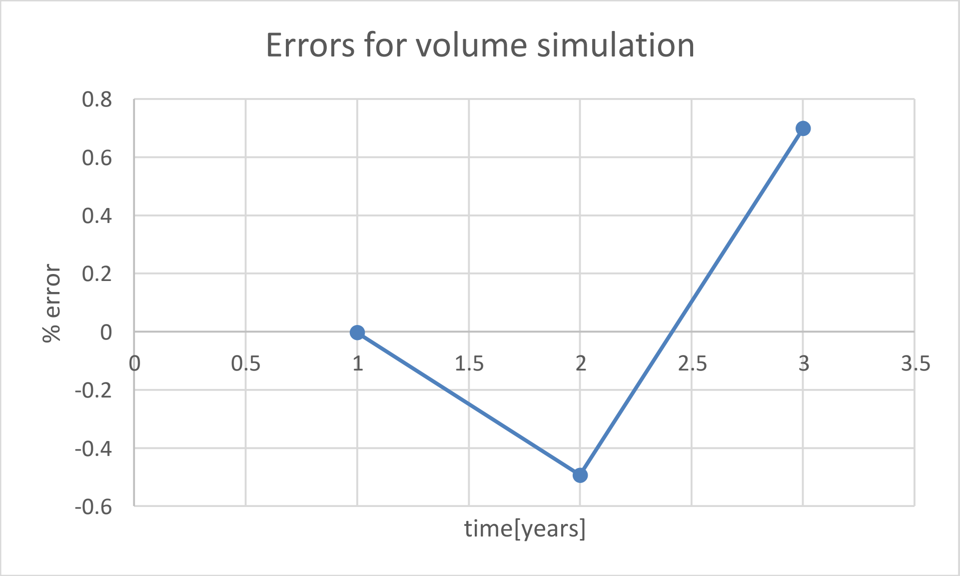

Figure 6-37: Errors from models as a percentage

6.6 Summary

- Mathematical transformation of pits into a semi-ellipsoid to ensure mathematical elegance whilst growing them.
- Validation against uniform corrosion model that proved to be accurate.

7 Conclusion

In chapter 1, an introduction to the offshore wind industry has been emphasized globally and locally. Despite its growth though, the OPEX takes a major share of the budget contributing significantly in LCOE. In addition to that, a considerable number of accidents have been revealed helping to tarnish the image of a rather new industry. To circumvent those two effects, SHM is being explored as a viable option to change the inspection regime into a more efficient one. The project delves in the strain gauge sensors which are popular in the current and previous installations of offshore wind farms and turbines. It has been clear from the onset that the data used have not been effectively used and that an interpolation technique has to be used to improve the current practice in a data drive approach of SHM using data fusion. Chapter 2 looks at the technical aspects of fatigue and pitting corrosion both being flagged and identifies as major problems. The fatigue explores the usage of the input data being in the form of bending strain data as input and looks at the various theories required for its transformation to a conclusive damage model in that case Miner’s Linear damage. The corrosion problem in the offshore wind industry took the engineers and designers by surprised that assumed that monopiles based structures would be watertight. Unfortunately numerous leakages have been observed during inspection which caused corrosion as a result. Different corrosion mechanisms were observed including pitting corrosion which is known to contribute to major damage for structures. The chapter explores the pitting model and the various models from pit initiation, pit propagation, pit growth, pit to crack transition and crack propagation. Chapter 3 explores the interpolation techniques both circumferentially and longitudinally. The circumferential interpolation uses the strain gauges at the same height and requires a minimum of the strain gauge values at the same time stamps. The longitudinal one uses linear interpolation where the monopile is assumed to be a cantilever. The welds employed are all assumed to have the same Young’s modulus as steel being 200GPa. In this study, the heat affected zone is not taken into consideration. Different SN curves for welds have been employed to make the structure as realistic as possible to give a damage map across the whole monopile based on the strain data history of a set of strain gauges placed 1m from the root of the monopile.

Using the interpolation principle, the stress was calculated at the pits from the strain gauges using appropriate SCF. It was then tested using the Kondo hypothesis if there is a pit to crack transition effect based on the crack growth and pit growth rate respectively in chapter 4. The Miner's damage was also calculated to determine the life of the structure.

From chapter 4, it came apparent that the pit distribution both in number and dimensions required some characterisation. A field experiment was set up that involved 20 coupons at sea to profile the corrosion and explained in chapter 5. After 111 days, 5 of the coupons were recovered and cleaned whilst the others were lost at sea. A mass loss analysis was done and a corrosion rate as high as 0.8mm/year was observed. Using image analysis, the pits properties were found for the samples and statistical fits were assigned to them. Laser scanning was also employed but on different samples, those inside a monopile. An algorithm was developed that automatically cleans and corrects the data captured by the laser scanner. Using the data, the pit depth was determined.

Chapter 6 looked at the evolution of the pits with respect to time and was calibrated with the data from chapter 4. Three growth models were used; the linear model, the Melcher's model and the ANN. Quite a host of techniques were employed such as cluster analysis to isolate the pits and a threshold to characterise the pits. The topology was evolved for a period of 25 years.

7.1 Future Work

Referring to Chapter 3, the model can be improved by using more connections and also trying to apply it to a more complex structure, for example, jacket structures.

The development of a damage sensor and calibration check for the sensors are fundamental, not to say crucial, and need to be part and parcel of the structural monitoring framework. Determining if the damage is occurring as a result of degradation of the structure or the sensor will have to be clearly compartmentalised to avoid any confusion.

Examining Chapter 4, the model will need to be updated based on the population extrapolation from the coupon to the structure, while keeping a pattern to be replicated to a larger number of pits, which is not always proportional. The welded part, heat affected zone and parent metal will have to be captured to ensure that the model is fit for purpose and reflective of the actual scenario.

With regard to Chapter 5, the samples could be tested to breaking point by carrying out microstructure analysis and fatigue testing of the specimen.

8 References

[1] E. P. Agency, “Atmospheric Concentrations of Greenhouse Gases,” no. August, pp. 1–13, 2016.

[2] IRENA, “Africa RE report,” *World Dev.*, vol. 60, pp. 84–98, 2013.

[3] Wind Europe, “Wind in power 2016 European Statistics,” *EWEA Eur. Stat.*, no. February, pp. 1–12, 2016.

[4] ECCC, “2020 Renewable Heat and Transport Targets,” p. 55, 2016.

[5] EWEA, “Wind energy scenarios for 2030,” *Ewea*, no. August, pp. 1–8, 2015.

[6] The Royal Academy of Engineering, *Wind energy*, no. April. 2014.

[7] RenewableUK, “Wind Energy in the UK - State of the Industry Report,” no. October, 2015.

[8] M. McCaffery, “Windfarm nimbyism says no at a time when we need to say yes,” *The Guardian. Accessed online: http://www. guardian. co. uk/environment/cif--green/2011/feb/07/windfarm--nimbyism*. 2011.

[9] E. Bash, “Explaining NIMBY Opposition to Wind Power,” *PhD Propos.*, vol. 1, no. 9, pp. 1689–1699, 2015.

[10] BBC, “Five Powys wind farm projects rejected and one approved - BBC News.” 2015.

[11] LORC, “Vindeby Offshore Wind Farm,” *LORC Knowledge*, 2011. .

[12] A. Maria and K. Christian, “World Energy Resources Wind | 2016,” p. 71, 2016.

[13] R. UK, “Offshore wind prices tumble in record-breaking auction results – cheaper than nuclear and gas - RenewableUK,” 2017. .

[14] A. Smith, T. Stehly, and W. Musial, “Offshore wind technologies market

report," p. 112 pp, 2015.

[15] J. K. Kaldellis and D. Zafirakis, "The wind energy (r)evolution: A short review of a long history," *Renew. Energy*, vol. 36, no. 7, pp. 1887–1901, 2011.

[16] Z. Shahan, "History of Wind Turbines - Renewable Energy World," *Renewable Energy World*, 2014. .

[17] M. Pasqualetti, P. Gipe, and R. Righter, "Wind Energy , History of," *Encycl. Energy*, vol. 6, pp. 419–433, 2004.

[18] J. Lindgaard, "Science , Engineering and People with a Mission Danish Wind Energy in Context 1891-2010 Schumpeter Conference 2010 Publication date : SCIENCE , ENGINEERING AND PEOPLE WITH A MISSION Danish Wind Energy in Context 1891-2010 The International Schumpeter Soci," 2010.

[19] W. Tjiu, T. Marnoto, S. Mat, M. H. Ruslan, and K. Sopian, "Darrieus vertical axis wind turbine for power generation I: Assessment of Darrieus VAWT configurations," *Renew. Energy*, vol. 75, pp. 50–67, 2015.

[20] Wikipedia, "History of Wind Power Development,." .

[21] M. Rock and L. Parsons, "Fact Sheet: Offshore Wind Energy," *Environ. Energy Study Inst.*, no. October, 2010.

[22] W. Europe, *Deep water - The next step for offshore wind energy*, no. July. 2013.

[23] The Crown Estate, "Offshore Wind - Operational report 2015," *The Crown Estate*, no. December, p. 11, 2015.

[24] M. Bilgili, A. Yasar, and E. Simsek, "Offshore wind power development in Europe and its comparison with onshore counterpart," *Renew. Sustain. Energy Rev.*, vol. 15, no. 2, pp. 905–915, 2011.

[25] WindEurope, "Unleashing Europe's offshore wind potential - A new resource assessment," no. June, 2017.

[26] A. C. Levitt, W. Kempton, A. P. Smith, W. Musial, and J. Firestone, “Pricing offshore wind power,” *Energy Policy*, vol. 39, no. 10, pp. 6408–6421, 2011.

[27] Siemens, “What is the real cost of offshore wind?,” *Consum. Policy Rev.*, vol. 15, no. 3, pp. 1–7, 2014.

[28] M. Caduff, M. A. J. Huijbregts, H. J. Althaus, A. Koehler, and S. Hellweg, “Wind power electricity: The bigger the turbine, the greener the electricity?,” *Environ. Sci. Technol.*, vol. 46, no. 9, pp. 4725–4733, 2012.

[29] R. Wiser, M. Hand, J. Seel, and B. Paulos, “Reducing Wind Energy Costs through Increased Turbine Size: Is the Sky the Limit?,” *Berkeley Lab*, no. November 2016, p. 7, 2016.

[30] R. Wiser *et al.*, “Expert elicitation survey on future wind energy costs,” *Nat. Energy*, vol. 1, no. 10, 2016.

[31] G. Corbetta and A. Mbistrova, “The European offshore wind industry - key trends and statistics 2013,” no. January, 2014.

[32] EWEA, “The European offshore wind industry key 2015 trends and statistics,” *… — Doc. …*, no. January, p. 31, 2015.

[33] M. Shafiee, F. Brennan, and I. A. Espinosa, “A parametric whole life cost model for offshore wind farms,” *Int. J. Life Cycle Assess.*, vol. 21, no. 7, pp. 961–975, 2016.

[34] V. Mytilinou and A. J. Kolios, “A multi-objective optimisation approach applied to offshore wind farm location selection,” *J. Ocean Eng. Mar. Energy*, vol. 3, no. 3, pp. 265–284, 2017.

[35] GL Garrad Hassan, “A guide to UK offshore wind operations and maintenance,” *Scottish Enterp. Crown Estate*, p. 42, 2013.

[36] X. Wu *et al.*, “Foundations of offshore wind turbines: A review,” *Renew. Sustain. Energy Rev.*, vol. 104, no. July 2018, pp. 379–393, 2019.

[37] C. Pérez-Collazo, D. Greaves, and G. Iglesias, “A review of combined wave

and offshore wind energy," *Renew. Sustain. Energy Rev.*, vol. 42, pp. 141–153, 2015.

[38] O. Y. Miñambres, "Assessment of current offshore wind support structures concepts – challenges and technological requirements by 2020," 2012.

[39] Wind Europe, "Key trends and statistics 2017," *Offshore Wind Eur.*, 2017.

[40] J. Zhang, I. Fowai, and K. Sun, "A glance at offshore wind turbine foundation structures," *Brodogradnja*, vol. 67, no. 2, pp. 101–113, 2016.

[41] A. J. K. a F. P. B. E. Lozano-Minguez, "Multi-criteria assessment of offshore wind turbine support structures based on dynamic property optimization," *High Technol. Lett.*, vol. 20, no. 4, pp. 421–428, 2014.

[42] IRENA, "Floating Foundations: A Game Changer for Offshore Wind Power," pp. 1–8, 2016.

[43] Ö. Netland, I. B. Sperstad, M. Hofmann, and A. Skavhaug, "Cost-benefit evaluation of remote inspection of offshore wind farms by simulating the operation and maintenance phase," *Energy Procedia*, vol. 53, no. C, pp. 239–247, 2014.

[44] DNV, "DNV-OS-J101 Design of Offshore Wind Turbine Structures," *May*, no. May, pp. 212–214, 2014.

[45] M. Woebbeking, K. Argyriadis, and M. Dippel, "New Guideline for offshore wind turbines," *Ewea 2013*, pp. 1–9, 2013.

[46] G. Lloyd, "Guideline for the Certification of Offshore Wind Turbines, Edition 2012," 2012.

[47] International Renewable Energy Agency, *Nurturing Offshore Wind Markets*. 2018.

[48] D. Fh, J. Ole, D. Klaus, U. Drechsel, C. Drescher, and U. Maier, "Standard Design Minimum requirements concer ning the constructive design of offshore structures within the Exclusive Economic Zone (EEZ) Standard Design constructive design of offshore structures within," 2015.

[49] American Petroleum Institute, “API RP 580: Risk-Based Inspection,” no. November, p. 96, 2009.

[50] R. Patel, “Risk-based inspection,” *3rd MENDT - Middle East Nondestruct. Test. Conf. Exhib.*, pp. 1–7, 2005.

[51] W. Crisp, “Offshore windfarms ‘wild west’ of renewable energy, union warns,” *The Guardian*. 2014.

[52] P. Acker, J. E. Madsen, J. A. Doucette, A. Gomez, U. Stallhut, and J. Donnelly, *Wind turbine accident and incident compilation*. 2017.

[53] G+, “UK Offshore wind health and safety statistics Introduction from the Chairman,” 2016.

[54] J. Ching and J. L. Beck, *Structural Health Monitoring*. 2009.

[55] H. Sohn, C. R. Farrar, F. M. Hemez, and J. J. Czarnecki, “A Review of Structural Health Monitoring Literature : 1996-2001,” *Struct. Heal. Monit.*, vol. LA-13976-M, no. LA-13976-MS, pp. 1996–2001, 2003.

[56] H. Sohn, C. R. Farrar, F. Hemez, and J. Czarnecki, “A Review of Structural Health Monitoring Literature 1996 – 2001,” *Third World Conf. Struct. Control*, no. DECEMBER, pp. 1–7, 2002.

[57] P. A. Hero and I. Sampler, “Nyquist Sampling Theorem Q . Is there a minimum sampling rate necessary for good reconstruction ? Sampling of sinusoid Slower sampling of sinusoid Sampling of Sinusoid : Notes Under sampled sinusoid Poorly sampled sinusoid Poorly sampled sinusoid (ctd) .”

[58] N. Instruments, “National Instruments, Application Note 078, Strain Gauge Measurement – A Tutorial,” no. August, pp. 1–12, 1998.

[59] J. L. F. Freire, “ELECTRICAL RESISTANCE STRAIN GAGES.”

[60] P. Kołakowski, J. Szelążek, K. Sekuła, A. Świercz, K. Mizerski, and P. Gutkiewicz, “Structural health monitoring of a railway truss bridge using vibration-based and ultrasonic methods,” *Smart Mater. Struct.*, vol. 20, no.

3, p. 035016, 2011.

[61] OMEGA, “practical Strain Gage measurements.”

[62] P. S. Gages, *Precision Strain Gages*. .

[63] B. Technical, E. J. Eaton, and R. L. Burguete, “Modern Stress and Strain Analysis A state of the art guide to measurement techniques Diffraction Methods.”

[64] D. D. L. Chung, “Structural health monitoring by electrical resistance measurement,” *Smart Mater. Struct.*, vol. 10, no. 4, pp. 624–636, 2001.

[65] D. D. L. C. Pu-Woei Chen, “Carbon fiber reinforced concrete for smart structures capable of non-destructive flaw detection,” *Smart Mater. Struct.*, pp. 21–30, 1993.

[66] C. Boller, “Next generation structural health monitoring and its integration into aircraft design,” *Int. J. Syst. Sci.*, vol. 31, no. 11, pp. 1333–1349, 2000.

[67] A. Baker, N. Rajic, and C. Davis, “Towards a practical structural health monitoring technology for patched cracks in aircraft structure,” *Compos. Part A Appl. Sci. Manuf.*, vol. 40, no. 9, pp. 1340–1352, 2009.

[68] T. Chan, Z. Li, and J. Ko, “Fatigue analysis and life prediction of bridges with structural health monitoring data—Part II: application,” *Int. J. Fatigue*, vol. 23, pp. 55–64, 2001.

[69] K. Okubo, M. Yamamoto, Y. Fukumoto, and T. Ishihara, “Wind Loads on a Bottom-mounted Offshore Wind Turbine Tower,” pp. 739–746, 2016.

[70] M. B. and C. U. G. B Wondra and Chair, “Wireless monitoring of structural components of wind turbines including tower and foundations Wireless monitoring of structural components of wind turbines including tower and foundations,” 2016.

[71] Leine Linde Systems, “Strain measurement system for wind turbines – optimizing the control & condition monitoring.”

[72] C. Rebelo, M. Veljkovic, R. Matos, and L. Simões, “Structural Monitoring of a Wind Turbine Steel Tower – Part II : monitoring re- sults,” pp. 1–19.

[73] A. Mostböck and Y. Petryna, “Structural vibration monitoring of wind turbines,” no. July, pp. 3643–3650, 2014.

[74] R. Swartz, J. Lynch, S. Zerbst, B. Sweetman, and R. Rolfes, “Structural Monitoring of Wind Turbines Using Wireless Sensor Networks,” *Smart Struct. Syst.*, vol. 6, no. 3, pp. 1–8, 2010.

[75] J. Bas, R. Carriveau, S. Cheng, and T. Newson, “Strain Response of a Wind Turbine Tower as a Function of Nacelle Orientation,” no. c, pp. 2–8, 2012.

[76] M. Benedetti, V. Fontanari, and D. Zonta, “Structural health monitoring of wind towers : remote damage detection using strain sensors,” vol. 055009.

[77] C. Pitchford, B. L. Grisso, and D. J. Inman, “Structural health monitoring of wind turbine blades,” vol. 6532, pp. 1–11, 2007.

[78] E. R. Jørgensen *et al.*, “Full scale testing of wind turbine blade to failure - flapwise loading,” vol. 1392, no. June, p. 30, 2004.

[79] W. Yang, “Testing and Condition Monitoring of Composite Wind Turbine Blades.”

[80] ABS, “Guide for Fatigue Assessment of Offshore Structures,” *Standardization*, vol. 2003, no. February, pp. 1–56, 2014.

[81] O. Adedipe, F. Brennan, and A. Kolios, “Review of corrosion fatigue in offshore structures: Present status and challenges in the offshore wind sector,” *Renew. Sustain. Energy Rev.*, vol. 61, pp. 141–154, 2016.

[82] D. Veritas, “Fatigue design of offshore steel structures,” *Recomm. Pract. DNV-RPC203*, no. April, 2005.

[83] S. D. Downing and D. F. Socie, “Simple rainflow counting algorithms,” *Int. J. Fatigue*, vol. 4, no. 1, pp. 31–40, 1982.

[84] ASTM E1049-85, “Standard practices for cycle counting in fatigue analysis,” vol. 85, no. Reapproved, pp. 1–10, 2017.

[85] S. C. Saunders, “a Review of Miner’S Rule and Subsequent Generalizations for Calculating Expected Fatigue Life,” 1970.

[86] A.A.Griffith, “The phenomena of Rupture and Flow in Solds.” 1921.

[87] G. Irwin, “‘Fracture Dynamics,’ Fracturing of Metals,” *, Am. Soc. Met. Cleveland, OH*, 1948.

[88] JULES POZZO, “CORROSION FATIGUE CRACK PROPAGATION OF BS355D STEEL AND WELD METAL,” 2014.

[89] L. P. Pook, “On fatigue crack paths,” *Int. J. Fatigue*, vol. 17, no. 1, pp. 5–13, 1995.

[90] P. Paris and F. Erdogan, “A Critical Analysis of Crack Propagation Laws,” *J. Fluids Eng.*, vol. 85, no. 4, pp. 528–533, 1963.

[91] D. N. Veritas, “DNV-OS-J101 Design of Offshore Wind Turbine Structures,” no. February, 2013.

[92] M. G. Fontana, *Corrosion Engineering*, Third. McGraw-HillBookCompany, 1987.

[93] B. A. Shaw and R. G. Kelly, “What is Corrosion?”

[94] W. Harris, B. W. Harris, and B. Sc, “Corrosion , its Causes , Cost and Prevention : A Brief History of the Growth of Corrosion Study,” 1957.

[95] B.W. Allcock and P. a Lavin, “Novel composite coating technology in primary and conversion industry applications,” *Surf. Coat. Technol.*, vol. 163–164, pp. 62–66, 2003.

[96] HILTI, “Corrosion Handbook,” 2008.

[97] M. H. Wood, A. V. Arellano, and L. Van Wij, *Corrosion-Related Accidents in Petroleum Refineries: Lessons learned from accidents in EU and OECD countries*, vol. 26331, no. January 2016. 2013.

[98] C. Hildebrandt, E. Mildner, C. Höbenreich, and C. Raschner, “Two Engines Separate from the Right Wing and Result in Loss of Control and Crash of Boeing 747 Freighter,” *Flight Saf. Found.*, vol. 45, no. 4, p. 352, 2011.

[99] N. Beresford *et al.*, “D-ERICA: an Integrated Approach to the Assessment and Management of Environmental Risks from Ionising Radiation,” p. 151, 2007.

[100] P.Tscheliesnig, “DETECTION OF CORROSION ATTACK ON SHIPS, ESPECIALLY OIL TANKERS, WITH ACOUSTIC EMISSION (AE),” 1989.

[101] K. A. Chandler, *Marine and Offshore Corrosion*. 1985.

[102] T. Tanupabrungsun, D. Young, B. Brown, and S. Nešić, “Construction and Verification of Pourbaix Diagrams for CO2 Corrosion of Mild Steel Valid up to 250°C,” *Corros. NACE Expo*, pp. C2012-0001418, 2012.

[103] R. Akid, “Corrosion of Engineering Materials,” *Handb. Adv. Mater.*, pp. 487–542, 2004.

[104] Winmate, “Anti-Corrosion _ Mechanical Design _ WINMATE,” 1996. .

[105] D. Brondel, R. Edwards, A. Hayman, D. Hill, and T. Semerad, “Corrosion in the Oil Industry,” 1994.

[106] Y. Wang, J. A. Wharton, and R. A. Shenoi, “Ultimate strength analysis of aged steel-plated structures exposed to marine corrosion damage: A review,” *Corros. Sci.*, vol. 86, pp. 42–60, 2014.

[107] R. E. Melchers, “Microbiological and abiotic processes in modelling longer-term marine corrosion of steel,” *Bioelectrochemistry*, vol. 97, pp. 89–96, 2014.

[108] D. Enning and J. Garrelfs, “Corrosion of iron by sulfate-reducing bacteria: New views of an old problem,” *Appl. Environ. Microbiol.*, vol. 80, no. 4, pp. 1226–1236, 2014.

[109] I. Beech, A. Bergel, A. Mollica, H. Flemming, V. Scotto, and W. Sand, “Simple methods for the investigation of of the role of biofilms in corrosion

SIMPLE METHODS FOR THE INVESTIGATION OF THE ROLE OF," *Biocorrosion Netw.*, no. September, pp. 0–27, 2000.

[110] H. A. Videla and L. K. Herrera, "Microbiologically influenced corrosion: looking to the future.," *Int. Microbiol.*, vol. 8, no. 3, pp. 169–180, 2005.

[111] T. R. Jack, "Biological corrosion failures," *Fail. Anal. Prev.*, vol. 11, pp. 881–890, 2002.

[112] J. Murray, "Major Ions ofSeawater," 1998, pp. 1–13.

[113] L. D. Talley, M. C. Maccracken, J. S. Perry, and T. Munn, "Salinity Patterns in the Ocean," *Earth Syst. Phys. Chem. Dimens. Glob. Environ. Chang.*, vol. 1, pp. 629–640, 2002.

[114] H. Möller, E. T. Boshoff, and H. Froneman, "The corrosion behaviour of a low carbon steel in natural and synthetic seawaters," *J. South African Inst. Min. Metall.*, vol. 106, no. August, pp. 585–592, 2006.

[115] H. APorte, "The effect of environment on the corrosion of metals," 1967.

[116] L. L. Machuca, R. Jeffrey, and R. E. Melchers, "Microorganisms associated with corrosion of structural steel in diverse atmospheres," *Int. Biodeterior. Biodegrad.*, vol. 114, pp. 234–243, 2016.

[117] C. Paper, D. Fern, R. Fundaci, and C. Tecnol, "Degradation and corrosion testing of materials and coating systems for offshore wind turbine substructures in North Sea waters," no. SEPTEMBER 2014, 2015.

[118] C. Pawsey, "The importance of corrosion protection on offshore wind farms," 2015.

[119] A. Momber, "Corrosion and corrosion protection of support structures for offshore wind energy devices (OWEA)," *Mater. Corros.*, vol. 62, no. 5, pp. 391–404, 2011.

[120] I. E. Agency, "Offshore wind," 2008.

[121] P. Plagemann and A. Momber, "Corrosion Protection of Offshore Wind

Energy Constructions in Germany : Challenges and Approaches," vol. 10, no. 2, pp. 1–4.

[122] S. Price and R. Figueira, "Corrosion Protection Systems and Fatigue Corrosion in Offshore Wind Structures: Current Status and Future Perspectives," *Coatings*, vol. 7, no. 2, p. 25, 2017.

[123] R. L. Kleinberg, S. Paltsev, C. K. E. Ebinger, D. A. Hobbs, and T. Boersma, "Tight oil market dynamics: Benchmarks, breakeven points, and inelasticities," *Energy Econ.*, vol. 70, pp. 70–83, 2018.

[124] T. Mathiesen, A. Black, and F. Grønvold, "Monitoring and Inspection Options for Evaluating Corrosion in Offshore Wind Foundations," no. March, 2016.

[125] A. Bjørgum and O. Ø. Knudsen, "Corrosion protection of offshore wind turbines," *Wind power R&D Semin.*, 2010.

[126] L. R. Hilbert, A. R. Black, F. Andersen, and T. Mathiesen, "Inspection and monitoring of corrosion inside monopile foundations for offshore wind turbines," *Eur. Corros. Congr. 2011, EUROCORR 2011*, vol. 3, no. 4730, pp. 2187–2201, 2011.

[127] A. R. Black, "Corrosion monitoring within offshore wind foundation structures Activities overview."

[128] L. R. Hilbert, T. Mathiesen, A. R. Black, C. Christensen, and F. Technology, "Mud zone corrosion in offshore renewable energy structures," *Eurocorr 2013*, no. Mic, pp. 1–5, 2013.

[129] C. E. Weinell, P. Allé, A. R. Black, and P. K. Nielsen, "New developments in coatings for extended lifetime for offshore wind structures," *NACE Corros. Conf.*, no. 9364, pp. 1–13, 2017.

[130] B. B. Jensen, "Specifying corrosion protection for the offshore wind turbine industry," no. 9091, pp. 1–11.

[131] B. A. R. Black , P. K. Nielsen, FORCE Technology, "Corrosion protection

of offshore wind farm structures – present understanding and future challenges," *Eurocorr 2011*, no. September, pp. 1–9, 2011.

[132] Elsyca, "Off-shore Wind Turbines Cathodic Protection Design."

[133] DNV GL, "RP-0416: Corrosion protection for wind turbines," 2016.

[134] O. Catapult, "OFFSHORE WIND FARM SUBSTRUCTURE MONITORING AND INSPECTION OPERATIONS AND MAINTENANCE," 2017.

[135] T. Corrosion, M. Under, and A. P. Conditions, "True Corrosion Monitoring Under The Corrosion Threat."

[136] H. Li, B. Brown, and S. Nešić, "Predicting Localized Co2 Corrosion in Carbon Steel Pipelines," *Corros. Pap.*, no. 11253, pp. 1–23, 2011.

[137] S. Caines, F. Khan, and J. Shirokoff, "Analysis of pitting corrosion on steel under insulation in marine environments," *J. Loss Prev. Process Ind.*, vol. 26, no. 6, pp. 1466–1483, 2013.

[138] J. Bhandari, F. Khan, R. Abbassi, V. Garaniya, and R. Ojeda, "Modelling of pitting corrosion in marine and offshore steel structures - A technical review," *J. Loss Prev. Process Ind.*, vol. 37, pp. 39–62, 2015.

[139] R. Newman, "The Pitting Corrosion of Metals," *Electrochem. Soc. Interface*, vol. 2, pp. 33–38, 2010.

[140] P. R. Roberge, *CorrosionEngineering: Principles and Practice*. 2006.

[141] D. W. Hoeppner, "Pitting Corrosion: Morphology and Characterization," *Framework*, vol. 25, pp. 5.1-5.16, 1985.

[142] G. S. Frankel, "Pitting Corrosion of Metals," *J. Electrochem. Soc.*, vol. 145, no. 6, p. 2186, 1998.

[143] P. G. R. Zaya, "Evaluation of Theories for the Initial Stages of Pitting Corrosion," no. October 1984, 1984.

[144] I. A. Chaves and R. E. Melchers, "Variability in Long-Term Corrosion of Mild Steel Tubular Sheet Piling," pp. 414–418, 2015.

[145] N. Bensalah, *Pitting corrosion*. .

[146] P. R.F.A, "Localised Corrosion of Stainless Steels – Limits and Mechanisms," 1997.

[147] R. E. Melchers, "Using models to interpret data for monitoring and life prediction of deteriorating infrastructure systems," *Struct. Infrastruct. Eng.*, vol. 11, no. 1, pp. 63–72, 2015.

[148] T. T. T.Shibata, "Pitting Corrosionas a Stochastic Process," *Nature*.

[149] A. Valor, F. Caleyo, L. Alfonso, D. Rivas, and J. M. Hallen, "Stochastic modeling of pitting corrosion: A new model for initiation and growth of multiple corrosion pits," *Corros. Sci.*, vol. 49, no. 2, pp. 559–579, 2007.

[150] G. Engelhardt and D. D. Macdonald, "Unification of the deterministic and statistical approaches for predicting localized corrosion damage. I. Theoretical foundation," *Corros. Sci.*, vol. 46, no. 11, pp. 2755–2780, 2004.

[151] J. C. Velázquez, J. A. M. Van Der Weide, E. Hernández, and H. H. Hernández, "Statistical modelling of pitting corrosion: Extrapolation of the maximum pit depth-growth," *Int. J. Electrochem. Sci.*, vol. 9, no. 8, pp. 4129–4143, 2014.

[152] J. K. Paik, A. K. Thayamballi, Y. Il Park, and J. S. Hwang, "A time-dependent corrosion wastage model for seawater ballast tank structures of ships," *Corros. Sci.*, vol. 46, no. 2, pp. 471–486, 2004.

[153] M. Jakubowski and A. Prof, "Influence of pitting corrosion on fatigue and corrosion fatigue of ship structures Part I," vol. 21, no. 81, pp. 62–69, 2014.

[154] R. E. Melchers, "Modeling and prediction of long-term corrosion of steel in marine environments," *Int. J. Offshore Polar Eng.*, vol. 22, no. 4, pp. 257–263, 2012.

[155] R. E. Melchers, "The effect of corrosion on the structural reliability of steel offshore structures," *Corros. Sci.*, vol. 47, no. 10, pp. 2391–2410, 2005.

[156] D. Urda, R. Marcos, L. Baena, and L. Franco, "Advances in Computational

Intelligence," vol. 7902, no. October, 2013.

[157] H. M. Mohammad, "Prediction of Pitting Corrosion Characteristics using Artificial Neural Networks," vol. 60, no. 4, pp. 4–8, 2012.

[158] V. Alar, "Development of Models for Prediction of Corrosion and Pitting Potential on AISI 304 Stainless Steel in Different Environmental Conditions," *Int. J. Electrochem. Sci.*, vol. 11, pp. 7674–7689, 2016.

[159] M. J. Jiménez-Come *et al.*, "Pitting corrosion behaviour of austenitic stainless steel using artificial intelligence techniques," *J. Appl. Log.*, vol. 10, no. 4, pp. 291–297, 2012.

[160] J. S. Chou, N. T. Ngo, and W. K. Chong, "The use of artificial intelligence combiners for modeling steel pitting risk and corrosion rate," *Eng. Appl. Artif. Intell.*, vol. 65, no. August 2016, pp. 471–483, 2017.

[161] D. A. Horner, B. J. Connolly, S. Zhou, L. Crocker, and A. Turnbull, "Novel images of the evolution of stress corrosion cracks from corrosion pits," *Corros. Sci.*, vol. 53, no. 11, pp. 3466–3485, 2011.

[162] N. O. Larrosa, R. Akid, and R. A. Ainsworth, "Corrosion-fatigue: a review of damage tolerance models," *Int. Mater. Rev.*, vol. 63, no. 5, pp. 283–308, 2018.

[163] Y.Kondo, "Prediction of Fatigue Crack Initiation Life based on pit growth." NACE, 1986.

[164] A. Turnbull, L. N. McCartney, and S. Zhou, "A model to predict the evolution of pitting corrosion and the pit-to-crack transition incorporating statistically distributed input parameters," *Environ. Crack. Mater.*, vol. 48, pp. 19–45, 2008.

[165] J. C. Newman and I. S. Raju, "An empirical stress-intensity factor equation for the surface crack," *Eng. Fract. Mech.*, vol. 15, no. 1–2, pp. 185–192, 1981.

[166] S. I. Chou, "Stresses Around Elliptic Holes in Circular Cylindrical Shells

elliptic holes of various sizes and eccentricities," pp. 487–492, 1973.

[167] A. Kolios, S. Srikanth, and K. Salonitis, "Numerical simulation of material strength deterioration due to pitting corrosion," *Procedia CIRP*, vol. 13, pp. 230–236, 2014.

[168] J. C. N. I.S.Raju, "Stress-Instensity Factors for circumferential surface cracks and rods under tension and bending," *NASA Tech. Memo.*, pp. 101–101, 2018.

[169] R. Jeffrey and R. E. Melchers, "The changing topography of corroding mild steel surfaces in seawater," *Corros. Sci.*, vol. 49, no. 5, pp. 2270–2288, 2007.

[170] A. Cosham, P. Hopkins, and K. A. Macdonald, "Best practice for the assessment of defects in pipelines - Corrosion," *Eng. Fail. Anal.*, vol. 14, no. 7, pp. 1245–1265, 2007.

[171] F. Castanedo, "A review of data fusion techniques," *Sci. World J.*, vol. 2013, 2013.

[172] M. Kartal, R. Molak, M. Turski, S. Gungor, M. E. Fitzpatrick, and L. Edwards, "Determination of weld metal mechanical properties utilising novel tensile testing methods," *Appl. Mech. Mater.*, vol. 7–8, pp. 127–132, 2007.

[173] ASTM, "Standard practices for cycle counting in fatigue analysis," *ASTM Stand.*, vol. 85, no. Reapproved 2017, pp. 1–10, 2017.

[174] A. International and F. indexed by mero, "Standard Practices for Cycle Counting in Fatigue Analysis 1," vol. 85, no. Reapproved 2017, pp. 1049–85, 1997.

[175] (DNV) Det Norske Veritas, "Fatigue Design of Offshore Steel Structures," *Recomm. Pract. DNV-RPC203*, no. October, p. 126, 2005.

[176] A. Mehmanparast, F. Brennan, and I. Tavares, "Fatigue crack growth rates for offshore wind monopile weldments in air and seawater: SLIC inter-

laboratory test results," *Mater. Des.*, vol. 114, pp. 494–504, 2017.

[177] N. I. Xiros and S. I. Publishing, *Handbook Ocean Engineering*. 2018.

[178] D. Fern, R. Fundaci, and C. Tecnol, "Degradation and corrosion testing of materials and coating systems for offshore wind turbine substructures in North Sea waters," no. SEPTEMBER 2014, 2015.

[179] ASTM G1-90, "ASTM G1 Standard Practice for Preparing, Cleaning, and Evaluation Corrosion Test Specimens," *Astm*, p. 8, 2003.

[180] R. B. Ribeiro, J. W. J. Silva, L. R. O. Hein, M. C. Pereira, E. N. Codaro, and N. T. Matias, "Morphology Characterisation of Pitting Corrosion on Sensitized Austenitic Stainless Steel by Digital Image Analysis," vol. 2013, 2013.

[181] M. Enikeev, I. Gubaydullin, and M. Maleeva, "Analysis of Corrosion Process Development on Metals by Means of Computer Vision," vol. 21, no. 4, pp. 183–192.

[182] D. Itzhak and T. Zilberberg, "PITTING CORROSION EVALUATION BY COMPUTER IMAGE PROCESSING *," vol. 21, no. March 1980, pp. 17–22, 1981.

[183] A. Mcandrew, "An Introduction to Digital Image Processing with Matlab Notes for SCM2511 Image Processing 1 Semester 1 , 2004," 2004.

[184] U. Maths, "Online: 3 unit maths 1," vol. 1, no. C, pp. 2–7, 2013.

[185] CEFAS, "DHIS2 Data Sets." .

[186] D. Beare, A. McQuatters-Gollop, T. van der Hammen, M. Machiels, S. J. Teoh, and J. M. Hall-Spencer, "Long-Term Trends in Calcifying Plankton and pH in the North Sea," *PLoS One*, vol. 8, no. 5, 2013.

APPENDICES

Appendix A Chapter 3 codes

```
clear all
close all
clc

format compact
format long
%% User define
% Case to analyse
CASE=[1];  % file to be saved
diameter = 'Outer'; % 'Outer' or
'Inner'

% Data imported
sheet=1;
range='D2:G216001';
xlsfilename='gud corrected
sample.xlsx';

average = 0;% average =1
calculating mean, average =0 no
mean calculation
radius = 2.6 %[m]
step_h =1  %[m] to set up for
data along height and plot
h=50; % height [m]
theta=
0*pi/180:30*pi/180:360*pi/180;
%% Define directories and make
folders
direction.main = pwd;
cd(direction.main)

mkdir('data');
mkdir('results');
mkdir('figures');

direction.data = [direction.main
'\data'];
```

```
direction.results =
[direction.main '\results'];
direction.figures =
[direction.main '\figures'];

addpath(genpath([direction.main]
))

%% Import data to Matlab
%
data=xlsread(xlsfilename,sheet,r
ange);
%  data = [data data(:,1)];
%extension of the matrix by
adding 360 degrees that
correspond to 0 deg
% cd(direction.data)
% save('gud_data', 'data',
'theta','h')
% cd(direction.main)

%% run  strain

bending_strain


%% cosine fit
cosinefit

%% height interpolation

height_interpolation

%% rainflow run
rainflowrun

%% rainflow analysis
rainflowanalysis
```

```
%% strain outer calculations
if diameter=='Outer'
```

```
    di = 5;             % change
as required
```

```
    d_o =5.2;           % change
as required
    str =
(d_o.*data*di.^4)/(di*((d_o.^4)-
(di.^4))); %strain*I/Y =constant
elseif diameter == 'Inner'
    str=data;
end

if average == 1
    data_m = str(:,1:4);%
data(:,2) data(:,3) data(:,4)];



    for kk =
1:size(data_m,1)/1200
        for iii =
1:size(data_m,2)
            sd=data_m(1200*kk-
1199:1200*kk,iii);
            strain(kk,iii) =
mean(sd);
        end
    end
elseif average==0
    strain=str;
end

disp('*************************
cosine fit
********************')

cd(direction.data)
load(['strain_avg'
num2str(average) '_' diameter
'_case' num2str(CASE)])
cd(direction.main)

%%

x1 = strain(:,1);
x2 = strain(:,2);
x3 = strain(:,3);
```

```
A= (x1+x3)/2;
z1 = -(4*x2-x1-
3*x3)./((sqrt(3))*(x3-x1));
k=atan(z1);
ik=find(k<0);
k(ik)=pi-abs(k(ik));

B = (x3-x1)./(2*cos(k));

strain_cs =
A*ones(1,length(theta)) -
B*ones(1,length(theta)).*cos(one
s(size(strain,1),1)*theta-
k*ones(1,length(theta)));




%% wind direction
wind_direction = acos(A./B);

il =
find(0<=wind_direction<=90*pi/18
0);
wind_direction(il) =
wind_direction(il);

im =
find(90*pi/180<wind_direction<=1
80*pi/180);
wind_direction(im) =
180*pi/180*ones(length(im),1)-
wind_direction(im);

in = find(-
90*pi/180<=wind_direction<0);
wind_direction(in) =
wind_direction(in);

io = find(-
180*pi/180<=wind_direction<-
90*pi/180);
wind_direction(io) =
180*pi/180*ones(length(io),1) +
wind_direction(io);
```

```
disp('******************** height *********************')
cd(direction.results)
load(['strain_cs_avg' num2str(average) '_' diameter '_case'
num2str(CASE)])
cd(direction.main)



strain_height = ones(size(strain,1),size(theta,2),h);
```

```
        for ii=1:h
            strain_height(:,:,ii)=-strain_cs/(h-1)*(h-ii);
        end
cd(direction.results)
save(['strain_height_avg' num2str(average) '_' diameter '_case'
num2str(CASE)],'strain_height')
cd(direction.main)


disp('******************** analysis ***********************')
cd(direction.results)
load(['rainflow_cs_h_avg' num2str(average) '_' diameter '_case'
num2str(CASE)])
cd(direction.main)
rainflowdata=savedata_cs_h;
minstress = [200E-3*rainflowdata(:,1,:,:)];
maxstress = 200E-3*rainflowdata(:,2,:,:);
numcycles = rainflowdata(:,3,:,:);
%     end
% end







stressrange = []
sumstressrange = []

stressrange = numcycles.*(maxstress - minstress).^3;

    sumsr=sum(stressrange,1)
    sum_cycles = sum(numcycles,1)




equivalentstress = sumsr.^(1/3)
N = 10^12.449./equivalentstress.^3
Dam_age = sum_cycles./N

for kk = 1:size(Dam_age,3)
    for mm = 1:size(Dam_age,4)
        Damage(kk,mm)  = Dam_age(:,:,kk,mm);
    end
end


cyl3d(dplot', theta(1), theta(end), radius,h,step_h,'surf',
'spline',0.0000001)

cd(direction.figures)
print -dpng rainflowanalysis_3.png
cd(direction.main)

save('sumstressrange','sumsr','sum_cycles','stressrange','rainflowdata
','numcycles','N','minstress','maxstress','equivalentstress','Damage')
```

```
cd(direction.results)
save(['rainflow_' num2str(CASE)]
,'theta','sumstressrange','sumsr','sum_cycles','stressrange','rainflow
data','numcycles','N','minstress','maxstress','equivalentstress','Dama
ge')
cd(direction.main)

disp('********************** rainflow ************************')
cd(direction.results)
load(['strain_height_' diameter '_case' num2str(CASE)])
cd(direction.main)

savedata_cs_h=ones(13,10,size(strain_height,3),nkw);

 for kx =1:size(strain_height,3)-1
    parfor kw = 1:size(strain_height,2)
        kx
        kw
        savedata_cs_h(:,:,kw,kx)=rainflowgud(strain_height(:,kw,kx));
    end
 end
save('savedata_cs_h')


% clear all
% close all
% clc
% format long
disp('******************** analysis ***********************')
cd(direction.results)
load(['rainflow_cs_h_avg' num2str(average) '_' diameter '_case'
num2str(CASE)])
cd(direction.main)
%straindatagudmean%straindatagudmean
% rainflowdata=xlsread(['rainflow_' namefit])
%load(['savedata_m_ean' namefit])
rainflowdata=savedata_cs_h;
% for kk = 1:size(rainflowdata,3)
%     for ll = 1:size(rainflowdata,4)
minstress = [200E-3*rainflowdata(:,1,:,:)];
maxstress = 200E-3*rainflowdata(:,2,:,:);
numcycles = rainflowdata(:,3,:,:);
%     end
% end




stressrange = []
sumstressrange = []

stressrange = numcycles.*(maxstress - minstress).^3;

    sumsr=sum(stressrange,1)
```

```
    sum_cycles = sum(numcycles,1)



equivalentstress = sumsr.^(1/3)
N = 10^12.449./equivalentstress.^3
Dam_age = sum_cycles./N

for kk = 1:size(Dam_age,3)
    for mm = 1:size(Dam_age,4)
        Damage(kk,mm) = Dam_age(:,:,kk,mm);
    end
end


Radius= radius*ones(1,length(theta))


ind_d=h:-step_h:1
dplot=Damage(:,ind_d)% dplot=Damage
figure(1)

cyl3d(dplot', theta(1), theta(end), radius,h,step_h,'surf',
'spline',0.0000001)

cd(direction.figures)
print -dpng rainflowanalysis_3.png
cd(direction.main)

save('sumstressrange','sumsr','sum_cycles','stressrange','rainflowdata
','numcycles','N','minstress','maxstress','equivalentstress','Damage')

cd(direction.results)
save(['rainflow_' num2str(CASE)]
,'theta','sumstressrange','sumsr','sum_cycles','stressrange','rainflow
data','numcycles','N','minstress','maxstress','equivalentstress','Dama
ge')
cd(direction.main)
```

Appendix B Chapter 4 codes

```
clear all
close all
clc
format long

%% main
direction.main =pwd;
cd(direction.main);

mkdir('data');
mkdir('results');
mkdir('figures');

direction.data = [direction.main
'\data'];
direction.results =
[direction.main '\results'];
direction.figures =
[direction.main '\figures'];

addpath(genpath([direction.main]
))
%%
coupon_creation
%t = number of days
ipit=[]
time_over = 3;
t = [1:time_over]'
newpopulation = 28*(t.^2) %-
5*(t-ones(length(t),1).^2)
new_y =[]
new_x =[]

depth_pit =
zeros(length(newpopulation(1)),1
)
m =3
cp=0.005 % to be changed
d=[]
growth_rate =[];
c=.5
transition=[];
ispit = [];
iscrack = [];
savenew_pop = [0];
corrected_time = [];
% strain_height = [];
for sk = 1:time_over%length(t)
    sk
    new_pop = newpopulation(sk)
coordinate_sampling_day1

cylindrical_transformation

height_interpolation

cosinefit_pits

rainflowanalysisPITTING

kondoanalysisgud

end

%% sampling distribution to
larger population
if sk==1

corrected_time=ones(new_pop,1)
else
    corrected_time =
[corrected_time+ones(length(corr
ected_time),1);sk* ones(new_pop-
savenew_pop,1)];
end % Extrapolation techniques
required(to be discussed with
mahmood)
% at initial stage use random
for the x and y co-ordinates
% d is depth of pit
%length of circumference =
2*pi*5 ==) r = 5m
circumference = 2*pi*5;% in
metres
y_max = 10 %in meters
%new_pop = 7  %has to be
determined from distance
software
d_max = max(pits_depth{1,1})
savenewx = new_x
savenewy = new_y
% save_d = d
% if sk ==1
%     new_x =
% else
new_x = circumference*rand(1,
new_pop-savenew_pop)';
new_y = y_max*rand(1,new_pop-
savenew_pop)';
% end
for gg = 1:new_pop-savenew_pop
ioverx=find(new_x(gg)==savenewx)
iovery=find(new_y(gg)==savenewy)
new_x(ioverx)=circumference*rand
(1,length(ioverx))';
new_y(iovery)=y_max*rand(1,lengt
h(iovery))';

end
new_x =[savenewx ;new_x]
```

```
new_y =[savenewy ;new_y]

newd = d_max*rand(1,new_pop-
savenew_pop)'
new_growthrate =
rand(1,length(newd))
% d=d+depth_pit'
% d = [save_d newd]
d = [d ;newd]
growth_rate =
[growth_rate;new_growthrate'];
cd(direction.results);

save(['pittingcorrsam_1_'
num2str(sk)],'new_pop','d','new_
x','new_y')

cd(direction.main);


%% for height strain prediction
% if height==1
%     load('gud_data');
% % elseif cosinef==1
% disp('********************
height *********************')
cd(direction.data)
load('gud_data')
cd(direction.main)
%

% end
%
%
% %% User define
% if meanon==1
%        save(['strain_height_'
num2str(CASE)],'data')
% else
%     h1=1:49;
%     h2=0:48;

    %% Calculation
%     nh1=length(h1);
%     nh2=leng9th(h2);
%     ndata1=size(strain_cs,1);
%     ndata2=size(strain_cs,2);
    % 3-dimensional matrix in
the form of(strain
values,height,theta)
%     for k =1:ndata2
%
strain_height(:,:,k)=strain_cs(:
,k)*ones(1,nh1)./(h*ones(ndata1,
nh1)-
ones(ndata1,1)*h1).*(h*ones(ndat
a1,nh2)-ones(ndata1,1)*h2);
```

```
%
% end
% for ik = 1:length(z)
%     strain_height(:,:,ii)=-
strain_cs/(h-1)*(h-ii);
% end

%% strain_height = (strain
data,population points,theta(0
120 180 240))
npop = newpopulation(sk)
clear strain_height
strain_height=
ones(size(data,1),size(data,2),n
pop);
structure_height = 50;
for kk = 1:size(data,2)
%strain_height(:,:,kk)= -((-
structure_height*ones(size(data,
1),1)./data(:,kk))*z' -50) ;
%
strain_height(:,kk,:)=data(:,kk)
/(-structure_height)*z' +
data(:,kk)*ones(1,length(z));

end



cd(direction.results);

save(['pittingheight_1_'
num2str(sk)],'strain_height')

cd(direction.main);

    %save(['strain_height_'
num2str(CASE)],'strain_height')

% end
%
disp('**************************
**********')
% disp('       strain saved to
file')
%
disp('**************************
**********')




%% cosine fit for pits
%change theta to something
else!!!!!!
```

```
disp('*************************
cosine fit
********************')

% cd(direction.data)
% load(['strain_avg'
num2str(average) '_' diameter
'_case' num2str(CASE)])
% cd(direction.main)

%%
strain =strain_height;
x1 = squeeze(strain(:,1,:));
x2 = squeeze(strain(:,2,:));
x3 = squeeze(strain(:,3,:));
%% FORMULA AFTER SOLVING
SIMULTANEOUS EQNS FOR S1 S2 S3
D= (x1+x3)/2;
z1 = (4*x2-x1-3*x3)./(-
(sqrt(3))*(x3-x1));

zn = (4*x2-x1-3*x3);
zd= (-(sqrt(3))*(x3-x1));

%% QUADRANT SEARCH FOR SELECTION
OF APROPRIATE ANGLE
zi = find((zd>0)==(zn>0));%0-90
deg
zii=find((zd<0)==(zn>0));%90-180
deg
ziii =
find((zd<0)==(zn<0));%180-270
deg
ziv=find((zd>0)==(zn<0));%270-
360

angle1=abs(atan(zn./zd));

k =
ones(size(data,1),size(angle1,2)
);

k(zi) = angle1(zi);
k(zii) =
pi*ones(length(angle1(zii)),1)-
angle1(zii);
k(ziii)
=pi*ones(length(angle1(ziii)),1)
+ angle1(ziii);
k(ziv)
=2*pi*ones(length(angle1(ziv)),1
)- angle1(ziv);
% k=atan(z1);
% ik=find(k<0);
% k(ik)=pi-abs(k(ik));
k = reshape(k,[size(data,1),
npop]);
```

```
B = (x3-x1)./(2*cos(k));

%strain_cs =
A*ones(new_pop,length(theta)) -
B*ones(1,length(theta)).*cos(one
s(size(strain,1),1)*theta-
k*ones(1,length(theta)));
cd(direction.results);
save(['cosine_pits_'
num2str(sk)],'D','B','k')
cd(direction.main);

%strain_good are the value of
the strain at the pit
%% cylindrical cordinate
transformation
% (x,y,d) where x = new-x cord,
y= new-y cord, d =depth of crack
% (r,theta,z) r1 is original
radius of structure
% transformation = (r1-d,x/r1,y)
%theta in radians


r1=2.5;
r = r1-d;
angle_gud = new_x/r1;
z = new_y;

cd(direction.results);
save(['cyl_trans1_'
num2str(sk)],'r','angle_gud','z'
)
cd(direction.main);

%%
strain_cs =
D*ones(npop,length(angle_gud)) -
B.*cos(ones(size(strain_height,1
),1)*(angle_gud*180/pi)'-k);



savedata_cs_h=ones(13,10,size(st
rain_cs,2));
%,size(strain_height,3));
% strain_height=datacs
% if height==1
   %kw = angle
   %kx = height

%  for kx =1:size(strain_cs,2)
   parfor kx =
1:size(strain_cs,2) %
        kx
        %kw
```

```
%savedata_cs_h(:,:,kw,kx)=rainflowgud(strain_cs(:,kw,kx));% rainflow, angle, height


savedata_cs_h(:,:,kx)=rainflowgudpit(strain_cs(:,kx));
   end
cd(direction.results);
save(['rainflowpits_' num2str(sk)],'savedata_cs_h','strain_cs')
cd(direction.main);

% %% wind direction
% wind_direction = acos(A./B);
%
% il = find(0<=wind_direction<=90*pi/180);
% wind_direction(il) = wind_direction(il);
%
% im = find(90*pi/180<wind_direction<=180*pi/180);
% wind_direction(im) = 180*pi/180*ones(length(im),1)-wind_direction(im);
%
% in = find(-90*pi/180<=wind_direction<0);
% wind_direction(in) = wind_direction(in);
%
% io = find(-180*pi/180<=wind_direction<-90*pi/180);
% wind_direction(io) = 180*pi/180*ones(length(io),1) + wind_direction(io);

%%
% cd(direction.results)
% save(['strain_cs_avg' num2str(average) '_' diameter '_case' num2str(CASE)],'strain_cs')%,'wind_direction')
% cd(direction.main)




rainflowdata=savedata_cs_h;
minstress = [200E-3*rainflowdata(:,1,:)];
maxstress = 200E-3*rainflowdata(:,2,:);
numcycles = rainflowdata(:,3,:);



stressrange = []
sumstressrange = []

stressrange = numcycles.*(maxstress - minstress).^3;

    sumsr=sum(stressrange,1)
    sum_cycles = sum(numcycles,1)



equivalentstress =squeeze(sumsr.^(1/5))


cd(direction.results)
save(['pitting_equistress_1_' num2str(sk)],'equivalentstress')

cd(direction.main)


%% pit competition day 1
%the aspect ratio is taken as 0.7 as suggested by kondo
%dkpit = stress intensity factir of pit
%equivalent_stress = equivalent stress

%For Q determination = Newman and Raju
% Q = 1+1.464*(a/c)^1.65

% FOR F DETERMINATION USE TABLE NEWMAN RAJU a/D = crack length/diameter
%        a/c = 1.0        a/c = 0.8          a/c = 0.6
% a/D    A        B        A        B     A        B
% 0.05   1.012    1.156    1.056    1.054    1.107    0.933
% 0.125 1.015    1.189    1.083    1.101    1.176    0.999
```

```
% 0.2   1.038   1.26    1.131
1.2     1.316   1.129
% 0.275 1.087   1.356   1.227
1.335   1.565   1.329
% 0.35  1.175   1.475   1.387
1.509   1.835   1.516

%Y =F/(Q)^0.5
dia =5;%m
thickness = .100;%[m]

ar = 0.7;
d_t = d/thickness*0.5;
% Q =  1+1.464*(ar)^1.65;
% time = 1:t(sk)

G1 = -1.22-0.12*(ar);
G2 = 0.55-
1.05*(ar)^0.75+0.47*(ar)^1.5;
M1 = 1.13 -0.09*(ar);
M2 = -0.54+(0.89/(02.+ar));
M3 = 0.5-(1/(0.65+(ar)))+14*(1-
(ar)^24);
fw = 1;
phi = sqrt(1+1.464*(ar)^1.65);
f = 0.3;
N = .3*365.25*24*3600;
 Q = 1+1.464*(ar)^1.65;
%
% ratio= d./dia;
% F = 21.63*ratio
%
% Y = F/sqrt(Q);

m = 3
C = 1.65E-11;

% ipit=1:npop
savetransition=transition
% for ik=1:npop
%     if
prod(ik~=savetransition)||
isempty(savetransition)
%         dkpit(ik,:) =
2.24*sqrt(pi*d(ik))*((equivalent
stress(ik)'))/Q;
%         dkcrack(ik,:) =
equivalentstress(ik)'*Y(ik)*sqrt
(pi*d(ik));
%         if
dkpit(ik)<dkcrack(ik) %1=pit,%0
= crack
%
transition=sort([transition
;ik]);
%         end
%     depth_pit(ik,:) =
cp*time(sk)^(-1/3)
```

```
%     else
% % else
%     depth_pit(ik,:) =
(25920*c*((equivalentstress(tran
sition).*Y).^m)*pi^(m/2)*(2-
m)/(2*m)+d.^(1-m/2)).^(1/(1-
m/2))
%     end

kt =5;


% dkpit =
2.24*sqrt(pi*d).*((equivalentstr
ess))/Q;
% dkcrack =
equivalentstress.*Y.*sqrt(pi*d);

dc_pit =
((growth_rate).*cp.*f.^(-
growth_rate).*N.^(growth_rate-
ones(size(growth_rate,1),size(gr
owth_rate,2))).*d);
Y =
(1+G1*d_t+G2*d_t.^2).*(M1+M2*d_t
.^2+M3*d_t.^4);

Ca = C*(1.12^m)*pi^(m/2);
dc_crack =
0.1*((kt*equivalentstress.*d).^m
)*Ca.*Y.^(-m/2);

% dKtr =
(0.5*pi*(1.12*kt*equivalentstres
s).^4).*(c./Ca).*((ar).^2./Q.^4)
.^(1/m+4)*(1/0.3)^(1/m+4);
% dkcrack =
equivalentstress.*Y.*sqrt(pi*d);
if sk == 1 % first day the
transition test is for the whole
population
    itotest =1:new_pop
else
    itotest = [ispit
;[savenew_pop+1:new_pop]'] % any
other day it is only the pit
end
% totest =
zeros(1,length(new_pop));
% totest(itotest) =
ones(1,length(itotest));

% iscrack = find(dkpit>dkcrack)
% ispit =
find((dkpit(totest)<dkcrack(tote
st)).*(totest));% prob here
```

```
ispit =
find((dc_pit(itotest)>dc_crack(i
totest)));%

iscrack = [iscrack
;find((dc_pit(itotest)<dc_crack(
itotest)))];

% %      if ispit == 1 &
%1=pit,%0 = crack

%
depth_pit(itotest(ispit)) =
[cp*corrected_time(itotest(ispit
)).^(-1/3)]';

depth_pit(itotest(ispit)) =
[cp*corrected_time(itotest(ispit
)).^(growth_rate(itotest(ispit))
)]';

% %
% %      elseif ispit == 0 ||
sum(ik==transition)
% %
transition=sort([transition
;ik]);
       %
depth_pit(itotest(iscrack)) =
ones(1,length(itotest(iscrack)))
*(25920*c*((equivalentstress(ito
test(iscrack))).*Y).^m)*pi^(m/2)
*(2-m)/(2*m)+d.^(1-m/2)).^(1/(1-
m/2));

depth_pit(itotest(iscrack)) =
0.1*abs(ones(1,length(itotest(is
crack)))*(25920*c*((equivalentst
ress(itotest(iscrack)).*Y(iscrac
k)).^m)*pi^(m/2)*(2-
m)/(2*m)+d(iscrack).^(1-
m/2)).^(1/(1-m/2)));

%      end
% end
% ipit=find(1:npop.*npit)%
% end
d=d+depth_pit'


disp('##########################
##########')
disp(itotest(iscrack))
savenew_pop = new_pop;
cd(direction.results);

 save(['kondopits_'
num2str(sk)],'dc_pit','dc_crack'
,'d');
cd(direction.main);
```

Appendix C Chapter 5 codes

```
clc
close all
clear all

%% opening and image conversion
ncoupon = 47;
Ia = imread('47f.jpg');
%original image
figure
subplot(1,4,1)
imshow(Ia)
title('original')

Ib = rgb2gray(Ia);  %grayscale
image
 subplot(1,4,2)
imshow(Ib)
title('grayscale')


Ic = imcomplement(Ib);
%complement image
subplot(1,4,3)
imshow(Ic)
title('inverted colours')
figure
I = imbinarize(Ib,0.55);
% subplot(1,4,4)
imshow(I)
title('black and white')

figure
Ic = imcomplement(I)
imshow(Ic)

H=0.5:0.01:0.6;
figure(4)

for i =1:length(H)
        subplot(4,3,i)
        I = imbinarize(Ib,H(i));
%only black and white image
        imshow(I)
        title(['Threshold of
conversion: ' num2str(H(i))])
end
figure(5)
I = imbinarize(Ib,0.55);
% subplot(2,2,4)
imshow(I)
title('black and white and
chosen threshold = 0.55')

figure
I = imcomplement(I);
imshow(I)

%% thresholding
% [r,c] = size(I);
% im = zeros(r,c);
% for i= 1:r
%     for j = 1:c
%         if I > 8 % pixel
length
%             im(i,j) =1;
%         end
%     end
% end
%
% im= bwareaopen(im,5); %
objects of pixel length of 5
will be deleted.
% im = imfill(im,'holes'); %
objects deleted are replaced

I2 = I;
imshow(I2)
%% Segmentation
cc = bwconncomp(I2);
n = cc.NumObjects; %connected
objects

%% Feature extraction
Area = zeros(n,1);
Perimeter = zeros(n,1);
MajorAxis = zeros(n,1);
MinorAxis = zeros(n,1);
Centroid = zeros(n,2);

k = regionprops(I2, 'Area',
'Perimeter', 'MajorAxisLength',
'MinorAxisLength',
'Centroid','Orientation')
kk = struct2cell(k);
kk = kk';

Area = cell2mat(kk(:,1));
Centroid = cell2mat(kk(:,2));
Centroid_x = Centroid(:,1);
Centroid_y = Centroid(:,2);
MajorAxis = cell2mat(kk(:,3));
MinorAxis = cell2mat(kk(:,4));
Perimeter = cell2mat(kk(:,5));
Aspect_ratio =
(MinorAxis./MajorAxis)
Orientation = cell2mat(kk(:,6));
hh = [Area Centroid_x Centroid_y
Perimeter Aspect_ratio
Orientation];
```

```
pp=[];
% filtering small pixels (white)


num_of_pits = size(hh,1);
Centroid_x = hh(:,2);
Centroid_y = hh(:,3);
Area = hh(:,1);
dd= Centroid_y;
d1 = dd*(-1);
Centroid_y=d1;

figure
plot(Centroid_x,Centroid_y,'o')
title('Centroid x v/s Centroid
y')

axis equal

%% remove beginning and end ends

Centroid_x_mm =
(100/size(Ic,2)*Centroid_x)-20;
Centroid_y_mm =
150/size(Ic,1)*Centroid_y;




filt_centroid_x =
(find(hh(:,2)<15 | hh(:,2)>450 |
hh(:,3)<20 | hh(:,3)>741));
% Centroid_x_mm(filt_centroid_x)
= [];
% Centroid_y_mm(filt_centroid_x)
= [];

figure
plot(Centroid_x_mm,Centroid_y_mm
,'o')
title('Centroid x v/s Centroid
y')
ylabel('Centroid-y[mm]')
xlabel('Centroid-x[mm]')
axis equal
% Area(filt_centroid_x)=[];
```

```
Area_xy =
((150*100)/((size(Ia,2)*size(Ia,
1))))*Area;

MajorAxis_g =
sqrt(((150*MajorAxis.*cosd(Orien
tation)/size(Ia,1)).^2)+...

((100*MajorAxis.*sind(Orientatio
n)/size(Ia,2)).^2));
MinorAxis_g =
sqrt(((150*MinorAxis.*cosd(Orien
tation+90)/size(Ia,1)).^2)+...

((100*MinorAxis.*sind(Orientatio
n+90)/size(Ia,2)).^2));

% Area_xy=Area_xy;


pits_charac = [Area_xy
Centroid_x_mm Centroid_y_mm
Orientation MajorAxis_g
MinorAxis_g];
pits_charac(filt_centroid_x,:) =
[];
format short
pp = find(pits_charac(:,1)<1.1 |
pits_charac(:,1) >60);
pits_charac(pp,:) = [];


figure
plot(pits_charac(:,2),pits_chara
c(:,3),'o')
title('Centroid x v/s Centroid
y')
ylabel('Centroid-y[mm]')
xlabel('Centroid-x[mm]')
axis equal

save(['pits_'  num2str(ncoupon)
],'pits_charac')

xlim([0 10])
ylim([-0.4 0.8])
```

Appendix D Chapter 6 codes

```
clear all
close all
clc

load('test_var_rand_1.mat')


[xi,yi] = meshgrid(0:1:400,
0:1:90);
zi = griddata(x,y,del_z,xi,yi);

figure
contourf(xi,yi,zi,'ShowText','of
f')
colormap(jet)

figure(35)
surf(xi,yi,zi)
pp = length(xi)*size(yi,1);
zik = reshape(zi,[pp,1]);
xik = reshape(xi,[pp,1]);
yik = reshape(yi,[pp,1]);
ave_delz = mean(del_z);
%%

po = 0.1
zik_1 = find(zik<=po*ave_delz);
xik_1a = xik(zik_1);
yik_1a= yik(zik_1);
zik_1a = zik(zik_1);
z_id=[];
for hh = 1:length(zik_1)-1
    z_id(hh) = zik_1(hh+1)-
zik_1(hh);
        if z_id(hh) == 1
                 z_id(hh) = 1;
        else
                 z_id(hh) = 0;
        end
end
z_id = z_id';
z_id = [0;z_id];

% z_id=[0 ; zik_1(2:end)-
zik_1(1:end-1)==1];

mk = find(z_id == 1);
z_g = zik_1a(mk);
x_g = xik_1a(mk);

y_g = yik_1a(mk);
figure(30)
scatter3(x_g,y_g,z_g,'r')
figure(31)
scatter3(x_g,y_g,z_g,'r')
hold on
surf(xi,yi,zi)
hold off
all = [x_g y_g z_g];

figure(33)
scatter3(x_g,y_g,zeros(length(z_
g),1),'r')
hold on
contourf(xi,yi,zi,'ShowText','of
f')
colormap(gray)

%% cluster analysis and pit
extraction


T =
clusterdata(all,'Maxclust',10);
figure(39)
scatter3(all(:,1),all(:,2),all(:
,3),100,T,'filled')
pit_c = cell(1,max(T))% pits
coordinates from cluster
analysis
for kkl = 1: max (T)

    ww1=find(T==kkl)
    x_pit = x_g(ww1);
    y_pit =y_g(ww1);
    z_pit = z_g(ww1);
 pit_c{kkl}= [x_pit y_pit
z_pit];


end
%% ellipsoid extrema and theta
x_d=zeros(max(T),2);
y_d=zeros(max(T),2);
y_xmax=zeros(max(T),1);
z_dmin=zeros(max(T),1);

centroid=zeros(max(T),3);
for kkj = 1:max(T)

    pit_d = pit_c{kkj} ;

    y_d=pit_d(:,2);
    x_d = pit_d(:,1);
       [MAX_X ind_xmax]=
max(x_d);
```

```
        [MIN_X ind_xmin]=
min(x_d);
        [MAX_Y ind_ymax] =
max(y_d);
        [MIN_Y ind_ymin] =
min(y_d);

        centroid(kkj,:) =
[mean([MAX_X MIN_X]) mean([MAX_Y
MIN_Y]) min(pit_d(:,3))];

        diff_x = MAX_X - MIN_X;
        diff_y = MAX_Y - MIN_Y;

        test = diff_x - diff_y ;

        if test>0

y_theta=y_d(ind_xmax);
            x_theta=MAX_X;
            maj_length=1; %1=x
2=y
        else
            y_theta=MAX_Y;

x_theta=x_d(ind_ymax);
            maj_length=2; %1=x
2=y
        end

        angle(kkj,1) = atand((-
centroid(kkj,2) + y_theta)/(-
centroid(kkj,1) +x_theta));

        four_extreme(:,:,kkj) =
[MIN_X y_d(ind_xmin); MAX_X
y_d(ind_xmax); x_d(ind_ymin)
MIN_Y; x_d(ind_ymax) MAX_Y];
        majorlength(kkj)
=maj_length;

end
%% ellipsoid pits
coord_dash = cell(max(T),1);
pit_coordinate = cell(max(T),2);
coord_ellipse=cell(max(T),1);
coord_ellipse_centred=cell(max(T
),1);
dash_ellipse=cell(max(T),1);
for ikk=1:max(T)
  x_ell_min =
four_extreme(1,1,ikk);
  x_ell_max =
four_extreme(2,1,ikk);
  y_ell_min =
four_extreme(3,2,ikk);
```

```
  y_ell_max =
four_extreme(4,2,ikk);

  a=(x_ell_max-x_ell_min)/2;
%k/2
  b=(y_ell_max-y_ell_min)/2;
%l/2

  x_ell= [-a :0.1: a]';

y_ell_1 = sqrt(b^2*...

(ones(size(x_ell,1),size(x_ell,2
))...
    -((x_ell).^2/a^2)));

y_ell_2=-y_ell_1;

coord_ellipse_centred{ikk} =
[x_ell y_ell_1 y_ell_2];


x1_dash = x_ell*cosd(angle(ikk))
+y_ell_1*sind(angle(ikk));
x2_dash = x_ell*cosd(angle(ikk))
+y_ell_2*sind(angle(ikk));

y1_dash =
y_ell_1*cosd(angle(ikk)) -
x_ell*sind(angle(ikk));
y2_dash =
y_ell_2*cosd(angle(ikk)) -
x_ell*sind(angle(ikk));
dash_ellipse{ikk} = [x1_dash
x2_dash  y1_dash y2_dash];

x1_d_2=x1_dash+centroid(ikk,1)*o
nes(size(x1_dash,1),size(x1_dash
,2));
x2_d_2=x2_dash+centroid(ikk,1)*o
nes(size(x2_dash,1),size(x2_dash
,2));

y1_d_2=y1_dash+centroid(ikk,2)*o
nes(size(y1_dash,1),size(y1_dash
,2));
y2_d_2=y2_dash+centroid(ikk,2)*o
nes(size(y2_dash,1),size(y2_dash
,2));

coord_ellipse{ikk}=[x1_d_2
x2_d_2 y1_d_2 y2_d_2];


figure(23)
hold on
```

```
plot(x_ell,y_ell_2,'k')
plot(x_ell,y_ell_1,'k')

plot(x1_dash,y1_dash,'r')
plot(x2_dash,y2_dash,'r')

plot(x1_d_2,y1_d_2,'g')
plot(x2_d_2,y2_d_2,'g')

c = centroid(ikk,3);
[X11 Y11] =
meshgrid(x_ell,y_ell_1);

T1=1-
(((X11)/a).^2+((Y11)/b).^2);
indpos1=find(T1>0);
z11 = c*sqrt(T1(indpos1));

[X22 Y22] =
meshgrid(x_ell,y_ell_2);

T2=1-
(((X22)/a).^2+((Y22)/b).^2);
indpos2=find(T2>0);
z22 = c*sqrt(T2(indpos2));

x11=X11(indpos1);
x22=X22(indpos2);
y11=Y11(indpos1);
y22=Y22(indpos2);

x11_dash = x11*cosd(angle(ikk))
+y11*sind(angle(ikk));
x22_dash = x22*cosd(angle(ikk))
+y22*sind(angle(ikk));

y11_dash = y11*cosd(angle(ikk))
-x11*sind(angle(ikk));
y22_dash = y22*cosd(angle(ikk))
-x22*sind(angle(ikk));

x11c=centroid(ikk,1)*ones(size(x
11,1),size(x11,2));
y11c=centroid(ikk,2)*ones(size(y
11,1),size(y11,2));
x22c=centroid(ikk,1)*ones(size(x
22,1),size(x22,2));
y22c=centroid(ikk,2)*ones(size(y
22,1),size(y22,2));

x11pit=x11_dash+x11c;
y11pit=y11_dash+y11c;

x22pit=x22_dash+x22c;
y22pit=y22_dash+y22c;
```

```
pit_coordinate{ikk,1}=[x11pit,y1
1pit,z11];
pit_coordinate{ikk,2}=[x22pit,y2
2pit,z22];

figure(24)
hold on
plot3(x11pit,y11pit,z11,'b.')
plot3(x22pit,y22pit,z22,'r.')

end
```